Kanazawa, T., Sager, W.W., Escutia, C., et al., 2001
Proceedings of the Ocean Drilling Program, Initial Reports Volume 191

4. Site 1179[1]

Shipboard Scientific Party[2]

BACKGROUND AND OBJECTIVES

The main objective at Site 1179 was to drill a borehole ~100 m into the basaltic top of the ocean crust, install a guidebase and casing in the hole, and emplace a seismometer with a recording package that would allow later data retrieval by submersible vehicles. Site 1179 was chosen as one of three locations in the northwest Pacific Ocean where broadband seismometers are to be installed in Ocean Drilling Program (ODP) boreholes (Fig. F1). The other two locations are the inner wall of the Japan Trench, where two seismometers were installed during Leg 186 at Sites 1150 and 1151 (Sacks, Suyehiro, Acton, et al., 2000), and another to be installed at proposed Site WP-1 on the Philippine Sea plate during ODP Leg 195. Together, these seismometers augment the local network of land seismometers in Japan, eastern Russia, China, the Philippines, and elsewhere. The Leg 191 and other ocean borehole seismometers fulfill two needs identified by proponents of the International Ocean Network (ION) (Purdy and Dziewonski, 1988). They provide better coverage of earthquakes occurring at the subduction zones of the northwest Pacific, and they fill a gap in the global coverage of earthquake ray paths needed for more accurate tomographic studies of the Earth's mantle. For local seismicity and tectonic studies, oceanic seismometers lessen the asymmetry of station coverage, making it possible to determine more accurate earthquake locations and focal mechanisms. In its northwest Pacific location (Fig. F2), Site 1179 fills a gap in the global array of seismic stations for tomographic studies. Such studies would be more accurate and have better resolution if the global array of seismometers was regularly spaced rather than having stations clustered on the 29% of the Earth's surface covered by land. By filling a large gap, the Site 1179 seismometer will record seismic rays passing through parts of the mantle that would not be imaged otherwise.

F1. Location map of seismic station coverage in the northwest Pacific, p. 51.

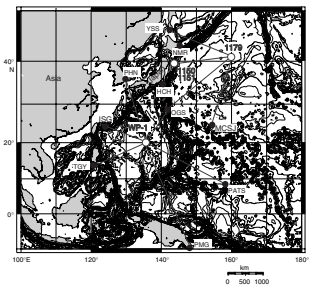

F2. Locations of Leg 191 drill sites, p. 52.

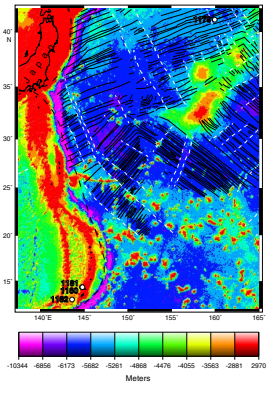

[1]Examples of how to reference the whole or part of this volume.
[2]Shipboard Scientific Party addresses.

Another compelling reason for emplacing borehole seismometers in the oceans, an expensive undertaking, is that submerged boreholes have been shown to be extraordinarily quiet environments (e.g., Stephen et al., 1999). For this reason, a seismometer situated at the bottom of an ocean borehole should have a better signal-to-noise ratio than similar land stations, allowing smaller earthquakes to be recorded and more accurate studies of earthquake waveforms. Both are the basis for detailed studies of the Earth's interior structure.

Naturally, a borehole into oceanic basement in the northwest Pacific also allows the addressing of many scientific problems more commonly attacked during ODP drilling: sediment and basalt geochemistry, regional history of sedimentation, heat flow, fossil distribution and time scales, paleoceanography, paleolatitude and plate tectonics, physical properties of the basaltic crust and sediment column, and occurrence of microbes in the crust. Although the 100-m penetration into the igneous crust at Site 1179 is not great, it is nonetheless one of a small number of boreholes to sample more than a few meters into the upper igneous crust, making the data collected in this section of particular value. Studies of the igneous section undertaken by Leg 191 scientists include igneous geochemistry and isotopic signatures to learn about magma sources and emplacement, radiometric geochronology for better dating of the crust and magnetic lineations, paleomagnetism for plate tectonic drift studies, seismic velocity and other physical properties measurements to better characterize the geophysical properties of the crust, and structure and fracture geometry to illuminate volcanic processes and hydrology. Sediment column studies include sedimentation history of the northwest Pacific, paleontology of siliceous and calcareous microfossils and palynomorphs to broaden our knowledge of fossil time scales and paleoceanography, the occurrence and timing of ash layers to understand the eruptive histories of western Pacific island arcs, magnetic stratigraphy to better define the polarity reversal time scale, magnetic reversal transitions to understand the geodynamo, and the occurrence of microbes to define the depth and extent of the deep biosphere. In addition to these studies with their regional and global implications, scientific description of the boreholes and their properties was necessary to characterize borehole wall properties both for finding the best depth to install the seismometer and for making local corrections to propagation paths.

Geologic and Tectonic Setting

Site 1179 (proposed Site WP-2A) is located on abyssal seafloor northwest of Shatsky Rise, ~1650 km east of Japan (Fig. F2). This part of the Pacific plate was formed during the Early Cretaceous, as shown by northeast-trending M-series magnetic lineations that become younger toward the northwest (Larson and Chase, 1972; Sager et al., 1988; Nakanishi et al., 1989). As shown by recent anomaly mapping, the site is situated on magnetic Anomaly M8 (Nakanishi et al., 1999), corresponding to an age of ~129 Ma and the Hauterivian stage of the Early Cretaceous (Gradstein et al., 1994, 1995). We plotted the magnetic anomaly data around Site 1179 and confirmed its location near the center of Anomaly M8 (Fig. F3). Paleomagnetic data indicate that the Pacific plate has drifted northward ~30° since the Cretaceous (Sager and Pringle, 1988; Larson et al., 1992), which suggests that the crust at Site 1179 likely formed ~10° north of the equator. If plate drift continues at its

F3. Magnetic anomalies in the vicinity of Site 1179, p. 53.

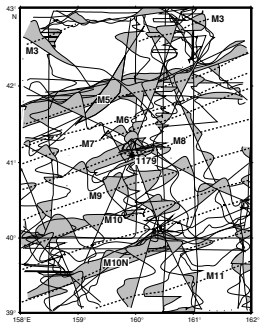

present speed and direction, after 7–8 m.y. the lithosphere, including Site 1179, will be subducted beneath the southern Kuril Trench.

Northwest Pacific Stratigraphy

Cores collected in the northwest Pacific basin by the Deep Sea Drilling Project (DSDP) (Legs 6, 20, 32, and 86) and ODP (Legs 185 and 191) over the last 30 yr show similar stratigraphy with three primary layers (Fisher, Heezen, et al., 1971; Heezen, MacGregor, et al., 1973; Larson, Moberly, et al., 1975; Heath, Burckle, et al., 1985; Plank, Ludden, Escutia, et al., 2000). At the top is a Miocene to Pleistocene blanket of siliceous clay and oozes that contains numerous ash layers. In these sediments, diatoms and radiolarians are common to abundant but few calcareous microfossils are found. This Neogene layer can be >200 m thick. Comparison with holes located southeast of Shatsky Rise (Fig. **F4**) indicates that this layer is largely absent or attenuated in that region. This observation implies that the thick Neogene layer results from productivity in divergent waters northeast of the western boundary current. In its lower reaches, the Neogene clayey layer may contain zeolite. The gray to olive siliceous clays and oozes typically pass downward to barren brown or reddish brown clays. Although the age of these clays is usually undetermined, at some sites it belongs to the mid- to Late Cretaceous (e.g., Sites 51, 194, and 195) but it may contain a highly condensed Tertiary section as well (e.g., Site 576). Beneath the barren clays is an often poorly recovered layer consisting of calcareous oozes, chalk, or marl deposited soon after the formation of the crust while it was at a depth above the calcite compensation depth (CCD). This layer suffered poor recovery because it is associated with chert and porcellanite layers that are ubiquitous in the northwest Pacific. During rotary drilling using water as a flushing agent, the chert causes the formation to be ground up and the softer parts to wash away, generally leaving only rounded chert fragments and slight traces of the softer matrix. In many holes, the top of the chert layer seems to correspond to the top of the calcareous section (Fig. **F4**) but this relationship is difficult to discern in some holes owing to poor recovery. In some other holes, however, the chert appears higher in the section with the barren brown clays.

F4. Comparison of stratigraphic sections from DSDP and ODP holes drilled in the northwest Pacific, p. 54.

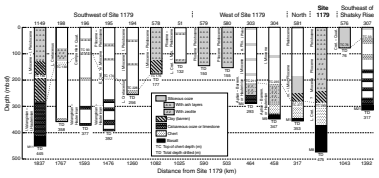

OPERATIONS

Transit and Site Occupation

After a day of speeches by Yokosuka officials and ODP luminaries and music by the Tahoka Junior High School orchestra, the *JOIDES Resolution* departed Yokosuka Pier 2 at 0745 hr on 22 July 2000 (all times Universal Time Coordinated + 9 hr) headed for proposed Site WP-2A, ~1000 nmi distant. The ship made good time, traveling at an average of 12.5 kt, collecting magnetic and echo-sounder data en route, arriving at the site at 2116 hr on 25 July after a transit of 85 hr, 31 min. Because of time pressures and the fact that proposed Site WP-2 is located at the intersection of two Global Positioning System (GPS)-navigated multichannel seismic lines, it was decided that additional seismic profiling work would be of limited utility and no additional site survey data were collected. Upon reaching the site, the *Resolution* slowed, the thrusters were lowered, and the ship was positioned by GPS over the site. Two beacons were dropped at 2215 hr on 25 August to establish Site 1179.

Hole 1179A

By 2215 hr on 25 July, the advanced hydraulic piston corer/extended core barrel (APC/XCB) bottom-hole assembly (BHA) was being lowered. The first APC core extended prematurely and returned empty. Nonetheless, it was discovered that the core cutting shoe had traces of mud, indicating that the BHA was near the seafloor. The drill string was lowered an additional 6 m, and the next APC core fired successfully. Upon retrieval, this core was found to be completely full, having overshot the mudline. The core was curated as Core 1H, but it was necessary to establish the mudline by pulling the pipe up, so Hole 1179A was terminated at 1615 hr on 26 July (Table T1).

T1. Coring summary, p. 133.

Hole 1179B

After raising the drill string by 4 m, Hole 1179B was spudded with the APC/XCB BHA at 1700 hr on 26 July. The core barrel returned with a valid mudline and 7.6 m of siliceous ooze, establishing the seafloor at 5574.9 meters below rig floor (mbrf). APC coring proceeded ahead to Core 6H. The tensor tool was run on Cores 4H through 6H, and the Adara temperature tool collected data on Core 4H. In addition, a perfluorocarbon tracer (PFT) injection was made into the drill pumps during Core 5H coring as a microbiological test for drilling fluid contamination in the cores.

Trouble occurred during the deployment of what would have been Core 7H. The drill-string accelerometer (DSA) tool, deployed for the first time in a redesigned configuration, caused the core barrel to become lodged in the drill string ~650 m below the ship. Efforts to free the core barrel were ineffective, and it became necessary to pull up 18 stands of pipe to retrieve the stuck tool. This ended Hole 1179B, after we reached a depth of 55.1 meters below seafloor (mbsf).

Hole 1179C

Upon the completion of Hole 1179B, problems were encountered with the core winch that required repair, causing a delay of several hours. The ship was offset 10 m south (Fig. F5), and Hole 1179C was spudded at 1400 hr on 27 July with Core 1H reestablishing the mudline at 5576.7 mbrf. The interval from 5.8 to 48.8 mbsf was drilled without coring to save time. Coring resumed at 48.8 mbsf with Core 2H, positioned to overlap the cores of Hole 1179B by 5 m. APC cores were retrieved from 48.8 to 266.8 mbsf (Cores 2H through 24H), recovering Neogene siliceous clays and oozes with ash layers. The tensor tool was used to orient Cores 4H–11H and 13H–24H; the Adara temperature tool was run on Cores 3H, 6H, 9H, and 12H; and a PFT test was run on Core 21H. During coring of Core 24H, the formation became too stiff for further use of the APC. Coring was switched to the XCB, and Cores 25X through 27X were cut between 266.8 and 292.9 mbsf. An unsuccessful PFT test was run on the last XCB core. The cutting time for Core 27X increased dramatically, and only chert fragments were recovered. It was decided that the XCB was not the optimal coring apparatus for the chert-infested layers expected at greater depth, so Hole 1179C was terminated at 1200 hr on 29 July, having cored to a depth of 292.9 mbsf.

F5. Relative positions of holes drilled at Site 1179, p. 55.

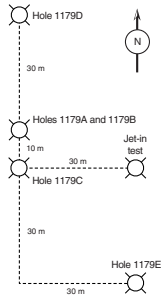

Hole 1179D

The drill pipe was raised to pull out of the hole, and the ship was offset 30 m to the east of Hole 1179C. A jet-in test for the casing was performed, and then the drill string was recovered. Drilling operations were suspended briefly while ship's personnel lowered the video camera to detorque a new coaxial cable.

After moving the ship ~30 m north of Holes 1179A and 1179B, a rotary core barrel (RCB) BHA was assembled and run to the seafloor. Hole 1179D was spudded at 0300 hr on 31 July. Drilling continued with a center bit to a depth of 281 mbsf, ~11 m above the depth at which the previous hole had been terminated. RCB coring commenced and chert layers were encountered in the next nine cores. Apparently the chert layers were interbedded with soft sediments, because only chert fragments were recovered in this interval; the speculation is that the chert layers fragmented and ground up the soft sediments, which were in turn flushed away by the circulated fluid. Of the 86.5 m of cherty layers penetrated, only 5.8 m of chert fragments was recovered.

Core 10R brought a surprise: basalt. The contact with igneous basement was expected at a depth of >400 m, based on seismic reflection data. Drillers estimated the basement depth at 375 mbsf by the depth of the drill pipe when increased resistance was encountered. Coring proceeded in basaltic rock until 100 m of basement penetration had been achieved (Core 22R), making the total depth of Hole 1179D 475.0 mbsf. Recovery in the basaltic section ranged from 18–19 cm (Cores 15R and 16R) to 6.42 m (Core 22R), with an average of 44%. The penetration rate in basement averaged 1.9 m/hr.

After coring ended, the bit was released at 0215 hr on 5 August, a wiper trip was made to ream the hole, and sepiolite mud was pumped into the hole in preparation for downhole logging. Rigging for logging was completed by 0730 hr, and the Schlumberger triple-combination (triple combo) tool string was run down with the addition of the Lamont-Doherty Earth Observatory (LDEO) temperature tool at the bottom and an additional gamma-ray tool at the top. The tool string passed down to 300 mbsf and was run back up the hole ~100 m for calibration purposes. Upon resuming its downward trip, the tool was unable to pass 253 mbsf; the hole evidently collapsed or bridged. The logging tool string was returned to the derrick and rigged down at 2245 hr on 5 August. A cement plug was pumped into the hole to seal it, and the drill string was tripped to the surface, the end reaching the rotary table at 1150 hr on 6 August.

Hole 1179E

While the drill string was being disassembled and pulled back to the surface, the ship was offset ~70 m to the south and 30 m to the east of Hole 1179D. A reentry cone was assembled and centered in the moonpool. The casing shoe joint and four additional joints of 16-in casing were made up and attached to the cone. A BHA with a 14.75-in tricone drill bit was made up and engaged with the hanger assembly of the casing string. The reentry cone and casing assembly were run to the seafloor and landed at 1115 hr on 7 August. Within 1.75 hr, the 64 m of casing was jetted in and the running tool was released from the drill string. By 0230 hr on 8 August, the drill string was recovered.

During the upward trip of the drill pipe from the casing deployment, the vibration-isolated television (VIT) camera was lowered to image an

acoustic release test. The camera winch had difficulty raising the camera frame in depths greater than ~4600 m. To make sure that the new coaxial cable was not wrapping around the drill string, the cable was detorqued by lowering the camera sled to successively greater depths and reeling it back in. This exercise was finished by 1400 hr on 8 August, and the crew began making up the 14.75-in drilling assembly to be used in drilling Hole 1179E.

By 0200 hr on 9 August, the camera and drill string were in position to attempt reentry and after 5 hr, 15 min, the reentry was accomplished. At 1015 hr on 9 August, drilling commenced. Igneous basement was contacted at 5948 mbrf (~371 mbsf), ~4 m higher than at Hole 1179D. The 14.75-in hole was terminated at 2330 hr on 10 August, after penetrating about 28 m into basement. The hole was swept with sepiolite mud, and a wiper trip was made to a depth of 80 mbsf. After additional flushing of the hole with sepiolite mud, the drill string was recovered. The reentry cone was cleared at 0645 hr on 11 August, and the bit cleared the rotary table at 1830 hr on the same day.

A 10.75-in casing string was assembled for insertion inside the borehole. A total of 30 casing joints were assembled, including a cementing shoe on the bottom and a casing hanger on top. The BHA was made up and attached to the casing, and the downward trip began. At 0600 hr on 12 August, it was discovered that the casing was constructed with one joint too many. The drill string was pulled back to the surface, and the mistake was corrected. By 0045 hr on 13 August, the drill pipe and VIT camera were in position for reentry.

At 0230 hr that same day, the hole was reentered for the second time. The casing hanger landed without incident with the casing shoe at a depth of 5970 mbrf (393.4 mbsf). Latch engagement was verified and the casing was cemented in place with 50 bbl of cement slurry. The running tool was released, and the pipe trip back to the surface began. The pipe trip was slowed again by difficulties with the winch raising the VIT camera frame. However, all tools were clear of the rotary table by 0300 hr on 14 August.

Drilling at Hole 1179E was interrupted owing to inclement weather. Forecasts predicted that a tropical storm, named Ewiniar, would turn and head toward the site location without leaving enough time to make a round trip of the pipe and do a significant amount of drilling.

The drill collars were laid out in preparation for bad weather while the ship stood by at Site 1179 waiting on weather forecast updates. At 1530 hr on 14 August, the ship began moving east, out of the path of the storm, which was predicted to cross the site. By 15 August, the storm had intensified into a typhoon and the ship turned south to move farther out of the storm path. When the storm moved north, rather than east, the ship turned north-northeast at 0700 hr on 17 August to head back to Site 1179 in hopes of reoccupying the site as soon as the storm passed. As the ship approached the site, the storm began to lose strength and continued a slow northward drift. At 0930 hr on 18 August, thrusters were lowered and the *Resolution* reoccupied Site 1179, having lost ~104 hr to weather. During its flight from the typhoon, the *Resolution* covered 909 nmi, collecting magnetic and bathymetry data all the while. Ewiniar stayed northwest of the site, ~220 nmi away, until it faded to a tropical depression and finally to a low-pressure cell that lost its identity.

The drill string was assembled and lowered to the reentry cone with the VIT camera. After 45 min of attempts, Hole 1179E was reentered at 2230 hr on 18 August. Once the camera frame was recovered, the pipe

trip was resumed and by 0315 hr on 19 August, the bit had been lowered to 5965 mbrf (388 mbsf). The cement shoe was drilled out in ~3 hr, and drilling in basement commenced. Drilling continued to a depth of 6052 mbrf (475 mbsf), which was reached at 0115 hr on 21 August. A wiper trip was made through the bottom of the hole and sepiolite mud was pumped in. The drill string was tripped back to 56 mbsf, where 15 min was taken to flush the upper casing and reentry cone. The pipe trip then continued until the bit reached the rotary table at 1445 hr on 21 August. Hole 1179E was complete and preparations began for installing the seismometer assemblies.

After the drill string was on board, construction began on the 4.5-in casing to hold the seismometers inside the borehole. The two seismometers were attached to the bottom part of the casing string, and electrical cables were connected. The cables were run up the outside of the casing and attached with tie wraps and tape. Centralizer spacers were attached to the casing every 1.5 m. Technicians and crew members continued with this assembly for ~11 hr, until 0200 hr on 22 August. The riser hanger was mated to the riser, and the cables were cut to length and terminated, a process that continued until 2200 hr. Installation and the connection of the electrical package (G-box) to the seismometer cables required another 3.5 hr.

The casing and seismometers were run to the seafloor and were positioned for reentry at 0945 hr on 23 August. Reentry was accomplished at 1110 hr, and the casing was run in the hole without incident. Fifty barrels of cement slurry were pumped down the drill string to the casing to cement the seismometer assembly to the rock of the borehole walls. The VIT camera frame was winched back to the ship so that the battery frame could be deployed.

Assembly of the battery frame halves around the drill string over the moonpool commenced at 1830 hr and was finished by 0215 hr on 24 August. The battery frame was attached to a bridle hung from the logging line. Because it was too dark to see obstructions in the moonpool, deployment was delayed until daylight at 0415 hr. The battery frame was lowered through the moonpool without incident, despite occasional surges from the ship's heave. The battery frame landed at 0915 hr, and an acoustic signal was sent to the release mechanism, which confirmed having released the frame. By 1230 hr, the logging line was recovered and the VIT camera was lowered for a visual inspection of the installation. The battery frame was found to have landed properly. At 1415 hr, all hands watched the J-tool rotate and release the casing, successfully ending the seismometer deployment. The VIT camera was recovered, and the drill string was tripped back to the ship. The BHA cleared the rotary table at 0515 hr, and the derrick was readied for transit.

SITE GEOPHYSICS

Site Survey Data

Survey data were collected for Site 1179 in August 1996, during cruise KH96-3-1 of the *Hakuho Maru* from the University of Tokyo Ocean Research Institute (Fig. F6). The ship was navigated by GPS satellite and collected standard underway geophysical data, including magnetic field measurements and 3.5-kHz echo-sounder profiles. The magnetic data were used to define magnetic anomalies around the site,

F6. Site survey cruise tracks, p. 56.

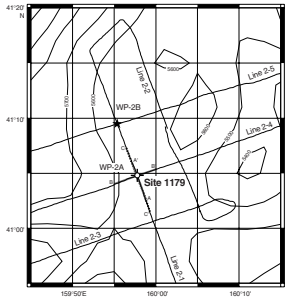

and the echo-sounder profiles were used to show shallow sediment layers. To define the complete sedimentary section, a 1.2-km-long 24-channel multichannel seismic (MCS) streamer was used to collect reflection seismic data over the site. The MCS data were stacked, filtered, and migrated for final interpretation. Because Site 1179 is situated at the intersection of two GPS-navigated MCS lines, it was decided that additional seismic data collection by the *JOIDES Resolution* was unlikely to provide significantly better characterization of the sedimentary sequence so no additional seismic data were collected over the site during Leg 191.

Seismic Stratigraphy

Most knowledge of sediment thickness and character in the northwest Pacific basin has come from single-channel seismic profiles collected by various expeditions over the past several decades. These profiles show that sediments in this region are generally thin, typically <500 m from seafloor to acoustic basement, which is often presumed to be the top of igneous ocean crust (Ludwig and Houtz, 1979). Ewing et al. (1968) characterized the appearance of single-channel seismic lines in the region, dividing the sediment section into as many as four layers: an upper transparent layer (weakly reflective), an upper opaque layer (well stratified and more reflective or reverberant), a lower transparent layer, and acoustic basement (a strong reflector below which no coherent reflections are seen). In older single-channel seismic profiles, the lower opaque layer is often highly reflective owing to the bubble pulse of the seismic source reverberating in an interval of multiple strong impedance contrasts. As a result, the lower opaque layer may mask the top of the igneous crust and acoustic basement may not correspond to the sediment/basalt contact. Flat-lying acoustic basement is often an indicator that the reverberant layer masks true igneous basement.

In the northwest Pacific near Site 1179, seismic sections typically show only one transparent and one reverberant layer. DSDP and ODP drilling in the region (Legs 6, 20, 32, 86, and 185) showed that the transparent layer consists of Late Cretaceous and late Cenozoic siliceous oozes and clay, frequently with ash layers. The reverberant layer appears to correspond to pervasive chert layers (Fig. **F4**) (Fischer et al., 1971; Heezen, MacGregor, et al., 1973; Larson, Moberly, et al., 1975; Heath, Burckle, et al., 1985; Plank, Ludden, Escutia, et al., 2000). In the cherty interval, host sediments are frequently poorly indurated and washed away during coring; however, the few samples that have been recovered suggest the layers containing chert range from siliceous and calcareous oozes to chalk and marl (e.g., Larson, Moberly, et al., 1975; Plank, Ludden, Escutia, et al., 2000). In much of the northwest Pacific, the lower layer of calcareous sediments indicates a period when the lithosphere was young and shallow above the CCD, whereas a highly condensed barren clay interval and siliceous oozes above were formed after the lithosphere subsided beneath the CCD. In the midgyre region of the north Pacific, Neogene sediments are thin. Beneath the western boundary currents, however, Miocene to Pleistocene sediments can be >200 m thick (Heath, Burckle, et al., 1985; Plank, Ludden, Escutia, et al., 2000).

Site 1179 seismic profiles display a seismic stratigraphy similar to that outlined by Ewing et al. (1968), with a transparent layer ~0.32 s thick and a reverberant layer 0.13 s deep. Acoustic basement is a high-amplitude reflector at a depth of 0.44 s two-way traveltime below the

seafloor (Fig. F7). This reflector displays relief on the order of 0.1 s, including diffractions and offsets, and little coherent seismic energy at greater times. Such characteristics are typical of the top of oceanic crust, which is how this reflector is interpreted at Site 1179. On one seismic line, the site appears to be located at the bottom of a flat-floored graben, ~1 km across, with a relief of 0.05 s (~50 m). On the perpendicular seismic profile (Fig. F8), this graben is not evident but the basement reflector shows downward deflection and discontinuous reflectors 0.05 s higher in the section. This appearance may be the result of being near the edge of the graben, with diffracted energy and imperfect migration causing the shallower reflectors.

Seismic lines show sedimentary layers draping conformably on layers below, so seafloor undulations reflect basement topography (Figs. F7, F8, F9). This character is also seen in greater detail in 3.5-kHz profiles showing the uppermost sediments (Fig. F9). These observations imply that sedimentation has been laterally uniform and likely originates from pelagic sources. In seismic profiles, the sedimentary section consists of an upper transparent layer from the seafloor to a depth of ~0.30 s two-way traveltime. Weak, discontinuous reflectors characterize this layer. The lower sedimentary section contains two strong reflectors at depths of 0.30 and 0.38 s two-way traveltime. Beneath these horizons is another transparent layer, ~0.06 s two-way traveltime in thickness, overlying acoustic basement (Figs. F7, F8).

Figure F10 shows the correlation between one of the seismic lines over Site 1179, the Site 1179 lithostratigraphic column developed from core data, and predicted depths of unit boundaries, using a velocity-depth relation derived from ocean drilling velocity data (Carlson et al., 1986) (See "Physical Properties," p. 35). Using this velocity-depth relationship, the predicted depths of the sediment/basalt contact and the tops of Units III and IV all correspond to strong reflectors. The basalt/sediment contact correlates to the reflector, supposed to be acoustic basement at 0.44 s two-way traveltime below seafloor. The top of the chert section (at the boundary between Units III and IV) and the boundary between the red-brown pelagic clays (Unit III) and the diatom-bearing radiolarian ooze (Unit II) line up with the two parallel reflectors at depths of 0.38 and 0.30 s two-way traveltime, respectively. Unlike the other unit boundaries, the boundary between Units II and I does not align with a prominent reflector but this boundary is not sharp, nor does it have a large change in physical properties. The weak, discontinuous reflectors in the upper transparent layer appear to correlate with groups of ash layers.

SEDIMENTOLOGY

Sediments and sedimentary rock recovered from the 377-m sedimentary column at Site 1179 are clayey siliceous ooze, clay, and chert. We recovered one core from Hole 1179A, six cores from Hole 1179B, 27 cores from Hole 1179C, and 11 cores from Hole 1179D. Recovery averaged 98.8% in the ooze and clay above 283 mbsf, with lowest recoveries (90%) in the stiff brown clay (246–283 mbsf). Recovery ranged from 2% to 11% in the cherty section below. Sediments above 283 mbsf are soft, mainly massive, and varied in color and composition. The sediments below 283 mbsf, mostly cherts and porcellanite, are more compact and show less variation. Cores of softer sediments drilled using the APC are largely undisturbed to slightly disturbed by drilling. The cherty rocks,

F7. Multichannel seismic line corresponding to A–A′, p. 57.

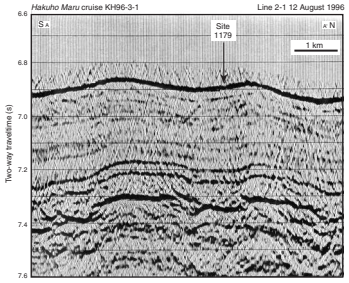

F8. Multichannel seismic line corresponding to B–B′, p. 58.

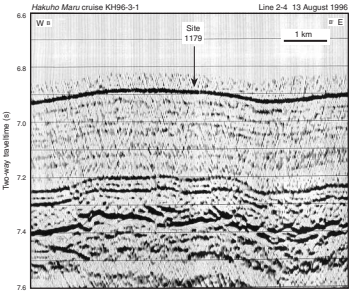

F9. Echo-sounder profile corresponding to C–C′, p. 59.

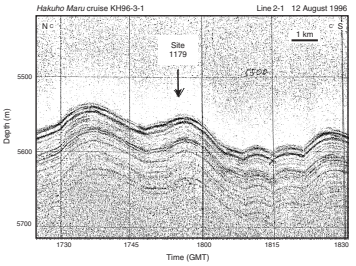

F10. Correlation between seismic line A–A′, the lithostratigraphic column, and predicted depths of unit boundaries, p. 60.

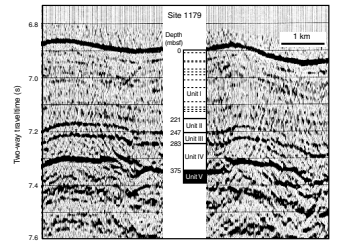

drilled with the RCB, are highly fragmented by drilling. Lithology and recovery are similar to those of pelagic northwest Pacific sites drilled during earlier DSDP and ODP legs (see Fig. F4). Based on composition and color, we divide the section at Site 1179 into four lithostratigraphic units (Fig. F11) and describe their sedimentary features below.

Lithostratigraphic Unit I

Interval: Core 191-1179A-1H; Core 191-1179B-1H through 6H-CC; and Core 191-1179C-1H through Section 20H-2, 22 cm.
Depth: 0.0–10.2 mbsf (Hole 1179A); 0.0–55.25 mbsf (Hole 1179B); and 0.0–221.52 mbsf (Hole 1179C)
Thickness: 221.52 m
Age: late Miocene to Holocene (lower contact at base of Chron C4n.1n [~7.562 Ma])
Description: clay- and radiolarian-bearing diatom ooze

Cores 191-1179A-1H through Section 191-1179C-20H-2, 22 cm, contain predominantly diatoms, radiolarians, and clay. The proportion of these three major components varies from core to core and even from section to section. Generally diatoms dominate, but clay and radiolarians are also common. According to the classification shown in Figure F3, p. 40, in the "Explanatory Notes" chapter, this lithostratigraphic unit is typically composed of clay-rich to clay-bearing radiolarian-bearing diatom ooze (Fig. F12A) with intervals of diatom-rich clay (Fig. F12B).

Sediments show a moderate range of coloration, mainly in the green part of the spectrum. Olive gray is the dominant background color through this unit. Other colors include greenish gray, purplish gray, brown, pale olive, and grayish green. Furthermore, the unit is ~35% mottled in terms of variegated coloration. Colors had faded markedly in some cores that were reexamined a few days after initial splitting.

Texturally, the sediments are classified as immature. Silt-sized particles commonly dominate over sand- and clay-sized particles in this lithostratigraphic unit. Silt-sized particles include small whole and fragmented frustules of diatoms and tests of radiolarians and less numerous grains of silicic light-colored glass. Trace components include quartz, feldspar, and silicoflagellate tests. Authigenic zeolite, where present, is silt sized. Sand-sized skeletal remains of diatoms and radiolarians or clay-sized clay dominate locally. The maximum particle size ranges from 100 to 300 µm; the minimum particle size is <2 µm. Opaline particles have organic shapes; diatoms are mainly discs and flakes, radiolarians are irregular, and the spines of radiolarians and sponge spicules are largely rod and horn shaped. Glass and quartz grains are subangular to angular in shape.

Overall, sediments of this lithostratigraphic unit are massive in appearance (Fig. F13), although thin to thick (i.e., a few millimeters to 35 cm) laminations and beds (Fig. F14) are observed across Unit I. These layered features are discriminated largely in terms of color contrast and changes in texture, which apparently are related to local composition (i.e., changes in the proportion of siliceous ooze to clay). In this sense, they are considered to be primary bedding features and are mentioned as thus in the visual core description (VCD) forms. If the siliceous ooze content in one of these beds is >75%, the sediments are largely fine sand to coarse silt; whereas if the ooze content is lower than ~65%, the sediments are medium silt to clay. Internal sedimentary structures within the interbedded laminae and beds include planar laminae (Fig.

F11. Lithologic column divided into four lithostratigraphic units based on color and composition, p. 61.

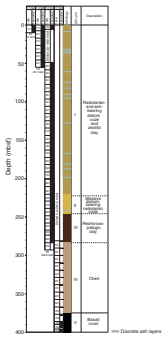

F12. Photomicrographs revealing characteristic lithologic components of Units I, II, and III, p. 62.

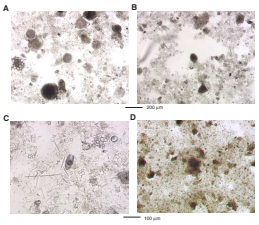

F13. Characteristic appearance of the clay- and radiolarian-bearing diatom ooze of Unit I, p. 63.

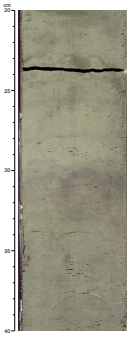

F14. Thin to thick beddinglike features of Unit I, p. 64.

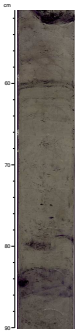

F15), silt laminae, flaserlike laminae, and isolated laminae, as well as wavy parallel bedding, cross laminae, bioturbation, concretions, and nodules. The first four types of laminae mentioned above are found randomly throughout the oozes. Vertical continuity of >4 cm is rare. Oscillatory ripples, wavy parallel bedding, and cross laminae are very rare. Overall, Unit I is ~35% bioturbated, as evidenced by colored mottles, which can be subtle in places. The degree of bioturbation ranges from common to rare and generally decreases with depth. The marks are largely 1–3 cm in size. Marks are commonly laterally oriented, although a few vertical escape burrows are present. The marks are mostly subrounded, tubular, and cylindrical in shape, but a few branching ones were also found. Some groups of marks represent an ichnocoenosis. Vertical distribution patterns of bioturbation resemble tiering in a few places (Fig. F16). Ichnogenera include *Planolites, Zoophycos, Granularia, Phycosiphon, Helminthopsis, Chondrites,* and possibly *Teichichnus*. Isolated single or multiple nodules and hard concretion-like structures were found. The nodules streak sooty black across cut cores and presumably are manganese oxide. The indurated masses are clay-poor siliceous but dominantly dolomitic fillings of burrows, including an *Ophiomorphia*-like filling with a patterned burrow lining (Fig. F17).

In petrographic detail, biogenic constituents of Unit I include the opaline-silica remains of diatoms (40%–85%), radiolarians (10%–35%), sponges (3%–9%), silicoflagellates (trace to 4%), and, less commonly, the phosphatic remains of fish (trace to 1%). Whole and large pieces of frustules of discoidal centric diatoms are especially common, but many other shapes of whole and broken frustules are common throughout the unit. Countless broken pieces range in size from medium sand down to fine silt. Radiolarians are present as whole tests, broken tests, and broken spines. Sponge spicules are remarkable in size (up to 400 µm long × 100 µm across) and appearance in terms of their central tube and, where present, surface ornamentation. No trace of diagenetic alteration of the siliceous tests is found in the smear slides high in this unit, but near its base and continuing in the radiolarian ooze below, phillipsite commonly fills and coats radiolarian tests. Inorganic constituents include clay, commonly with zeolites (10%–40%), volcanic glass (1%–7%), quartz (trace to 1%), and opaque minerals (trace). X-ray diffraction (XRD) results show the prevalence of quartz and that illite is the principal clay, with some mixed-layer chlorite (corrensite). The diatomaceous siliceous ooze (Fig. F18A, F18B) shows several of these constituents.

Accessory lithologies include at least 12 gray to light gray volcanic ash layers (Fig. F11) and numerous green and brown zeolitic and ashy clay layers. The ash layers, which are 2–10 cm thick, show thin beddinglike features with sharp basal contacts and diffuse tops (Fig. F19). Ash beds are largely unbioturbated. The proportion of glass in these ash layers is as much as 90% (Fig. F18C, F18D). The glass is mainly in the fine sand to coarse silt range and is predominantly transparent and light (rather than brown); tubular vesicles are common. Green zeolitic and ashy firm clay layers have been previously noted as characteristic of the Neogene north and west of this area at Sites 579, 580, and 581 (Heath, Burkle, et al., 1985). Here, they are 1 mm to 5 cm thick but are mainly ~1 cm in thickness. Typically, they are firmer than the adjacent ooze, perhaps from the zeolite and clay alteration products of ash. Brown zeolitic clay layers show thin bedding, planar laminae, flaserlike laminae, isolated laminae, and bioturbation. The bedding contacts are largely gradational or bioturbated. In these green and brown zeolitic clay layers, the proportion of zeolitic clay can be as large as 85%.

F15. Planar laminae of Unit I, p. 65.

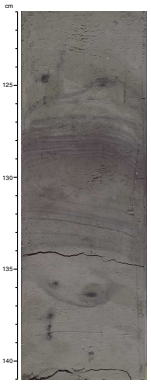

F16. Vertical distribution pattern of bioturbation of Unit I, p. 66.

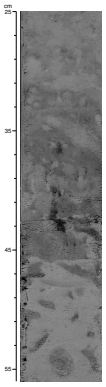

F17. Indurated burrow fill (cf. *Ophiomorphia*) of Unit I, p. 67.

F18. Photomicrographs documenting accessory lithologies of Unit I, p. 68.

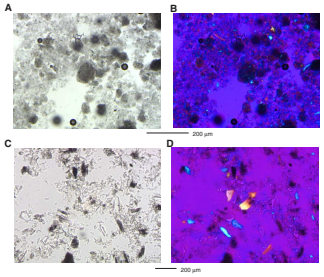

In the upper part of Core 191-1179C-20H, a gradual change in color from the top of Section 191-1179C-20H-1 to the base of Section 20H-3 indicates a gradual downcore increase in the proportion of radiolarian to diatom remains. Smear slides show the gradation. The lower contact of Unit I is placed at the base of Chron C4n.1n, which is approximately the level below which radiolarians predominate. The sedimentation rate (see "Sedimentation Rates," p. 25) changes at this depth; the diatom ooze of Unit I accumulated at ~29.29 m/m.y., and the radiolarian ooze of Unit II accumulated at ~7.56 m/m.y.

Lithostratigraphic Unit II

Interval: Sections 191-1179C-20H-2, 22 cm, through 22H-5, 127 cm
Depth: 221.52–246.0 mbsf
Age: early late Miocene to middle late Miocene (from the base of Chron C4n.1n [~7.562 Ma] to just above the base of Chron C5n.2n [~10.95 Ma]).
Thickness: 24.48 m
Description: clay-rich and diatom-bearing radiolarian ooze

Sections 191-1179C-20H-2, 22 cm, through 22H-5, 125 cm, contain radiolarians as the dominant component. Clay or zeolitic clay and diatoms are significant additional components. The proportion of these three major components varies from core to core and from section to section, so that the lithologic names of this unit are clay-rich and diatom-bearing radiolarian ooze, clay-bearing radiolarian ooze, or clay-rich radiolarian ooze.

Unit I is green and Unit II is brown. A gradational color change from pale olive to yellowish brown in Core 191-1179C-20H indicates a gradual change in lithology from diatomaceous to radiolarian ooze. The rest of Unit II is light yellowish brown, light brown, and brownish gray, with mottles in some places.

Silt-sized particles dominate over sand- and clay-sized particles through much of this lithostratigraphic unit, but locally, sand or clay size may predominate. The maximum particle size ranges from 100 to 400 µm. The minimum particle size is <2 µm, although the clay is largely in aggregates held together by zeolite. The characteristic particle shape is rodlike, owing to the many fragments of spines.

Sediments of Unit II are massive in appearance (Fig. **F20**). In terms of sedimentary structures, the unit is featureless except for rare planar laminae, flaserlike laminae, silt laminae, and isolated lamination. The degree of bioturbation is rare to moderate, as evidenced by subtle mottles (Fig. **F21**). Marks are either vertically or laterally oriented; the vertical ones resemble escape burrows. They are 1 mm to 2.5 cm in size and rounded to subrounded and cylindrical in shape. The ichnogenera include *Planolites, Granularia, Chondrites,* and *Techichnus.*

Petrographically, the unit is a radiolarian siliceous ooze (Fig. **F12C**). Biogenic constituents include the tests, broken tests, and broken spines of radiolarians (40%–60%) with lesser amounts of whole and broken diatom frustules (13%–17%), sponge spicules (trace to 2%), silicoflagellates (1%–4%), and fish remains (trace). Inorganic constituents include illite and some corrensite as clays, phillipsite (20%–35%), volcanic glass (trace to 2%), feldspar (trace to 1%), and opaque minerals (trace). Phillipsite is present as masses in clay but more characteristically as fillings

F19. Ash layer accessory lithology of Unit I, p. 69.

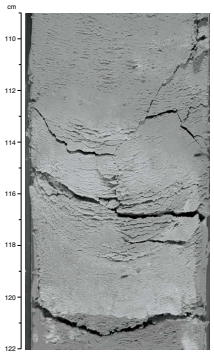

F20. Characteristic appearance of the radiolarian ooze of Unit II, p. 70.

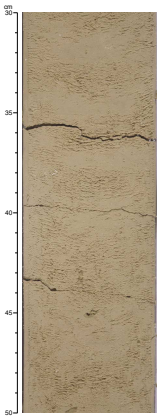

F21. Isolated bioturbation marks of Unit II, p. 71.

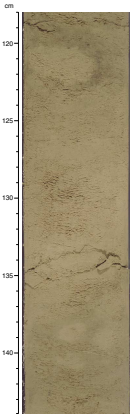

of radiolarian tests and coatings on radiolarians, large sponge spicules, and, in some instances, on grains of glass.

Accessory lithology is almost absent in this unit. A layer of light gray-colored vitric ash in Section 191-1179C-22H-3, 40 cm, contains volcanic glass (90%), feldspar (5%), and clay (5%). The contact of Unit II with Unit III is gradational both in color and composition within Section 191-1179C-22H-5 and is placed at 127 cm, where a smear slide has only a few corroded radiolarians in clay. The entire gradation is within, but near, the base of Chron C5n.2n.

Lithostratigraphic Unit III

Interval: Sections 191-1179C-22H-5, 127 cm, through 26X-CC
Depth: 246.0–283.53 mbsf
Thickness: 37.53 m
Age: late Miocene and older (top near the base of Chron C5n.2n [~10.95 Ma]; base unknown, but older than the top of Chron C5Dr [17.6 Ma])
Description: pelagic clay

Sections 191-1179C-22H-5, 125 cm, through 26X-CC contain pelagic brown clay, which by composition is zeolitic clay or ferruginous zeolitic clay. The clay is sticky to waxy on its cut surface, and it is compact.

As was noted for the top contact of Unit II, the top contact of Unit III also represents a change in the rate of sediment accumulation. Paleomagnetic results (see **"Sedimentation Rates,"** p. 25) show the top part of the clay (246.0–256.6 mbsf) to have accumulated at 1.56 m/m.y. Downhole increases in gamma radiation, with peak gamma radiation logged at ~246 mbsf, witness the slow accumulation of clay (See **"Downhole Measurements,"** p. 40).

Sediments recovered from this unit show a wide range of coloration, although it is characteristically brown, including medium brownish gray, light brownish gray, yellowish brown, medium dark to dark gray, dusky yellow brown, and chocolate colors. There are numerous mottles of contrasting colors, including orange pink.

Clay-sized (75%–99%) particles dominate over silt- (1%–21%) and sand- (0%–6%) sized particles. Sand- or silt-sized particles are chiefly zeolite. Clays are largely in aggregates, cemented with zeolite (Fig. **F12D**).

Recovered sediments are completely massive, and apparently they are structureless, except for a rare to intense degree of bioturbation in the form of contrastingly colored mottles (Fig. **F22**) in some parts of each section. The bioturbation marks are very subtle in a few sections where they are outlined with ferruginous globules or micronodules. The marks are 1 mm to 2 cm in diameter and are largely subrounded in shape. They are laterally or vertically oriented. These ichnofossils provide an ichnocoenosis worthy of further study. The ichnogenera include *Planolites, Granularia, Chondrites,* and *Phycosiphon.* Besides these bioturbation marks, rare planar laminae, flaserlike laminae, isolated laminae, and silt laminae were noted in the Unit III clay.

Petrographically, the sediments are composed of clay (75%–99%), phillipsite (3%–20%), iron oxide (0%–20%), opaque minerals (trace to 2%), and volcanic glass (0%–10%). Phillipsite, at the top of the pelagic clay, is largely of coarse silt to fine sand size, but the deeper parts of the clay have no phillipsite. Ferruginous materials (e.g., iron oxide) are found as globules, and some chert is present as an aggregate of tiny lep-

F22. Characteristic appearance of the pelagic clay of Unit III, p. 72.

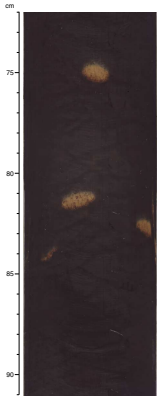

tispheres, ball-like masses of ~0.2 mm that may have filled a radiolarian test. Unit III is apparently barren except for rare fragments of fish bone.

Lithostratigraphic Unit IV

Interval: Section 191-1179C-27X-CC and Section 191-1179D-2R-2, 5 cm, through 10R-1, 14 cm
Depth: 283.53–377.15 mbsf (Hole 1179D)
Thickness: 93.62 m
Age: unknown
Description: chert

Core 191-1179C-27X and Core 191-1179D-2R through Section 191-1179D-11R-1, 14 cm, contain pieces of chert with a few pieces of porcellanite. The top of the cherty interval was within Core 191-1179C-27X, but recovery was poor in these cores. Cores 191-1179D-4R, 7R, and 10R had better recovery, 10.3%, 11.5%, and 11.4%, respectively. Note that the variously colored and moderately compact zeolitic clay layers in Section 191-1179D-1R-1 were recovered from anywhere across several meters of section; the core should have been designated a wash core.

Drilling disturbance was intense in this brittle rock. By analogy with other Pacific sites containing Cretaceous chert where recovery was marginally better or that were logged, perhaps Unit IV has an alternation of several centimeters of chert and several decimeters of such softer lithologies as chalk, siliceous limestone, and porcellanite that were not recovered. Indeed, the finest pieces broken during drilling must have been circulated out of the hole rather than recovered. Most of the recovery was of pieces ranging from equant ones 5 cm in diameter or less down to 1-cm chips. A few larger pieces that are cylindrical to ovoid are the only ones certain to have their tops still in the proper stratigraphic position.

Recovered pieces of chert display a remarkable range of coloration, which includes brown, very light olive gray, yellowish brown, reddish yellow, dark yellowish orange, moderate reddish brown, pink, dark brown, very pale brown, dark reddish gray, moderate reddish orange, dusky yellowish brown, pale blue, light olive brown, dark to light greenish gray, olive brown, strong brown, gray, light gray, bluish gray, dark red, dusky red, very dusky red, greenish white, dark to moderate yellowish brown, and dusky blue green. Several pieces show more than one color (Fig. **F23**).

Chert pieces are fractured along their surfaces with subconchoidal to conchoidal patterns. Chert pieces show subvitreous or waxy to dull lusters. The dullest pieces, porcellanites, have a microporous surface and are less dense. Porcellanite pieces are less common. They contain both cristobalite and quartz. Some porcellanite pieces contain replacements or internal molds of radiolarians by chalcedonic quartz. Some chert pieces show conspicuous mottles, which are 1 mm to 4 cm in size and are subrounded and tubular in shape. In a few pieces, large (>2 cm) mottles are composed of lighter colored (gray, light gray, or brown) porcellanite. These mottles represent ichnofossils. The ichnogenera include *Planolites, Granularia,* and *Phycosiphon*?. At least two episodes of post-chertification brecciation and resilicification or healing can be seen in the subtle color contrasts and distinct fracture-filling veins of some of the larger pieces that were recovered. Some of the 1- to 2-mm-thick veins retain vugs lined with drusy quartz (see **"Site 1179 Core Descriptions,"** p. 46, for the drawing of Sample 191-1179D-9R-1, 0–4 cm).

F23. Coloration of chert pieces of Unit IV, p. 73.

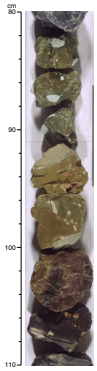

Lithostratigraphic Unit V

Interval: Sections 191-1179D-10R-1 through 22R-6
Depth: 375–475 mbsf
Thickness: 100 m
Age: Early Cretaceous
Description: basaltic crust

Basaltic crust was encountered below 375 mbsf. A detailed description of the basalt rocks from Hole 1179D can be found in "Igneous Petrology," p. 26.

Discussion

Deep-sea sedimentary columns, like those elsewhere, represent changes in the source, deposition, preservation, and diagenesis of sediments through a period of time. All the siliceous sediments, including cherts, represent one element of the sediment, and clay and ash are the two other elements recovered at Site 1179. Presumably, biogenous production of carbonate was an additional element but our information about carbonate is skimpy here.

Most of the silica formed as organic skeletons high in the water column. The first-order variation results from the early Miocene increase in silica preservation in the Pacific, here of radiolarians, and the middle Miocene increase in diatom production in the North Pacific. Little can be learned of the Cretaceous and Paleogene history of silica at this site.

Textural terms of grain size and sorting that are used to indicate sediment maturity have little significance in this realm of mixed deposition of fine detrital clay and coarser biogenous silica that settled through the water column, with reworking by bioturbation and gentle traction as the main early postdepositional physical processes. The siliceous remains and the other elements were deposited largely by settling, grain by grain, or more likely they accumulated in fecal pellets, sedimentation processes that provided a sediment relatively homogenous in composition and texture. Modest, ephemeral deep-sea currents apparently were the source of the subtle thin layerlike pattern of fine sand- and silt-textured siliceous ooze overlain by coarse silt- to clay-textured siliceous ooze found in lithostratigraphic Units I and II. Such currents may have sorted silica-rich and -poor layers in Unit IV before its chertification. Local ephemeral currents are also indicated by intervals with a vertical distribution of planar laminae, flaserlike laminae, silt laminae, and isolated laminae.

Deposition of Units II, III, and IV occurred at slow rates in an oxic environment, as evidenced by their ichnofossils and brown colors. The conclusion about rates is confirmed for Units II and III by paleomagnetic dating (see "Sedimentation Rates," p. 25). Unit I has green colors as well as bioturbation, indicating dysoxic conditions from relatively more rapid deposition, which also is confirmed by paleomagnetism. In all four lithostratigraphic units, the oxic or dysoxic ecological state was at times interrupted by anoxia, as is observed from discontinuities of the bioturbated intervals. Nevertheless, environments lasted long enough for the trace-making organisms to forage or dwell within the deposited sediments for a while, as the bioturbation marks are largely of living rather than of escaping burrow patterns. Absence of significant carbonate deposits indicates that the ocean floor was below the CCD through the deposition of the brown pelagic clay of Unit III and the sil-

iceous oozes of Units II and I. Poor recovery prevents a definitive answer to whether or not the cherts are interbedded with any carbonates.

The clays may have had any or all of the three sources that have been proposed for pelagic clay. Some are likely wind-blown detrital grains from a continental source. Eolian components generally increase in the upper Cenozoic pelagic sediments of the Pacific. The Pacific plate moved ever closer to Asia, and the interior of Asia became dryer, providing a source of "hot" loess. The finest grained clay, suspended in seawater, may have moved in ocean currents far from its fluvial sources. These detrital particles of eolian and fluvial origin were deposited and subjected to the local postdepositional processes mentioned in the previous paragraphs. Some of the clay, and in particular that with zeolites or in ashy intervals, is presumably of authigenic origin. XRD results may clarify clay sources.

Ash layers and grains of glass high in the section indicate the approach of the Pacific plate to the circum-Pacific volcanic source, although there also have been proposals that the latest Cenozoic was a time of globally increased rates of volcanism.

In summary, all the sedimentary data indicate that Site 1179 sediments were deposited in a deep-water, quiet pelagic environmental setting. Investigations here make a modest contribution to the analysis of ichnofossils and to the histories of the silica budget and volcanism.

BIOSTRATIGRAPHY

Siliceous microfossils (radiolarians, diatoms, and silicoflagellates) are common and generally well preserved in lithostratigraphic Units I and II at Site 1179 (see "Sedimentology," p. 9). They are absent from the red pelagic clays (lithostratigraphic Unit III) and generally poorly preserved (recrystallized) in the cherts (lithostratigraphic Unit IV). Numerous radiolarian datums can be identified, and upper Miocene to upper Pleistocene sediments can be assigned to established radiolarian zones, providing good biostratigraphic resolution (Fig. F24). Two species are identifiable in a single chert sample near the basaltic basement, providing an Early Cretaceous age for the oldest sediments at this site.

The only core-catcher sample that contains calcareous microfossils (calcareous nannofossils and planktonic and benthic foraminifers) is Sample 191-1179B-4H-CC (36.02 mbsf). The foraminifers are not biostratigraphically useful, but calcareous nannofossils provide an early Quaternary age for this sample. There is no explanation at this time for the preservation of calcareous microfossils in this sample and in several other samples within cores of late Pliocene to early Pleistocene age where routine inorganic geochemical analysis and palynological processing identified anomalously high $CaCO_3$ contents (Table T2). Agglutinated foraminifers are present in some upper Miocene to upper Pliocene samples, and the presence of the finely agglutinated taxon *Spirosigmoilinella compressa* constrains the interval from 229.77 to 181.94 mbsf to the middle to late Miocene. No calcareous nannofossils or foraminifers were found in lithostratigraphic Units III or IV.

Terrestrial spores and pollen and marine dinocysts and acritarchs are present and moderately to well preserved in all samples examined in the upper ~144 m of lithostratigraphic Unit I. All of these samples are of late Pliocene to late Pleistocene age except for the lowermost palynomorph-bearing sample examined, Sample 191-1179C-11H-CC (143.84 mbsf), which is of late early Pliocene age. All other sediments in litho-

F24. Ages of sediment, p. 74.

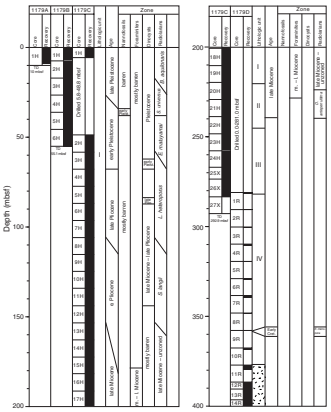

T2. Sediment carbon, nitrogen, sulfur, and hydrogen results, Site 1179, p. 136.

stratigraphic Unit I and all of lithostratigraphic Units II, III, and IV are barren of palynomorphs. A number of dinocyst datums can be identified, providing good stratigraphic resolution in sediments of late Pliocene to Pleistocene age. Terrestrial palynomorphs (pollen and spores) are most abundant in sediments of Pleistocene age, where they sometimes outnumber dinocysts, and in those upper Pliocene sediments with anomalously high $CaCO_3$ content (see Table T2).

Calcareous Nannofossils

The depths at which we drilled (below the CCD) make it almost impossible for nannofossils to be preserved in the sediment. Samples 191-1179B-1H-CC through 6H-CC were examined. Samples 1H-CC through 3H-CC are barren of nannofossils. Sample 4H-CC contains a small assemblage of nannofossils. These are *Coccolithus pelagicus,* small *Gephyrocapsa* (<5 µm), large *Gephyrocapsa* (>5 µm), *Emiliania huxleyi,* and *Pseudoemiliania lacunosa*. This assemblage can be assigned to Zone NN19 using the Martini zonation and late Subzone CN13b using the Okada and Bukry zonation. An early Pleistocene age is indicated by the absence of *Discoaster brouweri*. The presence of *E. huxleyi* is considered contamination of the sample because its first occurrence (FO) is at the beginning of Zone NN21. Cores 191-1179B-5H and 6H are barren of nannofossils.

Samples 191-1179C-2H-CC through 27X-CC are barren of calcareous nannofossils. Calcium carbonate content measurements in some intervals record $CaCO_3$ peaks that could indicate the presence of nannofossils (see Table T2). Sample 191-1179C-6H-4, 90 cm, was made into a smear slide because of a peak in the carbonate concentration of >1 wt%. Nannofossils are present in this sample, but the assemblage may be the result of contamination because it is the same assemblage as Sample 191-1179B-4H-CC, some 60 m above Sample 191-1179C-6H-4, 90 cm. Further investigation is required.

In Hole 1179D, Cores 191-1179D-1R through 10R recovered chert using the RCB. Recovery was poor, and no interbedded soft sediment was recovered. Samples were taken at various intervals where indurated sediment was in contact with the chert layers in Hole 1179D. These were Samples 191-1179D-4R-1, 25 cm; 6R-1, 40 cm; 6R-1, 60 cm; and 7R-1, 60 cm. Unfortunately, these samples are barren of nannofossils.

Foraminifers

All core-catcher samples were examined for foraminifers. Only Sample 191-1179B-4H-CC contains calcareous fossils. The washed residues from the core catchers contain very well-preserved and unbroken radiolarians, diatoms, and sponge spicules. Sample 191-1179B-4H-CC contains a well-preserved planktonic foraminiferal fauna with common *Neogloboquadrina pachyderma* (mainly sinistral), *Globorotalia inflata, Globigerina bulloides, Globigerinoides ruber,* and *Orbulina universa,* together with a few specimens of the benthic species *Cibicides* sp. and *Astrononion stelligerum.*

The first downcore appearance of a small number of poorly preserved agglutinated foraminifers was observed in Sample 191-1179C-7H-CC, where fragments of *Pseudonodosaria* sp. are recognized together with an increase in diatoms. A few fragments of *Rhabdammina* sp. were observed in the subsequent core catchers down to Sample 191-1179C-18H-CC. The largest number of agglutinated foraminifers (30 and 23 specimens

per 25 cm^3) was found in Samples 191-1179C-19H-CC and 20H-CC, which contain moderately preserved *Pseudonodosaria* sp. and very well preserved *Spirosigmoilinella compressa*. A few *S. compressa* were also found in Samples 191-1179C-15H-CC and 17H-CC, giving an age of middle to late Miocene for Samples 191-1179C-15H-CC through 20H-CC.

Fish teeth were observed in Samples 191-1179C-19H-CC, and bryozoa were observed in Samples 191-1179C-20H-CC, 21H-CC, and 22H-CC. Samples 191-1179C-23H-CC, 24H-CC, 25X-CC and 191-1179D-1R-CC are barren, and in Sample 191-1179C-26X-CC, only a few radiolarians were observed.

Palynomorphs

Palynomorphs are moderately to well preserved in the upper part of lithostratigraphic Unit I (0 to ~144 mbsf), but all samples examined below Sample 191-1179C-11H-CC are essentially barren (Fig. **F25**). Dinocyst concentrations are generally low, ranging from fewer than a hundred to several hundred cysts per cubic centimeter in sediments of late early Pliocene to late Pleistocene age (143.84–0.92 mbsf). Terrestrial palynomorph (pollen and spores) concentrations are also generally low, ranging from a few hundred to several hundred grains per cubic centimeter in the Pliocene section, but are generally higher in the Pleistocene section (especially in the upper ~55 mbsf), where they may exceed a thousand grains per cubic centimeter.

Samples 191-1179B-1H-1, 92–94 cm (0.92 mbsf), through 6H-CC (55.2 mbsf) are assigned to the Pleistocene. The dinocyst genus *Brigantedinium* and *Picea* pollen are common to abundant in Samples 191-1179B-1H-1, 92–94 cm (0.92 mbsf), 191-1179A-1H-CC (9.87 mbsf), and 191-1179B-5H-2, 39–43 cm (38.01 mbsf). The cool surface water and continental climates recorded by the abundance of these palynomorphs suggest that these sediments were deposited during a glacial interval. Warmer sea-surface and continental conditions, and thus presumably interglacial conditions, are recorded in Samples 191-1179B-3H-4, 90–94 cm (22.62 mbsf), 4H-3, 44–48 cm (30.06 mbsf), 4H-CC (36.02 mbsf), and 6H-CC (55.2 mbsf) by thermophilous dinocyst taxa such as *Impagidinium aculeatum, Impagidinium sphaericum,* and *Impagidinium strialatum,* together with various *Spiniferites* spp. *Pinus* pollen is abundant in these samples, and angiosperm pollen is common. *Tsuga* is also common in some Pleistocene samples interpreted as interglacial. *Picea* is rare in these samples, which is consistent with the warmer conditions recorded by the dinocysts.

Sample 191-1179C-3H-CC (67.70 mbsf) is assigned an early Pleistocene age (older than 1.3 Ma) based on the common presence of *Operculodinium israelianum* together with long-ranging taxa such as *Brigantedinium* spp., *Bitectatodinium tepikiense,* and various species of *Impagidinium*.

Sample 191-1179C-5H-CC (86.93 mbsf) is late Pliocene in age, based on the presence of rare *Spiniferites* cf. *pseudofurcatus* and *Impagidinium japonicum* together with *Operculodinium eirikianum*. Long-ranging taxa such as *Operculodinium centrocarpum* and *I. strialatum* are also common.

Late Neogene dinocysts, such as *Operculodinium janduchenei* and *Habibacysta tectata,* are consistently present in Samples 191-1179C-6H-4, 90–94 cm (92.22 mbsf), through 11H-CC (143.84 mbsf). The presence of few *Corrudinium harlandii* in Samples 191-1179C-9H-CC (124.84 mbsf) and 8H-CC (115.62 mbsf) and of rare *Hystrichokolpoma* sp. 1 of

F25. Dinoflagellate cyst distribution, p. 75.

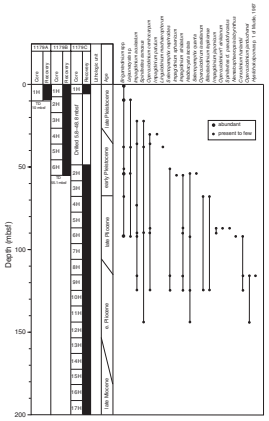

Mudie (1987) in Sample 191-1179C-8H-CC constrains this interval to late Miocene to late Pliocene age. A number of long-ranging dinocysts are common over this interval, including *I. aculeatum, I. strialatum, Selenopemphix nephroides, O. israelianum, B. tepikiense,* and various species of *Spiniferites*. Pollen assemblages in Pliocene samples are very similar to the Pleistocene section, with a variety of gymnosperm and angiosperm (e.g., *Carya, Betula,* and *Alnus*) pollen grains, although absolute pollen abundances are generally much lower.

Samples 191-1179C-12H-4, 90–94 cm (149.22 mbsf), 13H-4, 90–94 cm (158.72 mbsf), 15H-CC (181.94 mbsf), 19H-CC (219.88 mbsf), 23H-CC (256.80 mbsf), and 24H-CC (266.43 mbsf) are barren of palynomorphs.

Radiolarians

The radiolarians present in sediments from Site 1179 lithostratigraphic Units I and II core-catcher samples range in age from late Miocene to Quaternary. Common to abundant radiolarians are present in most sediments, with the exception of Samples 191-1179B-4H-CC and 191-1179C-5H-CC, 9H-CC, and 12H-CC (Table T3). The low concentration of radiolarians in Samples 191-1179C-5H-CC, 9H-CC, and 12H-CC (Table T3) possibly resulted from an increase in diatom and silicoflagellate production. The concentration of radiolarians in Sample 191-1179B-4H-CC was decreased by the presence of volcanic ash and calcareous microfossils. Samples 191-1179C-22H-CC (~248 mbsf) through 25H-CC (~273 mbsf) are barren of radiolarians, but fish teeth are present in these samples. Radiolarians reappear in Samples 191-1179C-26R-CC (~283 mbsf) and 27R-CC (~293 mbsf) and continue down through the chert layers. Sample 191-1179D-9R-1, 58–62 cm (~358 mbsf), contains radiolarians of Early Cretaceous age.

T3. Radiolarian range chart, p. 138.

Radiolarian preservation is good in lithostratigraphic Unit I (0 to ~221.5 mbsf). Radiolarian preservation is moderate in lithostratigraphic Unit II (~221.5 to ~246 mbsf). Many of the radiolarians in these samples have broken tests and show evidence of silica dissolution and recrystallization. Radiolarian preservation is poor in Units III and IV. In Samples 191-1179C-26R-CC (~283 mbsf) and 27R-CC (~293 mbsf), identification of species was hindered by a high degree of silica recrystallization. Sample 191-1179D-9R-1, 58–62 cm, had a moderately high degree of silica recrystallization; certain species were less affected by the recrystallization, allowing identification.

Samples 191-1179B-1H-CC (7.53 mbsf) and 2H-CC (16.74 mbsf) are assigned to the late Quaternary *Botryostrobus aquilonaris* Zone (Hays, 1970). The beginning of the middle Quaternary *Stylatractus universus* Zone (Hays, 1970) is marked by the appearance of *Stylacontarium acquilonium* in Sample 191-1179B-3H-CC (27.14 mbsf). Also, the faunal assemblages found in Sample 191-1179B-3H-CC and the absence of *B. aquilonaris* suggest that the boundary between the *B. aquilonaris* Zone and the *S. universus* Zone occurs between Cores 191-1179B-2H and 3H. The appearance of *S. universus* in Sample 191-1179B-4H-CC (36.06 mbsf) confirms that this sample is in the *S. universus* Zone.

Sediments in Samples 191-1179B-5H-CC (46.16 mbsf), 6H-CC (55.25 mbsf), and 191-1179C-2H-CC (58.28 mbsf) have been assigned to the early Quaternary *Eucyrtidium matuyamai* Zone (Hays, 1970; Foreman, 1975) on the basis of the presence of *E. matuyamai*. The faunal assemblage in Sample 191-1179B-3H-CC (67.87 mbsf) suggests that the boundary between the *E. matuyamai* Zone and the late Pliocene *Lampro-*

cyrtis heteroporos Zone (Hays, 1970; Foreman, 1975) occurs between Cores 191-1179C-2H and 3H. The *L. heteroporos* Zone continues through Sample 191-1179C-7H-CC (105.92 mbsf).

The boundary between the *L. heteroporos* Zone and the middle Pliocene *Sphaeropoyle langii* Zone (Foreman, 1975) is marked by the disappearance of *S. acquilonium* in Sample 191-1179C-8H-CC (115.81 mbsf). The faunal assemblage suggests that the sediments remain in the *S. langii* Zone through Sample 191-1179C-12H-CC (153.97 mbsf). The boundary between the *S. langii* Zone and the *Stichocorys peregrina* Zone (Riedel and Sanfilippo, 1970, 1978) is marked by the appearance of *Stichocorys delmontensis* and abundant *S. peregrina*. This boundary occurs between Samples 191-1179C-12H-CC and 13H-CC (162.95 mbsf).

Radiolarians present in Samples 191-1179C-13H-CC through 18H-CC indicate that the section is of middle to late Miocene age, based on the presence of *S. delmontensis, S. peregrina,* and *Sphaeropoyle robusta*. The early late Miocene *Didymocyrtis antepenultima* Zone (Riedel and Sanfilippo, 1970) begins in Sample 191-1179C-20H-CC. This zone is marked by the presence of *D. antepenultima* and *Diartus hughesi*. These species are also found in Sample 191-1179C-21H-CC.

Sample 191-1179D-9R-1, 58–62 cm (~358 mbsf), contains radiolarians of Early Cretaceous age. This is evident from the presence of *Eucyrtis micropora,* a species that ranges from the Valanginian to Barremian.

MICROBIOLOGY AND GEOCHEMISTRY

Sediment samples from Holes 1179B and 1179C were collected to characterize both the chemistry and the microbial activities in this environment. Microbial activities will be inferred from incubation experiments and from shore-based lipid analyses. As indicated in **"Microbiology and Inorganic Geochemistry,"** p. 14, in the "Explanatory Notes" chapter, whole-round cores (WRCs) were collected from four different depths (5, 30, 100, and 200 mbsf) for incubation experiments. WRCs were collected from all of the depths indicated in Table **T4** for analyses of bacterial lipids. Because certain cell membrane lipids are diagnostic of particular groups of bacteria, the lipid analyses may reveal the presence of different types of bacteria within the sediment column. Interstitial pore waters were also collected for chemical analyses from the same approximate depths as samples taken for lipids in order to relate the microbial communities with the geochemistry of the sedimentary environment. Whole rounds cut on the catwalk were also sampled on two occasions for contamination tests using perfluorocarbon tracers. A list of all of the samples taken at Site 1179 for geochemical and microbiological analyses are shown in Table **T4.**

T4. Core samples collected for microbiological and chemical analyses, p. 139.

Geochemical Pore-Water Profiles

Compounds whose concentrations in pore waters are strongly influenced by bacterial activities include sulfate, methane, dissolved iron(II), dissolved manganese(II), nitrate, ammonia, and phosphate. Of these, the first five are generally associated with successive changes in redox chemistry that accompany the anaerobic degradation of organic carbon by bacteria. Measured changes in the redox chemistry can help define the environments in which particular groups of anaerobic bacteria reside. For example, once oxygen becomes consumed with depth in the sediments during oxidation of organic matter, the subsequent disap-

pearance of nitrate usually reflects a zone of denitrification. Beneath this zone, the appearance of dissolved Mn(II) followed by Fe(II) in pore waters generally identifies the suboxic zone where Mn(III, IV)-reducing and Fe(III)-reducing bacteria exist, respectively. Deeper yet, in more reduced sediments, the appearance of sulfide and then methane identifies increasingly anaerobic regions where dissimilatory sulfate reduction and methanogenesis occurs. Therefore, measured changes in the pore-water concentrations of these various compounds provide a useful diagnostic tool for identifying the habitats of these anaerobic bacteria. Most of the pore-water measurements, down to a depth of 221 mbsf, were made in lithostratigraphic Unit I (see "Sedimentology," p. 9) and correspond to a similar sequence sampled from 0 to 115 mbsf during Leg 185 at Site 1149 (Plank, Ludden, Escutia, et al., 2000). The bottom two samples of Hole 1179C, at 250 and 278 mbsf, were composed of the red pelagic clays of Unit III, which at Site 1149 corresponds to a depth interval of ~115 to 175 mbsf. For Leg 191, shipboard measurements of pore-water phosphate and nitrate concentrations were completed (Table T4) but they await shore-based analysis.

Pore-Water Ammonium

Dissolved NH_4^+ concentration gradually increases from 0 µM at the sediment/water interface to a maximum of ~300 µM between 90 and 100 mbsf, reflecting its release during the degradation of organic matter (Fig. F26). A second maximum of ~285 µM may exist at 62.8 mbsf, producing a bimodal peak, with a small drop in concentration at 72.2 mbsf. This drop may be real, as a bimodal peak in NH_4^+ also occurred at Site 1149 within lithostratigraphic Unit I (Plank, Ludden, Escutia, et al., 2000). At Site 1149, the corresponding drop in NH_4^+ occurred at a depth of ~45 mbsf. This drop could be due to uptake during clay diagenesis.

The gradual decline in NH_4^+ concentration from its maximum at ~100 mbsf to a concentration of 114 µM at 278 mbsf may be due to uptake during clay diagensis, as was previously suggested for Site 1149 (Plank, Ludden, Escutia, et al., 2000). However, at this time, one cannot rule out possible microbial consumption throughout the sedimentary column, even if the rate is very low.

F26. Concentration profile of dissolved NH_4^+, p. 76.

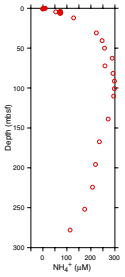

Pore-Water Mn(II) and Fe(II)

The dissolved Mn(II) profile at Site 1179 revealed a very sharp and steady increase in concentration from the sediment/water interface to a depth of 6.5 mbsf, where a maximum concentration of 260 µM was measured (Fig. F27). Below 6.5 mbsf to a depth of 30 mbsf, concentrations dropped to ~100 µM. Fe(II) concentrations were much lower than Mn(II) concentrations and were more scattered (Fig. F27). However, several profile trends were similar to those of Mn(II). Fe(II) also showed a distinct maximum of ~30 µM at 6.5 mbsf, with a general decline to 31 mbsf. It is apparent from these profiles that the zones of iron and manganese reduction occurred near 6.5 mbsf and reflect the anaerobic degradation of organic carbon in surface sediments. Beneath 31 mbsf, concentrations of Mn(II) and Fe(II) both rise and fall, with a smaller subsurface maxima in Mn(II) of 128 µM at a depth of 40 mbsf. Both Mn(II) and Fe(II) show minima of 74 and 2.6 µM, respectively, at 100 mbsf. The covariance of these changes in Mn(II) and Fe(II) concentrations between 30 and 100 mbsf suggest that they may reflect dynamic

F27. Concentration profiles of dissolved Mn(II) and Fe(II), p. 77.

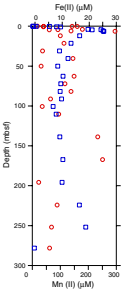

redox processes rather than simple analytical artifacts. Although the Mn(II) concentrations are relatively consistent from 100 to 196 mbsf, showing only a slight increase to 109 µM at 167 mbsf, Fe(II) showed a pronounced subsurface maximum of 25 µM at 167 mbsf and a distinct minimum of 1.4 µM at 196 mbsf. Although carbon, nitrogen, and sulfur (CNS) analyses of the acidified and nonacidified sediments have not been completed, results might indicate whether the minima in Fe(II) at 196 mbsf and some of the other depths might be due to formation of $Fe_{(x)}S_{(y)}$. Below 200 mbsf, Fe(II) concentrations show a moderate rise, whereas the dissolved Mn(II) shows a distinct subsurface maximum of 191 µM at 252 mbsf in the upper portions of lithostratigraphic Unit III. Near the bottom of the red clays at 278 mbsf, Mn(II) shows a distinct minimum of 7.4 µM, which agrees with results from Site 1149 (Plank, Ludden, Escutia, et al., 2000).

Pore-Water Sulfate

In general, the pore-water sulfate showed a relatively gradual decline in concentration from 29 mM near the sediment/water interface to 21 mM in the deepest sample collected at 278 mbsf within the pelagic red clays. The profile suggests a slow and gradual removal of sulfate by dissimilatory sulfate reduction throughout the sedimentary column (Fig. F28). The largest drop in sulfate appears to occur between 0 and 40 mbsf. From 40 to 196 mbsf, the decrease in sulfate concentration is small, suggesting low rates of sulfate reduction. In combination with the pore-water profiles observed for dissolved Mn(II) and NH_4^+, it appears that to a depth of ~200 mbsf the sedimentary column is suboxic. Concentrations of sulfate again drop more steeply between 196 and 278 mbsf. These changes in sulfate gradients with depth may reflect different zones where rates of sulfate reduction change. Confirmation of the bacterial activity associated with sulfate reduction will come from postcruise stable isotopic analyses of the sulfate collected from the pore waters and from analysis of the microbial incubation experiments.

F28. Concentration profile of dissolved SO_4^{2-}, p. 78.

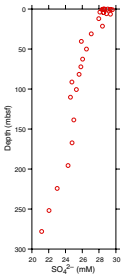

Carbon and Elemental Analyses

Standard shipboard measurements of sedimentary carbonate, organic carbon, C, N, S, and H content are presented in Table T2.

Microbial Incubation Experiments

Sediments collected from 4.5, 31, 101, and 196 mbsf and incubated with gas headspace were analyzed by gas chromatography (GC) after 12–14 days (t = 1) for changes in CH_4 and CO_2 concentrations. Vials sampled at t = 0 showed a small background concentration of methane between 10 and 13 ppmv, which was consistent for replicates prepared from each sample depth. Apparently, the methane is a trace contaminant of the anaerobic gas mixture. None of the incubation vials showed detectable changes in methane, indicating that neither methane production nor consumption had occurred. In contrast, concentrations of CO_2 were higher in some of the t = 1 vials relative to the t = 0 controls. The increase was most apparent in the 196-mbsf samples, which were incubated at 20°–22°C. These samples showed an approximate 15% increase in CO_2 headspace concentration during the first 12-day period.

Whether this increase represents microbial respiration or simply CO_2 degassing will be confirmed with continued time-course measurements.

Perfluorocarbon Tracer Measurements

PFTs were used during the drilling of Cores 191-1179B-5H and 191-1179C-21H to test for contamination of collected sediments by drilling fluids. Sediments collected were immediately stored in a 3°C refrigerator and were analyzed by GC/electron capture detector (ECD), although the data awaits further analysis. However, several PFT-methanol standards were prepared with varying PFT concentrations as indicated in previous studies (Smith et al., 2000). As control blanks, we added 10 µL of fresh methanol to the crimp-sealed 20-mL headspace vials without any PFT. For 0.5-mL injection volumes of the prepared PFT-methanol standards that had been stored at 70°C, a linear fit of the data was observed for PFT concentrations >4.4×10^{-11} g when plotted on a log-log plot (Fig **F29**), as previously reported (Smith et al., 2000). However, we observed that at PFT concentrations <4.4×10^{-11} g, the GC response was not linear. By subtracting the average peak height measured for the methanol control blanks from the PFT standards in this lower concentration range, a linear fit was again obtained (Fig. **F29**). However, the slope of this line was different from that obtained at PFT concentrations >4.4×10^{-11} g. This blank correction also improved the sensitivity of the method by approximately two orders of magnitude relative to that previously reported (Smith et al., 2000). However, it is questionable whether the curve in this lower concentration range is relevant to samples measured (which lack the methanol addition).

Using GC injections of 5 mL volume, PFT standards also provided a linear fit on a log-log plot, although the regression was consistently shifted downward relative to the curve generated from 0.5-mL injections (Fig. **F29**). This indicates a slight decrease in peak height and GC sensitivity for a given concentration (as total grams of PFT injected) when using the 5-mL injection volume. This might be explained by sample loss that results from withdrawing a 5-mL gas sample from a 20-mL headspace vial. Heating the vials from ~25° to 70°C effectively increases the headspace volume by ~3 mL (using the ideal gas law, $PV = nRT$) and creates an overpressure of 3 mL inside the vial. However, withdrawing 5 mL will still deplete ~2 mL of headspace gas from a total of 20 mL, resulting in a ~10% loss. The shift downward of the standard curve using the 5-mL injections rather than the 0.5-mL injections might be explained by this sample loss.

F29. Standard log-log curve of PFT concentration vs. GC/ECD peak area, p. 79.

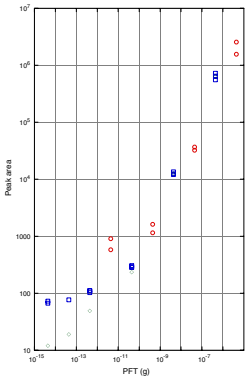

PALEOMAGNETISM

Methods

Measurements of natural remanent magnetization (NRM) were made every 5 cm on the archive halves of all sediment cores from Holes 1179A, 1179B, and 1179C using the shipboard pass-through cryogenic magnetometer. The measurements were of continuous cores from Holes 1179A through 1179C, of discrete sediment samples from Holes 1179B and 1179C, and of basalt samples from Hole 1179D. Alternating-field (AF) demagnetization of the continuous sediment cores was generally performed using steps of 20, 30, and 40 mT. Discrete sediment samples were AF demagnetized by steps of 5, 10, 15, 20, 25, 30, 35, 40, 50, 60,

and 70 mT. Inclination, declination, and maximum angular deviation were determined from principal component analysis of Zijderveld plots of the discrete sample AF-demagnetization measurements. The majority of discrete basalt samples were thermally demagnetized after it was determined that AF demagnetization worked poorly on these samples.

Sedimentary Paleomagnetism

NRM intensities (Fig. **F30A**) of the sediments cored in the upper section at Site 1179 ranged from strong (>10^{-1} A/m) to moderate (7 × 10^{-3} A/m). The NRM was dominated by a downward-directed overprint, likely imparted to the cores by their exposure to the drill string (Fig. **F31**). As is typical with 10- to 20-mT AF demagnetization, the overprint was removed and measurements at higher demagnetization steps gave consistent directions. Zijderveld plots from sediment samples often showed univectorial decay toward the origin for steps >10–20 mT (Fig. **F32**), implying that this procedure isolated the characteristic remanent magnetization (ChRM) direction. Some samples gave magnetic directions at higher AF-demagnetization steps that appeared to diverge from univectorial decay. These measurements are thought to be affected by an anhysteretic remanent magnetization imparted on the samples by the in-line demagnetization coils at AF field levels >40–60 mT.

Magnetic intensities display a systematic variation through the section, apparently related to lithology. The variation is best seen in intensity values after AF demagnetization (i.e., with the drill-string overprint removed). In lithostratigraphic Unit I (see **"Sedimentology,"** p. 9), the magnetic intensities of the upper part, Cores 191-1179B-1H through 6H and 191-1179C-1H and 2H through 12H, are consistent at a level of 1 × 10^{-3} to 1 × 10^{-2} A/m (Fig. **F30B**), with occasional spikes and dips an order of magnitude higher or lower. Many spikes seem to correspond to significant ash layers. A slow decrease by an order of magnitude is seen in the lower part of this unit, from 4 × 10^{-3} A/m (Core 191-1179C-12H) to 1 × 10^{-4} A/m (Core 191-1179C-19H). A sharp increase of nearly two orders of magnitude occurs in Sections 191-1179C-19H-5 through 20H-2, just above the boundary between Units I and II. Intensity values in deeper APC/XCB cores are consistently high at about the magnitude of the upper part of Unit I, but a small dip occurs in Core 191-1179C-24H, below which magnetic intensity rises to >10^{-2} A/m through Core 191-1179C-26X.

Magnetic susceptibility values are low in Units I and II, typically <50 × 10^{-5} SI, except for higher spikes apparently caused by ash layers and perhaps metallic contamination at some core tops (Fig. **F33**). These lower values evidently reflect the fact that the sediments primarily consist of siliceous ooze and clay with little magnetic material. Values near the seafloor are higher, 25 × 10^{-5} to 50 × 10^{-5} SI (Cores 191-1179C-2H through 9H), and lower in Cores 191-1179C-9H through 19H (<25 × 10^{-5} SI), with an increase back to ~25 × 10^{-5} SI in Cores 191-1179C-19H through 20H. In Unit II, susceptibility values are steady near 25 × 10^{-5} SI (Cores 191-1179C-20H through 21H). In Unit III, susceptibility increases to ~140 × 10^{-5} SI from Cores 191-1179C-22H through 23H. Susceptibility values vary through the rest of Unit III, with lower values at the bottom of Core 191-1179C-23H, at the top of Core 24H, and in Core 24H. Values >400 × 10^{-5} SI were measured in Cores 191-1179C-25X through 26X. The higher values in Unit III are consistent with the high iron content of these sediments.

F30. NRM intensity before and after AF demagnetization, p. 80.

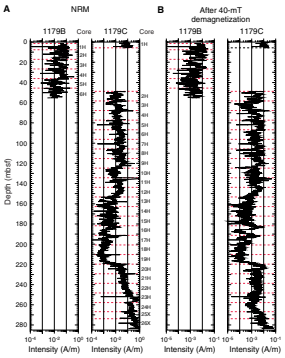

F31. NRM of the drill-string overprint before and after AF demagnetization, p. 81.

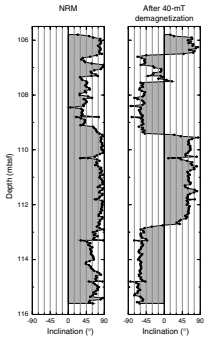

F32. Zijderveld plot of Sample 191-1179C-12H-1, 130–132 cm, p. 82.

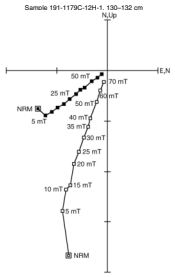

F33. Magnetic susceptibility vs. depth, p. 83.

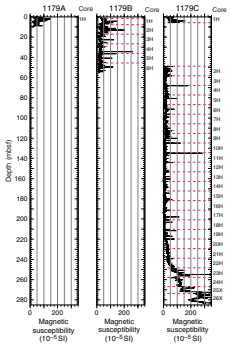

Peaks in magnetic susceptibility are used to correlate Cores 191-1179A-1H, 191-1179B-1H and 2H, and 191-1179C-1H (Fig. F34A) and Cores 191-1179B-6H and 191-1179C-2H (Fig. F34B). The tie-point depths in each hole are listed in Table T5.

Magnetostratigraphy

The combined sediment cores of Site 1179 contain an excellent magnetic polarity reversal sequence (Fig. F35) from the early Miocene (Chron C5Dr) to the present (Chron C1n [Brunhes]). The single core from Hole 1179A records the present normal polarity Chron C1n. The six cores from Hole 1179B record five magnetic polarity reversals, including the Cobb Mountain cryptochron (C1r.2r-1n) (Table T6). The first core of Hole 1179C was taken at the sediment/water interface and is in Chron C1n (Brunhes). Cores 191-1179C-2H through 23H span Chrons C1r.2r (Matuyama) through C5Dr (Table T6). The remaining cores of Hole 1179C, Cores 191-1179C-24H, 25X, and 26X, are predominantly of normal polarity with no recognizable magnetic polarity sequence.

Measurements of discrete samples from Holes 1179B and 1179C show excellent agreement with the whole-core measurements. These samples confirmed that two distinct polarities could be isolated after removal of a large vertical overprint with AF demagnetization (Fig. F31).

Basalt Magnetism

Basalt samples give NRM intensities varying from 1.1 to 9.4 A/m, similar to other such rocks recovered elsewhere. AF-demagnetization experiments on pilot samples showed irregular behavior, making polarity determination difficult (Fig. F36). Zijderveld plots of thermal demagnetization experiments indicated that the downward overprint remained to temperatures in excess of 200°–300°C. Therefore, most samples were first treated to a low AF field (15 mT) to remove the drill-string overprint before thermal demagnetization to isolate the ChRM. Even with thermal demagnetization, a significant fraction of the samples displayed irregular demagnetization behavior. Isothermal remanent magnetization acquisition experiments showed rapid saturation, implying that some samples have soft magnetizations (i.e., a small applied field induces significant magnetization). Those samples that gave apparently reliable results show what may be two polarities. One group of samples gives low, negative inclinations, typically –5° to –20°, implying reversed polarity slightly north of the equator. Other samples give positive inclinations of about the same magnitude, perhaps indicating normal polarity. Additional measurements are needed to determine whether two polarities occur in the basement section or whether the combination positive and negative inclinations are due to some other cause.

SEDIMENTATION RATES

Sedimentation rates at Site 1179 have been calculated from paleomagnetic and biostratigraphic data.

F34. Magnetic susceptibility correlations, p. 84.

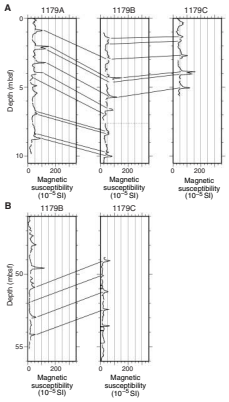

T5. Magnetic susceptibility tie point depths, Holes 1179A, 1179B, and 1179C, p. 140.

F35. Magnetic polarity reversal sequence (after AF demagnetization), p. 85.

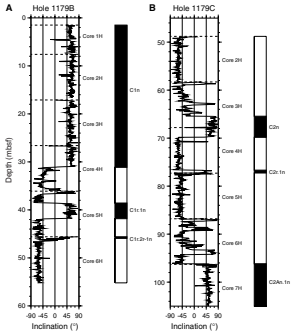

T6. Magnetic polarity reversal boundary depths, Holes 1179B and 1179C, p. 141.

F36. Zijderveld plots of basalt samples, p. 88.

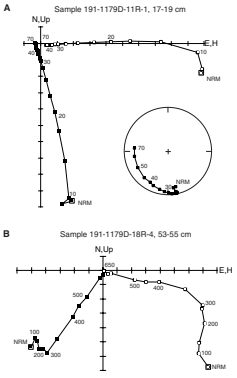

Sedimentation Rates from Paleomagnetism

Figure F37 shows a depth vs. age curve for sedimentation at Site 1179 derived from magnetic stratigraphy and the magnetic polarity reversal time scale (See "Paleomagnetism," p. 21, in the "Explanatory Notes" chapter). Cores 191-1179C-24H through 26X have been excluded, because no magnetic stratigraphy has been defined in these cores. The sedimentation rate curve can be divided into three segments. There are three sedimentation rates that correspond to the first three lithostratigraphic units (see "Sedimentology," p. 9). Cores 191-1179C-22H and 23H, which consist of pelagic brown clay, display a slow sedimentation rate of 1.56 m/m.y. for the upper part of Unit III. Sedimentation rates increase upward. Unit II, a massive diatom-bearing radiolarian ooze, which spans Cores 191-1179C-20H through 22H, has a sedimentation rate of 7.56 m/m.y. Unit I, consisting of radiolarian-bearing diatom oozes with ash layers and zeolitic clays, has a sedimentation rate of 29.29 m/m.y. The curve implies either that Site 1179 drifted into an area of increased productivity in the late Miocene and Pliocene or that oceanographic conditions changed in such a way as to lead to a 200-fold increase in sedimentation.

F37. Sedimentation rate curve based on magnetostratigraphy, p. 89.

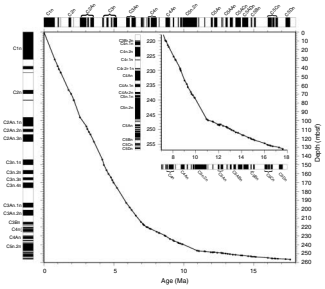

Sedimentation Rates from Biostratigraphic Data

Sediment ages derived from biostratigraphic datums (radiolarians, dinoflagellate cysts, benthic foraminifers, and calcareous nannofossils) in the upper Miocene to Holocene sequence at Site 1179 are plotted against depth in Figure F38. Except for one Lower Cretaceous sample at 358 mbsf, sediments below 240 mbsf are barren of biostratigraphically useful microfossils. Biostratigraphic resolution is highest in Pleistocene sediments and lowest in the upper Miocene–lower Pliocene sediments. The shaded area encompasses the minimum and maximum ages for each sample, constraining sediment accumulation rates. Sedimentation rates were high and increased gradually throughout the late Cenozoic, averaging between ~19 and ~30 m/m.y. during the late Miocene and ~35 m/m.y. during the Pliocene–Pleistocene.

F38. Sedimentation rates based on radiolarians, dinoflagellate cysts, foraminifers, and nannofossils, p. 90.

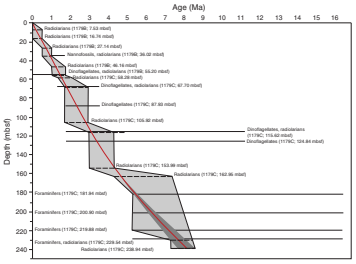

IGNEOUS PETROLOGY

Basement was encountered in Sections 191-1179D-10R-1 through 22R-6 (375–475 mbsf). Basement rocks recovered from Hole 1179D consist mostly of fresh aphyric basalts in massive flows, pillows, and breccia with a minor amount of interpillow sediments. The section is divided into 48 units based on lithology and flow and/or cooling unit criteria. All basalts are classified into three petrographic categories based on mineral occurrence: olivine-free basalt, olivine-poor basalt, and olivine-rich basalt. The basalt of the upper eight units is mostly olivine-poor basalt (Group I); the basalt of the middle 16 units is mostly olivine-free basalt (Group II); and all the basalt of the lower 24 units is olivine-rich basalt (Group III). The most distinct petrologic change among cored basalts can be seen between Units 24 and 25.

The basalts of the two upper groups are fine grained with subophitic texture; in the lowermost group, there is a tendency for medium grain size with ophitic fabric in thick massive lava flows. The glass rims from chilled margins on pillows and massive lava flows are mostly palag-

onitized; near-border parts are now hyalopilitic or cryptocrystalline to microcrystalline.

The groundmass of the basalts consists dominantly of lathlike plagioclase and clinopyroxene (Ti augite) and almost completely devitrified glass/palagonite as mesostasis. Very fine grained magnetite is concentrated in the former glass; Cr spinel, apatite, and very rare zircon are subordinate accessories. Olivine in the groundmass of the Group III basalts is nearly totally changed to iddingsite, as are the olivine phenocrysts in Groups I and III. Plagioclase phenocrysts are mostly fresh but in part corroded or replaced.

The primary mineralogy of the basalts from Site 1179 shows no features of an alkali-basaltic tendency.

The alteration of the basalts is surprisingly low. The alteration belongs to the low-grade zeolite facies in a possible temperature range between 10° and 30°C. Secondary alteration-related mineralogy includes calcite, celadonite, saponite, smectite, and zeolites that fill fissures, veins, and vesicles. Moreover, glass has been replaced in grains or patches, and, to a limited extent, plagioclase is affected. X-ray fluorescence (XRF) analyses show that all samples of basalt from Hole 1179D are geochemically characterized as tholeiitic basalt with mid-ocean-ridge basalt (MORB) affinity.

Lithostratigraphic Units

Prior to identification of lithostratigraphic units, petrographical descriptions based on hand-specimen examination of all basement cores from Hole 1179D were made using a hand lens and binocular microscope. All chilled or glassy contacts, decreases in grain size toward the margins of pillows or flows, and presence of breccia or hyaloclastite were described as indications of unit boundaries. Thin intervals (<10 cm) of sediment or interpillow material and breccia are noted as boundaries between units, whereas thicker intervals (>10 cm) are distinguished as individual units. Furthermore, 46 thin sections were examined to confirm the above descriptions. The VCD form for basement rocks includes all the igneous core description data for Hole 1179D (see **"Site 1179 Visual Core Descriptions,"** p. 35): unit number, depth, interval thickness, lithology, texture, structure, color, presence or absence of chilled margins, comments, and the location of shipboard samples. The thin-section descriptions are summarized in **"Site 1179 Thin Sections,"** p. 112. The basement stratigraphy is summarized in Figure **F39.**

Basement of Hole 1179D consists mostly of microcrystalline to fine-grained basaltic flows, pillows, and breccia with subordinate amounts of sediment intercalations. The igneous section is divided into 48 units based on lithology and flow and/or cooling unit criteria (see **"Site 1179 Visual Core Descriptions,"** p. 35; Fig. **F39**). All basalts are classified into three petrographic categories based on mineral occurrence: olivine-free basalt, olivine-poor basalt, and olivine-rich basalt. The basalts of the upper eight units (Units 1–8) mostly belong to olivine-poor basalt, forming Group I, which contains very small amounts of olivine (<<1%) and plagioclase as phenocrysts. The basalts of the middle 16 units (Units 9–24) mostly belong to olivine-free basalt with a small amount of plagioclase (<1%) as phenocrysts, forming Group II. The basalts of the lower 24 units (Units 25–48) belong to olivine-rich basalt, forming Group III, which contains olivine as both phenocryst (<1.5%) and groundmass (±3%) phases. Additional basalts of the lower 24 units partly contain a

F39. Basement stratigraphy and unit boundaries, p. 91.

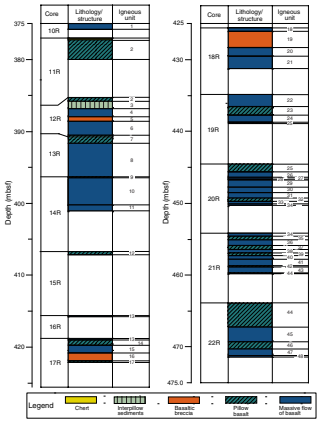

small amount of Cr spinel as phenocrysts, indicative of their relatively primitive nature. There is a marked change in color between Units 24 and 25 in Hole 1179D. The upper 24 units show greenish color, whereas the lower 24 units show brownish color. This change appears to result from their original and secondary mineral compositions. The formation of the secondary minerals, such as celadonite, smectite, and saponite, which were formed in vesicles and veins or glassy parts in basalt during alteration process, makes the host rock change to a greenish color. In the lower 24 units, almost all of the olivine crystals have been changed into brownish iddingsite, resulting in the brownish color of olivine-rich basalts. The difference between those two parts is distinct not only in color but also in petrological and geochemical features. This will be referred to in the next two sections. The following paragraph summarizes some of the important characteristics of each lithostratigraphic unit and additional information for the VCD form.

Unit 1 consists of an aphyric basalt flow. The contact between the overlying sediments and basement was not recovered in a single core. Section 191-1179D-11R-1 contains fragments of dark brown chert in the upper 43 cm and aphyric basalt from 43 to 124 cm. The top of the basalt is made up of a highly altered chilled margin (Figs. **F40, F41**). We conclude that the loss of any igneous core in this interval is very small (i.e., this part might be assigned to the top or almost the top of the basement). The degree of alteration for the basalt throughout Unit 1 is moderate and dark gray in color with pronounced greenish gray and brownish gray concentric alteration halos forming Liesegang structures, which are indicative of an infiltration through the surrounding cracks (Fig. **F42**). Unit 2 is made up of rather thick (3.31 m) pillows of aphyric basalt with thin calcareous interpillow materials (Fig. **F43**). Several chilled pillow rims are present within Unit 2, and these define the individual pillows or cooling units. Basalt in the pillow interiors is fresh, and there are very few vesicles throughout Unit 2. Such features are more or less common in other pillow units above Unit 25, such as Units 7, 9, 12, 14, 17, and 23. Unit 3 is an interpillow or interflow volcaniclastic sediment up to 1.0 m thick, which consists of pillow breccia and hyaloclastite with a considerable amount of calcareous matrix (Fig. **F44**). Because the calcareous matrix contains a high density of calcified radiolarian fossils (see Fig. **F45**), the matrix is thought to have originally accumulated as radiolarian ooze, indicative of marked cessation of volcanism after the formation of Unit 4. Units 5, 16, 19, and 28 consist mainly of basaltic breccia. All these breccias are composed of moderate to highly altered glassy or microcrystalline basaltic fragments derived from pillow rims or flow margins. They contain considerable amounts of hyaloclastite and carbonate matrix (Fig. **F46**), with the exception of Unit 19, which has a very small amount of matrix materials. Unit 19 is rather thick (2.25 m), and for the most part, the basalt fragments are subangular to angular and vary from a few millimeters to 10 cm in size. Units 8 and 10 show typical thick (4.65 and 3.78 m, respectively) massive flow structure, although their flow margins are not recovered. Lithology of both units is quite similar, showing fine-grained aphyric basalt, gray to greenish gray in color, with fresh to slight alteration, very rare vesicles, and randomly oriented smectite, calcite, or zeolite veins. All these features are more or less common in other massive flow units above Unit 25, such as Units 4, 6, 11, 13, 15, 18, 20, 21, 22, and 24. There are some massive flow units rich in vesicles (up to 10% in volume) in the lower part, especially in Units 29, 33, 47, and 48 (Fig. **F47**). The abundance of vesicles in the other massive flow units in the lower

F40. Highly altered aphyric basalt flow margin covered by brown chert, p. 92.

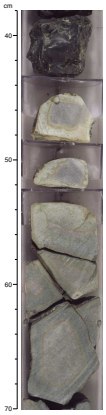

F41. Photomicrograph of basalt at the top of basement, p. 93.

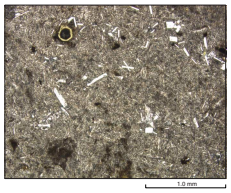

F42. Close-up of a liesegang structure in a basalt flow of Unit 1, p. 94.

F43. Pillow and interpillow materials, p. 95.

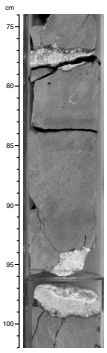

part vary from <1% to a maximum of 5% from piece to piece. Unit 44 (3.46 m) consists of rather thick pillows of aphyric basalt with subordinate amounts of pillow breccia. Many chilled pillow rims occur within Unit 44, and thin intervals of hyaloclastite with altered glassy shards occur along pillow rims (Fig. F48). The degree of alteration in the pillow interior is slight, whereas it is moderate in the pillow rim. The amount of vesicles in Unit 44 varies from 1% to 5%. Other pillow units, such as Units 25, 32, 35, 37, 39, 42, and 46 in the lower part, show similar lithology to Unit 44. Fresh glass was found in Unit 28 (Section 191-1179-20R-2 [Piece 4]) and Unit 42 (Section 191-1179-21R-1 [Piece 4]).

Petrology

The following discussion of petrology at Site 1179 is the result of visual core description and optical microscopy. Problems with the inductively coupled plasma–atomic emission spectrometer during Leg 191 prevented us from generating geochemical data. The 48 units, varying between massive lava flows and pillow lavas, can be categorized by their olivine contents into three major groups (Table T7).

The uppermost Group I consists of fine-grained aphyric basalt with sparse plagioclase and olivine. Less than 1% of tiny olivine phenocrysts is present in massive flows and pillows, and the groundmass is olivine free. Fine-grained to microcrystalline Group II basalts are aphyric to sparsely plagioclase phyric; olivine is not present. All fine- to medium-grained basalts of the lowermost Group III contain olivine not only as phenocrysts (up to 1.8%) but also in the groundmass (~3%). They are sparsely olivine- and olivine and plagioclase-phyric basalts without differences between massive and pillow lavas. Table T8 shows the phenocryst contents in the three groups. In spite of the low percentage of phenocrysts, the differences between the groups are unequivocal. This subdivision is essential for petrologic discussion.

Generally, plagioclase phenocrysts in all three groups are labradorite, normally euhedral, rarely subhedral, simply twinned (most likely after Manebach's law), and partly fresh (Fig. F49A). Some crystals are zoned with a large core and a small rim poorer in anorthite. The majority of phenocrysts are, however, more or less corroded, and a few are totally replaced by smectite, calcite, and zeolite. Some plagioclase phenocrysts contain numerous tiny groundmass inclusions, of which the composition can not be resolved by microscope (Fig. F49B). The lengths of the crystals differ between the three groups and between flow and pillow basalts (except in the chilled margins), as seen above.

Olivine phenocrysts are generally almost totally altered to iddingsite (Fig. F49C), although in many cases, euhedral olivine phenocrysts are observed. No grain-size distinctions could be observed between flow and pillow basalts, but olivines in Group III are three times larger than those from Group I.

A third mineral forming phenocrysts is Cr spinel. However, it was only observed as a very rare accessory phase in four thin sections from Units 30, 41, 45, and 47, which correspond to massive lava flows of Group III. The maximum spinel grain size is 0.25 mm (Fig. F49D).

Two additional rare accessory phenocrysts are apatite and zircon. In all thin sections, only five zircon crystals (10–30 µm) were found within clinopyroxene. Figure F50A shows an example with a small halo and plagioclase. Apatite, in contrast, is clearly more common as 10- to 75-µm large crystals within plagioclase and clinopyroxene (Fig. F50B).

F44. Interpillow or interflow volcaniclastic sediment, Unit 3, p. 96.

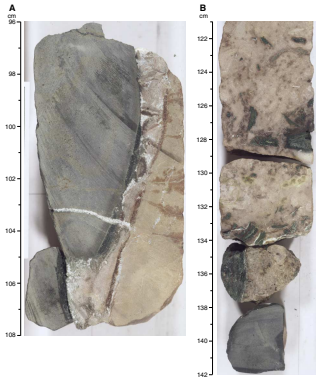

F45. Photomicrograph of calcified radiolarian fossils and basalt fragments, p. 97.

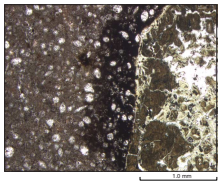

F46. Basaltic breccia with hyaloclastite and pillow breccia, p. 98.

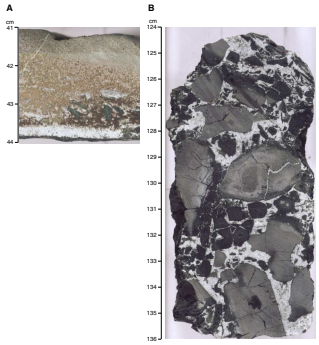

F47. Calcite- and saponite-filled vesicles in a massive flow, p. 99.

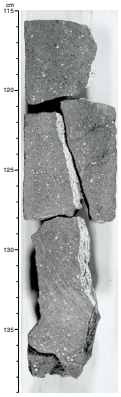

Whereas zircon is limited to the massive basalts, apatite is observed in massive and pillow basalts.

The groundmass of pillow and flow basalts in all three groups has the same features. Glassy quenched margins show a wide devitrification spectrum as an expression of different cooling velocities. They are classified into four textural categories in ascending order of degree of devitrification as follows: (1) glass/palagonite radial clusters of initial, impure clinopyroxene ± magnetite (Fig. **F50C, F50D**); (2) a carpetlike pattern of clinopyroxene bunches with sporadic plagioclase (Fig. **F51A**); (3) variolitic plumose plagioclase crystallites (Fig. **F51B**) and variolitic branching plumes of plagioclase or clinopyroxene, the latter commonly with plagioclase crystal nuclei; and (4) plagioclase clusters with associated clinopyroxene and magnetite grains (Fig. **F51C**) and skeletal crystals.

Somewhat farther from the contact with the older underlying flow or overlying seawater, hyalopilitic and microcrystalline textures may be present (Figs. **F51D, F52A**). Rosettelike bundles of plagioclase crystals and sub- to anhedral dirty clinopyroxene are observed in this matrix (Fig. **F52B, F52C**). Within the main internal part of the massive flows and pillows of Groups I and II, subophitic textures dominate (Fig. **F52D**). In Group III, with distinctly larger grain size, a strongly ophitic fabric is present (Fig. **F53A, F53B**). Within this sequence, the portion of crystallized phases increases and that of glass/palagonite decreases toward zero: the transition from a hypocrystalline to a holocrystalline basalt has taken place.

Table **T9** shows a simplified summary of the distribution of glass/palagonite. The data in this table distinctly reflect the higher portion of glass within the pillows against the massive basalts with a maximum in Group II and a tendency of regression in the massive lava flows with increasing depth. We consider this to be a primary feature and not a consequence of aging or superposition.

Within the groundmass, euhedral to subhedral plagioclase is the dominant mineral phase in all textural varieties. Long, stretched lathlike needles are simply twinned and fresh and sometimes skeletal (Fig. **F53C**), even if some show partial corrosion (Fig. **F53D**). Anhedral clinopyroxene and glass/palagonite fill the space between the plagioclases as a kind of mesostasis. Based on their optical properties, the clinopyroxenes belong essentially to the Ti augites, especially in the larger grain-sized Group III. The clinopyroxenes are the essential bearers of the Ti content of the basalts from Hole 1179D. No ilmenite was observed, and the Ti content of the magnetites awaits microprobe examination. Very fine grained partly skeletal magnetite, frequently in single lines or nestlike, is restricted to the glass or its later devitrified products, mainly clinopyroxene.

The average amount of vesicles is generally low, ≤1% in Groups I and II and ~2% in Group III. The small diameter of the vesicles, commonly between 0.1 and 1 mm and only rarely >3 mm, is clear evidence for a deep-water emplacement of the massive and pillow lava flows. The basalts must have been emplaced above ~4000 m, the depth of the CCD, because on and between pillows and at the top of some massive flows, an interpillow material is embedded. It consists of very fine grained carbonatic sediment (pure calcite after XRD) with peeled-off crumbs and shards of volcanic glass, forming hyaloclastite. As the possible depth for the emplacement of the lava flows from Hole 1179D, <2000 m seems to be realistic after consideration of the vesicle sizes. From all these facts and data, the following conclusions for the petrogenesis can be drawn:

F48. Pillows with altered glassy shard and interpillow materials, p. 100.

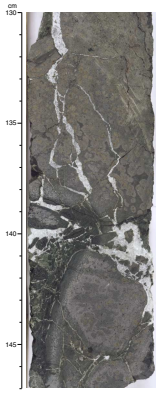

T7. Subdivision of the basalt recovered from Hole 1179D, p. 142.

T8. Phenocryst distribution in basalts, Hole 1179D, p. 143.

F49. Photomicrographs showing phenocrysts in basalts, p. 101.

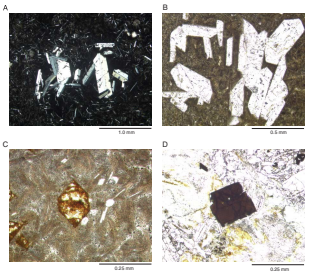

F50. Photomicrographs showing accessory minerals and microcrystalline texture in basalts, p. 102.

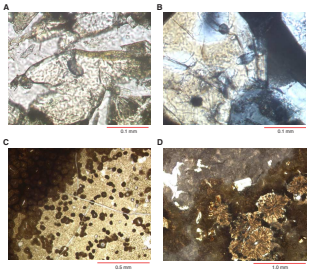

1. Based on their mineralogy, all basalts from Hole 1179D are more or less primitive. An alkali-basaltic tendency can be excluded, but the melts from Group II were somewhat more fractionated than those of Group I and especially those of Group III. For the geochemistry this would mean, for instance, somewhat higher contents of MgO, Cr, and Ni in Group III.
2. Rapidly extruded lava flows have generated the massive basalts from Hole 1179D. For the pillow lavas, a somewhat lower effusion speed can be surmised. The lack of large amounts of phenocrysts in each group suggests a slow degree of fractionation. This may be the consequence of relatively small and short-lived magma chambers.
3. The basalts from Hole 1179D contain a low percentage of phenocrysts. Within the erupted basalt melts, plagioclase and subordinated olivine ± Cr spinel appear to be the first solidus phases, followed by clinopyroxene, and lastly, interstitial glass. Magnetite has crystallized almost exclusively within the glass. Altogether, solidification and crystallization took place rapidly.
4. The quenched glass at the chilled margins has undergone, for the most part, palagonitization and devitrification. The glassy mesostasis is more or less crystallized to microcrystalline clinopyroxene, plagioclase, and magnetite.
5. All in all, alteration does not play a considerable role. The basalts from Hole 1179D are surprisingly fresh. Alteration scheme is discussed in more detail in the following section.
6. Site 1179 is situated near Shatsky Rise, off its northwestern flank on magnetic lineation M8, indicating an Early Cretaceous age for the basement. Shatsky Rise, together with such huge oceanic plateaus as Ontong Java, Manihiki, Mid-Pacific Mountains, and Hess Rise, are assumed to have formed over a mantle plume (Neal et al., 1997; for the general question of the global plume activity also see Wilson, 1992). These extensive submarine volcanic accumulations can be compared with continental flood basalts and should be designated as oceanic flood basalts (OFBs). From geochemistry and isotopic characteristics, it differs clearly from MORB and shows a certain affinity to oceanic island basalt.

Janney and Castillo (1996, 1997) have postulated that a mantle plume formed Shatsky Rise. Unfortunately, none of the numerous holes drilled on Shatsky Rise has recovered basalt. If the basalt recovered from Site 1179 is influenced by Shatsky Rise, or is even a part of this magmatic province, then indications of the postulated mantle plume would be substantiated and it may be geochemically distinct from MORB.

The petrographic examination of the Site 1179 thin sections does not indicate an alkali tendency for the basalts. A comparison of our results with those from the few nearby holes in the vicinity of the Shatsky Rise that have reached basement may follow. At Site 581 north of Shatsky Rise, a very similar profile was drilled: 343 m of Miocene-Pleistocene sediment followed by 9.5 m of chert over basalts of probable Early Cretaceous age. These basalts were unfortunately only very briefly described by Fountain et al. (1985) as MORB in two subgroups. One is somewhat more fractionated; the other is somewhat less. Mineralogy and degree of alteration are comparable to basalts from Hole 1179D.

To the west of Shatsky Rise are DSDP Sites 303 and 304, and to the southwest, DSDP Site 307. The basement is assumed to be of Early Cre-

F51. Photomicrographs showing groundmass textures of basalt, p. 103.

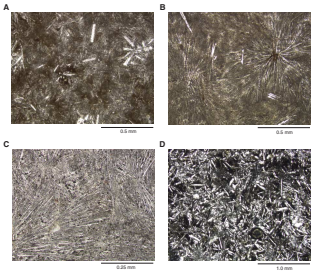

F52. Photomicrographs showing representative textures of basalts, p. 104.

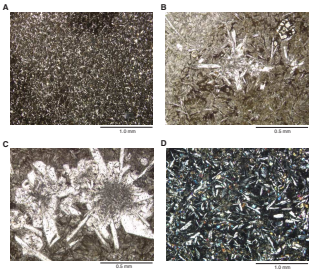

F53. Photomicrographs showing fine-grained groundmass textures of basalts, p. 105.

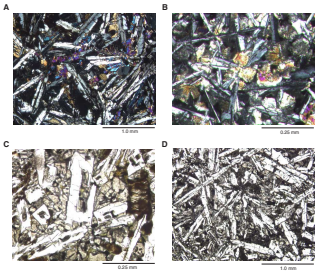

T9. Glass/palagonite contents of basalts, Hole 1179D, p. 144.

taceous age. All the basalts are classified as MORB, but they are extremely altered (Marshall, 1975).

Far from Shatsky Rise, another extensive OFB province of Cretaceous age lies in the Nauru Basin in the western Pacific. About 600 m of basalt was drilled during DSDP Legs 61 and 89 at Site 462. The mineralogy and alteration style of these rocks (Floyd, 1986; Floyd and Rowbotham, 1986) resemble Hole 1179D basalts. Their geochemical features are similar to mildly depleted (transitional) MORB, comparable with the Reykjanes Ridge volcanites (Castillo et al., 1986; Floyd, 1986; Saunders, 1986). These findings suggest that two geochemically different types of OFB provinces may exist. The Shatsky Rise volcanic complex could belong to the Nauru (MORB) type.

With all requisite prudence for such a comparison, we can state that Hole 1179D basalts are tholeiitic (= MORB) by petrography.

Geochemistry

Twenty-one samples of basaltic rocks from Hole 1179D were analyzed in a shore-based laboratory by XRF for major and trace elements (Table **T10**). The analytical technique, conditions, and accuracy are described in **"Igneous Petrology,"** p. 18, in the "Explanatory Notes" chapter. The samples analyzed represent the least-altered basalt. As previously described, basalt from Hole 1179D was classified into three petrographic groups: Group I is composed of olivine-poor basalt, Group II of olivine-free basalt, and Group III of olivine-rich basalt. The CIPW norm compositions show fairly good agreement with this classification (Table **T11**). Samples belonging to Group I have a small amount of olivine in the norm except for one sample (191-1179D-11R-1, 86–88 cm). The amount of normative olivine is also very small or zero for samples belonging to Group II except for one sample (191-1179D-14R-2, 63–65 cm). Additionally, samples from Group II, Units 18 to 23, show the presence of normative quartz. All samples in Group III carry olivine in the norm up to 7.7%. None of them provide normative nepheline, which is thus an alkaline-basaltic tendency that can be excluded. Samples in Groups I and III show distinctive composition ranges in the TiO_2 vs. FeO*/MgO field (Fig. **F54**). Those from Group III show higher Ti content relative to samples from Group I. On the other hand, samples from Group II show a wider compositional range. As for trace element composition, Group III basalt is distinguished by its high Cr, Ni, and Sr content. This feature shows good agreement with its specific mineral composition, such as an abundance of olivine and the presence of Cr spinel (Fig. **F49D**). The abundance of rare earth elements (REEs) is nearly homogeneous throughout the samples, showing moderate depletion in the light REEs. In contrast, Masuda and Nagasawa (1975) reported results from an altered basalt dredged from Shatsky Rise that shows strong enrichment in the light REEs. This difference suggests Site 1179 basalts are distinct from those of Shatsky Rise.

XRF analyses show that all samples of basalt from Hole 1179D are geochemically characterized as tholeiitic basalt with MORB affinity. About half of them show elemental composition close to primitive normal-MORB reported from the East Pacific Rise (Humphris et al., 1980; Srivastava et al., 1980; Thompson et al., 1989), and the rest show a wider range in composition. However, tholeiitic basalts of similar composition to MORB are reported from Nauru Basin and/or Ontong Java Plateau, where so-called oceanic plateau basalt has been widely erupted (Castillo et al., 1986; Floyd, 1986; Saunders, 1986; Mahoney et al.,

T10. Chemical analyses of basalts, Hole 1179D, p. 145.

T11. CIPW norm composition of basalts, Hole 1179D, p. 146.

F54. FeO*/MgO vs. TiO_2 plot for basalts, p. 106.

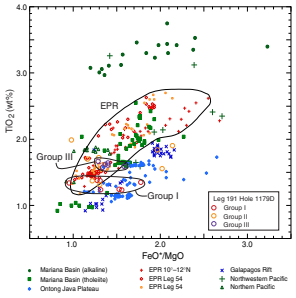

1993). Actually, some of samples from Hole 1179D have similar composition to those from Nauru Basin and/or Ontong Java Plateau (see Fig. F54). A study on why there is wider compositional variety in only one hole should be conducted in the context of the influence of the igneous activity that formed nearby Shatsky Rise. Such a study would require a more detailed analysis of isotope compositions.

Basement Alteration

All basaltic basement cores from Hole 1179D are surprisingly fresh by both visual core description and microscopic examination. Only ~20% of the pillow and lava flow material shows more than slight alteration. The maximum alteration is observed in very limited parts of Units 33 through 48 (~455–475 mbsf) and may amount to not more than 25%–30%. In Units 1 through 32, the degree of alteration usually amounts to <5%–10%. The minerals originating during the alteration process are restricted to very low temperature formation, such as calcite, celadonite, smectite/saponite, and zeolite(s). This secondary mineral association is more or less constant over the whole profile. Phases such as prehnite, pumpellyite, epidote, K feldspar (adularia), and quartz could not be detected. Even the presence of chlorite was not confirmed reliably.

Four main types of alteration features can be distinguished:

1. Hydration of volcanic glass from small pillow and flow rims to palagonite. This alteration is by no means complete, because considerable parts of the original glass remain nearly unchanged. Palagonitization converts the primary black and nearly opaque glass into more or less transparent, cryptocrystalline or amorphous products of brown to yellow color. The optical properties of palagonitized glass range from isotropic to weakly or moderately birefringent. Later crystallization starts with fine crystal skeletons at the borders and beside fissures. Palagonite shards are predominantly conserved within breccias and interpillow materials (Fig. F55A). The groundmass glass is also affected by palagonitization.
2. Fissures are predominantly filled with calcite. Typically the veins are 1–2 mm wide but may be as wide as 8–10 mm. The veins may include green to light green minerals, commonly at the borders, seldom over the whole width, that are part celadonite and part smectite. Figure F55B shows a sector of a calcite-celadonite vein in subophitic basalt partly replaced by smectite before the fissure was filled. In rare cases, vein calcite is associated with later zeolite.
3. Vesicles (usual diameter = <1 mm; maximum = 3 mm) are filled with one or more of four minerals: calcite, celadonite, smectite/saponite, and zeolite(s). Most calcite-filled vesicles are monomineralic. When subordinate minerals are present, they have a small initial layer of celadonite or smectite. In one thin section, some larger vesicles filled with calcite show some colorless clear grains of zeolite in the center (Fig. F55C). Otherwise, zeolites are clearly a subordinate mineral against the dominant phyllosilicates.

   Pale yellow and yellow-brown to ochre but also pale to yellowish green extremely fine grained smectite/saponite can fill the whole vesicle or form the first outer layer, followed by celadonite in the center, or vice versa (Fig. F55D). The proportions of

F55. Photomicrographs showing secondary minerals palagonite, calcite, celadonite, smectite, and zeolite in basalts, p. 107.

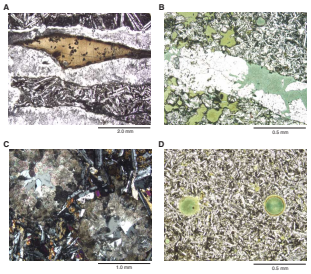

these two minerals vary widely within one concentrically filled vesicle.

Smectite and saponite cannot be distinguished microscopically. X-ray diffraction shows that saponite could be a possible phase in the alteration system under discussion. Celadonite was also proved in some samples. In most cases, the latter can be distinguished from smectite/saponite under the microscope in spite of the slight differences in their optical properties. Celadonite is bright to dark green, also bluish green, and in small vesicles is predominantly spherulitic or otherwise extremely fine grained (cryptocrystalline).

Rarely, in vesicles filled dominantly with celadonite, collomorphic precipitations of goethite/hematite are observed (Fig. F56A) together with smectite/saponite and euhedral pyrite crystals.

4. Replacement of glassy groundmass of the basalt to palagonite is ubiquitous but with considerable local variation. To a lesser degree, preexisting minerals may also be affected. Whereas calcite forms amorphous patches up to 1–2 mm, phyllosilicates replace in most cases only very small spots of glassy mesostasis between plagioclase and clinopyroxene (Fig. F56B). As an exception, plagioclase can be replaced in part by smectite or celadonite. Olivine phenocrysts are always transformed into iddingsite, consisting of goethite/hematite and some other phases (Fig. F56C). Clinopyroxene and the very small magnetite grains and crystal skeletons are not affected by replacement.

   The replacement of groundmass occurs in part irregularly, but next to veins there is commonly developed a more intensive accumulation of small blastic grains or patches of phyllosilicates (Fig. F56B). Smectite and celadonite exclude one another not only in one single grain but also in a limited "district of grains," and altogether smectite seems to be somewhat more common as a neogenic mineral than celadonite (Fig. F56D). Zeolite, as part of the alteration, could not be observed within the groundmass. There are no differences between pillow and flow basalts with respect to the occurrence of alteration minerals.

   Generally, the top and bottom walls of the lava flows are oxidized to a certain extent as a very early event in the alteration process. Somewhat later, during alteration by seawater along fissures but in some places without visible feeder channels, a slight infiltration with Fe and resulting impregnation of the whole groundmass by FeOOH took place. In some cases, the secondary mineral association is also affected and smectite and celadonite are intensely red colored.

F56. Photomicrographs showing secondary minerals celadonite, collomorphic FeOOH/hematite, and smectite in basalts, p. 108.

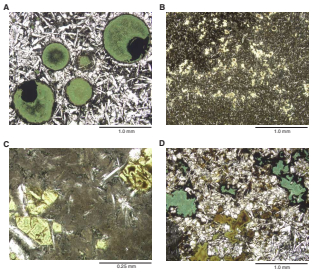

Conclusions

The restricted mineral paragenesis of the alteration with calcite, celadonite, smectite/saponite, and zeolite(s) indicates a very low temperature regime. According to Staudigel and Hart (1983), Floyd (1986), Floyd and Rowbotham (1986), and Alt (1993), this is reflected by moderate to high levels of water, low oxidation potential, and relatively low CO_2 content. The current visible hydration of glass to palagonite is restricted to the borders of different massive and/or pillow lava flows and onto interpillow material. The necessary high water flow for palagoniti-

zation was enabled by the clastic structure of these brecciated zones and their high permeability.

Smectite/saponite formation needs only low seawater/rock ratios, but the stability conditions of celadonite reflect higher seawater/rock ratios to provide a sufficient supply of potassium. A system of fissures, resulting from cooling of massive flows and pillows, has promoted the penetration of seawater. The compositional change of zoned vesicle fillings with smectite rims and celadonite cores, or vice versa, indicates a clear variability in the chemistry of penetrating seawater, especially with respect to the K and Fe contents and the redox potential.

The nearly total absence of sulfides, especially pyrite, in the secondary paragenesis is remarkable. This is a clear expression of S^{2-} deficiency within the percolating seawater and/or a redox potential that was too high for reducing SO_4^{2-} but not high enough for constant and more than partial oxidation of Fe^{2+}.

For an estimation of the alteration temperatures, we can only compare the existing secondary mineral paragenesis with data from former DSDP and ODP Legs (Muehlenbachs, 1980; Honnorez et al., 1983; Alt et al., 1992; Alt, 1993; Janney and Baker, 1995). From these data, especially $\delta^{18}O$ results, we can deduce that for the smectite/saponite formation, a temperature span between 0°–15°C is realistic. For celadonite, a somewhat higher temperature can be assumed and comparable data for calcite (also based on $\delta^{18}O$) imply a temperature range of 10°–45°C.

Therefore, using these data, we can conclude reliably that the subseafloor metamorphism of the basalts from Hole 1179D took place at temperatures <50°C, with a certain probability for a temperature range of 10°–30°C. The absence of chlorite is of concern with such a low-temperature regime and corresponds to Miyashiro's "low to middle zeolite facies" (Miyashiro, 1981). This very low temperature alteration of the basalts can be described also as a kind of "submarine weathering."

PHYSICAL PROPERTIES

Summary

Multisensor track (MST) measurements of magnetic susceptibility (MS), gamma-ray attenuation (GRA) bulk density, *P*-wave velocity, and natural gamma radiation (NGR) were made on APC and XCB whole cores from lithostratigraphic Units I, II, and III (Holes 1179A, 1179B, and 1179C). Index properties and *P*-wave velocities of these materials were also measured on discrete samples, and *P*-wave velocities and bulk densities were measured on 42 basalt samples from Unit V (Hole 1179D). In general, the measured physical properties correlate well with lithostratigraphy. *P*-wave velocities in the sediments are typically 1530–1550 m/s. Average bulk densities of the individual sedimentary units range from 1.265 to 1.450 g/cm^3, and average porosities range from 67% to 83%. Average bulk densities and velocities in the basalts are 2.745 g/cm^3 and 5002 m/s, respectively. Within Unit I, bulk density, thermal conductivity, and NGR decrease with depth in the upper 150 m of the section; porosity increases to >85%. We suspect that these seemingly paradoxical trends in density and porosity are caused by a progressive increase in the relative abundance of diatom fragments, which have low grain densities and contain large volumes of intragranular pore space, with depth. The contact between Units I and II is marked by small changes in the physical properties, but the transition from Unit II

to the pelagic clays of Unit III is dramatic. Densities increase, porosities fall to <70%, and there are marked increases in NGR and MS. Marked changes in NGR and MS at a depth of ~265 mbsf also suggest a compositional change within Unit III. The temperature gradient and average thermal conductivity in the upper 60 m of the sediment column are 0.0610° ± 0.002°C/m and 0.76 ± 0.01 W/(m·K), respectively. The conductive heat flow at Site 1179 is 46.40 ± 0.01 W/m².

Measurements on Cored Materials at Site 1179

For the purposes of physical properties, the geologic section at Site 1179 can be viewed as consisting of three intervals, a 283-m sequence of oozes and clays (Units I–III) cored using the APC and XCB, a 92-m section of interbedded cherts and softer sediments (Unit IV), and igneous basement (Unit V) below 375 mbsf. Cores from the first of these intervals (Holes 1179B [Cores 191-1179B-1H through 6H] and 1179C [Cores 191-1179C-1H through 26X]) were scanned on the MST. MS, GRA bulk density, and *P*-wave velocity were measured through the core liner at 2-cm intervals, and NGR was counted for 60 s at intervals of 20 cm. Thirty-six measurements of thermal conductivity were made on whole-round sections. One hundred seventy-one discrete measurements of index properties (wet bulk density, grain density, and porosity), 153 sonic velocities (PWS1, PWS2, and PWS3), and 94 automated vane shear (AVS) strength tests were made on the split cores. These data are summarized in Tables **T12, T13,** and **T14.** Measurements of sonic velocities using the PWS1 and PWS2 were discontinued after Core 191-1179C-3H (60 mbsf) because the sediments cracked when the transducer probes were inserted. Similarly, AVS measurements were abandoned when the cores split consistently during the test after Core 191-1179C-18H. No physical properties measurements were made on samples from the chert-bearing sediments because only a few chert cobbles were recovered in each core; softer sediments, which we believe are present in situ, were apparently washed away by the coring process. However, Wilkens et al. (1993) have made a detailed study of the properties of north Pacific deep-sea cherts. They report porosities of chert samples in the range 5.5% to 13%, with average bulk density and *P*-wave velocity of 2.506 g/cm³ and 5265 m/s (at 10 MPa confining pressure), respectively. Forty-two wet bulk densities and *P*-wave velocities (PWS3) were measured in 2-cm³ cubes cut from the basalt cores recovered from the basement section (Unit V). These data are summarized in Table **T15.** The measured physical properties from Site 1179 are plotted with the lithostratigraphic column in Figures **F57** and **F58.** In these profiles, a 19-point median filter has been applied to the MST data. The average properties of Units I–III and V are summarized in Table **T16.**

Sonic Velocities

The *P*-wave velocity profiles are shown in Figure **F57.** The PWS1, PWS2, and *P*-wave logger (PWL) velocities are in good agreement in the upper 25 m of the section. Below that depth, velocities measured on the split cores using PWS1 and PWS2 are lower than the PWL velocities. There is good agreement between PWS3 and the PWL velocities below ~80 mbsf. PWS3 velocities, which are measured through the core liner in a direction normal to the core axis, are distinctly higher than velocities measured using either PWS1 or PWS2, which are also measured on split cores. We believe that the difference between the PWS3 and PWS2

T12. PWS3 split-core *P*-wave velocities, p. 147.

T13. Index properties of discrete samples, Holes 1179A–1179C, p. 149.

T14. Thermal conductivity values, p. 152.

T15. Densities and *P*-wave velocities in basalts, p. 153.

F57. Variations of *P*-wave velocity, bulk density, and porosity with depth, p. 109.

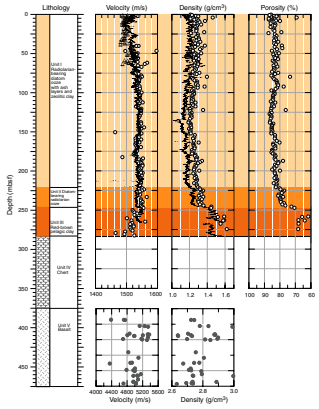

F58. Variations of thermal conductivity, natural gamma radiation, and magnetic susceptibility with depth, p. 110.

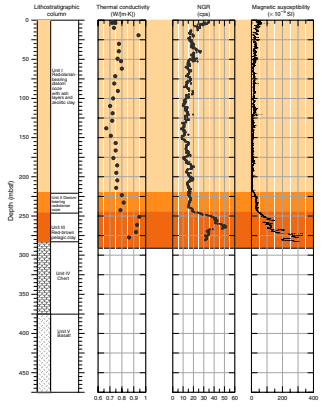

T16. Average physical properties by lithostratigraphic unit, p. 154.

velocities is caused by cracks that form in the core when the PWS1 and PWS2 probes are inserted in the sediment. We made several PWS2 and PWS3 measurements in the same intervals of Core 191-1179C-3H and found a systematic difference of 50 m/s. Consequently, PWS1 and PWS2 measurements were discontinued after Core 191-1179C-18H. PWS3 *P*-wave velocities in the sediments from Units I, II, and III are summarized in Table **T12.**

Within Units I and II, *P*-wave velocities increase very gradually from ~1535 m/s at a depth of 50 m in Unit I to ~1560 m/s at the boundary between Units II and III. Because of the discrepancy between velocities in samples from Unit III measured by PWL and PWS3 (Fig. **F57**), it is unclear whether sonic velocities are higher or lower in Unit III than they are in Unit II; PWS3 velocities are distinctly lower, with an average near 1530 m/s, whereas PWL velocities are slightly higher.

Sonic velocities and bulk densities were also measured on 42 ~8-cm^3 cubes cut from the cores of tholeiitic basalt (Unit V). The velocity measurements were made parallel to the core axis (z-direction) at bench pressure using the PWS3 velocimeter. Measurements were made only in the z-direction for two reasons. First, velocity anisotropy in oceanic basalt, diabase, and gabbro samples is generally minimal. For example, velocity anisotropy in gabbros recovered from Hole 735B is typically <3% (Iturrino et al., 1991) and the average is not statistically significant. Hence, only one measurement is needed to characterize these rocks. Second, the cubes tend to be slightly irregular in shape because opposite faces are often not quite parallel. The first cuts, made across the core perpendicular to the core axis, are most nearly parallel. Another consideration is that velocities in crystalline rocks are known to increase rapidly with increasing effective pressure, which is roughly equal to the difference between the confining pressure acting on the rock and the pore pressure. However, the effective pressure at the top of oceanic basement must be near zero, and the pore pressure is very likely to be near hydrostatic, at least in the upper part of the igneous crust. Thus, the in situ effective pressure is unlikely to be more than ~0.2 MPa (~300 psi) at a subbasement depth of 100 m. Measurements made at bench pressure are probably sufficient for estimating the properties of the basalt at sample scale. The measured properties of the basalt samples are summarized in Table **T15,** and the average velocity is 5002 m/s (Table **T16**). In situ velocities are almost certainly lower than this average owing to the presence of large-scale cracks and voids in the formation.

Bulk Density and Porosity

The index properties of sediments recovered from Holes 1179A, 1179B, and 1179C are summarized in Table **T13,** and the depth profiles are shown in Figures **F57** and **F58.** The approximate bulk densities of the basalt samples are given in Table **T15.** These values are approximate because the sample volumes were estimated from the measured dimensions of the cut samples, which are slightly irregular.

The GRA sediment densities are distinctly lower than the discrete sample densities, probably because the GRA density system is calibrated for aluminum and water as opposed to clays or siliceous sediments (Blum, 1997). The difference is slightly <1 g/cm^3. The depth trends, on the other hand, are very similar, suggesting that the pattern of density variations is well represented by both data sets. The porosity trend parallels the density profile, because bulk density depends largely on the

porosity and grain density. Average grain densities in Units I and II are near 2.47 g/cm³.

Although the average densities of samples from Units I (1.27 g/cm³) and II (1.33 g/cm³) are similar (Table T16), there is a clear correlation of density and porosity with lithology (Fig. F57). Densities in Unit II are nearly constant, but the densities of samples of the stiff clays from Unit III are higher, at ~1.54 g/cm³. We were able to measure the dry volumes of only two samples from the Unit III clays because their gas permeability is apparently so low the pycnometer failed to reach equilibrium during the time allotted by the software for the measurement of the dry volume. Six additional measurements of density and porosity in samples from Unit III were estimated from the dimensions and wet and dry weights of "plug" samples taken from the cores (see Table T13).

An interesting feature of Unit I is its very high porosity, which averages >80% to a depth of >220 m. Another interesting feature of the density and porosity profiles through the radiolarian-bearing diatom oozes of Unit I is that densities actually decrease from 1.3 g/cm³ near the surface to near 1.2 g/cm³ at a depth of ~150 mbsf. There is a corresponding increase in the total porosity to ~86% near 140 mbsf. Below 150 mbsf, densities gradually increase to ~1.3 g/cm³, with a corresponding decrease of porosity to near 80% at the bottom of Unit I. Grain densities (shown in Fig. F59) show a similar pattern, deceasing from 2.6 g/cm³ at the seafloor to 2.3 g/cm³ at 150 mbsf. These observations lead us to speculate that the high porosities we observe in Unit I reflect the abundance of diatom fragments in the sediment. Diatoms are composed of opaline silica, with a bulk density of 2.01 to 2.16 g/cm³, and their lacy morphology includes abundant small holes that are not filled with clay or other materials. A gradual increase with depth of the relative abundance of diatoms in the sediment would account for both the increase of porosity and the decrease of grain density in the upper 150 m of Unit I.

F59. Variation of bulk density with depth in Unit I, p. 111.

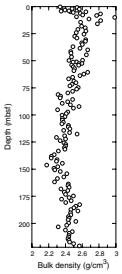

Thermal Conductivity and Heat Flow

The thermal conductivity, NGR, and MS profiles are shown in Figure F58. Thermal conductivity measurements were made in the third section of each core recovered from Holes 1179A, 1179B, and 1179C, through Core 191-1179C-26X. No measurements were made of thermal conductivity in the cherts (Unit IV) or basalts (Unit V). Thermal conductivities in Units I through III are summarized in Table T13 and range from 0.67 to 0.95 W/(m·K). Average values for Units I through III are listed in Table T16. Thermal conductivity increases with depth, and the three lithostratigraphic units have statistically distinguishable thermal properties that increase from 0.75 ± 0.01 W/(m·K) in Unit I to 0.80 ± 0.01 W/(m·K) in Unit II and 0.91 ± 0.01 W/(m·K) in Unit III. Worth noting is the fact that the variation of thermal conductivity in Unit I initially decreases with depth and reaches a minimum near 150 mbsf, mimicking the pattern we observed in the variation of bulk density and porosity. The thermal conductivity profile probably reflects the variation of porosity with depth.

Temperatures were measured with the Adara tool on several APC cores. Temperatures at the seafloor and at depths of 30 and 60 mbsf are 2.00°, 3.84°, and 5.66°C, respectively; the temperature gradient is 0.0610 ± 0.002°C/m. The average thermal conductivity of samples from the same depth interval (0–60 mbsf) is 0.76 ± 0.01 W/(m·K), and the conductive heat flow at Site 1179 is 46.40 ± 0.01 mW/m².

Natural Gamma Radiation

Strictly speaking, NGR is not a physical property. The intensity of natural gamma radiation is a measure of the abundance of potassium, thorium, and uranium in the cores. NGR was counted for 60 s at intervals of 20 cm in all APC and XCB cores from Holes 1179A, 1179B, and 1179C. The NGR profile shown in Figure F58 has been filtered using a 19-point median filter. Through Unit I, NGR shows a pattern similar to porosity, density, and thermal conductivity; NGR decreases gradually with depth to ~150 mbsf then begins to increase. Unit II does not appear to be distinguishable from Unit I, but there is a clear increase in NGR at the contact between Units II and III. NGR decreases abruptly at a depth of ~265 mbsf within the red-brown pelagic clay of Unit III. This change suggests a change in the mineral content, possibly a decrease in clay content, in Unit III that is not indicated by the physical properties, with the exception of magnetic susceptibility.

Magnetic Susceptibility

MS measurements were made for 3 s at 2-cm intervals on APC and XCB cores from Holes 1179A, 1179B, and 1179C. A 19-point median filter has been applied to the profile shown in Figure F58. Susceptibility correlates well with the lithostratigraphy of the sediments cored at Site 1179, increasing slightly at the contact between Units I and II and more strongly between Units II and III. There is also an abrupt increase in MS at ~265 mbsf. Like the change in NGR noted above, this suggests a change of mineral content within Unit III that is apparently not evidenced elsewhere.

Vane Shear Strength

Vane shear measurements were made near the bottom of each section of the APC cores from Holes 1179A, 1179B, and 1179C until the cores began to split, invalidating the shear strength measurements. Vane shear measurements were therefore discontinued after Core 191-1179C-18H. All vane shear measurements were made in cores recovered from Unit I. Vane shear strengths are summarized in Table T17, and the peak strength profile is shown in Figure F60. There is considerable scatter in these data. Shear strength is low (~5 kPa) in the shallow sediments, as expected, increasing to an average of ~60 kPa at a depth of 100 mbsf. Below that depth, peak strengths increase very gradually to average values of perhaps 70 or 75 kPa at a depth of 190 mbsf.

Correlation of the Lithologic Column with Seismic Reflection Profiles

Surveys by the *Hakuho Maru* in August of 1996 (cruise KH96-3-1) produced the two seismic multichannel profiles (2-1 and 2-4) across Site 1179 that are shown in Figures F61 and F62. In addition to the seafloor reflection, there are three prominent reflectors in the seismic section at ~0.15, ~0.17, and ~0.22 s one-way traveltime and a slightly weaker reflector near 0.25 s. There are also numerous weak and often discontinuous reflectors between the seafloor and the 0.15-s reflector.

We attempted to correlate the observed reflections with the lithostratigraphic column by calculating traveltimes from depths to possible reflecting horizons based on average *P*-wave velocities (PWS3 and PWL)

T17. Vane shear data, p. 155.

F60. Variation of peak shear strength with depth in Unit I, p. 112.

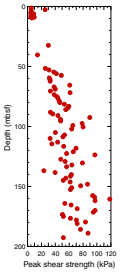

F61. Multichannel seismic profile across Site 1179 (line 2-1), p. 113.

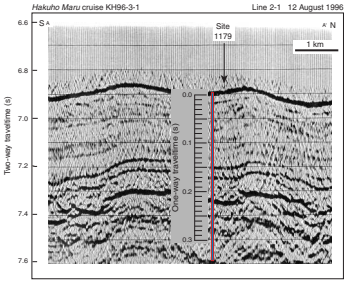

F62. Multichannel seismic profile across Site 1179 (line 2-4), p. 114.

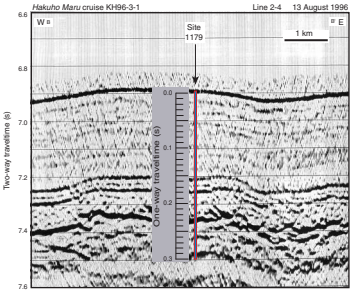

measured in the laboratory, but that produced a set of implausible one-way traveltimes. Because the sediments at Site 1179 have very high porosities, we next corrected the measured velocities for the local temperature profile, using dV/dT for seawater = 3.2 m/s/°C. We then made another forward calculation of the traveltimes to possible reflectors. The best correlation model generated by this method is summarized in Table **T18.** The model accounts for many of the weak reflections above the Unit II/III transition, but the correlations are problematical for a number of reasons. One is that the interval velocities are highly variable, and some are unreasonably high or low. More serious problems are that neither the strong reflection at 0.172 s nor the very strong reflection at 0.22 s corresponds to any horizon in the lithostratigraphic column, and the top of the chert (Unit IV) does not correspond to a reflection.

T18. Correlation of reflection traveltime with the lithostratigraphic column using measured *P*-wave velocities, p. 156.

As an alternative to using the shipboard data, we applied an empirical relationship between one-way traveltime and depth based on measured traveltimes and drilled depths to basement at DSDP sites worldwide (Carlson et al., 1986). According to the model,

$$z(t) = -3030 \times \ln(1 - 0.52t),$$

where

z = depth in meters, and
t = one-way traveltime in seconds.

The root-mean-square error reported by Carlson et al. (1986) is 26 m, and the corresponding velocity-depth function is

$$v(z) = 1590\exp(0.00033z).$$

This model was applied by computing depths from the observed traveltimes from both profiles (which are slightly different). The results are summarized in Table **T19.** Despite the fact that this correlation model is based on a global average time-depth model, the results are quite good. The model accounts for all of the major reflectors; from the line 2-1 traveltimes, it predicts the depths to all of the unit boundaries to within 10 m or less, and the major lithostratigraphic boundaries—the Unit II/III boundary (~246 mbsf), the top of the chert (~283 mbsf), and the top of igneous basement (375 mbsf)—correspond to the strongest reflections (Fig. **F10**). The success of this model suggests that *P*-wave velocities measured in the cored sediments can be too low by as much as 150 to 200 m/s. The probable cause of this rather large discrepancy is disruption of the grain-to-grain contacts by expansion of pore water when the cores are brought to the surface. From a depth of 5500 m, the volume expansion is nearly 2.5%.

T19. Correlation of reflection traveltime with the lithostratigraphic column, p. 157.

DOWNHOLE MEASUREMENTS

Logging data were recorded in Hole 1179D during Leg 191. One logging run was performed with the triple-combo tool string including the newly developed LDEO multisensor gamma-ray tool (MGT). Only the upper part of the borehole was logged because of a borehole obstruction at ~260 mbsf. The triple-combo measurements are affected by the large

hole size, particularly for the accelerator porosity sonde (APS) and high-temperature lithodensity logging tool (HLDT), so the density and porosity data should be treated cautiously. Despite the poor hole condition and an incomplete logged section, the natural radioactivity and resistivity measurements nicely recorded the lithologic changes described in the Hole 1179C sedimentary section (see "Sedimentology," p. 9).

Logging Operations

Logging operations were conducted in Hole 1179D after it had been drilled to a depth of 475 mbsf with a 9.75-in drill bit. The borehole was conditioned with sepiolite drilling mud mixed with seawater. The base of the BHA was set at 154.5 mbsf. Three tool-string runs were planned: triple combo, Formation MicroScanner sonic, and ultrasonic borehole imager. However, operational difficulties only allowed the triple-combo deployment.

The triple-combo tool string was deployed first. It included the APS, the hostile environment natural gamma sonde (HNGS), the HLDT, and the phasor dual induction–spherically focused resistivity tool (DIT). The new LDEO MGT was attached to the top of the tool string and the LDEO temperature/acceleration/pressure (TAP) tool was attached to the bottom of the tool string. The first triple-combo repeat pass was logged from 300 to 203 mbsf with the standard triple-combo probes. After this repeat pass, we attempted to lower the tool string but a bridge was encountered at ~260 mbsf. After several unsuccessful attempts to pass the tool string through the bridge, only the upper part of the borehole was logged and the remaining passes started from this point. The second and third passes were used for recording MGT data only and the fourth pass to run the standard triple combo. No further logging was conducted in Hole 1179D.

Data Quality

Degraded borehole width affects most measurements, particularly those that require eccentralization and good contact between the tool and the borehole wall (APS and HLDT). In Hole 1179D, the caliper data from 290 to 246 mbsf are very rough, ranging from 7 to 16.5 in (Fig. F63). From 246 mbsf to the pipe depth, the caliper remained fully opened (16.5 in, which is the full range of the tool). Poor borehole conditions, ranging from washed to constricted along the whole logged interval, resulted in logs of poor quality, especially for density and porosity. Furthermore, the HLDT developed a functioning problem with the far-spaced detector, resulting in erroneous spikes in the density and photoelectric (PEF) measurements. These poor-quality logs will not be discussed in the next section.

Despite the washed-out conditions, both gamma-ray (HNGS and MGT) and resistivity (DIT) from the upper part of the borehole are of good quality.

The results of both triple-combo passes have been spliced together to produce a composite and depth-corrected data set (see the "Related Leg Data" contents list).

F63. NGR measurements compared with lithostratigraphic units, p. 115.

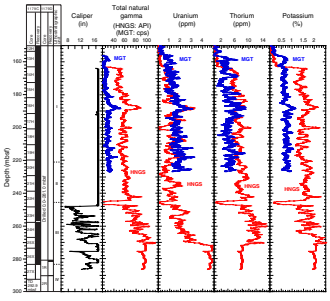

Natural Radioactivity

Natural radioactivity was measured downhole by both the HNGS and MGT. Both tools have scintillation detectors that measure the natural gamma radiation emitted by the formation and resulting from radioactive decay. In general, the total gamma-ray record shows an overall increase in natural radioactivity with depth (Fig. F63). There is, however, a significant decrease in the log data at 246 mbsf; this correlates with similar tool responses at this depth for resistivity and PEF. The strong decrease in resistivity recorded at 245 mbsf is probably linked to the tool response as a result of the poor hole conditions at this depth (caliper jumping from 7 to 16.5 in).

A number of distinctive peaks in the gamma-ray measurements in the uppermost part of the logged section at depths of 182.9, 188.0, 195.7, and 242.2 mbsf may correspond to the ash layers recovered in the sediment cores (see "Sedimentology," p. 9).

The downhole variations in potassium and thorium concentrations closely follow the pattern for the total gamma-ray record. The uranium log, however, shows a rather different pattern with a number of maxima and minima not identifiable on the total gamma-ray record. Peaks in the uranium data occur at depths of 195.7, 208.1, 217.7, 235.6, and 251.3 mbsf. A minimum in the uranium data at 200 mbsf mirrors peaks in the potassium and thorium logs and may correspond to a filled burrow located in the sediment core at this depth.

In general, the uranium concentrations measured by the MGT closely match HNGS data. Differences in potassium and thorium concentrations are caused by different calibration schemes for the tools. The average level of potassium measured by the MGT is more consistent with previous measurements in the similar environment (Leg 185, Site 1149) (Plank, Ludden, Escutia, et al., 2000).

The MGT data are well correlated with total NGR counts from HNGS and core data (MST) while presenting much higher vertical resolution and better defined layer boundaries (Fig. F64). All gamma-ray measurements indicate the presence of ash layers in the uppermost part of the logged section.

F64. Comparison between the HNGS and the MGT, p. 116.

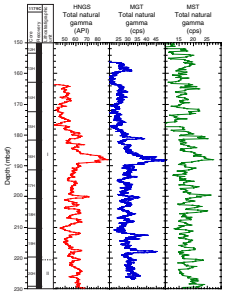

Electrical Measurements

The electrical measurements were made with the DIT. This tool provides three measurements of the formation electrical resistivity—deep, medium, and shallow (SFLU)—on the basis of the penetration depth of the focused current into the formation. The different measurements along the whole logged section are shown in Figure F65. The resistivity data clearly delineate the main lithologic types observed in the sediment column at Hole 1179C.

The electrical resistivity in lithostratigraphic Unit I (diatom ooze) is low, with small increases in resistivity at 180, 188, 200, and 212 mbsf. These increases in resistivity can be associated with ash layers or burrows described from the core description (see "Sedimentology," p. 9) and with the gamma-ray measurements as shown in Figure F65. The boundary between Units I and II (radiolarian ooze) is marked by a slight increase in resistivity at ~221.5 mbsf (only 0.01 Ωm of difference between Units I and II). The DIT data clearly record the lithologic change between Units II and III (pelagic clays) at ~243 mbsf, marked by an increase in the electrical resistivity (SFLU increases from 0.25 to 0.35 Ωm). The boundary between lithostratigraphic Units III and IV (cherts) at

F65. Electrical resistivity measurements compared with lithostratigraphic units, p. 117.

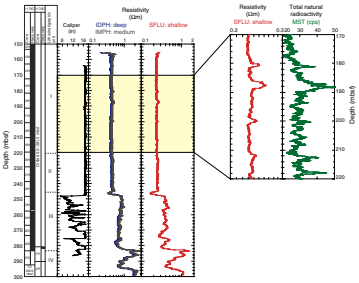

~283 m is marked by a strong increase in resistivity (from 0.25 to 1.5 Ωm). The chert-bearing formation consists of alternating high resistivity layers (nodules) and interbedded low resistivity layers (clay-rich layers).

The strong decrease in resistivity recorded at 245 mbsf is linked to the tool response because of the poor hole conditions at this depth (caliper jumping from 7 to 16.5 in).

Drill-String Acceleration Measurement Tool

The DSA tool operates as a memory tool recording the tool's acceleration, ambient pressure, and internal temperature. The tool uses two accelerometers: an axial (vertical) high-sensitivity accelerometer, and a three-axis low-sensitivity accelerometer (LSA).

The DSA tool was deployed on APC Cores 191-1179C-4H and 7H at 77.3 and 105.8 mbsf, respectively. Both deployments were successful: the tool started recording data at the predetermined depth (thus relieving pressure transducer concerns), and two full data sets were recovered without any problems (confirming proper functioning of the controller and memory card). The maximum pressure recorded by the tool was ~9000 psi, and shocks did not exceed 2.7 G. Plots of x- and y-axis acceleration data (Fig. **F66**) clearly show significant events during core barrel hole penetration and recovery, in particular, deviation of the core barrel from a vertical position at the beginning of coring, which could negatively affect core recovery. Figure **F67** clearly shows time variations of amplitude and visible frequency of downhole heave recorded by the LSA. The uphole heave from the wireline heave compensator accelerometer was also recorded, making possible the direct comparison of uphole and downhole heave and evaluation of the effectiveness of the drill-string heave compensator. Overall, the tool provides valuable information for monitoring the quality of drilling and coring processes.

F66. Acceleration along the x- and y-axes, p. 118.

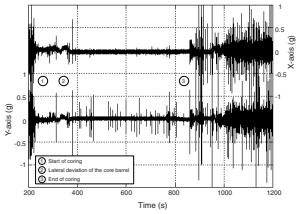

F67. Heave recorded during APC coring, p. 119.

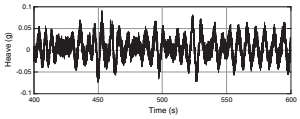

BOREHOLE INSTRUMENTS STATUS

Abstract

The establishment of the seafloor borehole seismological observatory (NEREID-191) was successful. An almost identical borehole observatory was set up at the Boso peninsula of Japan in August of 1998 as a prototype. The first (NEREID-I) and second (NEREID-II) seafloor borehole geophysical observatories were installed during Leg 186 on the inner wall of the Japan Trench in July and August of 1999, respectively (Sacks, Suyehiro, Acton, et al., 2000). Site 1179 is the third seismological observatory and is an important component of ION on the northwest Pacific abyssal seafloor. The design concept of the system was almost the same as those successfully installed systems of NEREID-I and -II. Although the borehole sensors are physically inaccessible, the seafloor components are designed to be replaceable by a remotely operated vehicle (ROV). The multiple-access expandable gateway (MEG-191) data controller can be replaced. The storage acquisition module (SAM-191) must be replaced as the data disks are filled up after ~1.5 yr of recording (72 GB). Batteries can be revived by replacing the magnesium anodes. The system status can be checked by a hardwire link to the SAM-191 using underwater mateable connector (UMC) cables. Site 1179 is located ~1600 km from Japan, and there are no nearby ocean cables to utilize

for data recovery and power. It is our plan to connect our observatory to Japan via an acoustic satellite communication link with a surface buoy anchored above the site. Although the speed of our underwater acoustic communication link between the bottom and sea surface is 9600 bits per second (bps), the communication speed will be lowered to the 2400 bps of satellite data telemetry, which is available at present. Then the data can be disseminated in almost real time.

Emplacement Depth of Seismometers in Hole 1179E

A major problem encountered during the seismometer installation was that logging data were not available in order to decide the depth of emplacement of the seismometers in Hole 1179E. Logging at Hole 1179D had to be terminated at a depth of ~300 mbsf owing to bridging of the hole (see "Downhole Measurements," p. 40). Basement rocks recovered in Hole 1179D consist mostly of fresh aphyric basalts in massive flows, pillows, and breccia with a minor amount of interpillow sediments (see "Igneous Petrology," p. 26). Rates of penetration at Hole 1179E were very consistent throughout the basement interval, averaging ~2.0 m/hr. Based on drilling data, Hole 1179E appeared to be in excellent condition for installation of the seismometers. Based on core descriptions from Hole 1179D and drilling data from Hole 1179E, it was decided to emplace the two seismometers into the basaltic basement at depths between 458.5 and 462.7 mbsf or between 87.5 and 91.7 m below the inferred top of the basaltic basement. Basement rocks at that depth were considered to be fresh aphyric basalts forming massive flows or pillows. From measurements of physical properties, average densities and velocities in the basalt section were 2.754 g/cm³ and 5002 m/s, respectively.

Operations

At 1445 hr on 21 August, installation of the seismic borehole observatory began in Hole 1179E, and at 1445 hr on 24 August, the J-tool was released from the riser/hanger after a long installation operation of 3 days. At that time, the seismological observatory was successfully installed at Hole 1179E. A timeline of instrument deployment operations is given in Table T20.

The borehole instrument assembly (BIA) (Fig. F68) was positioned between a 4.5-in casing and the stinger pipe (Fig. F69) and was then lowered down to the moonpool level using the 4.5-in casing elevators. Each of the two instrument cables were fed off of their respective reels, over sheaves (600 mm diameter × 84 mm groove width) hung below the rotary table, and connected to the two Guralp CMG-1T broadband seismometers (Fig. F70). After testing the seismometers through the instrument cables, the 4.5-in casing pipe (API-J55-STC, 10.5 lb/ft, and ~11.7 m length each) and cable deployment began at 1830 hr on 21 August.

The cables were attached to the casing pipe by tie wraps covered by duct tape (Fig. F71). Approximately every 1.5 m, a 4.5-in casing centralizer (9.625 in OD × 3 in height) was attached (Fig. F72). The 4.5-in casing was assembled at ~5 joints/hr. It took longer than normal drill-pipe handling because the "iron roughneck" could not be used.

T20. Instrument package deployment, p. 158.

F68. Borehole instrument assembly on the rig floor, p. 120.

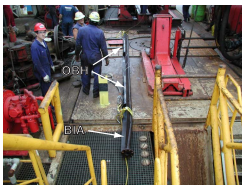

F69. Stinger pipe jointed to the lower end of the borehole instrument assembly, p. 121.

F70. Borehole instrument assembly in the moonpool area, p. 122.

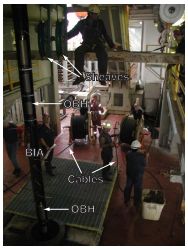

F71. Instrument cable connected to the OBH, p. 123.

The termination of the two instrument cables began at 0500 hr on 22 August and lasted for 17 hr. During the cable termination, it was discovered that an O-ring of one of the canister connections had been mislabeled and had to be replaced. This resulted in an additional 5-hr delay.

The MEG-191 was installed into the MEG frame on the riser/hanger, and the instrument string assembly associated with electrical checks was completed by 0130 hr on 23 August (Figs. F73, F74). Then the drill string was lowered, and Hole 1179E was reentered for the fourth and final time at 1115 hr (Figs. F75, F76A). The instrument package was lowered into the hole without incident, and, at 1500 hr, the riser/hanger landed at the correct depth (Fig. F76B).

The bottom of the hole was filled with cement having a density of 1.9 g/cm^3 and a volume of 8.0 m^3. Using theoretical hole volumes and displacements, the top of the cement slurry should have reached a level of ~112 m above the 10.75-in casing shoe. For the CMG-1T broadband seismometers, cementing provides the best coupling to the surrounding rocks compared to other methods that utilize mechanical arms, pads, or sand. Furthermore, cementing prevents water motion and temperature fluctuation from becoming sources of noise.

After successfully cementing the instruments, the battery frame (power access terminal [PAT]) was made up in the moonpool (Fig. F77). The PAT was hung at three points by three cables from the dual acoustic releases (Fig. F78). The drill pipe passes through the center of the PAT and the guide sleeve of the VIT frame. Upon release, three small glass sphere buoys attached to the three cables pull the cables up. Because the operation was complicated, involving many transfers of weight while the ship's heave was a few meters, the actual lowering began after sunrise at 0415 hr on 24 August (Fig. F79). The frame was lowered using the logging cable, allowing precise depth measurements and good heave compensation, and placed successfully on the reentry cone after a 4.75-hr trip. The PAT was released from the bridle by an acoustic command.

The VIT/subsea television system was deployed to survey the platform installation and observe the J-tool release from the riser/hanger. Proper platform installation was verified, and the J-tool was released. The installation of the seismic borehole observatory at Hole 1179E was successfully completed at this time and awaited the ROV *Kaiko* visit in November to start the system.

Borehole Instruments

The BIA consists of two sets of three-component CMG-1T broadband seismometers (top: SN T1036 and bottom: SN T1037). A 3.2-m-long "stinger" pipe with one centralizer was attached to the BIA bottom. The length of the stinger was chosen to optimize safe reentry.

Each of the sensors was checked two times through the MEG-191 and the SAM-191 during the installation and was confirmed to perform perfectly.

Seafloor-Borehole Link

The cable link between the hole bottom and the seafloor was to be supported by the 4.5-in casing pipes. This way, the cables can be protected, the installation depth is precisely predetermined, and the casing string does not heave inside the hole during the cementing because the

F72. Centralizer attached on the 4.5-in casing pipe, p. 124.

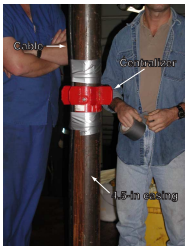

F73. MEG frame mounted on the riser/hanger, p. 125.

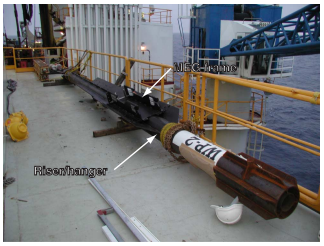

F74. MEG-191 installed on the MEG frame, p. 126.

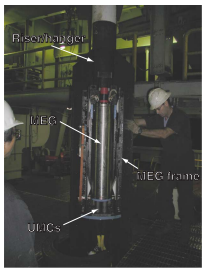

F75. MEG-191 on the riser/hanger, lowered into the moonpool, p. 127.

hanger/riser is coupled to the reentry cone. The centralizers further protect the cables.

A total of 38 joints of casing pipe hangs the instruments. The cables were cut at the moonpool 2.3 m longer than required to connect to the MEG-191 bottom stab plate in case there is a need for retermination. The cable termination required six people working on two cables in parallel for ~17 hr.

Seafloor Instruments

The seafloor instruments were successfully emplaced. The components are the PAT power supply, the SAM-191 data recorder, and the MEG-191 to merge data and control the observatory. The SAM-191 recorder unit was not installed on the PAT frame, but the installation was completed during the ROV visit in October. During Leg 191, the MEG-191 was slid into its holder attached to the hanger/riser pipe connected to the two cables at its bottom side. On the top of the battery frame, an ROV dummy receptacle was installed instead of the SAM-191 to avoid plug contamination. We decided at the last moment not to attach a stopper that prevents unwanted vertical upward motion of the MEG-191, which may disconnect the system. The stopper was not attached, because it needs to be removed in order to unplug the MEG-191 from the riser/hanger, which added an extra task for the ROV.

Zinc anodes were attached to the PAT frame, which is made of steel, to prevent corrosion. The anodes were not attached to other components that were made of titanium. Stainless steel canisters containing the accumulator, power control system (PCS), and data logger (DL) of the seawater battery (SWB) assembly were painted with epoxy-based anticorrosive paint.

The PAT had four SWB units and can generate a total electric power of 24 W, according to the manufacturer's specifications. The observatory constantly consumes 9 W of electric power. It is estimated that the SWB assembly will have enough capacity to provide electric power to the observatory for 5 yr. After the 5-yr period, the four magnesium anodes can be replaced by an ROV.

The output end of the oil-filled four-conductor UMC cable from the SWB via the PCS is laid on the top of the PAT (Fig. **F79**). An ROV must disconnect the end of the cable from the parking position and connect it to the top of the MEG-191 after removing the dummy UMC receptacle. Upon inspection with the VIT camera, the relative positions of the MEG-191 and the UMC were found to be farthest apart, 180° around the center (Fig. **F76C**). This arrangement of the MEG-191 and the UMC will force an ROV to perform a time-consuming operation in order to make a connection between the PAT and the SWB. Table **T21** depicts the tasks to be accomplished by the ROV.

F76. Snapshots from the VIT/subsea TV camera, p. 128.

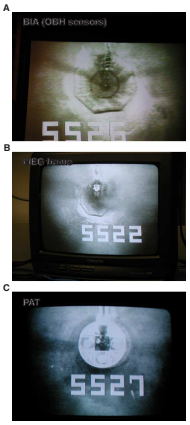

F77. Preparations for the deployment of the PAT battery frame, p. 130.

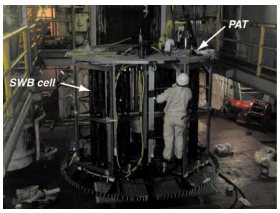

F78. Schematic diagram of the PAT bridle assembly, p. 131.

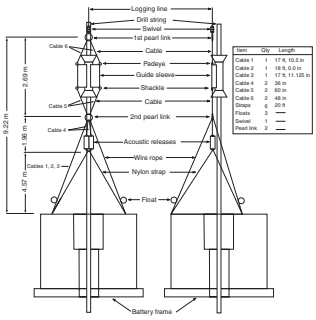

F79. PAT battery frame lowered into the sea through the moonpool, p. 132.

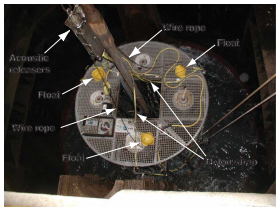

T21. ROV tasks to start the NEREID-191 system, p. 159.

REFERENCES

Alt, J.C., 1993. Low-temperature alteration of basalts from the Hawaiian Arch, Leg 136. *In* Wilkens, R.H., Firth, J.V., Bender, J., et al., *Proc. ODP, Sci. Results,* 136: College Station, TX (Ocean Drilling Program), 133–146.

Alt, J.C., France-Lanord, C., Floyd, P.A., Castillo, P., and Galy, A., 1992. Low-temperature hydrothermal alteration of Jurassic ocean crust, Site 801. *In* Larson, R.L., Lancelot, Y., et al., *Proc. ODP, Sci. Results,* 129: College Station, TX (Ocean Drilling Program), 415–427.

Blum, P., 1997. Physical properties handbook: a guide to the shipboard measurement of physical properties of deep-sea cores. *ODP Tech. Note,* 26 [Online]. Available from World Wide Web: <http://www-odp.tamu.edu/publications/tnotes/tn26/INDEX.HTM>. [Cited 2000-07-16]

Carlson, R.L., Gangi, A.F., and Snow, K.R., 1986. Empirical reflection travel time versus depth and velocity versus depth functions for the deep-sea sediment column. *J. Geophys. Res.,* 91:8249–8266.

Castillo, P., Batiza, R., and Stern, R.J., 1986. Petrology and geochemistry of Nauru Basin igneous complex: large-volume, off-ridge eruptions of MORB-like basalt during the Cretaceous. *In* Moberly, R., Schlanger, S.O., et al., *Init. Repts. DSDP,* 89: Washington (U.S. Govt. Printing Office), 555–576.

Ewing, J., Ewing, M., Aitken, T., and Ludwig, W.J., 1968. North Pacific sediment layers measured by seismic profiling. *In* Knopoff, L., Drake, C.L., and Hart, P.J. (Eds.), *The Crust and Upper Mantle of the Pacific Area.* Geophys. Monogr., Am. Geophys. Union., 12:147–173.

Fischer, A.G., Heezen, B.C., et al., 1971. *Init. Repts. DSDP,* 6: Washington (U.S. Govt. Printing Office).

Floyd, P.A., 1986. Petrology and geochemistry of oceanic intraplate sheet-flow basalts, Nauru Basin, Deep Sea Drilling Project Leg 89. *In* Moberly, R., Schlanger, S.O., et al., *Init. Repts. DSDP,* 89: Washington (U.S. Govt. Printing Office), 471–497.

Floyd, P.A., and Castillo, P.R., 1992. Geochemistry and petrogenesis of Jurassic ocean crust basalts, Site 801. *In* Larson, R.L., Lancelot, Y., et al., *Proc. ODP, Sci. Results,* 129: College Station, TX (Ocean Drilling Program), 361–388.

Floyd, P.A., and Rowbotham, G., 1986. Chemistry of primary and secondary phases in intraplate basalts and volcaniclastic sediments, Deep Sea Drilling project Leg 89. *In* Moberly, R., Schlanger, S.O., et al., *Init. Repts. DSDP,* 89: Washington (U.S. Govt. Printing Office), 459–469.

Foreman, H.P., 1975. Radiolaria from the North Pacific, Deep Sea Drilling Project, Leg 32. *In* Larson, R.L., Moberly, R., et al., *Init. Repts. DSDP,* 32: Washington (U.S. Govt. Printing Office), 579–676.

Fountain, J.C., Jacobi, R.D., and Fahey, T.J., 1985. Petrology and geochemistry of basalts from Deep Sea Drilling Project Leg 86, Site 581. *In* Heath G.R., Burckle, L.H., et al., *Init. Repts. DSDP,* 86: Washington (U.S. Govt. Printing Office), 691–697.

Gradstein, F.M., Agterberg, F.P., Ogg, J.G., Hardenbol, J., van Veen, P., Thierry, J., and Huang, Z., 1994. A Mesozoic time scale. *J. Geophys. Res.,* 99:24051–24074.

————, 1995. A Triassic, Jurassic and Cretaceous time scale. *In* Berggren, W.A., Kent, D.V., and Aubry, M.P., and Hardenbol, J. (Eds.), *Geochronology, Time Scales and Global Stratigraphic Correlation.* Spec. Publ.—Soc. Econ. Paleontol. Mineral., 54:95–126.

Hays, J.D., 1970. Stratigraphy and evolutionary trends of radiolaria in North Pacific deep sea sediments. *In* Hays, J.D. (Ed.), *Geological Investigations of the North Pacific.* Mem.—Geol. Soc. Am., 126:185–218.

Heath, G.R., Burckle, L.H., et al., 1985. *Init. Repts. DSDP,* 86: Washington (U.S. Govt. Printing Office).

Heezen, B.C., MacGregor, I.D., et al., 1973. *Init. Repts. DSDP,* 20: Washington (U.S. Govt. Printing Office).

Honnorez, J., Laverne, C., Hubberten, H.-W., Emmermann, R., and Muehlenbachs, K., 1983. Alteration processes in Layer 2 basalts from Deep Sea Drilling Project Hole 504B, Costa Rica Rift. *In* Cann, J.R., Langseth, M.G., Honnorez, J., Von Herzen, R.P., White, S.M., et al., *Init. Repts. DSDP,* 69: Washington (U.S. Govt. Printing Office), 509–546.

Humphris, S.E., Thompson, R.N., Gibson, I.L., and Marriner, G.F., 1980. Comparison of geochemistry of basalts from the East Pacific Rise, OCP Ridge and Siqueiros Fracture Zone, Deep Sea Drilling Project, Leg 54. *In* Rosendahl, B.R., Hekinian, R., et al., *Init. Repts. DSDP,* 54: Washington (U.S. Govt. Printing Office), 635–649.

Iturrino, G.J., and Christensen, N.I., 1991. Reflectivity modeling of the layer 3 gabbroic sequence drilled at the Atlantis II Fracture Zone. *In* Von Herzen, R.P., Robinson, P.T., et al., *Proc. ODP, Sci. Results,* 118: College Station, TX (Ocean Drilling Program), 245–252.

Janney, P.E., and Baker, P.E., 1995. Petrology and geochemistry of basaltic clasts and hyaloclastites from volcaniclastic sediments at Site 869. *In* Winterer, E.L., Sager, W.W., Firth, J.V., and Sinton, J.M. (Eds.), *Proc. ODP, Sci. Results,* 143: College Station, TX (Ocean Drilling Program), 263–276.

Janney, P.E., and Castillo, P., 1996. Basalts from the Central Pacific Basin: evidence for the origin of Cretaceous igneous complexes in the Jurassic western Pacific. *J. Geophys. Res.,* 101:2875–2893.

————, 1997. Geochemistry of Mesozoic Pacific mid-ocean ridge basalt: constraints on melt generation and the evolution of the Pacific upper mantle. *J. Geophys. Res.,* 102:5207–5229.

Larson, R.L., and Chase, C.G., 1972. Late Mesozoic evolution of the western Pacific Ocean. *Geol. Soc. Am. Bull.,* 83:3637–3644.

Larson, R.L., Moberly, R., et al., 1975. *Init. Repts. DSDP,* 32: Washington (U.S. Govt. Printing Office).

Larson, R.L., Steiner, M.B., Erba, E., and Lancelot, Y., 1992. Paleolatitudes and tectonic reconstructions of the oldest portion of the Pacific Plate: a comparative study. *In* Larson, R.L., Lancelot, Y., et al., *Proc. ODP, Sci. Results,* 129: College Station, TX (Ocean Drilling Program), 615–631.

Ludwig, W.J., and Houtz, R.E., 1979. Isopach map of sediments in the Pacific Ocean Basin and marginal sea basins. *AAPG Map Ser.,* 647.

Mahoney, J.J., Storey, M., Duncan, R.A., Spencer, K.J., and Pringle, M., 1993. Geochemistry and geochronology of Leg 130 basement lavas: nature and origin of the Ontong Java Plateau. *In* Berger, W.H., Kroenke, L.W., Mayer, L.A., et al., *Proc. ODP, Sci. Results,* 130: College Station, TX (Ocean Drilling Program), 3–22.

Marshall, M.C., 1975. Petrology and chemical composition of basaltic rocks recovered on Leg 32, Deep Sea Drilling Project. *In* Larson, R.L., Moberly, R., et al., *Init. Repts. DSDP,* 32: Washington (U.S. Govt. Printing Office), 563–570.

Masuda, M., and Nagasawa, S., 1975. Rocks with negative cerium anomalies, dredged from Shatsky Rise. *Geochem. J.,* 9:227–233.

Miyashiro, A., 1981. *Metamorphism and Metamorphic Belts:* London (George Allen & Unwin).

Mudie, P.J., 1987. Palynology and dinoflagellate biostratigraphy of Deep Sea Drilling Project Leg 94, Sites 607 and 611, North Atlantic Ocean. *In* Ruddiman, W.F., Kidd, R.B., Thomas, E., et al., *Init. Repts. DSDP,* 94 (Pt. 2): Washington (U.S. Govt. Printing Office), 785–812.

Muehlenbachs, K., 1980. The alteration and aging of the basaltic layer of the sea floor: oxygen isotope evidence from DSDP/IPOD Legs 51, 52, and 53. *In* Donnelly, T., Francheteau, J., Bryan, W., Robinson, P., Flower, M., Salisbury, M., et al., *Init. Repts. DSDP,* 51, 52, 53 (Pt. 2): Washington (U.S. Govt. Printing Office), 1159–1167.

Nakanishi, M., Sager, W.W., and Klaus, A., 1999. Magnetic lineations within Shatsky Rise, northwest Pacific Ocean: implications for hot spot–triple junction interaction and oceanic plateau formation. *J. Geophys. Res.,* 104:7539–7556.

Nakanishi, M., Tamaki, K., and Kobayashi, K., 1989. Mesozoic magnetic anomaly lineations and seafloor spreading history of the Northwestern Pacific. *J. Geophys. Res.,* 94:15437–15462.

Neal, C.R., Mahoney, J.J., Kroenke, L.W., Duncan, R.A., and Petterson, M.G., 1997. The Ontong Java Plateau. *In* Mahoney, J.J., and Coffin, M.J. (Eds.), *Large Igneous Provinces: Continental, Oceanic, and Planetary Flood Volcanism.* Am. Geophys. Union, Geophys. Monogr., 100:183–216.

Plank, T., Ludden, J.N., Escutia, C., et al., 2000. *Proc. ODP, Init. Repts.,* 185 [CD-ROM]. Available from: Ocean Drilling Program, Texas A&M University, College Station TX 77845-9547, USA.

PLATES Project, 1998. Atlas of paleogeographic reconstructions (PLATES Progress Report No. 215). *Univ. Texas Inst. Geophys. Tech. Rep.,* 181.

Purdy, G.M., and Dziewonski, A.M., 1988. *Proc. of a Workshop on Broadband Downhole Seismometers in the Deep Ocean.* Joint Oceanogr. Inst. and U.S. Sci. Advisory Comm.

Riedel, W.R., and Sanfilippo, A., 1970. Radiolaria, Leg 4, Deep Sea Drilling Project. *In* Bader, R.G., Gerard, R.D., et al., *Init. Repts. DSDP,* 4: Washington (U.S. Govt. Printing Office), 503–575.

————, 1978. Stratigraphy and evolution of tropical Cenozoic radiolarians. *Micropaleontology,* 24:61–96.

Sacks, I.S., Suyehiro, K., Acton, G.D., et al., 2000. *Proc. ODP, Init. Repts.,* 186 [CD-ROM]. Available from: Ocean Drilling Program, Texas A&M University, College Station, TX 77845-9547, USA.

Sager, W.W., Handschumacher, D.W., Hilde, T.W.C., and Bracey, D.R., 1988. Tectonic evolution of the northern Pacific Plate and Pacific-Farallon-Izanagi triple junction in the Late Jurassic and Early Cretaceous (M21–M10). *Tectonophysics,* 155:345–364.

Sager, W.W., and Pringle, M.S., 1988. Mid-Cretaceous to Early Tertiary apparent polar wander path of the Pacific Plate. *J. Geophys. Res.,* 93:11753–11771.

Saunders, A.D., 1986. Geochemistry of basalts from the Nauru Basin, Deep Sea Drilling Project Legs 61 and 89: implications for the origin of oceanic flood basalts. *In* Moberly, R., Schlanger, S.O., et al., *Init. Repts. DSDP,* 89: Washington (U.S. Govt. Printing Office), 499–517.

Smith, D.C., Spivack, A.J., Fisk, M.R., Haveman, S.A., Staudigel, H., and ODP Leg 185 Shipboard Scientific Party, 2000. Methods for quantifying potential microbial contamination during deep ocean coring. *ODP Tech. Note,* 28 [Online]. Available from the World Wide Web: <http://www-odp.tamu.edu/publications/tnotes/tn28/INDEX.HTM>. [Cited 2000-07-16]

Smith, W.H.F., and Sandwell, D.T., 1997. Global seafloor topography from satellite altimetry and ship depth soundings. *Science,* 277:1956–1962.

Srivastava, R.K., Emmermann, R., and Puchelt, H., 1980. Petrology and geochemistry of basalts from Deep Sea Drilling Project Leg 54. *In* Rosendahl, B.R., Hekinian, R., et al., *Init. Repts. DSDP,* 54: Washington (U.S. Govt. Printing Office), 671–693.

Staudigel, H., and Hart, S.R., 1983. Alteration of basaltic glass: mechanisms and significance for the oceanic crust-seawater budget. *Geochim. Cosmochim. Acta,* 47:337–350.

Stephen, R.A., Collins, J.A., and Peal, K.R., 1999. Seafloor seismic stations perform well. *Eos,* 80:592.

Thompson, G., Bryan, W.B., and Humphris, S.E., 1989. Axial volcanism on the East Pacific Rise, 10–12°N. *In* Saunders, A.D., and Norry, M.J. (Eds.), *Magmatism in the Ocean Basins.* Geol. Soc. Spec. Publ. London, 42:181–200.

Wessel, P., and Smith, W.H.F., 1995. New version of the Generic Mapping Tools released. *Eos,* 76:329.

Wilkens, R.H., Christensen, N.I., and Collins, J.A., 1993. Seismic properties and reflectivity of North Pacific Ocean cherts. *In* Wilkens, R.H., Firth, J., Bender, J., et al., *Proc. ODP, Sci. Results,* 136: College Station, TX (Ocean Drilling Program), 99–104.

Wilson, M., 1992. Magmatism and continental rifting during the opening of the South Atlantic Ocean: a consequence of Lower Cretaceous super-plume activity? *In* Storey, B.C., Alabaster, T., and Pankhurst, R.J. (Eds.), *Magmatism and the Causes of Continental Break-up*. Geol. Soc. Spec. Publ. London, 68:241–255.

Figure F1. Location map of seismic station coverage in the northwest Pacific. Solid circles indicate land stations; open circles indicate ODP borehole seismometer site locations, current and future. Note that the ocean observatories complement the land stations, making a more regular net. YSS = Yuzhno Sakhalinsk, Russia; NMR = Nemuro, Japan; HCH = Hachijojima, Japan; PHN = Pohang, Korea; OGS = Chichijima, Japan; MCSJ = Minami-torishima, Japan; ISG = Ishigakijima, Japan; TGY = Tagaytay, Philippines; PATS = Ponphei, Micronesia; and PMG = Port Moresby, Papua New Guinea.

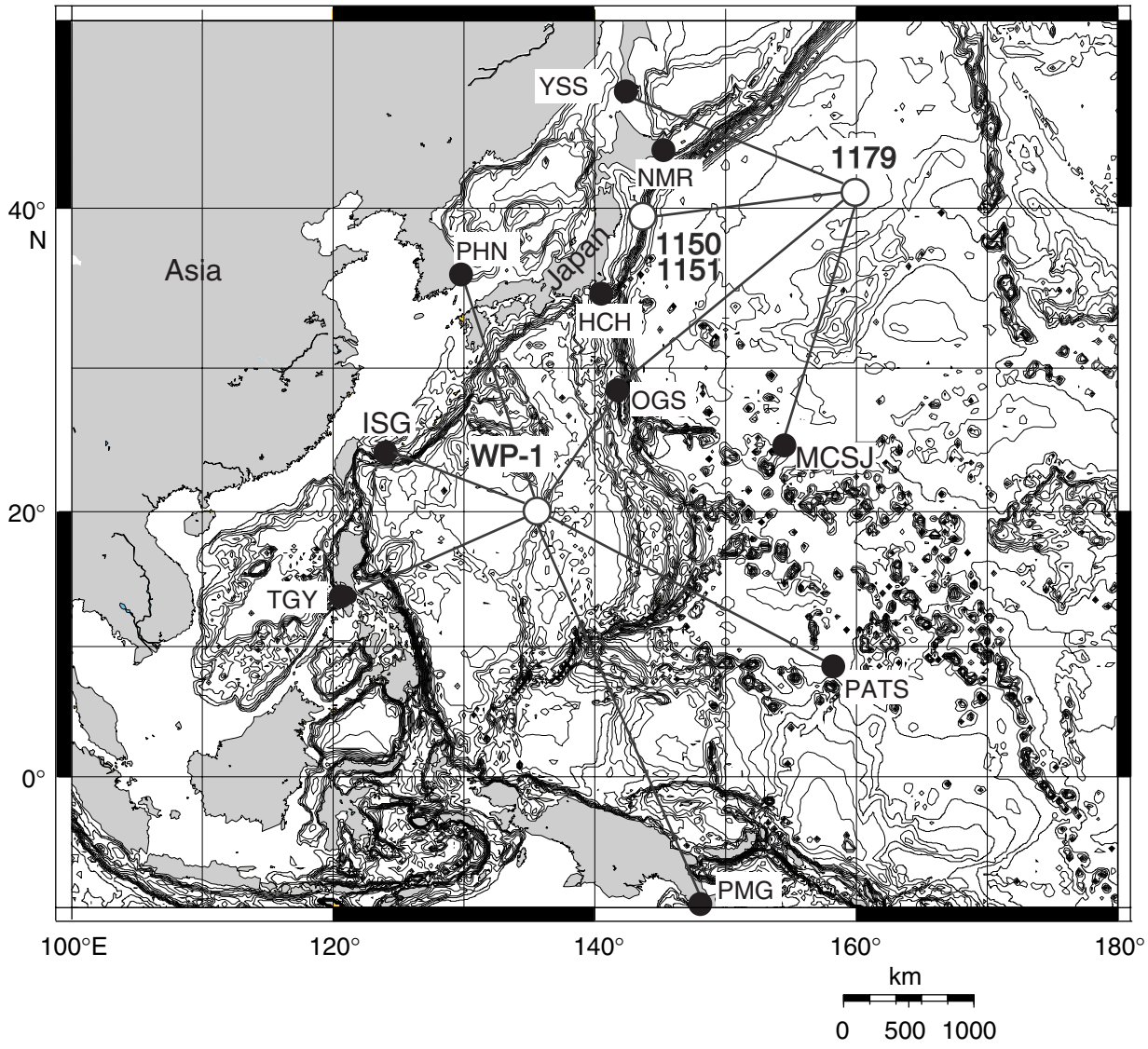

Figure F2. Locations of Leg 191 drill sites in the western Pacific. The chart shows predicted topography (Smith and Sandwell, 1997) and magnetic lineations (compiled from Nakanishi et al. [1989] and the PLATES Project [1998]). White dashed lines = fracture zones, black dashed lines = plate boundaries. The figure was generated using Generic Mapping Tools software (Wessel and Smith, 1995).

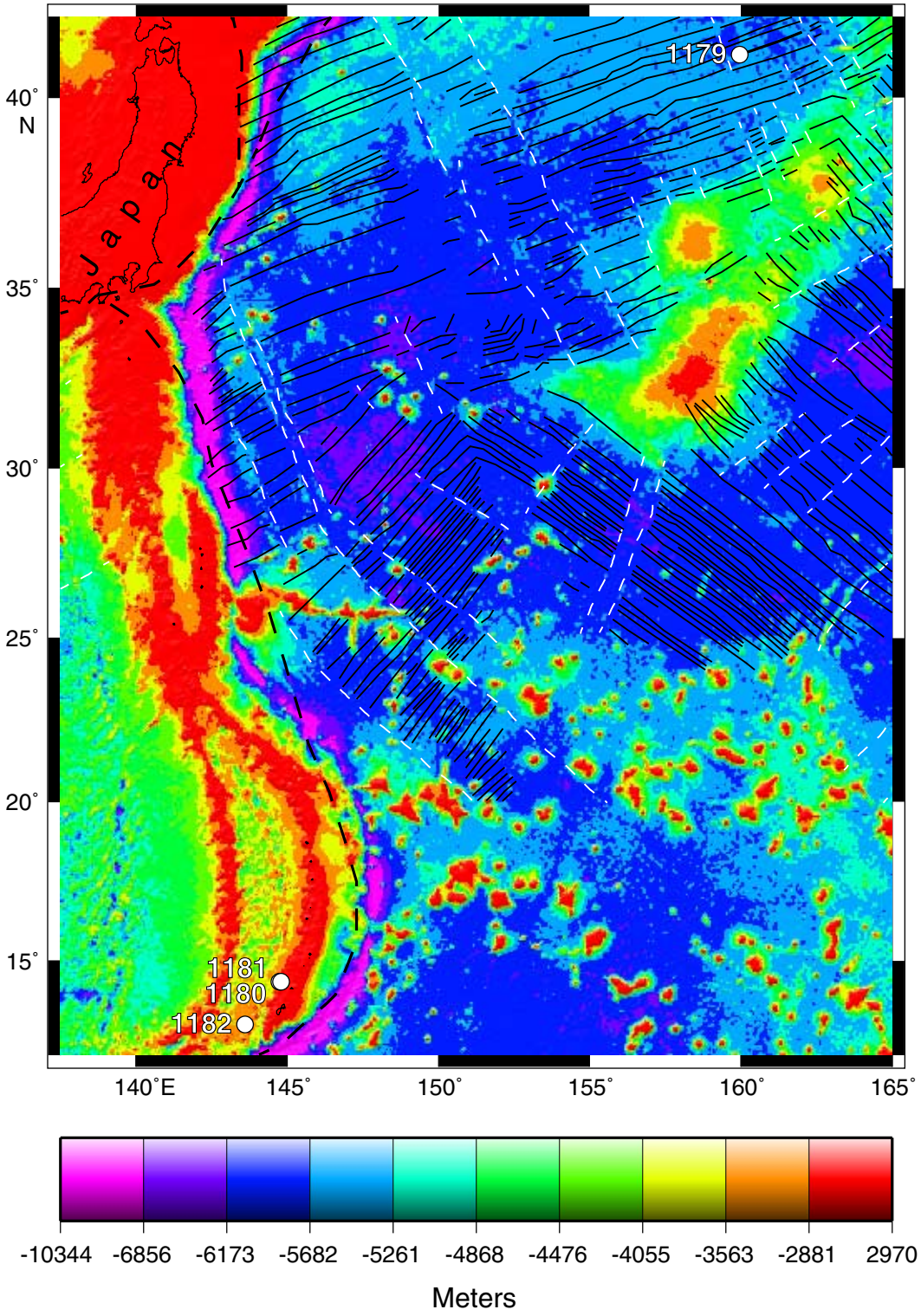

Figure F3. Magnetic anomalies in the vicinity of Site 1179. Thin curved lines show magnetic anomalies, which are shaded where positive. Anomaly identifications are after Nakanishi et al. (1999). Cross = the location of Site 1179.

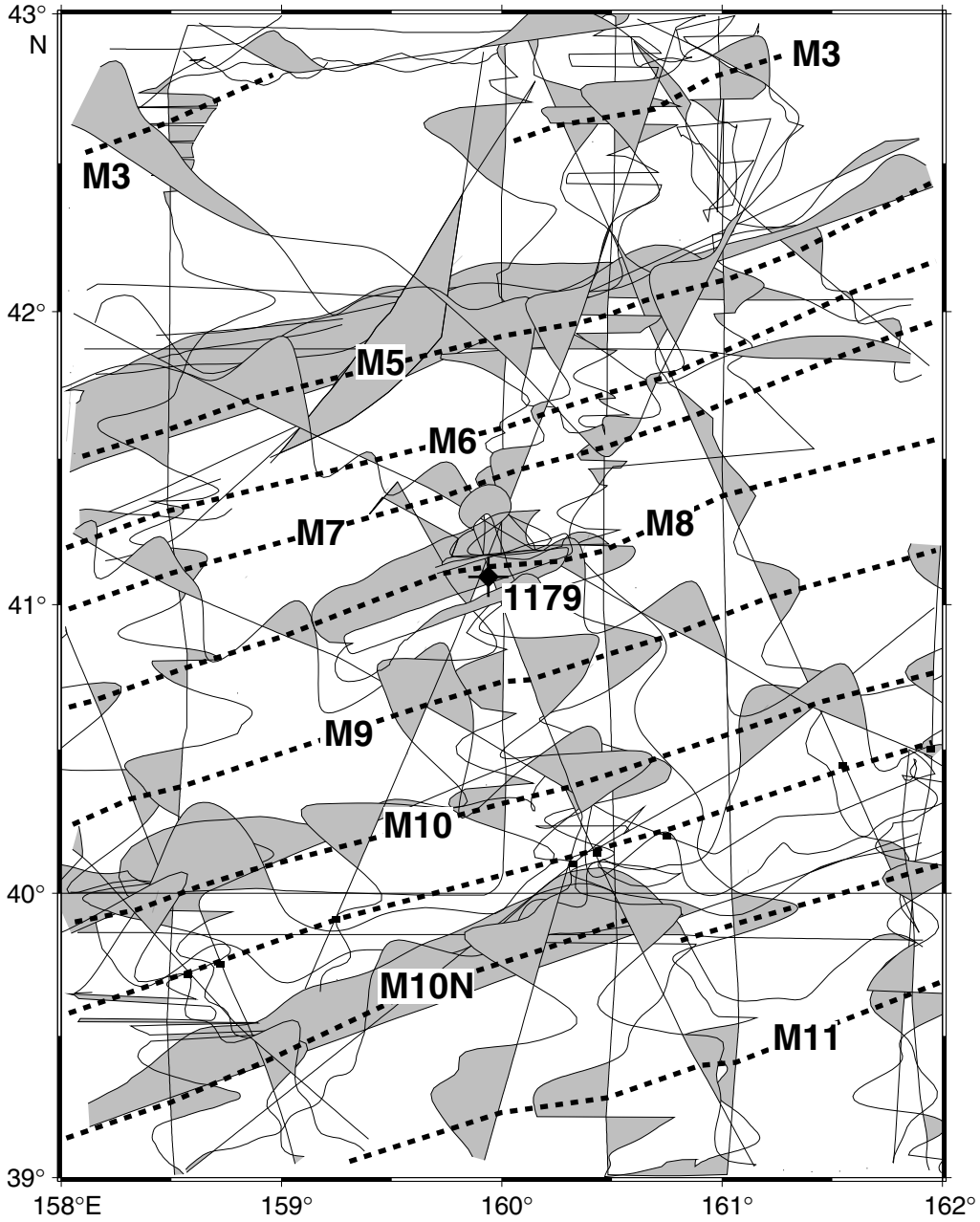

Figure F4. Comparison of stratigraphic sections from DSDP and ODP holes drilled in the northwest Pacific. The numbers at the top give site designations. Depth is plotted on the vertical axis. Biostratigraphic ages are along the left side of each column. The distance from Site 1179 is shown at the bottom.

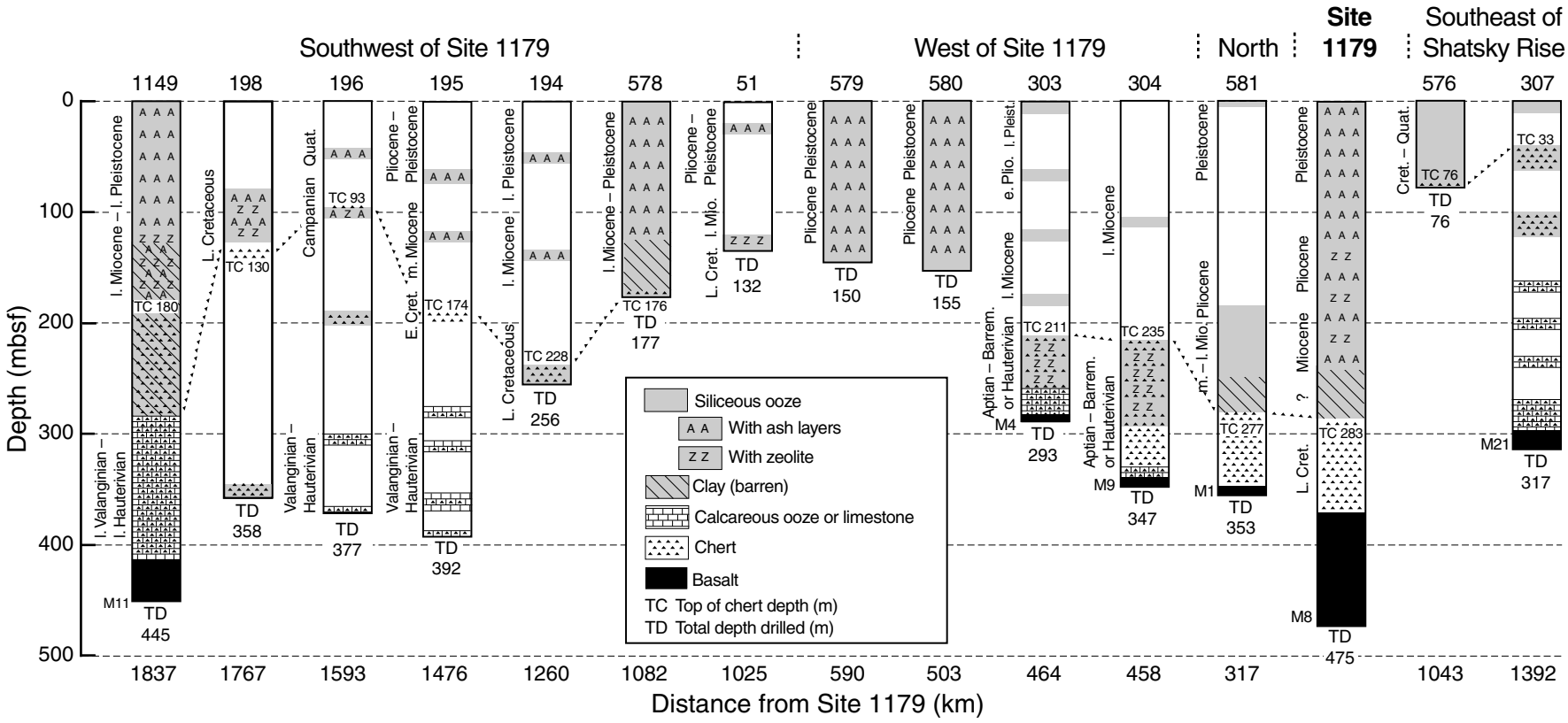

Figure F5. Diagram showing the relative positions of holes drilled at Site 1179.

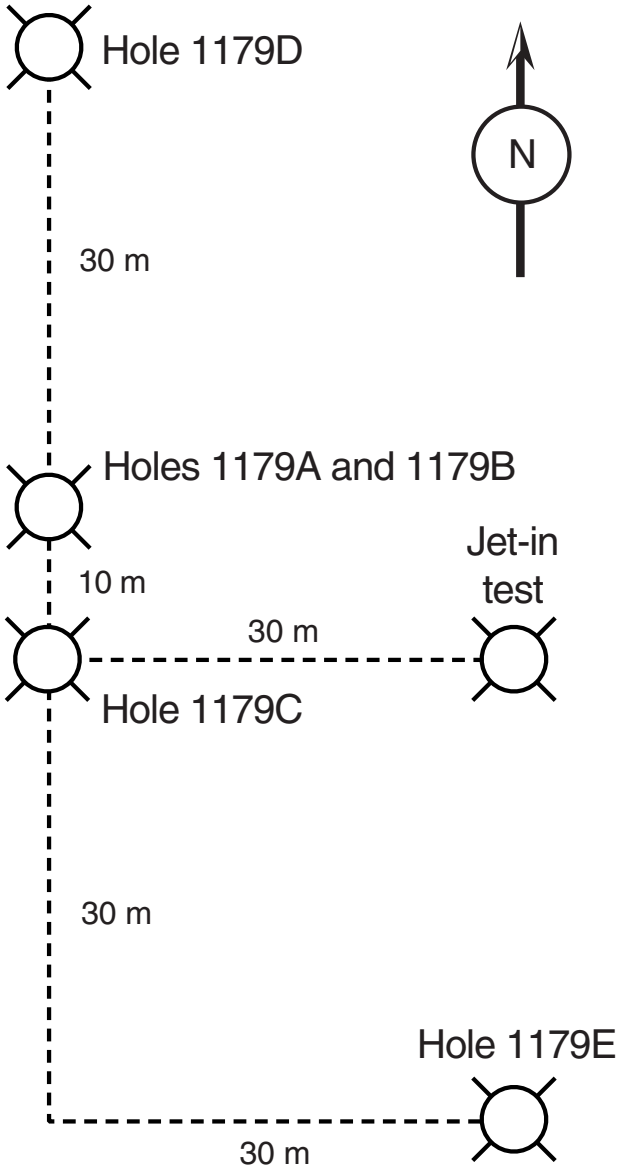

Figure F6. Site survey cruise tracks. Heavy lines show ship tracks of *Hakuho Maru* cruise KH96-3-1 used for the site survey of Site 1179. Cross = location of Site 1179, star = location of alternate proposed Site WP-2B. A–A′, B–B′, C–C′ denote portions of seismic lines shown in Figures F7, p. 57, F8, p. 58, and F9, p. 59, respectively. Thin lines = bathymetry contours, labeled in 100 meters below sea level intervals.

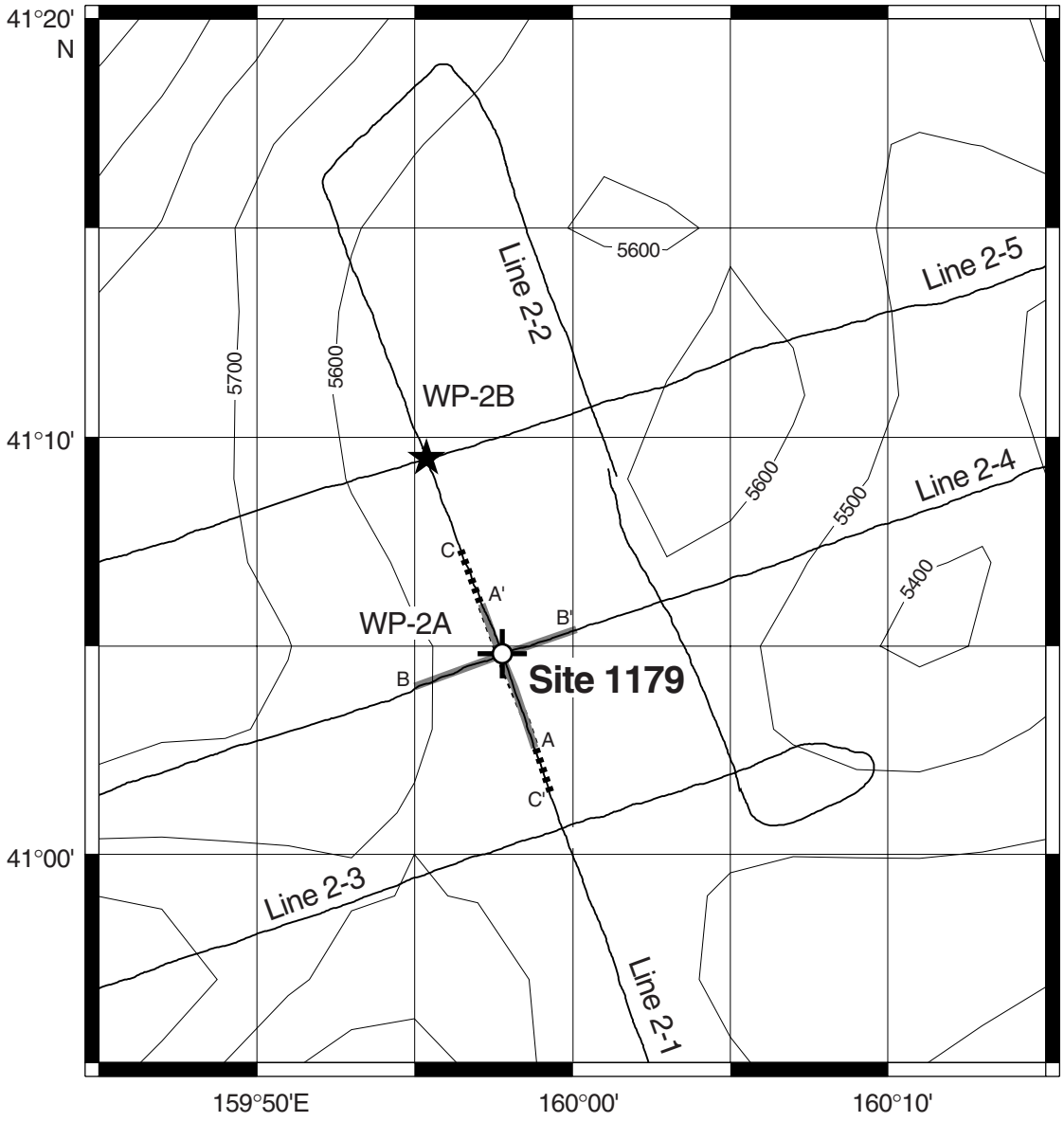

Figure F7. Multichannel seismic line over Site 1179. The location is shown by A–A′ in Figure F6, p. 56.

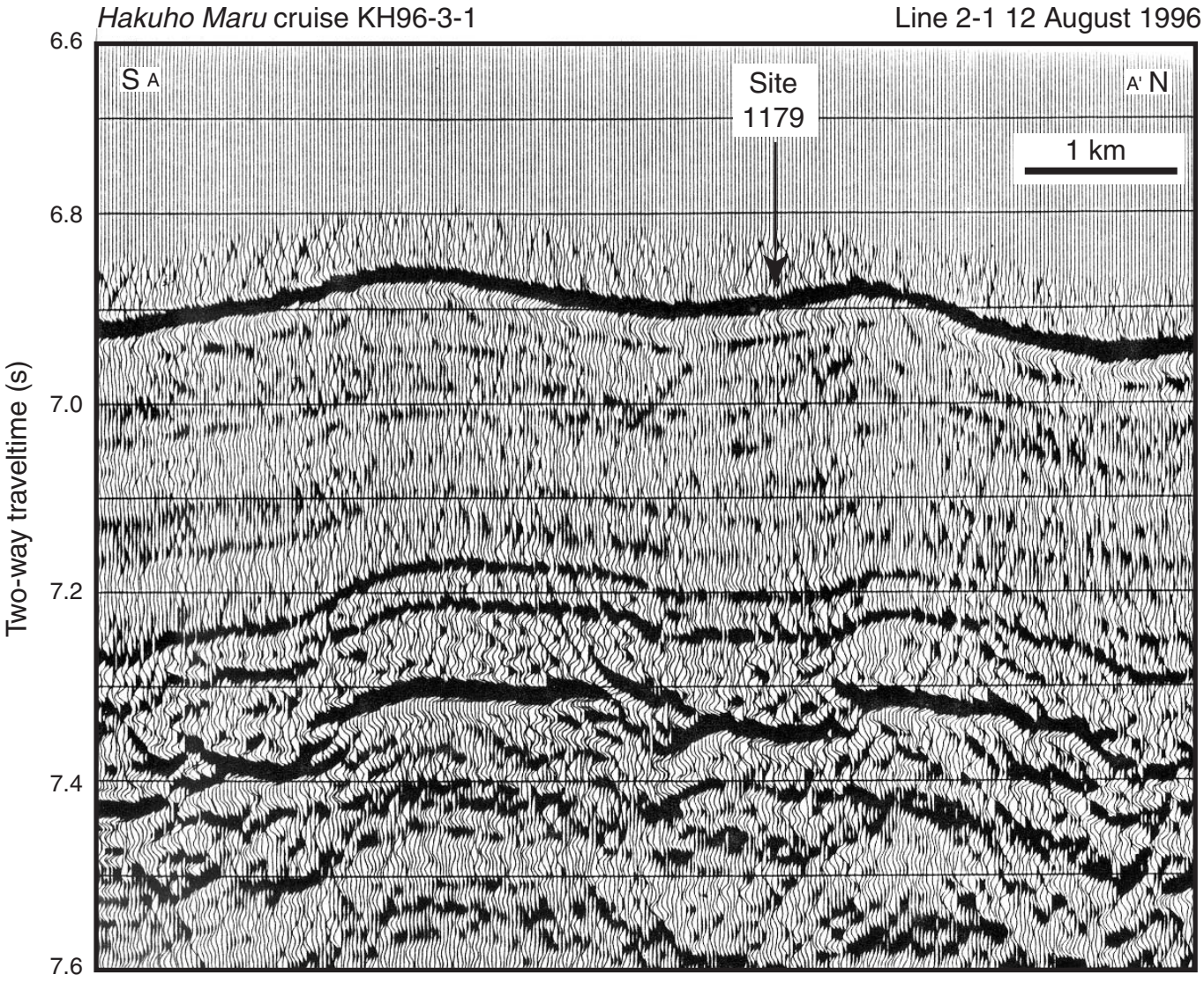

Figure F8. Multichannel seismic line over Site 1179. The location is shown by B–B′ in Figure F6, p. 56.

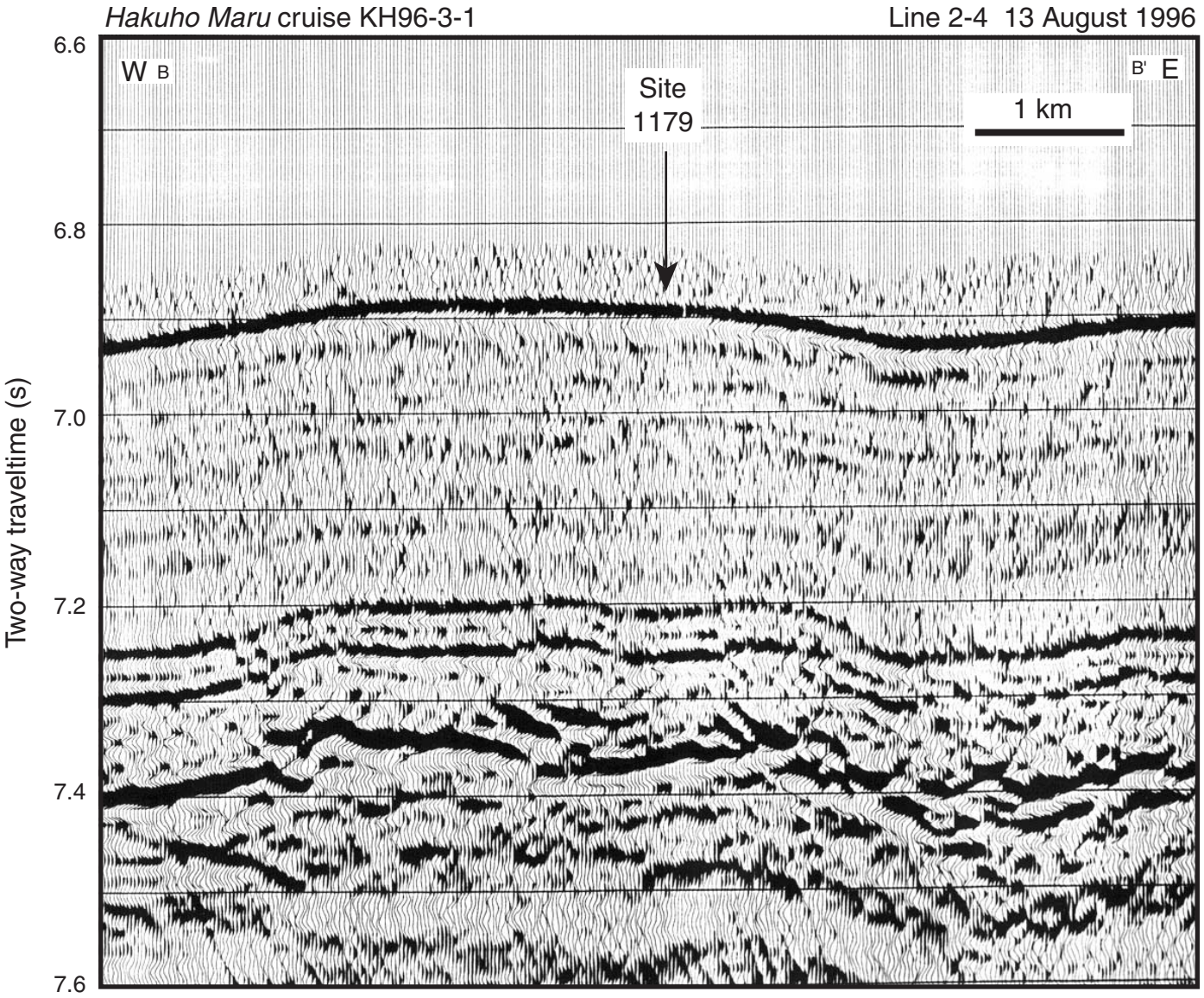

Figure F9. Echo-sounder profile (3.5 kHz) over Site 1179. The location is shown by C–C′ in Figure F6, p. 56.

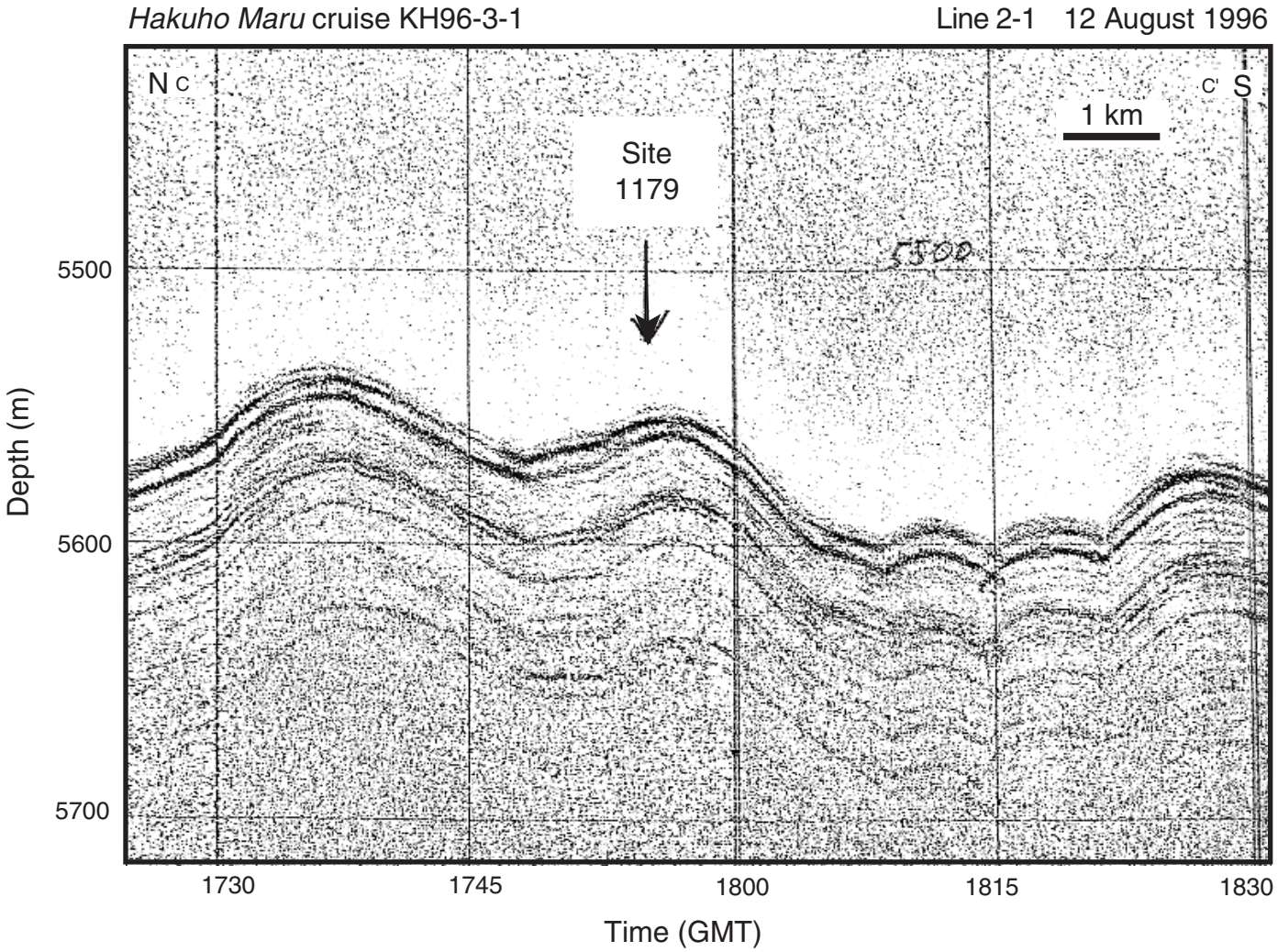

Figure F10. Correlation between multichannel seismic line A–A′ (Fig. F7, p. 57), the Site 1179 lithostratigraphic column, and predicted depths of unit boundaries. The lithostratigraphic column was scaled to the seismic section using the velocity-depth relationship of Carlson et al. (1986) to calculate the two-way traveltime of unit boundaries and ash layers derived from core observations. In the lithostratigraphic column solid lines = unit boundaries, dashed lines = ash layers. Lithologic boundary depths are given next to the column.

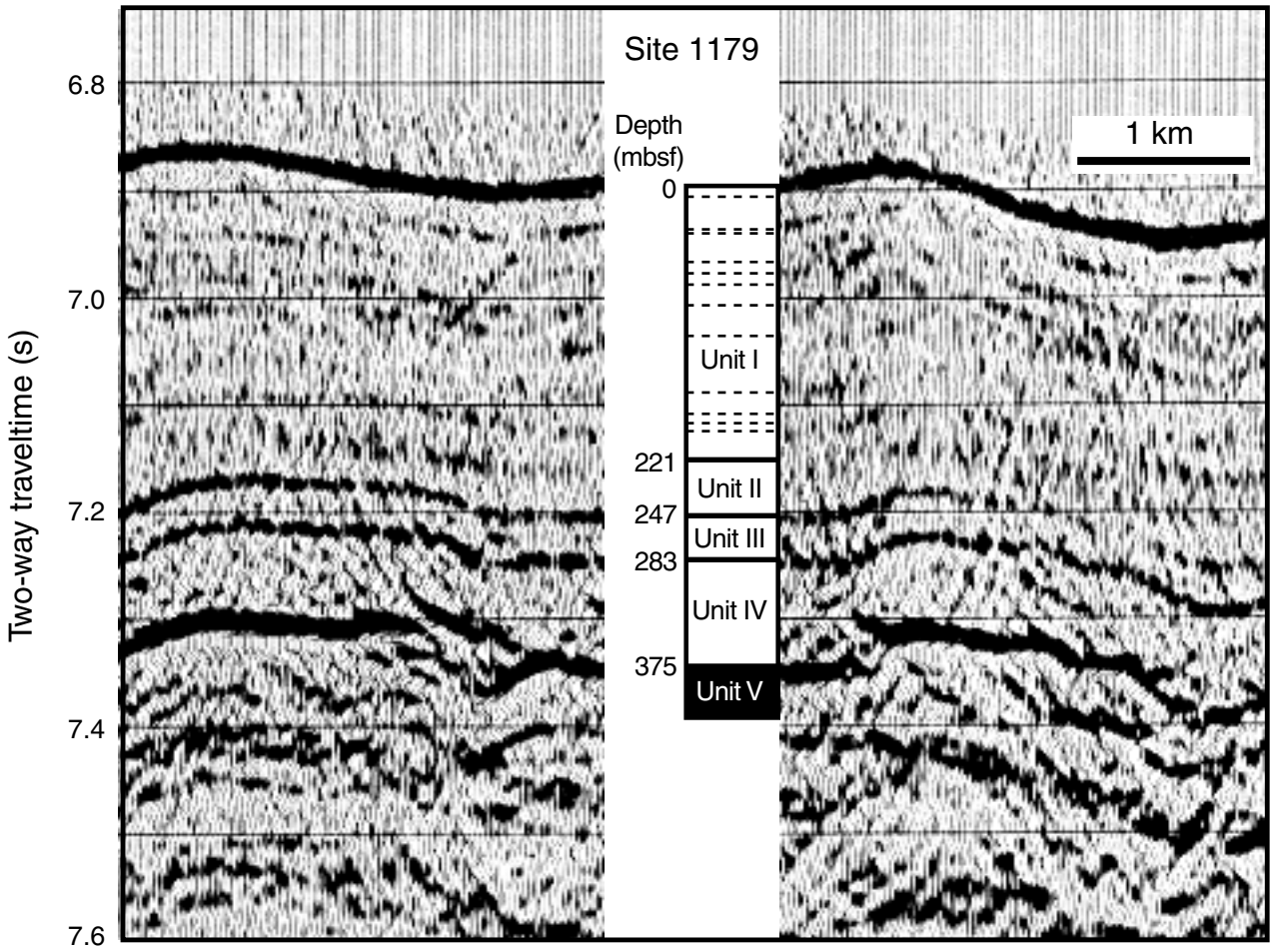

Figure F11. Site 1179 lithostratigraphic column, which is divided into four lithostratigraphic units on the basis of color and composition of the recovered cores. TD = total depth.

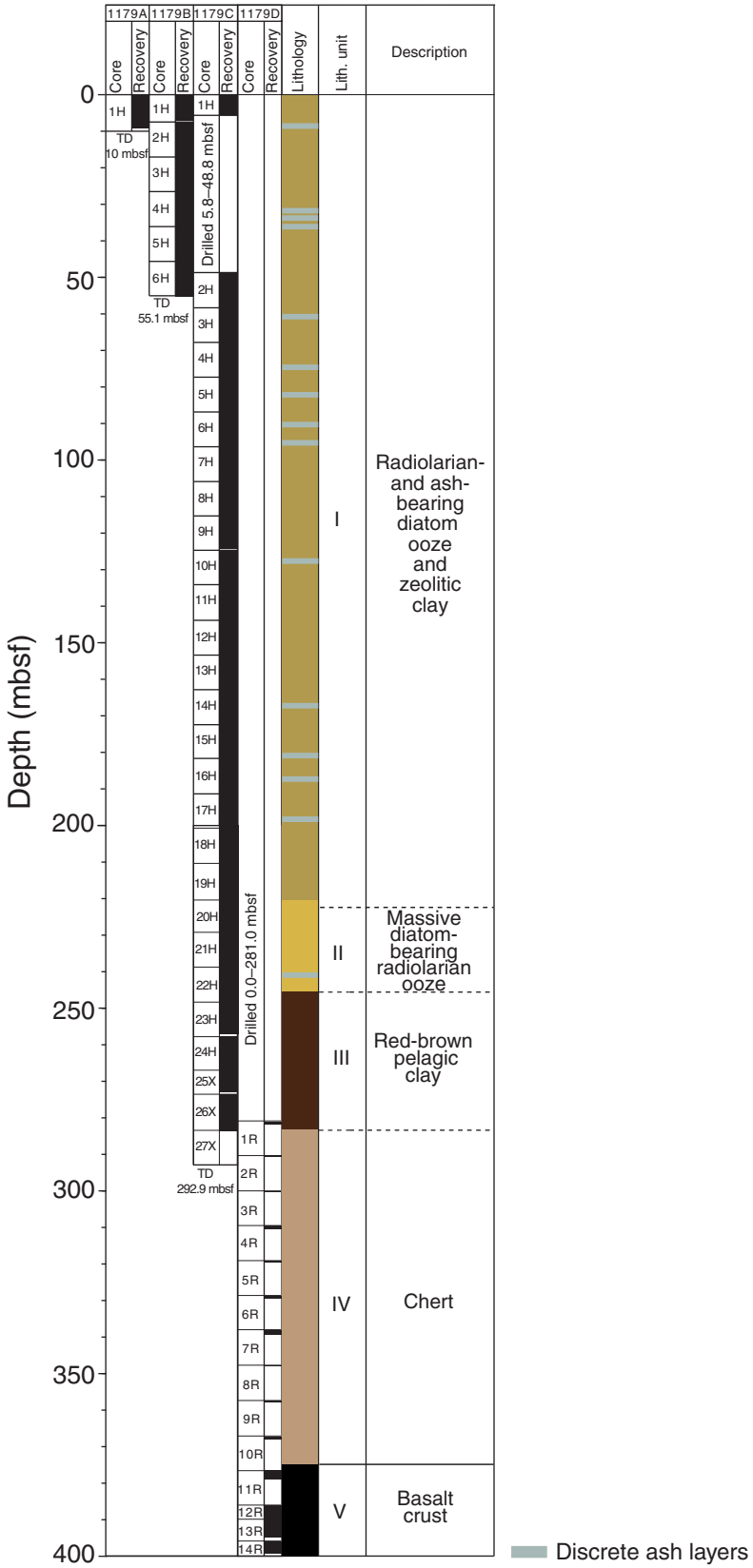

Figure F12. Photomicrographs in plane-polarized light reveal characteristic lithologic components of Units I, II, and III. **A.** Sample 191-1179B-4H-1, 100 cm, clearly shows rounded to subrounded tests of diatoms in the diatom ooze of Unit I. **B.** Sample 191-1179B-5H-3, 106 cm, documents diatom-rich clay, which is the predominant lithology in Unit I. **C.** Sample 191-1179C-20H-4, 40 cm, shows tests and spines of radiolarian ooze in Unit II. **D.** Sample 191-1179C-24H-4, 98 cm, documents ferruginous zeolitic clay in Unit III.

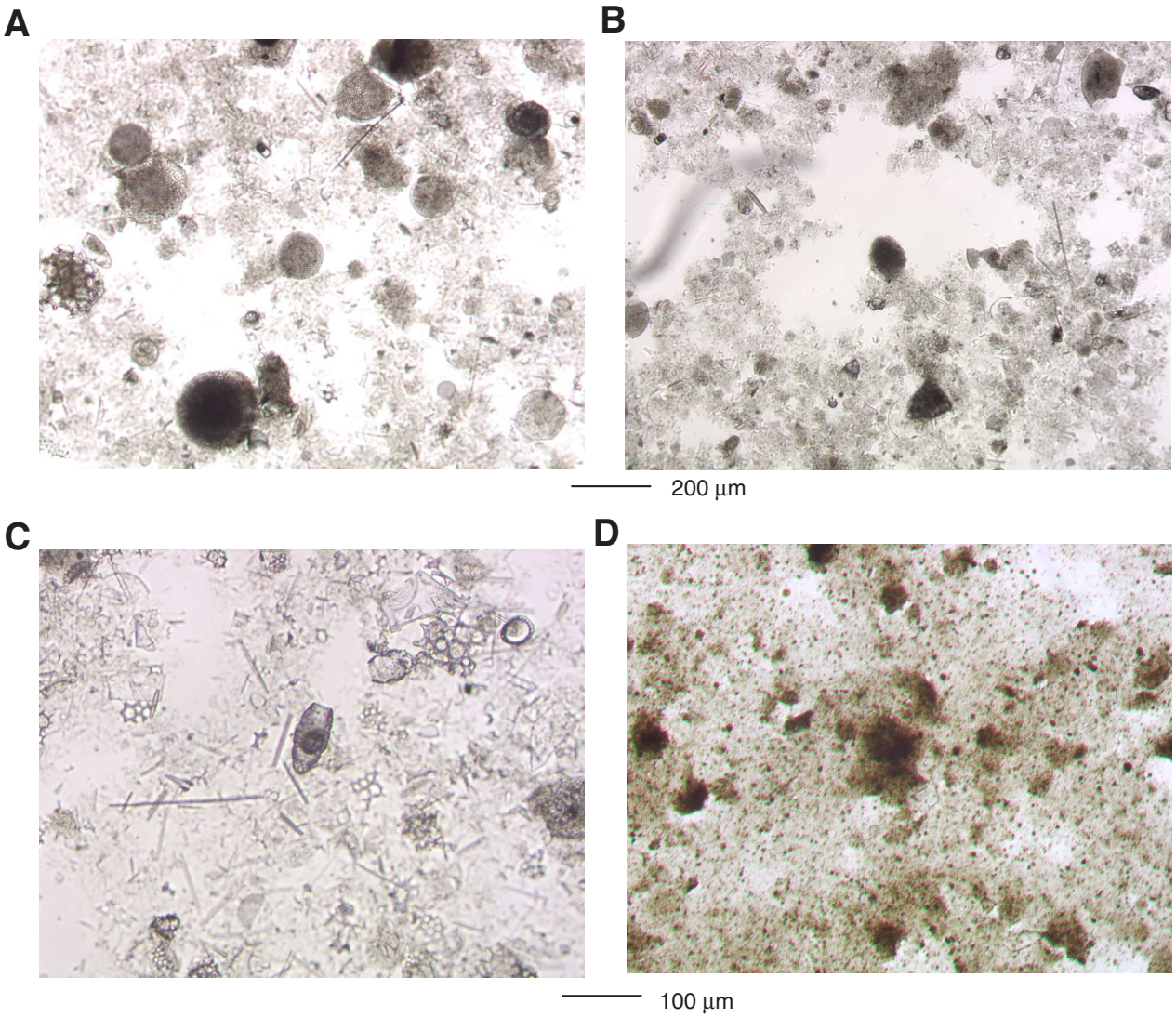

Figure F13. Close-up photograph showing the characteristic appearance of the clay- and radiolarian-bearing diatom ooze of Unit I (interval 191-1179C-3H-3, 20–40 cm).

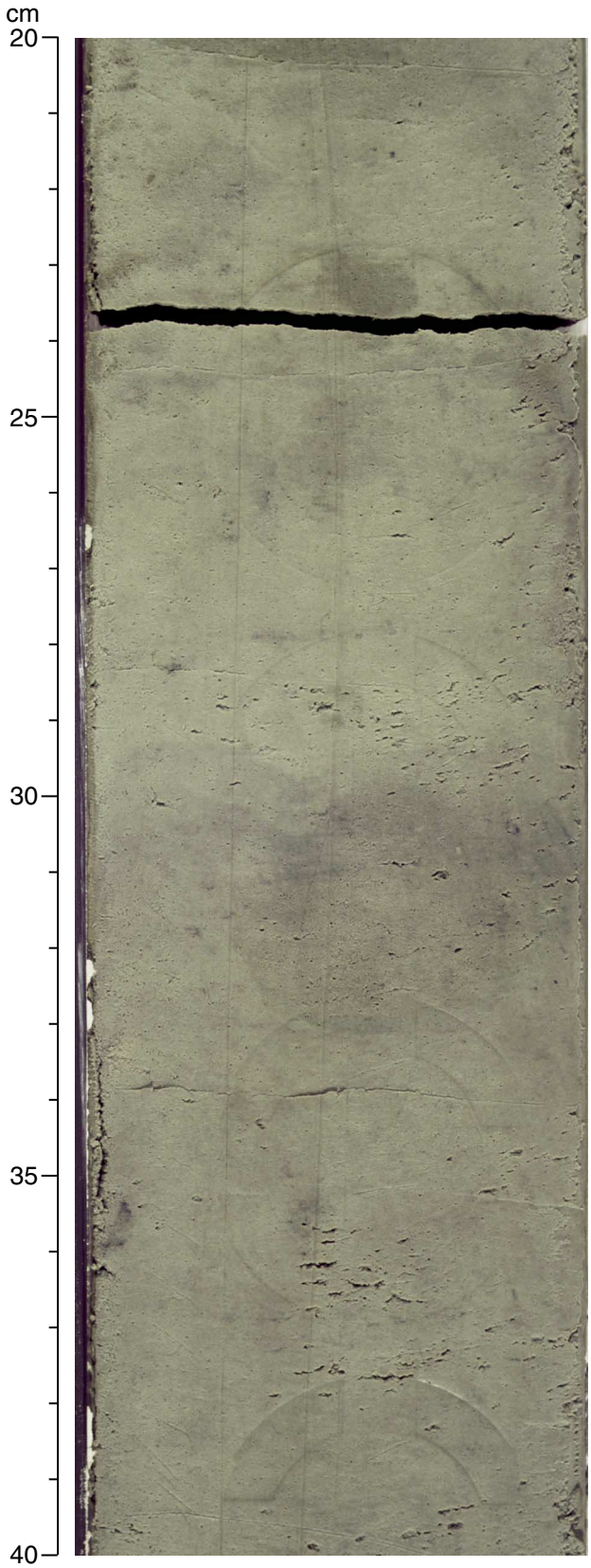

Figure F14. Close-up photograph showing the thin to thick beddinglike features of Unit I. These are defined on the basis of color contrasts rather than textural contrasts (interval 191-1179B-6H-5, 51–90 cm).

Figure F15. Close-up photograph showing planar laminae of Unit I (interval 191-1179C-4H-3, 121–141 cm).

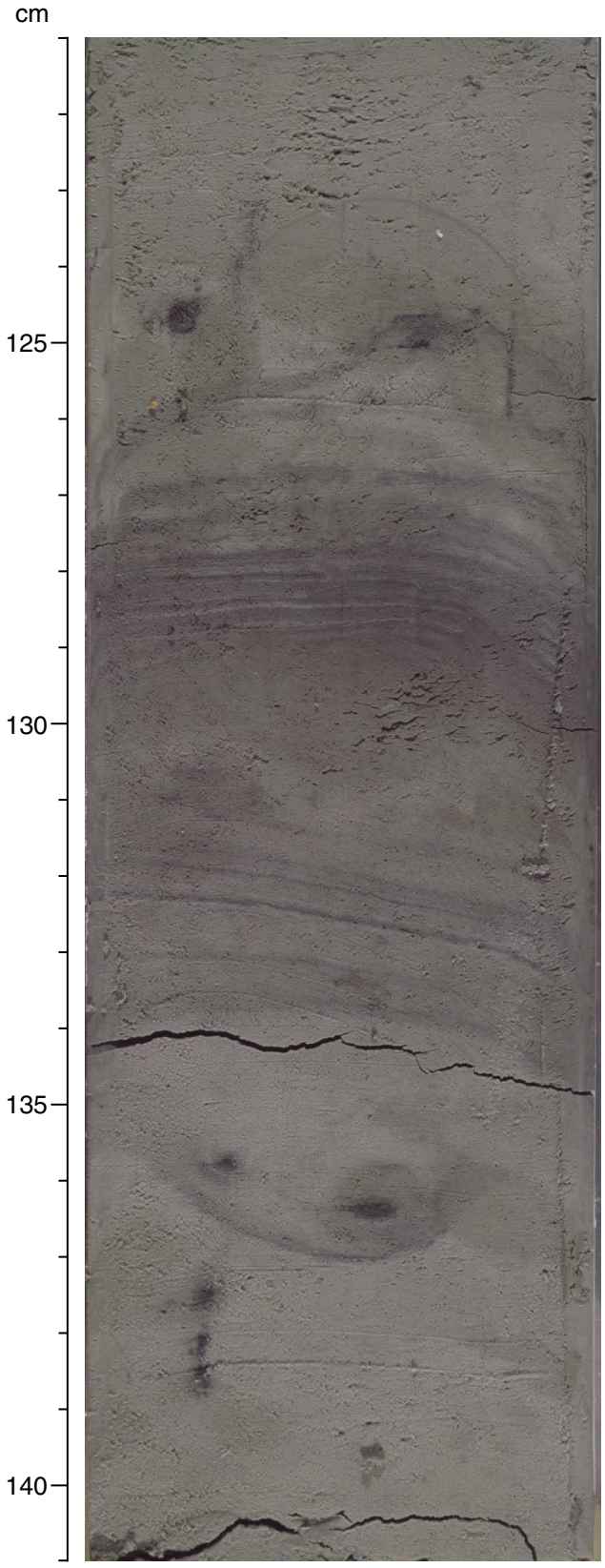

Figure F16. Close-up photograph showing the vertical distribution pattern of bioturbation of Unit I that resembles tiering (interval 191-1179C-9H-4, 25–56 cm).

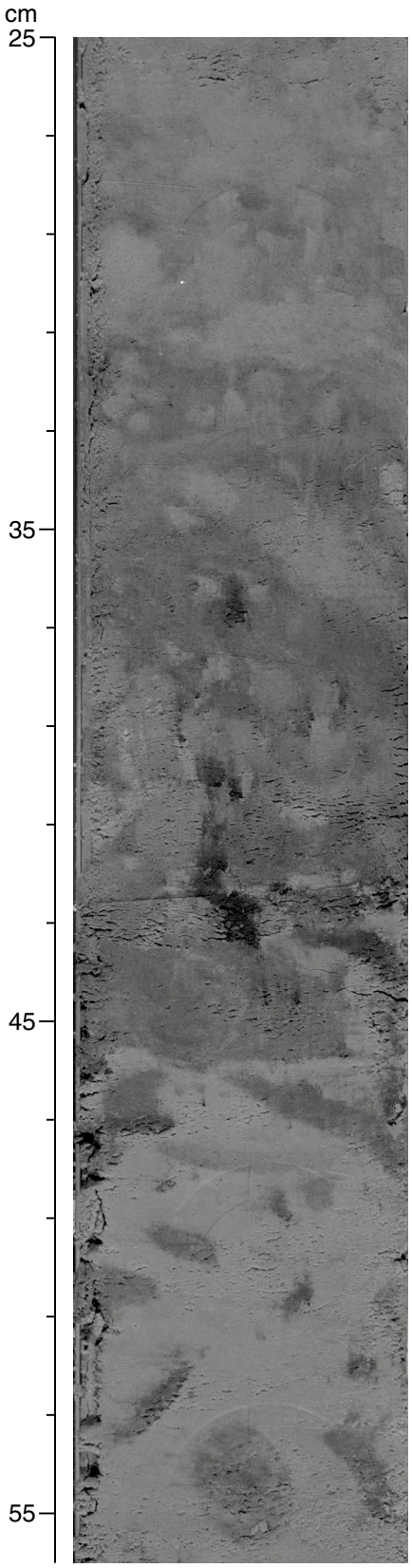

Figure F17. Close-up photograph showing the indurated *Ophiomorphia*-like burrow fill of Unit I (from interval 191-1179C-19H-5, 77–81 cm). The piece is ~7 cm long and was inadvertently disturbed from its diagonal position when the core was split.

Figure F18. Photomicrographs documenting the composition of accessory lithologies in Unit I. Green zeolitic clay layers are shown in (**A**) plane-polarized light (PPL) and (**B**) cross-polarized light (XPL) (interval 191-1179B-2H-5, 38.5 cm). Vitric ash layers are shown in (**C**) PPL and (**D**) XPL (interval 191-1179B-2H-2, 60 cm).

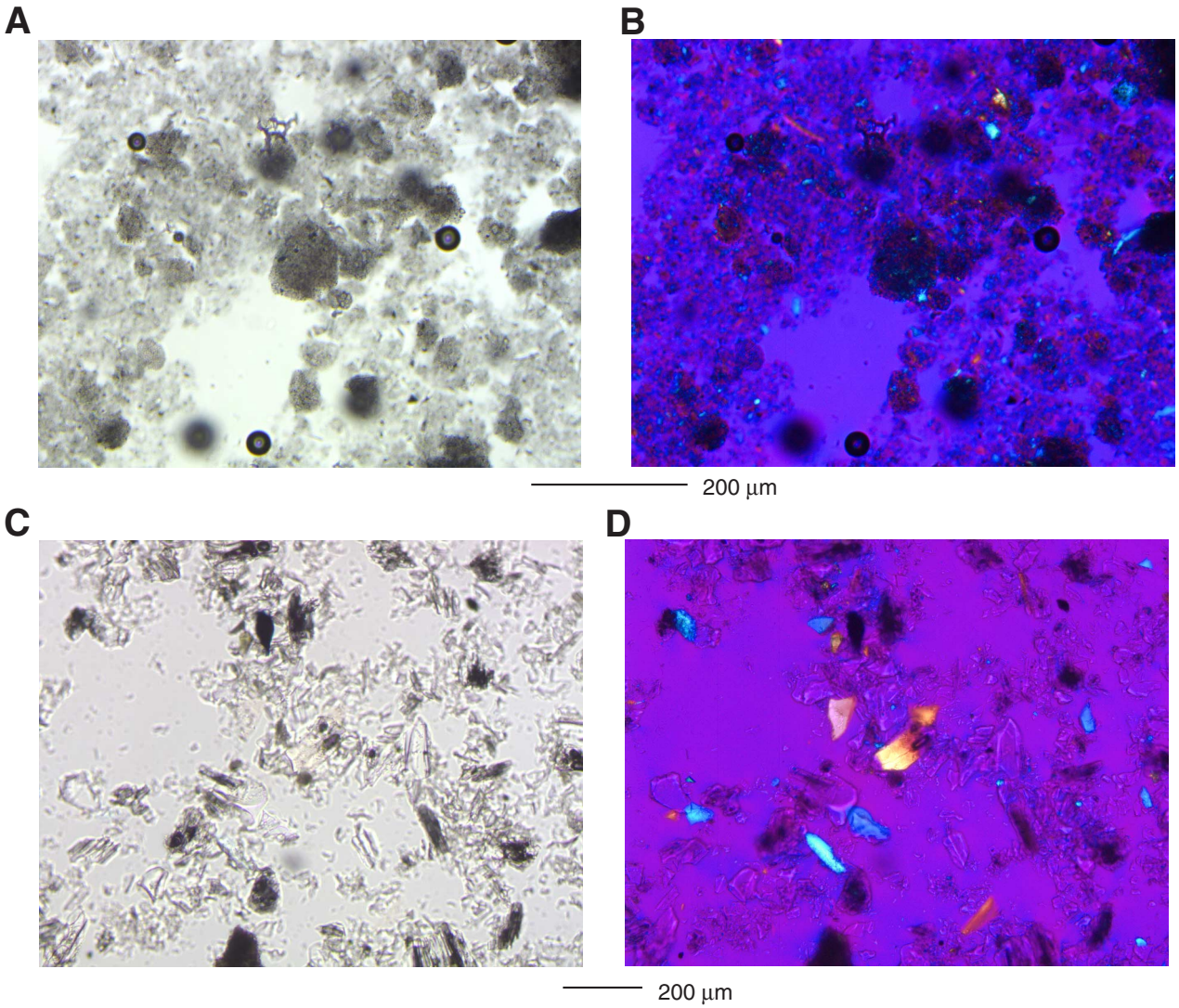

Figure F19. Close-up photograph showing an ash layer as an accessory lithology of Unit I (interval 191-1179C-17H-6, 109–122 cm).

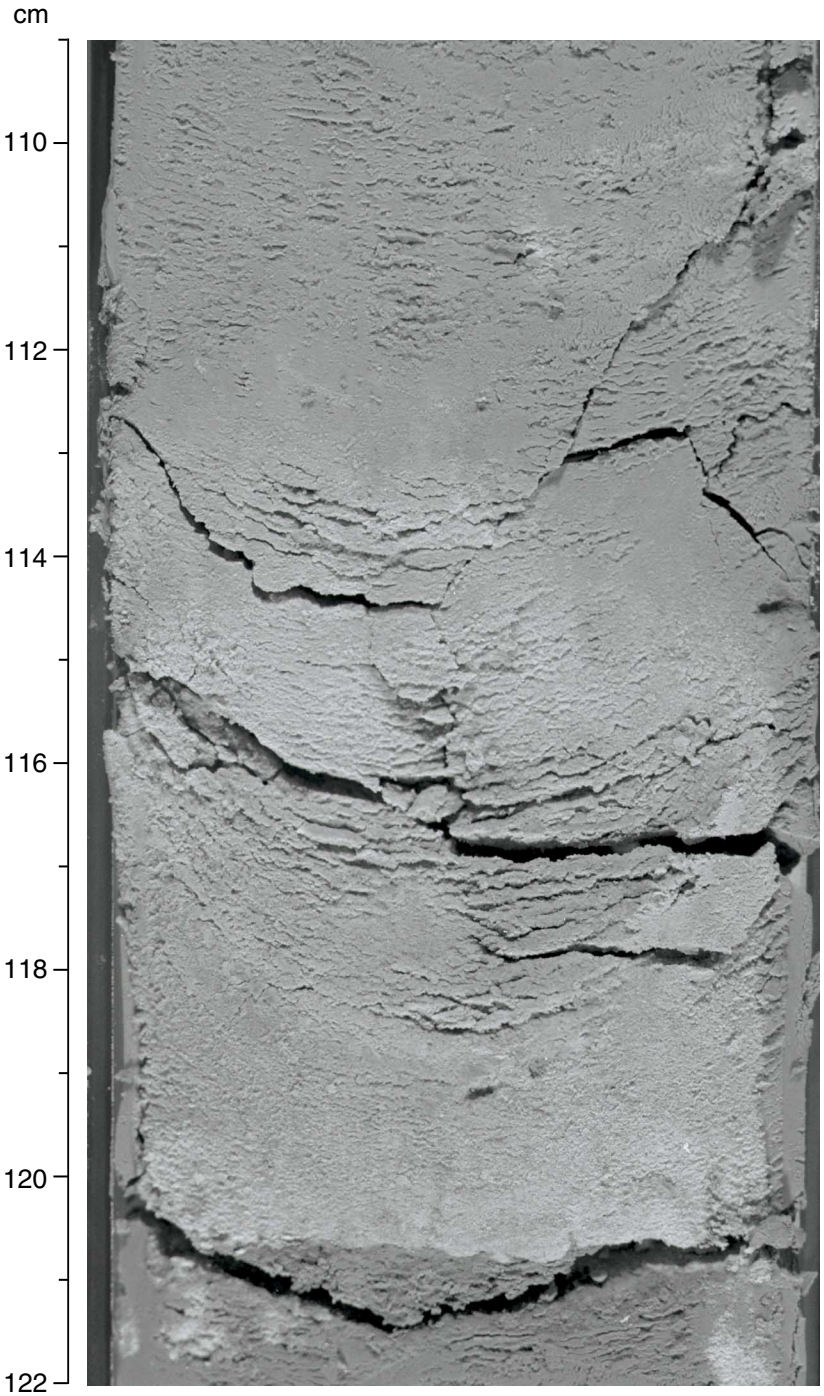

Figure F20. Close-up photograph showing the characteristic appearance of the radiolarian ooze of Unit II (interval 191-1179C-20H-6, 30–50 cm).

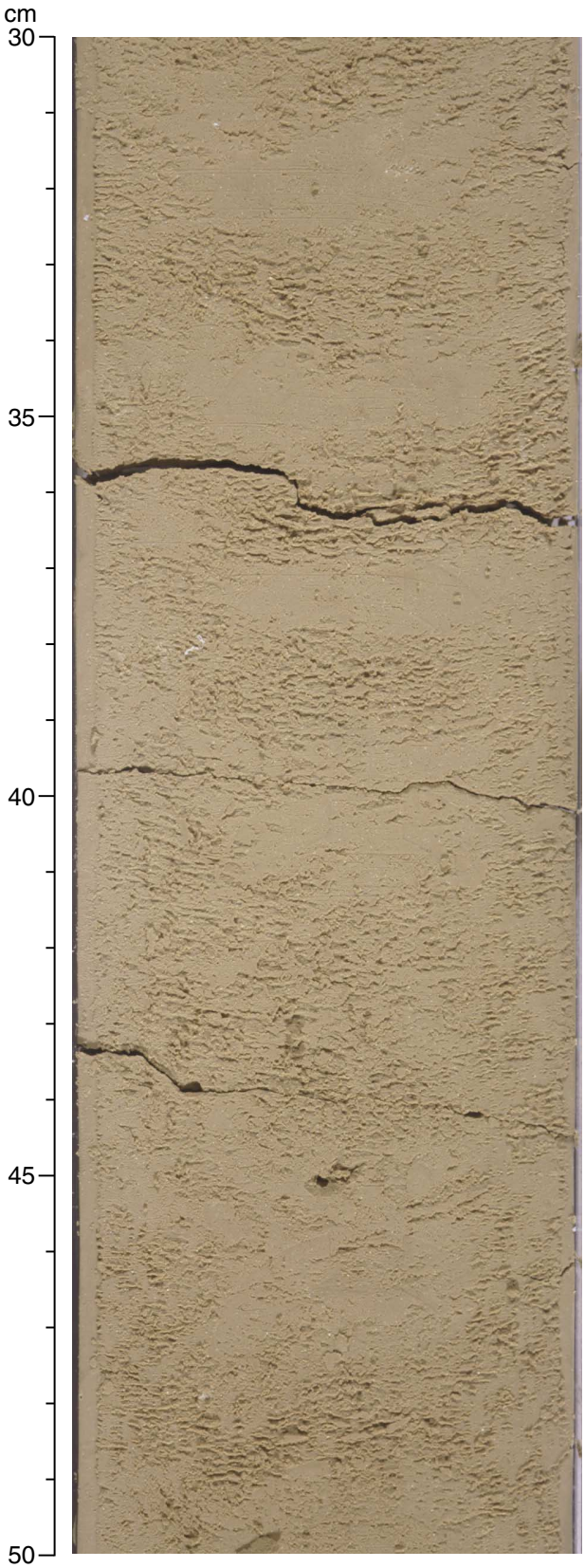

Figure F21. Close-up photograph showing isolated bioturbation marks of Unit II (interval 191-1179C-22H-2, 118–144 cm).

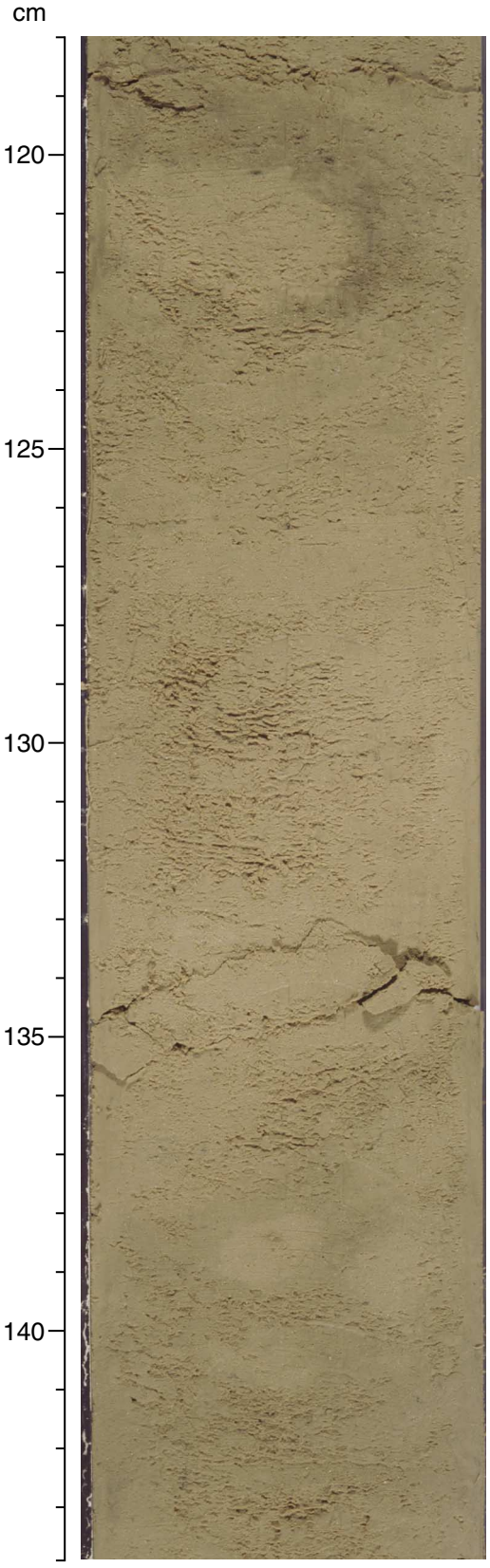

Figure F22. Close-up photograph showing the characteristic appearance of the pelagic clay of Unit III (interval 191-1179C-24H-5, 72–91 cm). Isolated bioturbation marks in the form of contrastingly colored mottles are distinct.

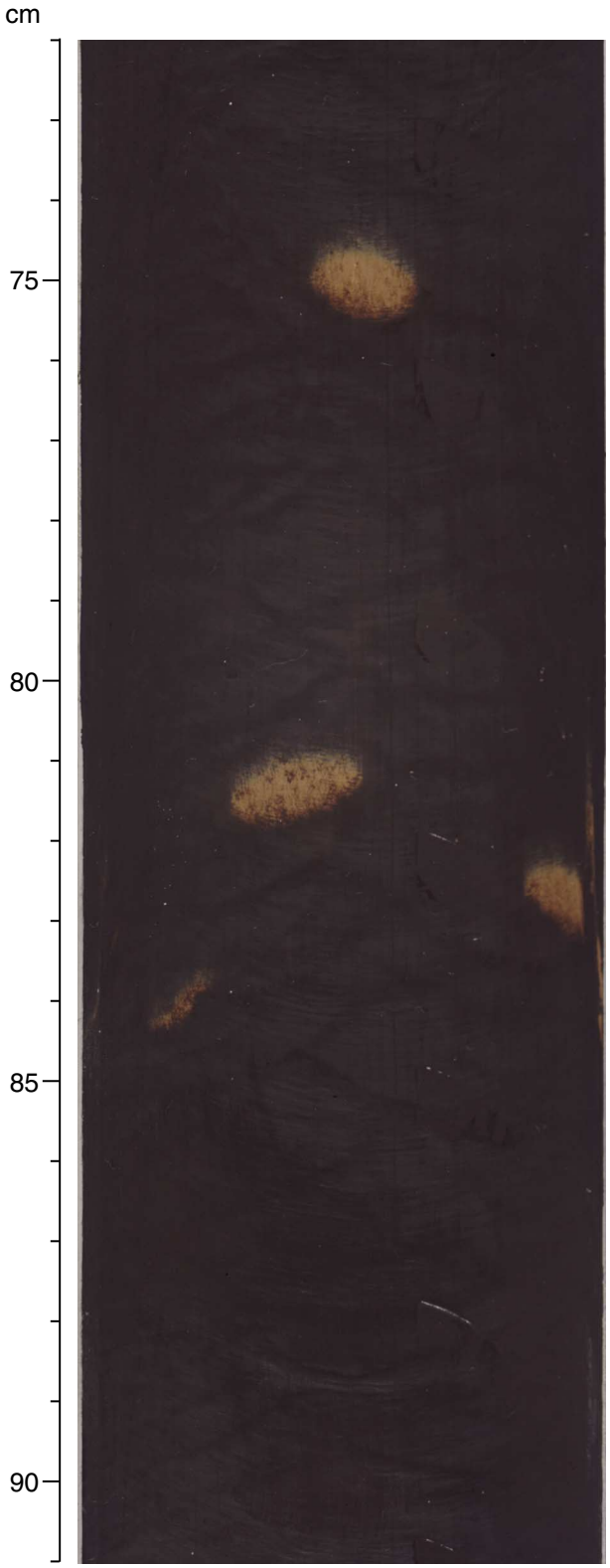

Figure F23. Close-up photograph showing the remarkable coloration of the pieces of chert in Unit IV (interval 191-1179D-6R-1, 80–110 cm). Bioturbation marks are present in some pieces of the chert.

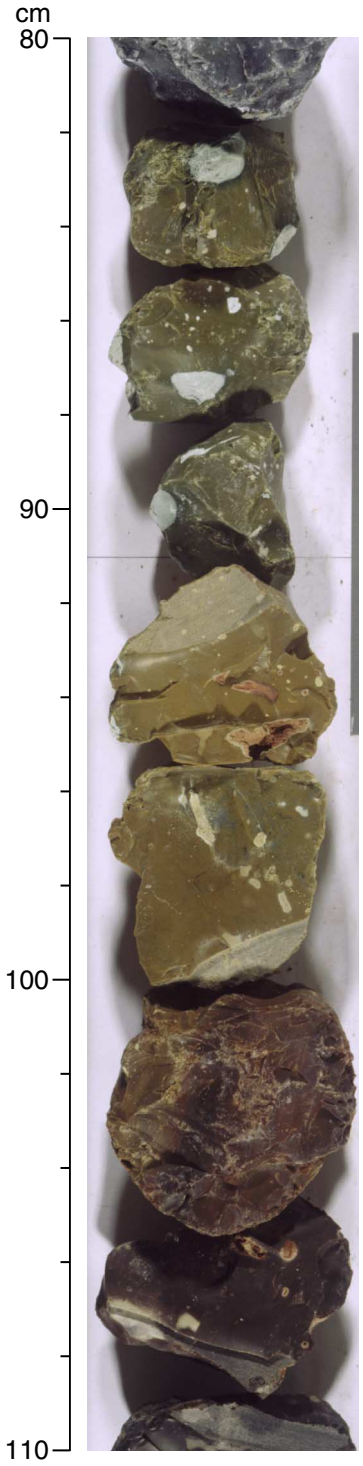

Figure F24. Ages of sediment based on nannofossil, foraminifer, dinoflagellate cyst, and radiolarian zonations. TD = total depth.

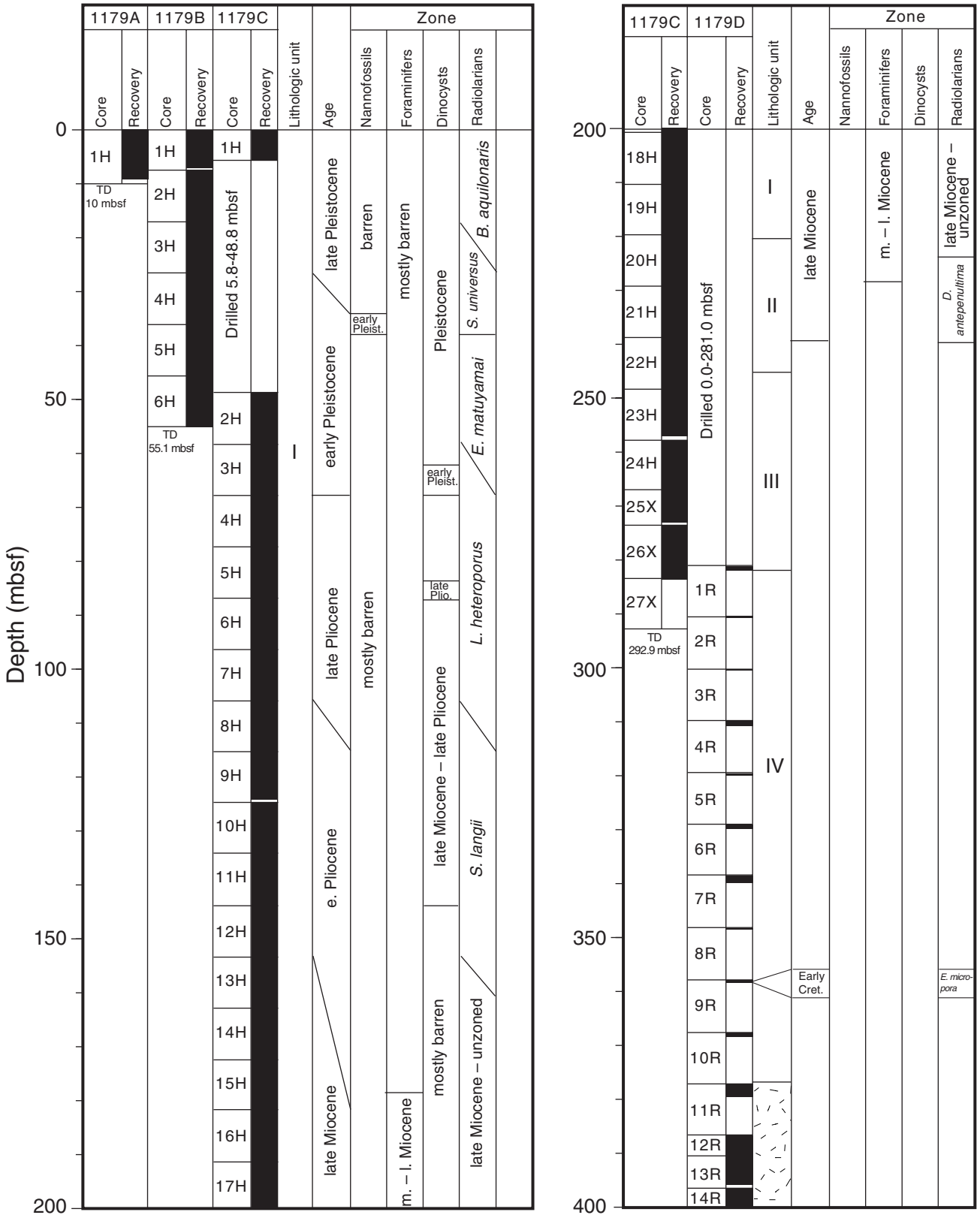

Figure F25. Diagram showing the distribution of dinoflagellate cysts.

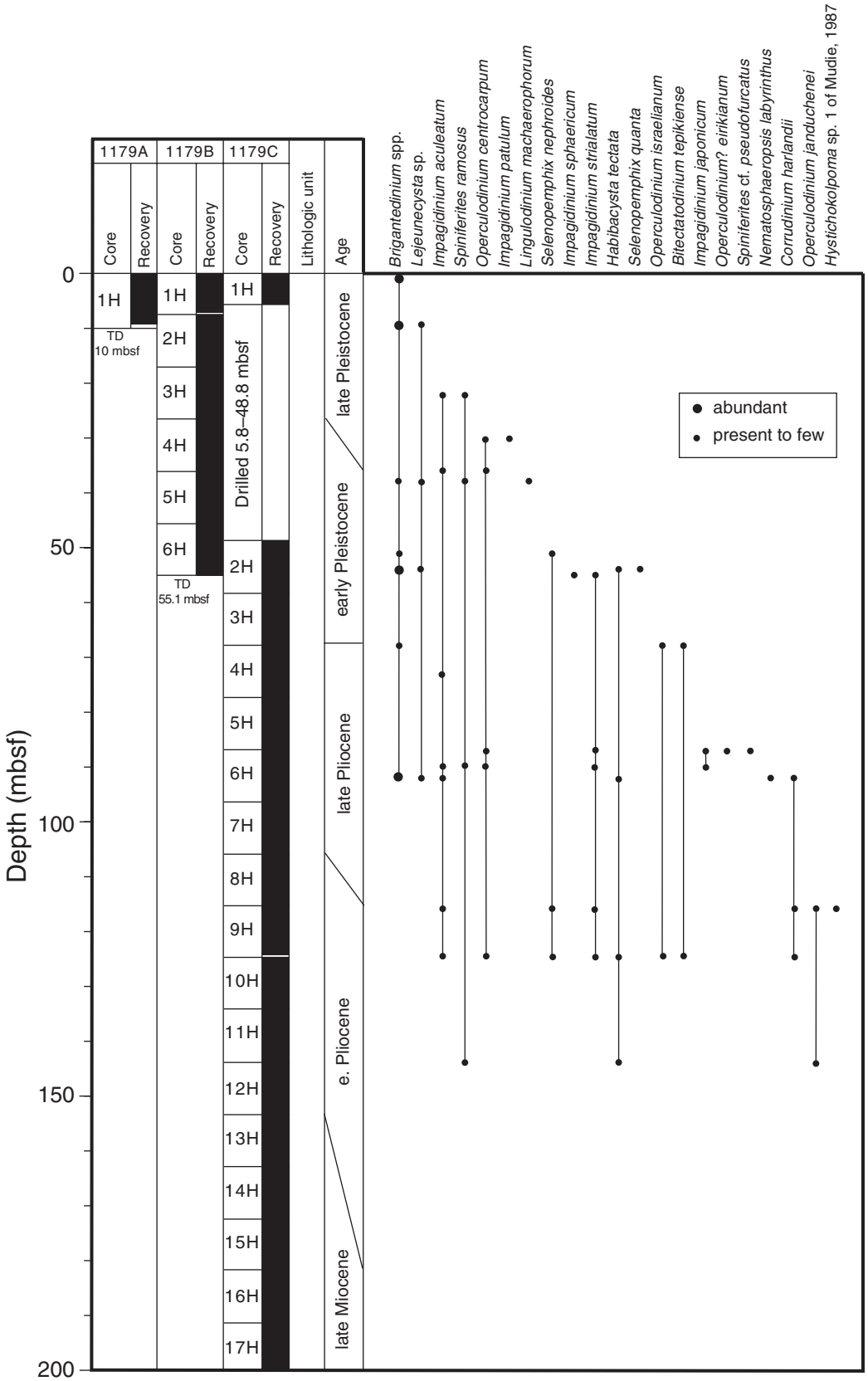

Figure F26. Concentration profile of dissolved NH_4^+ in pore waters.

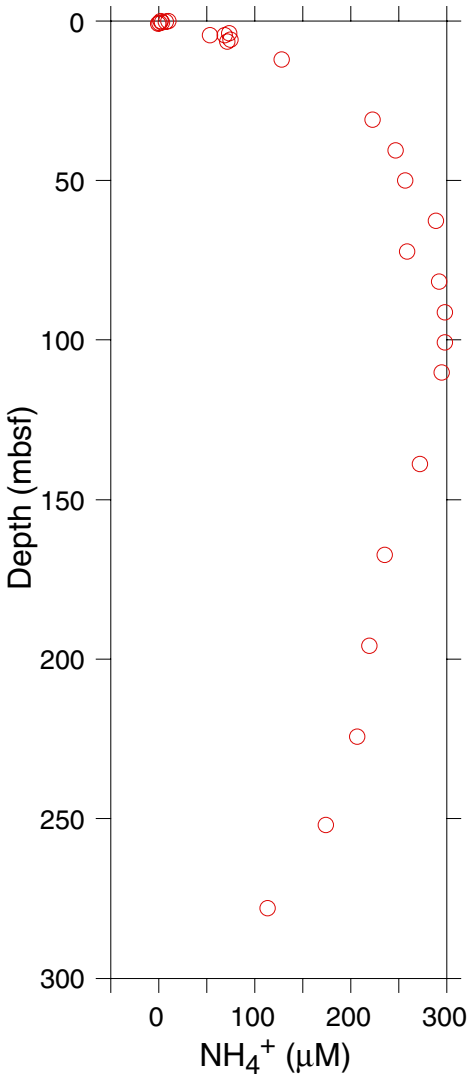

Figure F27. Concentration profiles of dissolved Mn(II) (open squares) and Fe(II) (open circles) in pore waters.

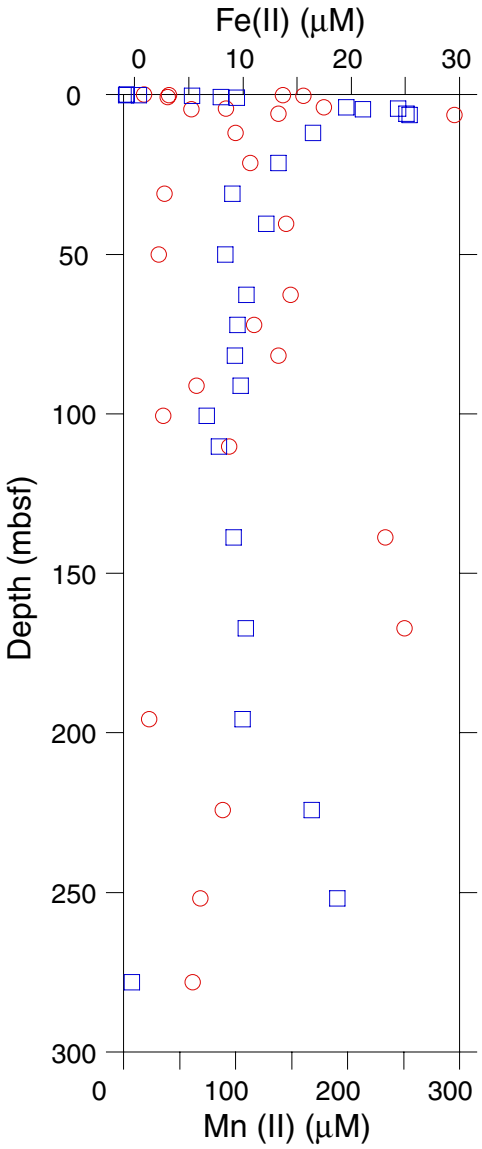

Figure F28. Concentration profile of dissolved SO_4^{2-} in pore waters.

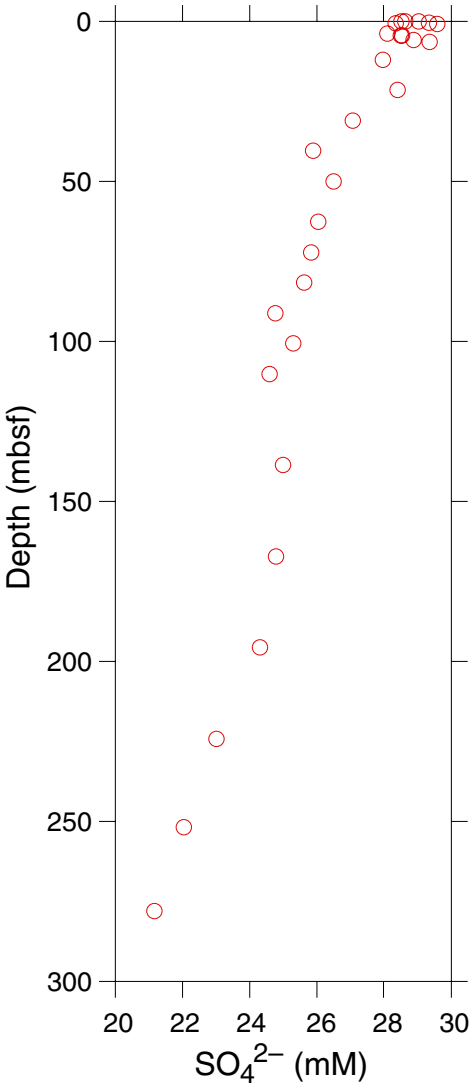

Figure F29. Standard log-log curve of PFT concentration vs. GC peak area using an electron capture detector. Two separate curves are generated from the injection of both 5-mL (circles) and 0.5-mL (diamonds and squares) volumes of perfluorocarbon tracer (PFT) standards onto the capillary column. The nonlinear effect that results from not correcting for the methanol blank at lower PFT concentrations during 0.5-mL injections is shown separately (squares).

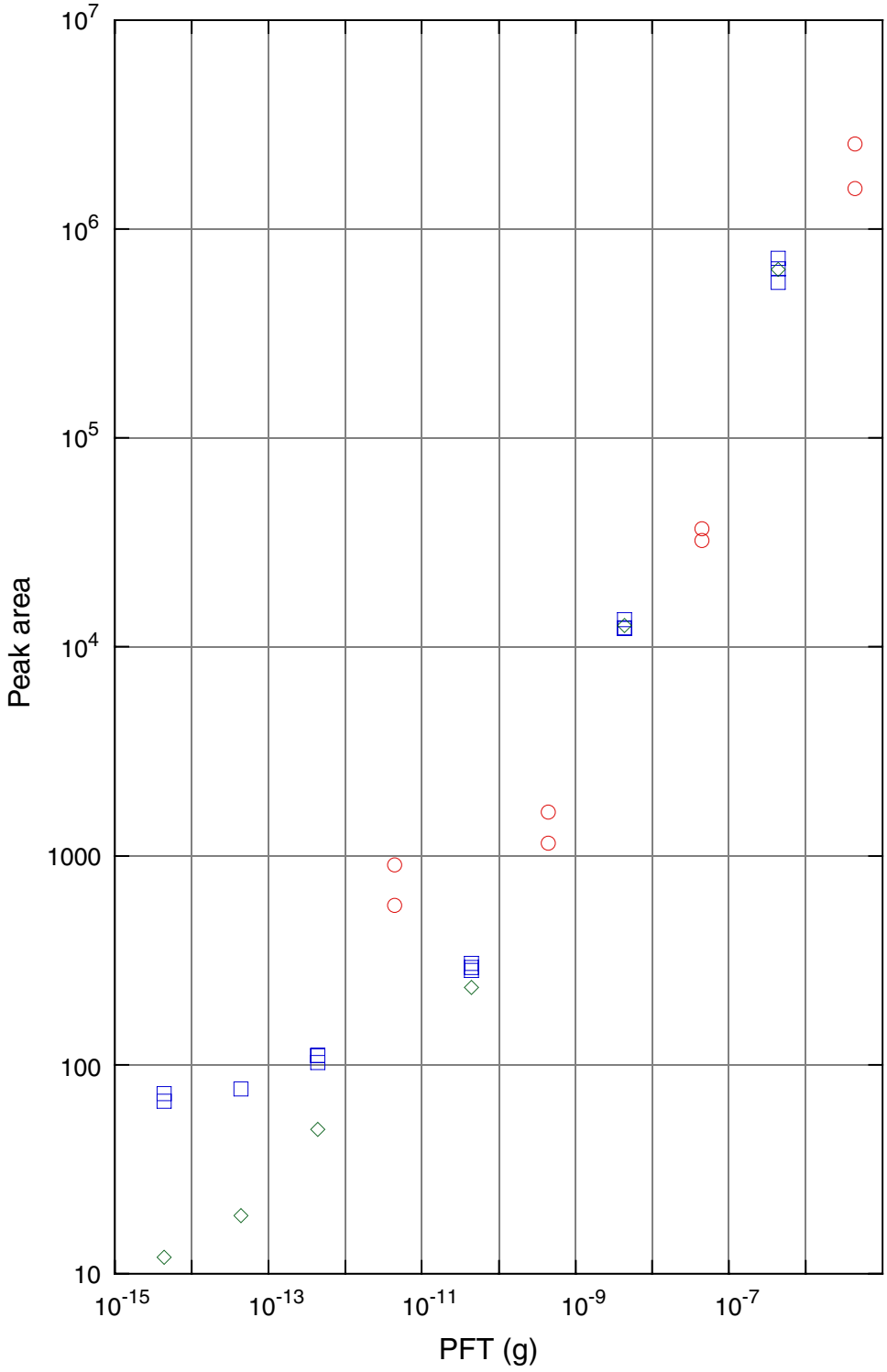

Figure F30. A. NRM intensity vs. depth, Holes 1179B and 1179C. **B.** NRM intensity vs. depth after 40-mT AF demagnetization. The dashed lines show the boundaries between cores.

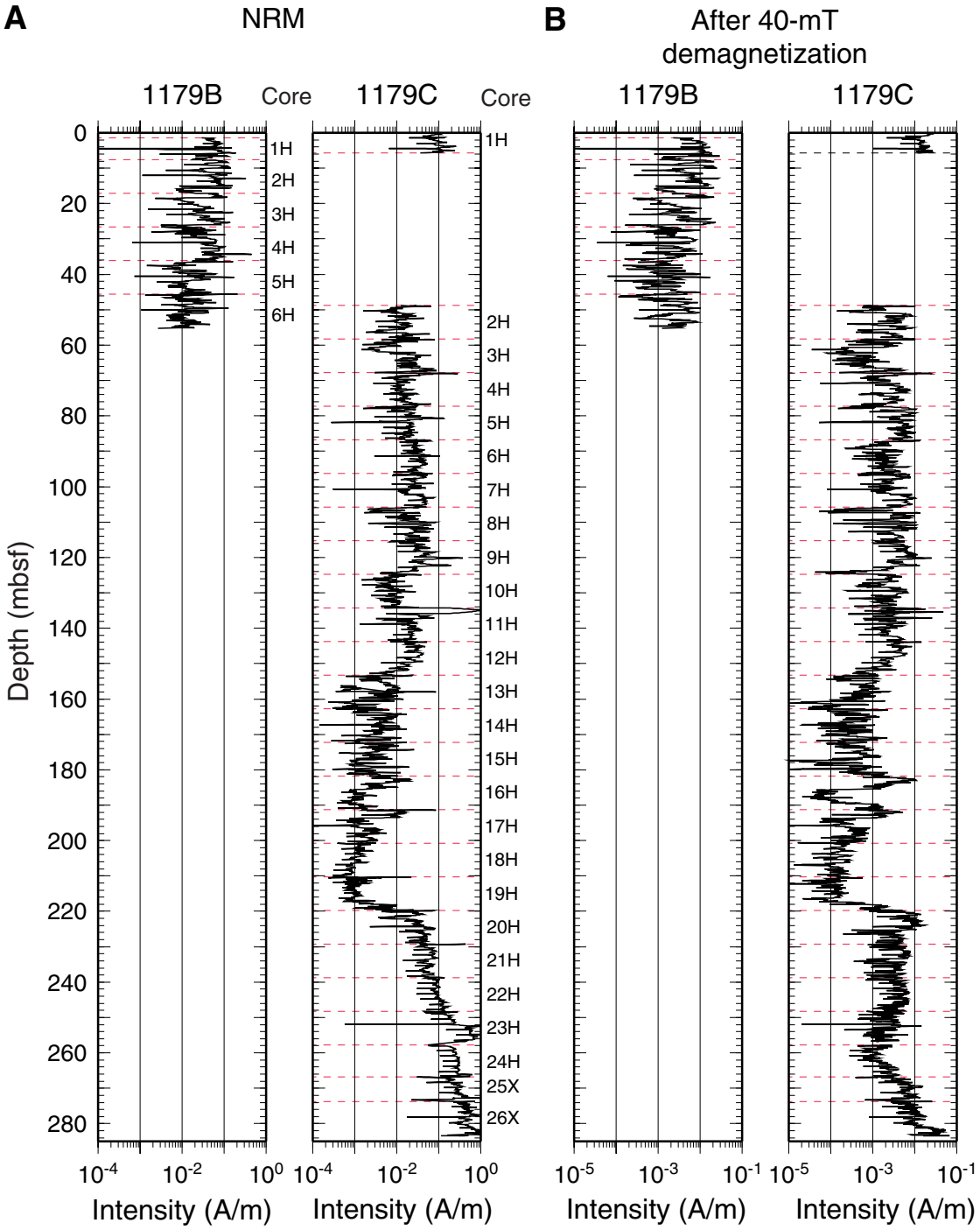

Figure F31. Paleomagnetic inclination record from Core 191-1179C-8H showing the drill-string overprint. The left plot shows NRM directions, which are all positive. After AF demagnetization (right plot), NRM directions are both positive and negative.

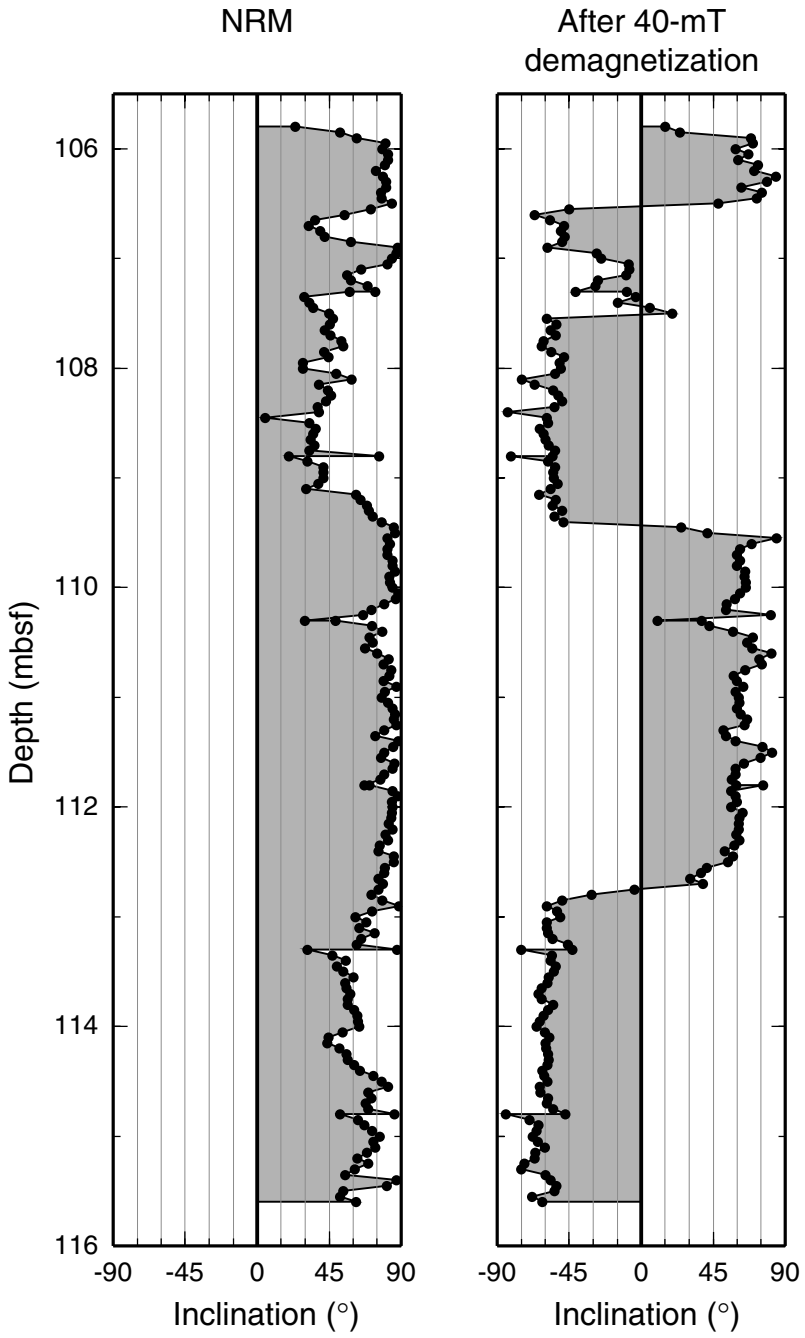

Figure F32. Zijderveld plot of Sample 191-1179C-12H-1, 130–132 cm. Open symbols = the vertical projections onto the up-north plane, closed symbols = horizontal projections onto the north-east plane.

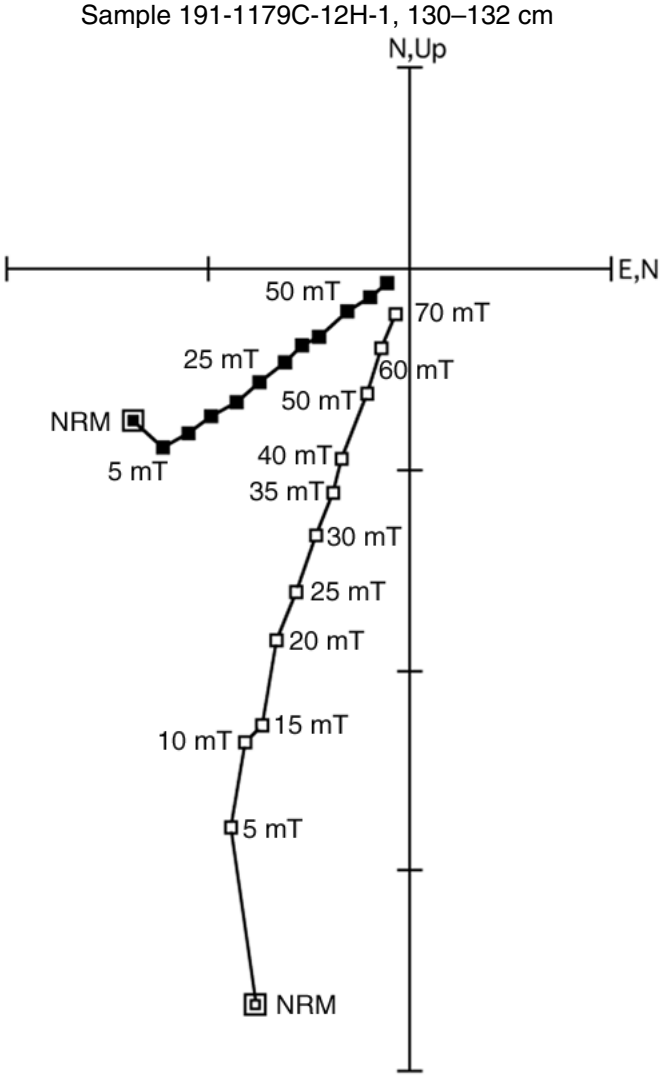

Figure F33. Magnetic susceptibility vs. depth. Dashed lines = the boundaries between cores.

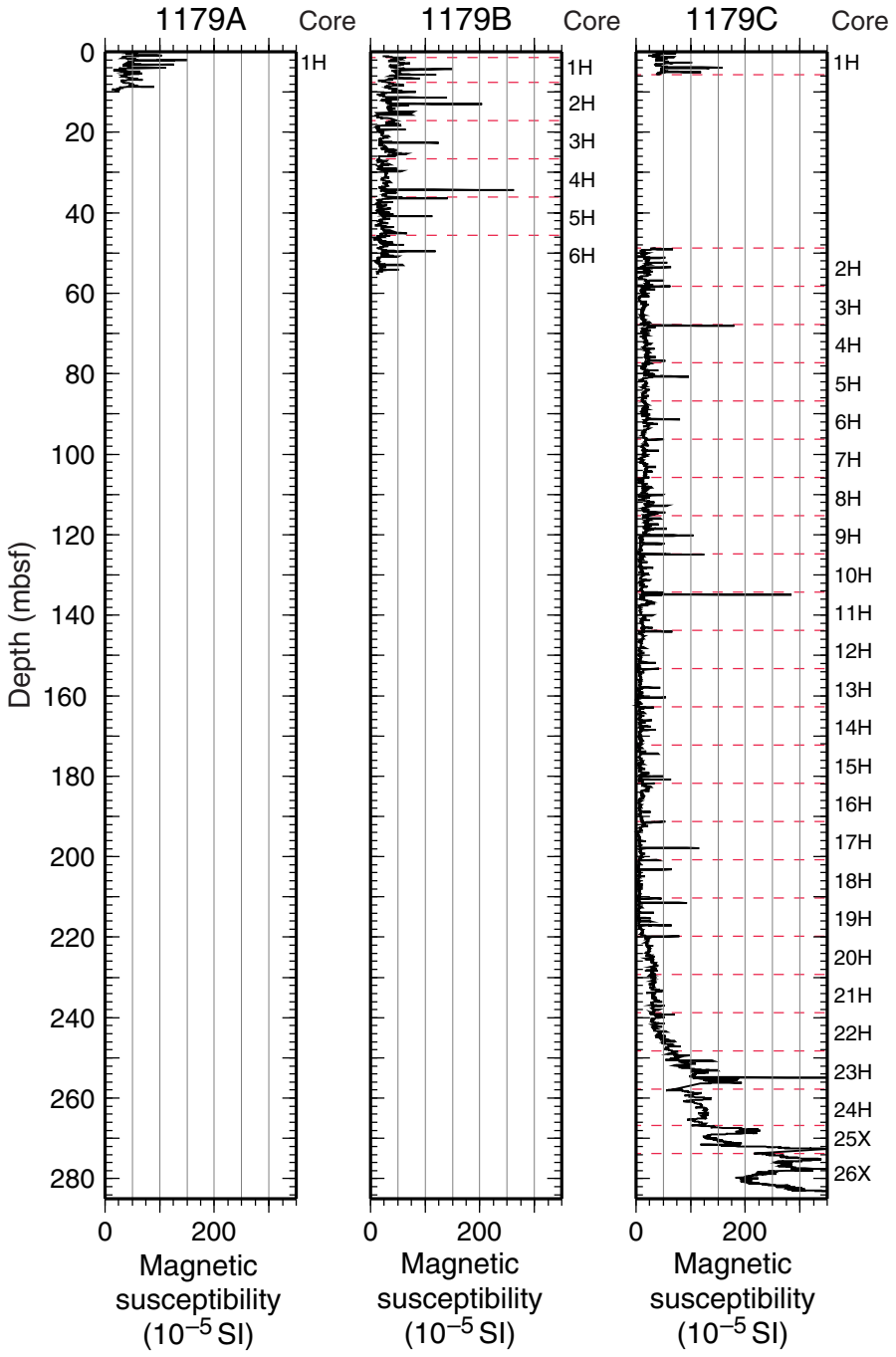

Figure F34. Magnetic susceptibility correlations. Data gaps occur at section and core boundaries. **A.** Correlations between Cores 191-1179A-1H, 191-1179B-1H and 2H, and 191-1179C-1H. Dashed line = the boundary between Cores 191-1179-B-1H and 2H. **B.** Correlations between Cores 191-1179B-6H and 191-1179C-2H.

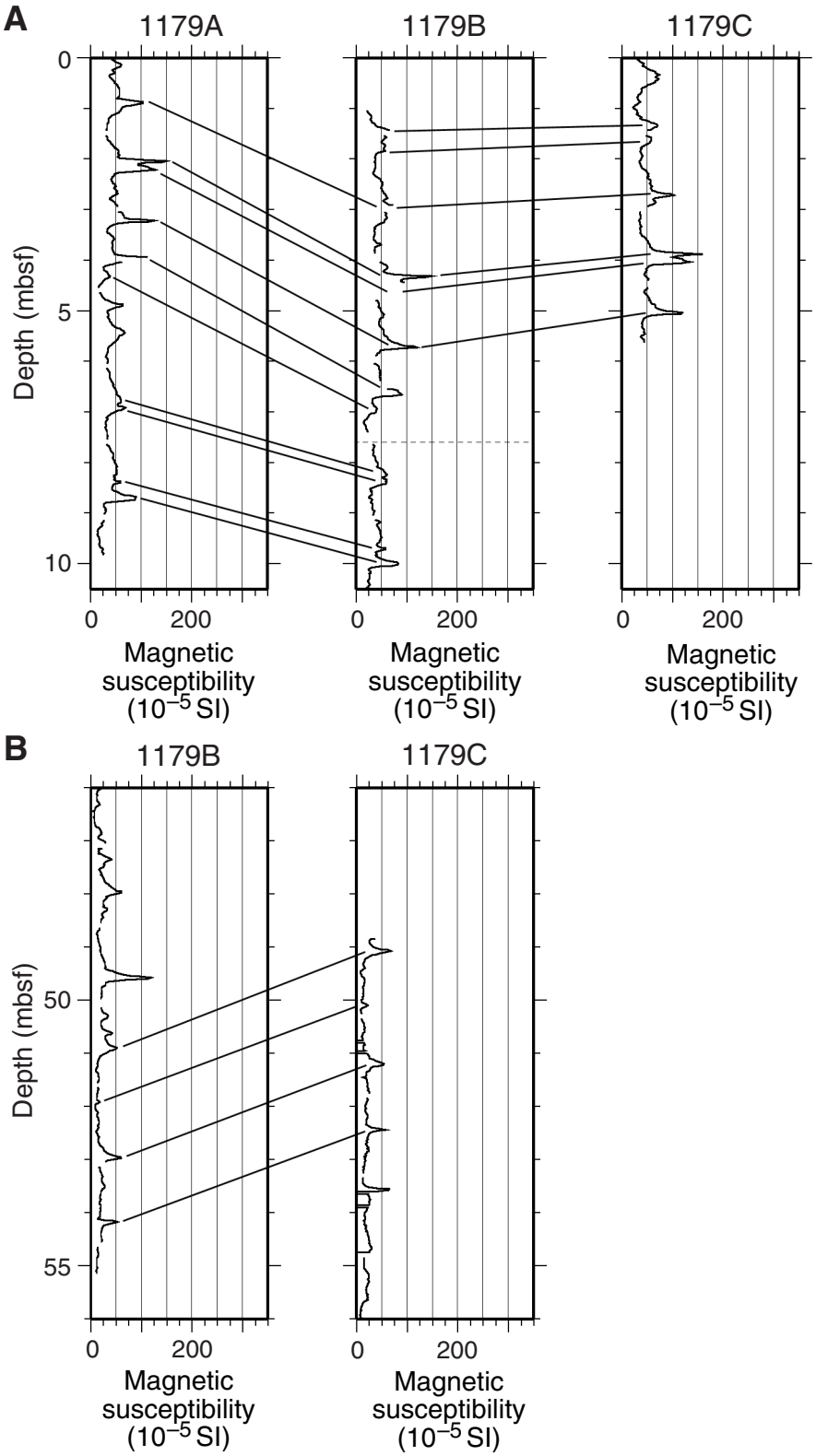

Figure F35. Magnetic polarity reversal sequence (inclination after 40-mT AF demagnetization) vs. depth from the pass-through magnetometer. The dashed lines indicate the locations of core tops. **A.** Hole 1179B (0–55.2 mbsf). **B.** Hole 1179C (48.85–105 mbsf). **C.** Hole 1179C (105–165 mbsf). **D.** Hole 1179C (165–225 mbsf). **E.** Hole 1179C (225–283.49 mbsf). Magnetostratigraphy ends at the bottom of Core 191-1179C-23H. Black bands = normal polarity, white bands = reversed polarity. (Continued on next two pages.)

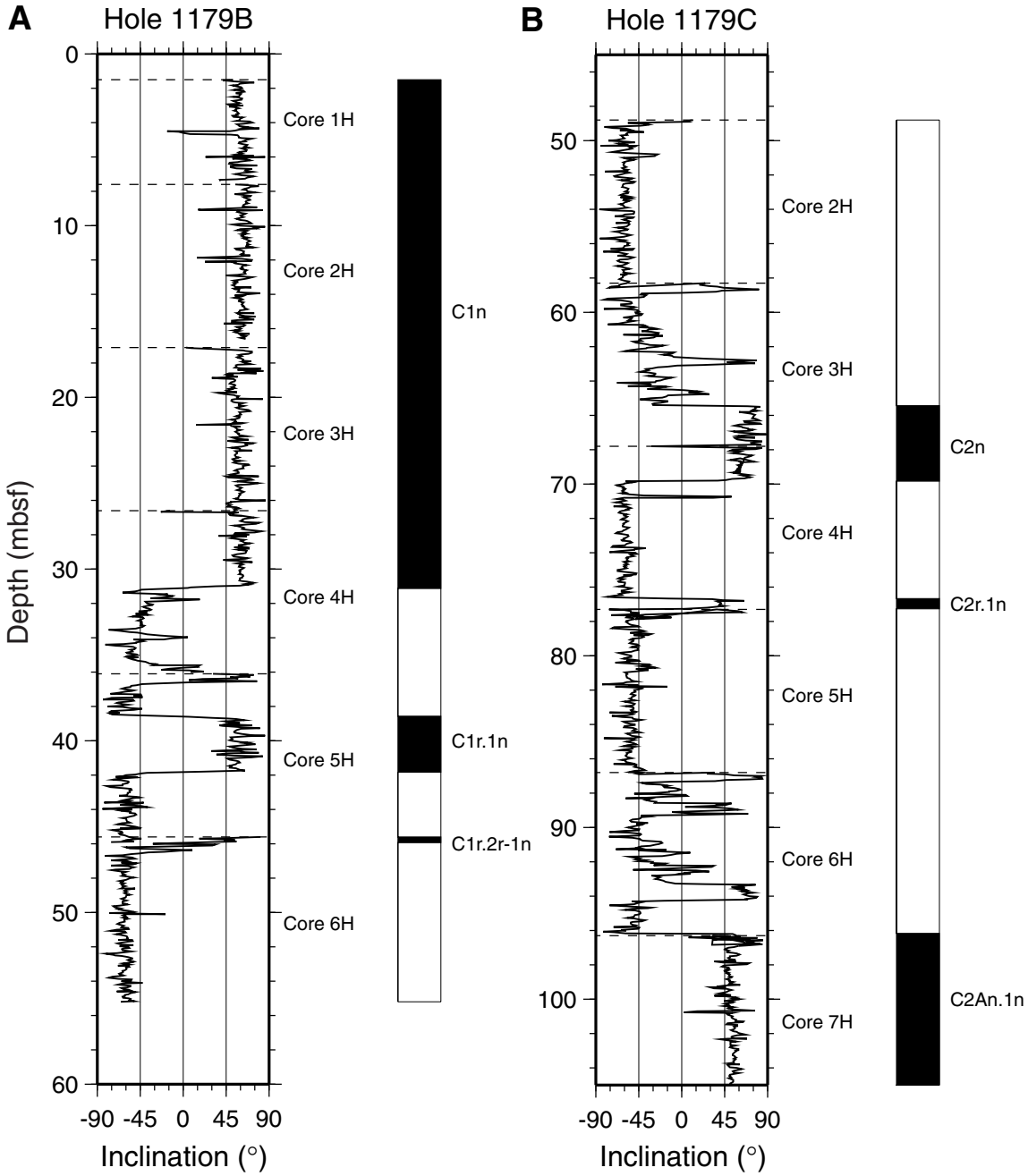

Figure F35 (continued).

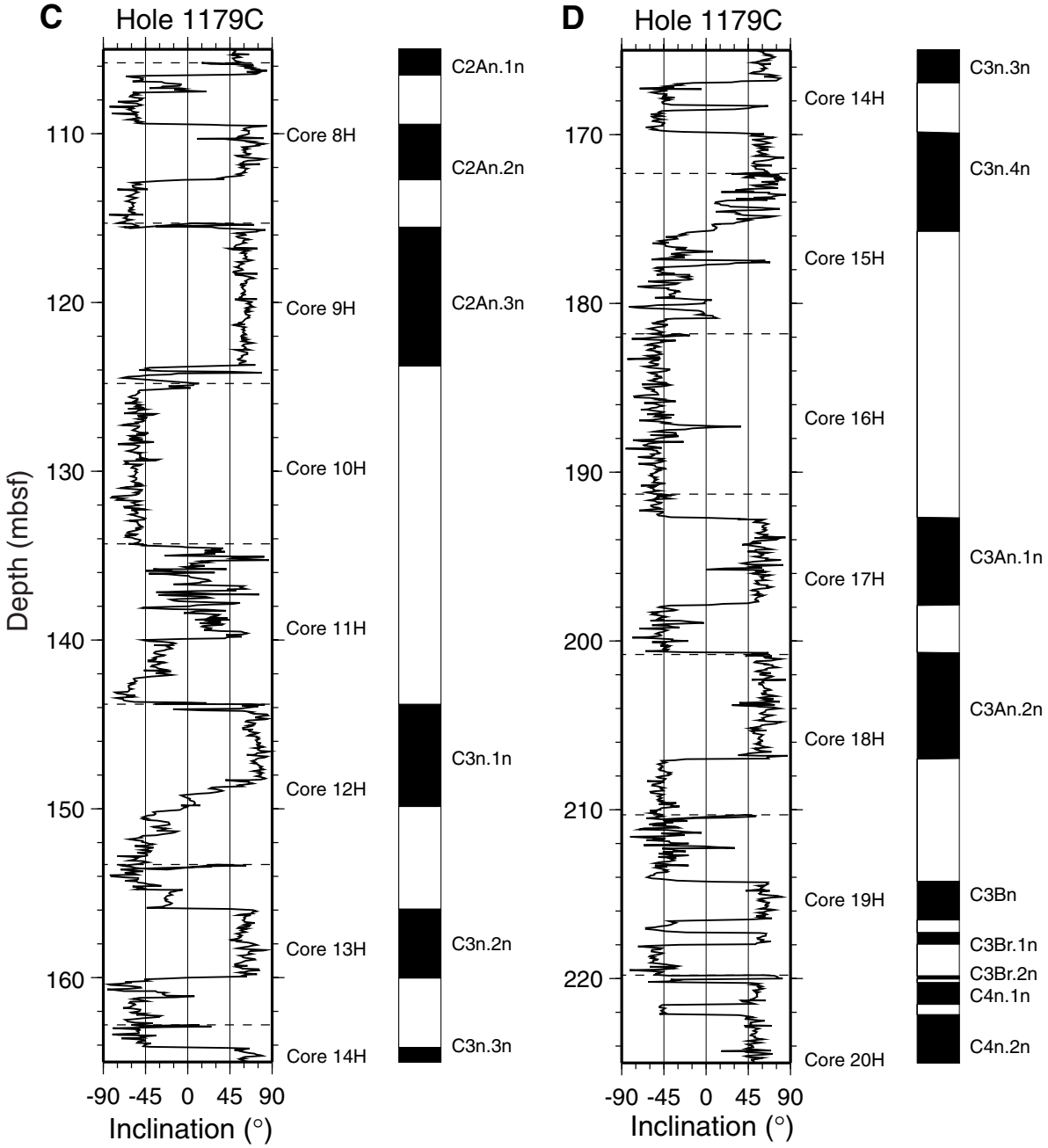

Figure F35 (continued).

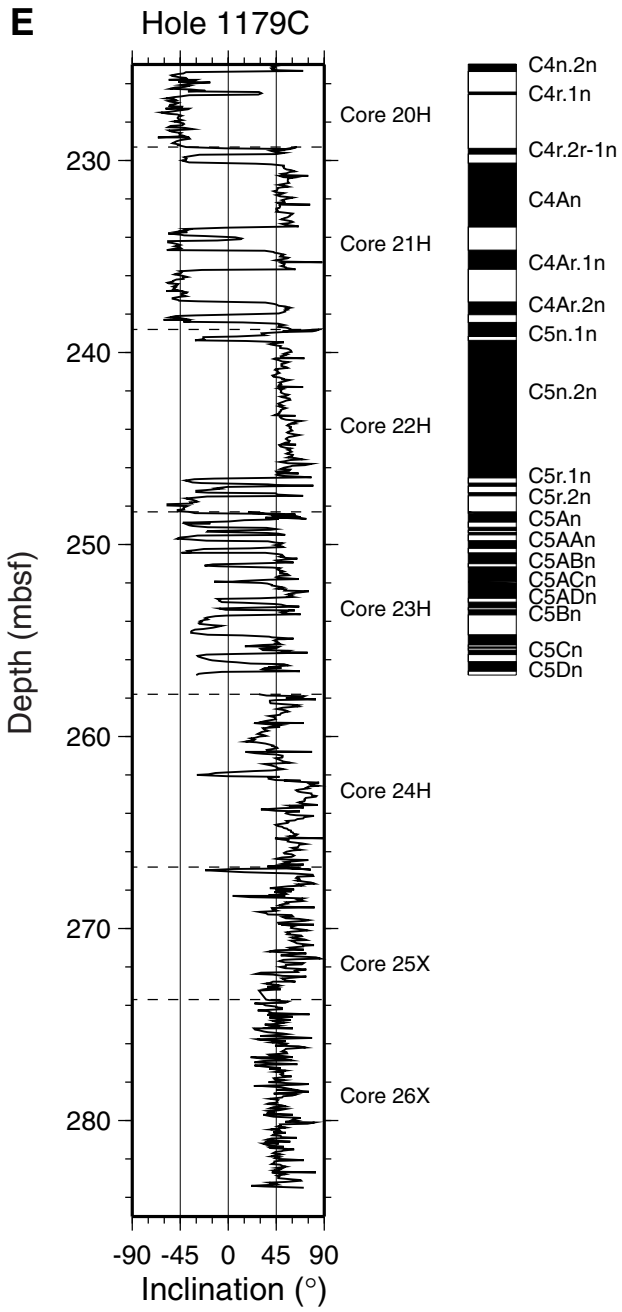

Figure F36. Basalt-sample Zijderveld plots. **A.** AF demagnetization of Sample 191-1179D-11R-1, 17–19 cm. This sample never reaches a stable direction, as shown on an equal area stereonet (circle inset). **B.** Thermal demagnetization of Sample 191-1179D-18R-4, 53–55 cm. This sample shows nearly univectorial decay after removal of an overprint at temperatures <300°C.

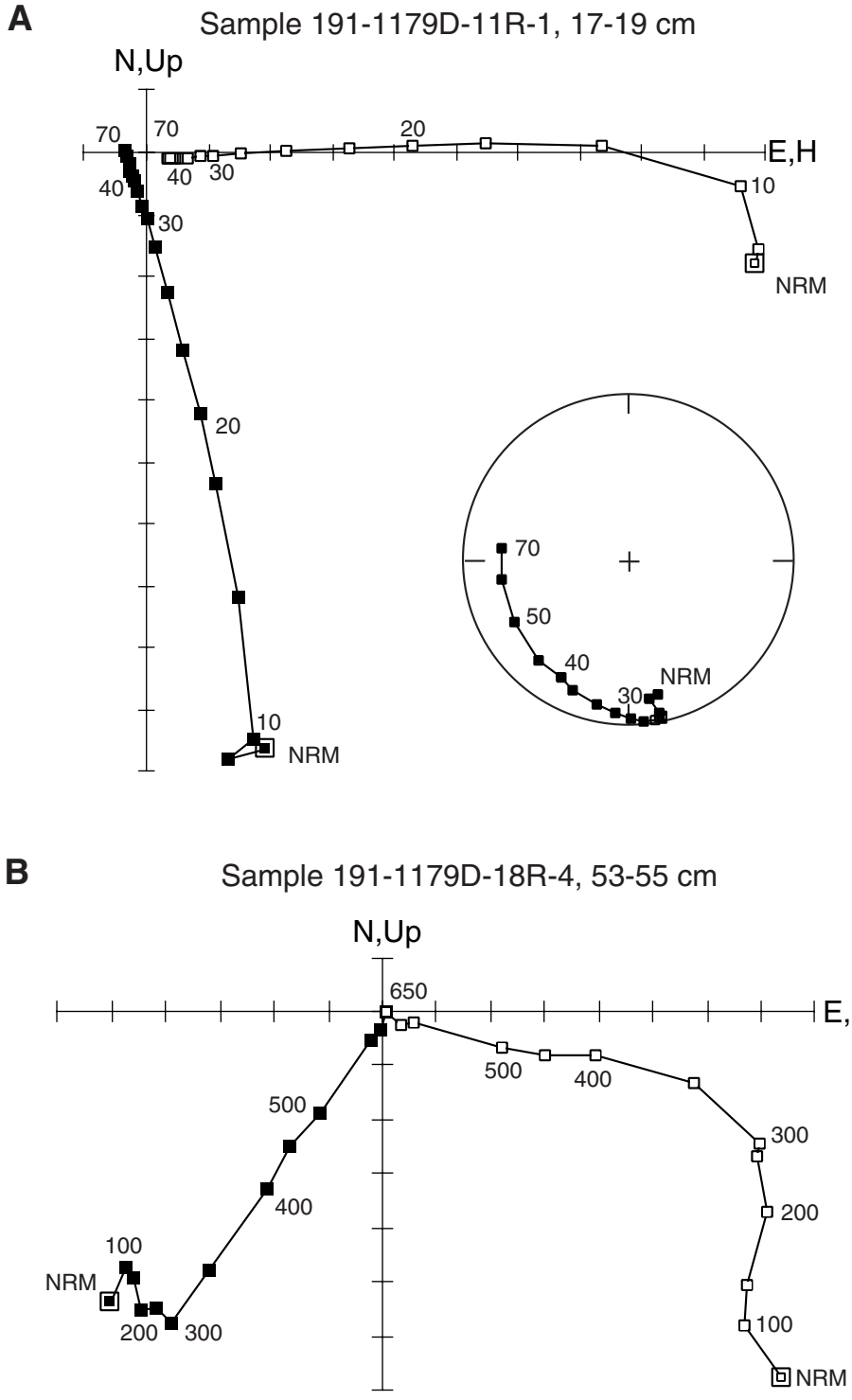

Figure F37. Sedimentation rate curve based on magnetostratigraphy. Magnetic polarity vs. depth is shown at the left, and magnetic polarity vs. age is shown at the top. White = normal polarity, black = reversed polarity. The inset shows an enlargement of lithostratigraphic Unit II and the upper part of Unit III, where magnetic stratigraphy is defined.

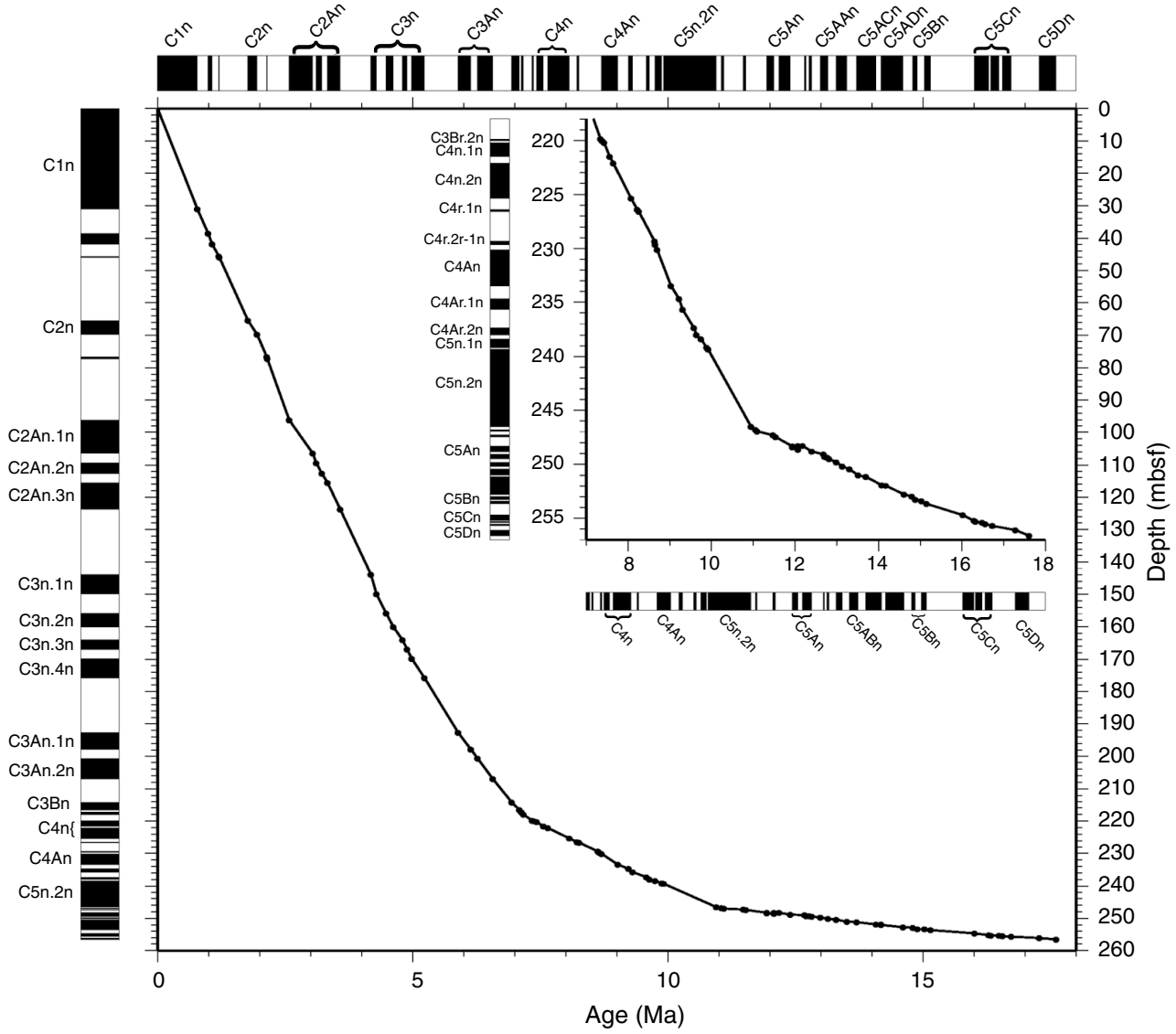

Figure F38. Sedimentation rates based on radiolarians (heavy dashed lines), dinoflagellate cysts, benthic foraminifers, and calcareous nannofossils. Minimum and maximum ages for each sample constrain sediment accumulation rates and are shown as shaded areas; a best-fit sedimentation rate curve was fitted through the shaded region, with uncertainty represented by the darker gray wedge.

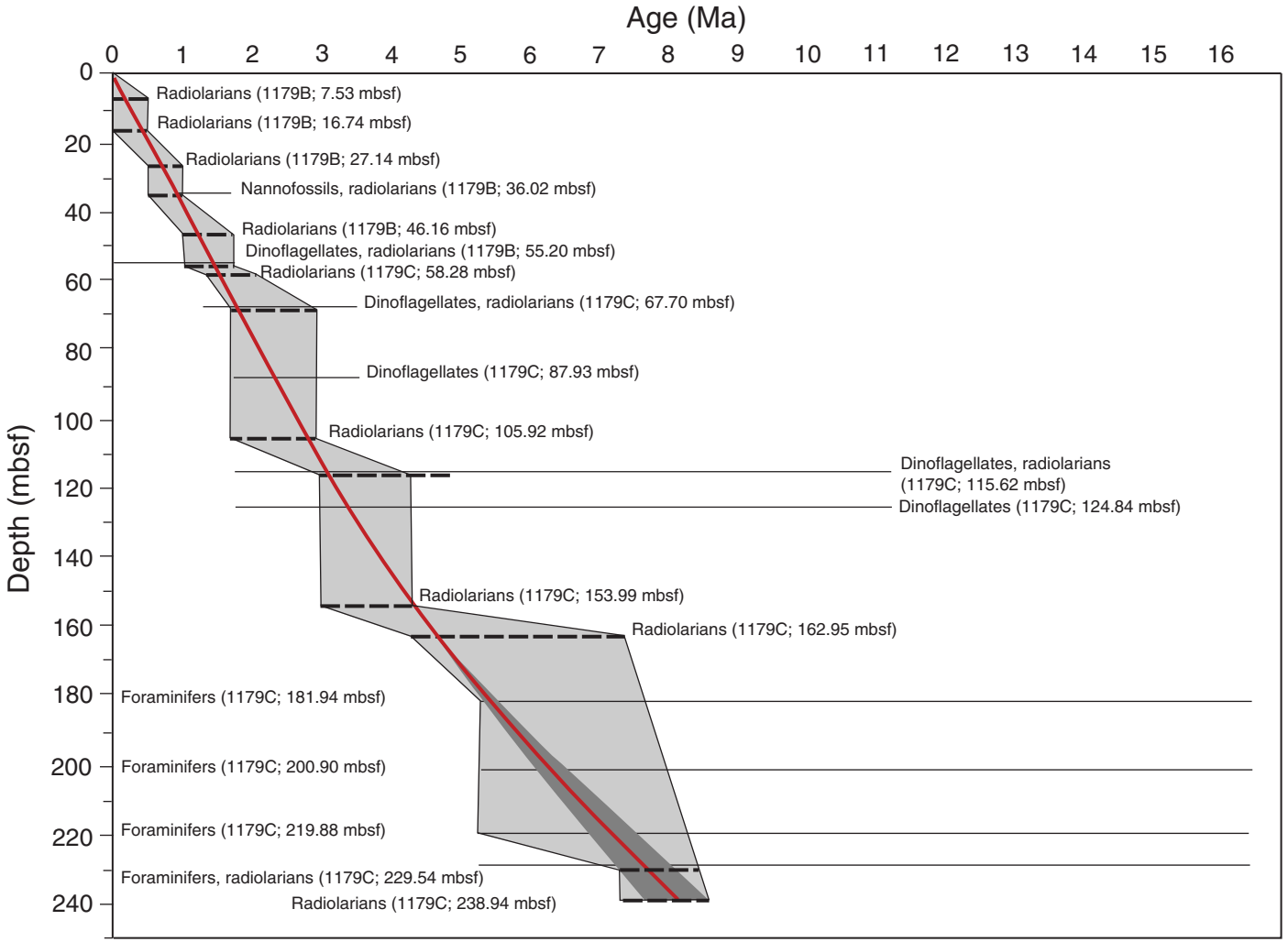

Figure F39. Basement lithostratigraphy and unit boundaries. In accordance with ODP convention, all core material is compressed to the top of each cored interval.

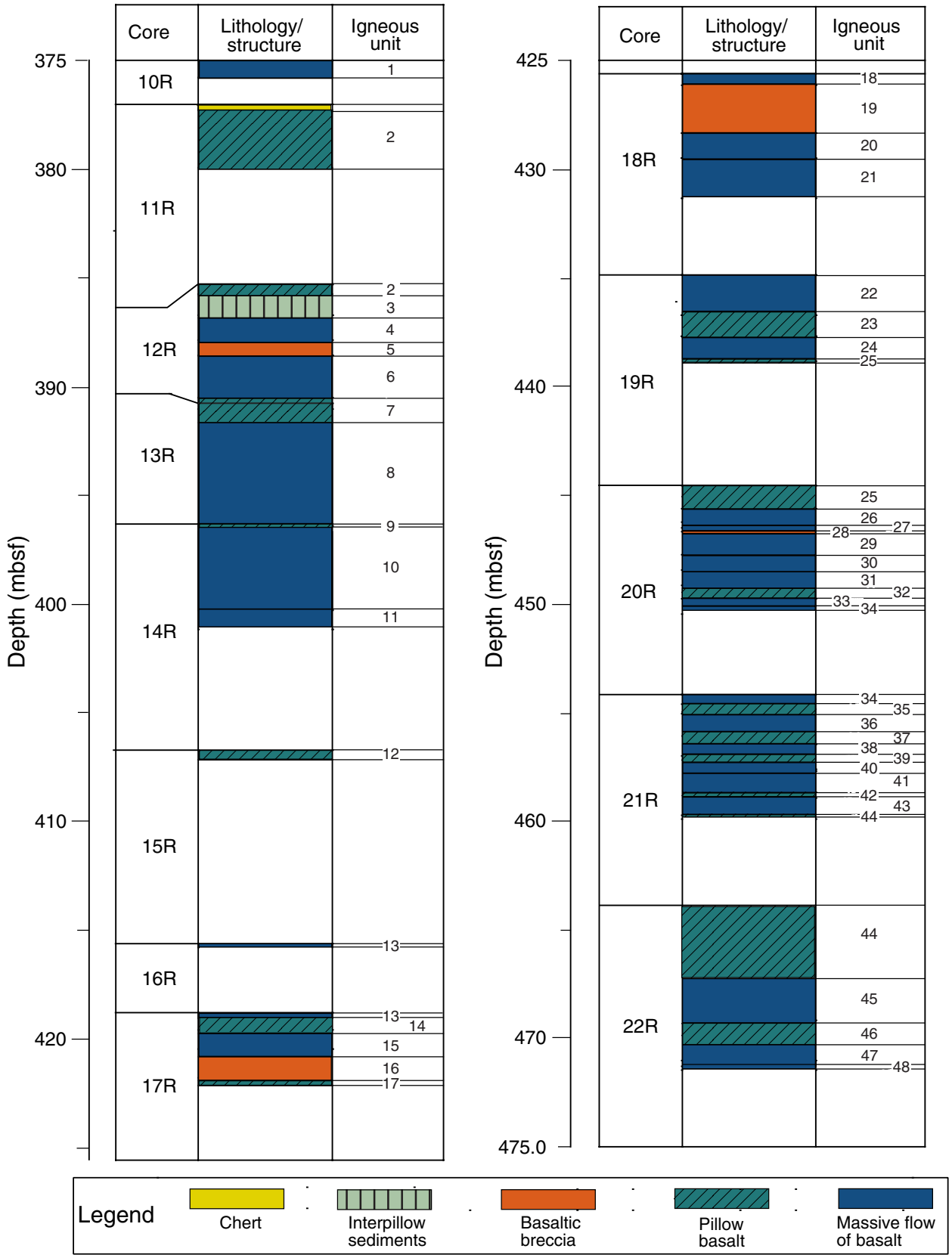

Figure F40. Close-up photograph of the top of basement in Hole 1179D. Highly altered aphyric basalt flow margin covered by brown chert (interval 191-1179D-10R-1, 38–70 cm). The sediment/basement contact was not recovered.

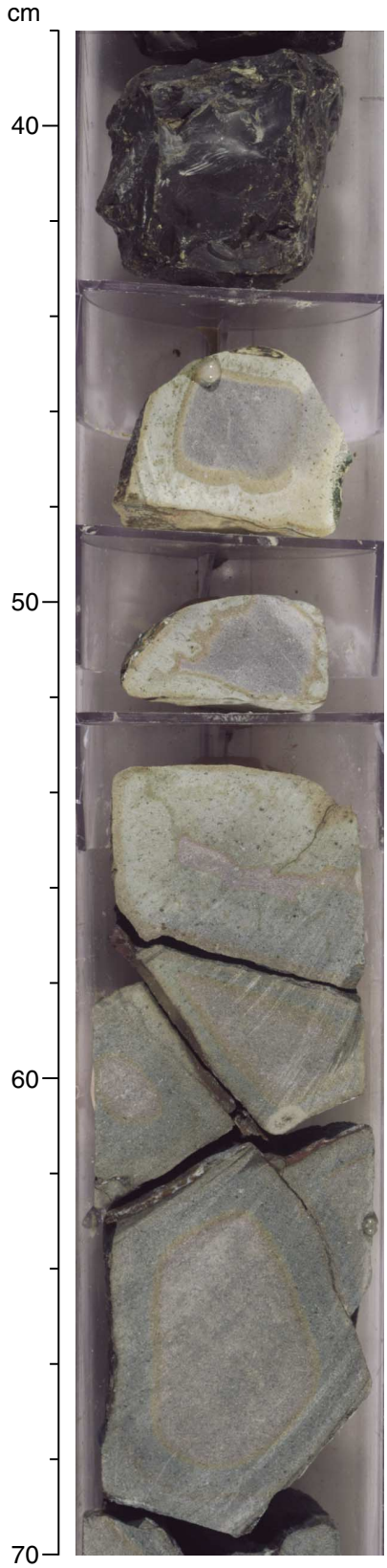

Figure F41. Photomicrograph in plane-polarized light of basalt at the top of basement. Aphyric to sparsely plagioclase phyric basalt, cryptocrystalline to microcrystalline groundmass, which is highly altered forming clay minerals (Sample 191-1179D-10R-1 [Piece 1, 44–46 cm]) (see **"Site 1179 Thin Sections,"** p. 115).

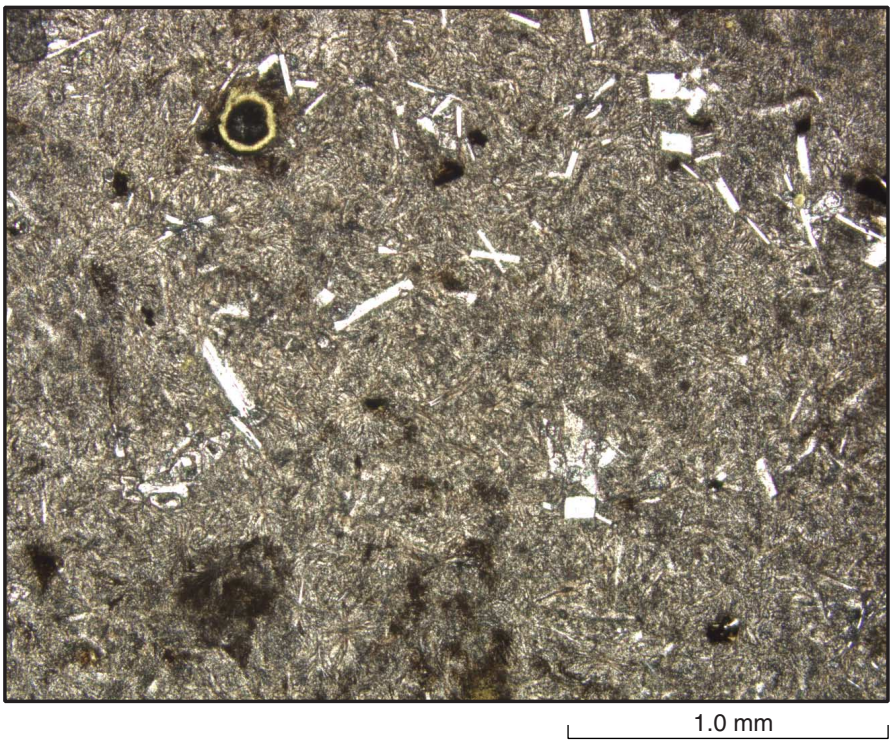

Figure F42. Close-up photograph of a liesegang structure in a basalt flow of Unit 1, formed by infiltration of fluids during alteration (interval 191-1179D-10R-1, 60–70 cm).

Figure F43. Close-up photograph of pillow and interpillow materials. Interpillow materials consist mainly of limestone with subordinate amounts of basalt fragments (interval 191-1179D-11R-1, 74–102 cm).

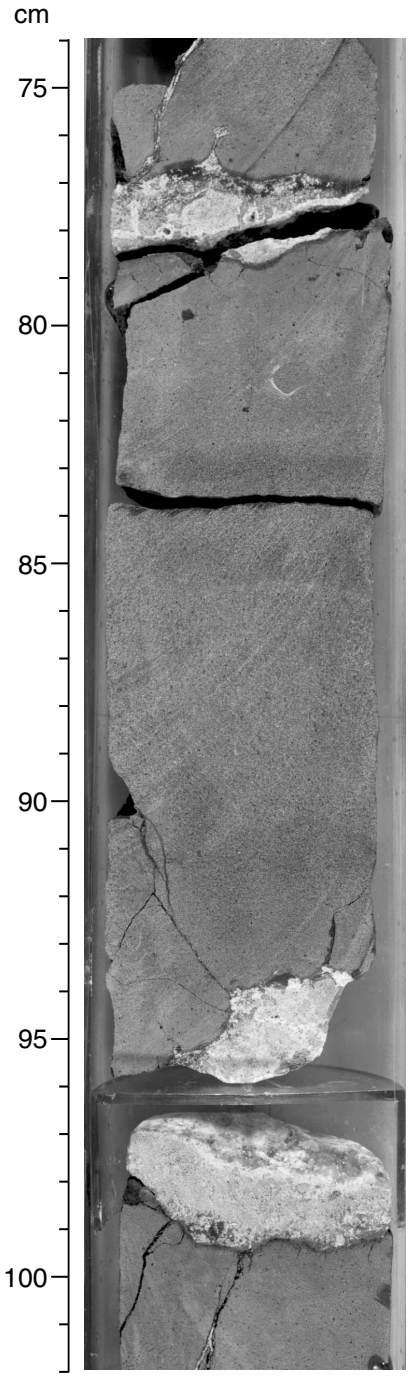

Figure F44. Close-up photographs of interpillow or interflow volcaniclastic sediment in Unit 3. **A.** Isolated pillow or pillow breccia (interval 191-1179D-12R-1, 96–108 cm). **B.** Hyaloclastite with calcareous sediment (interval 191-1179D-12R-1, 121–142 cm).

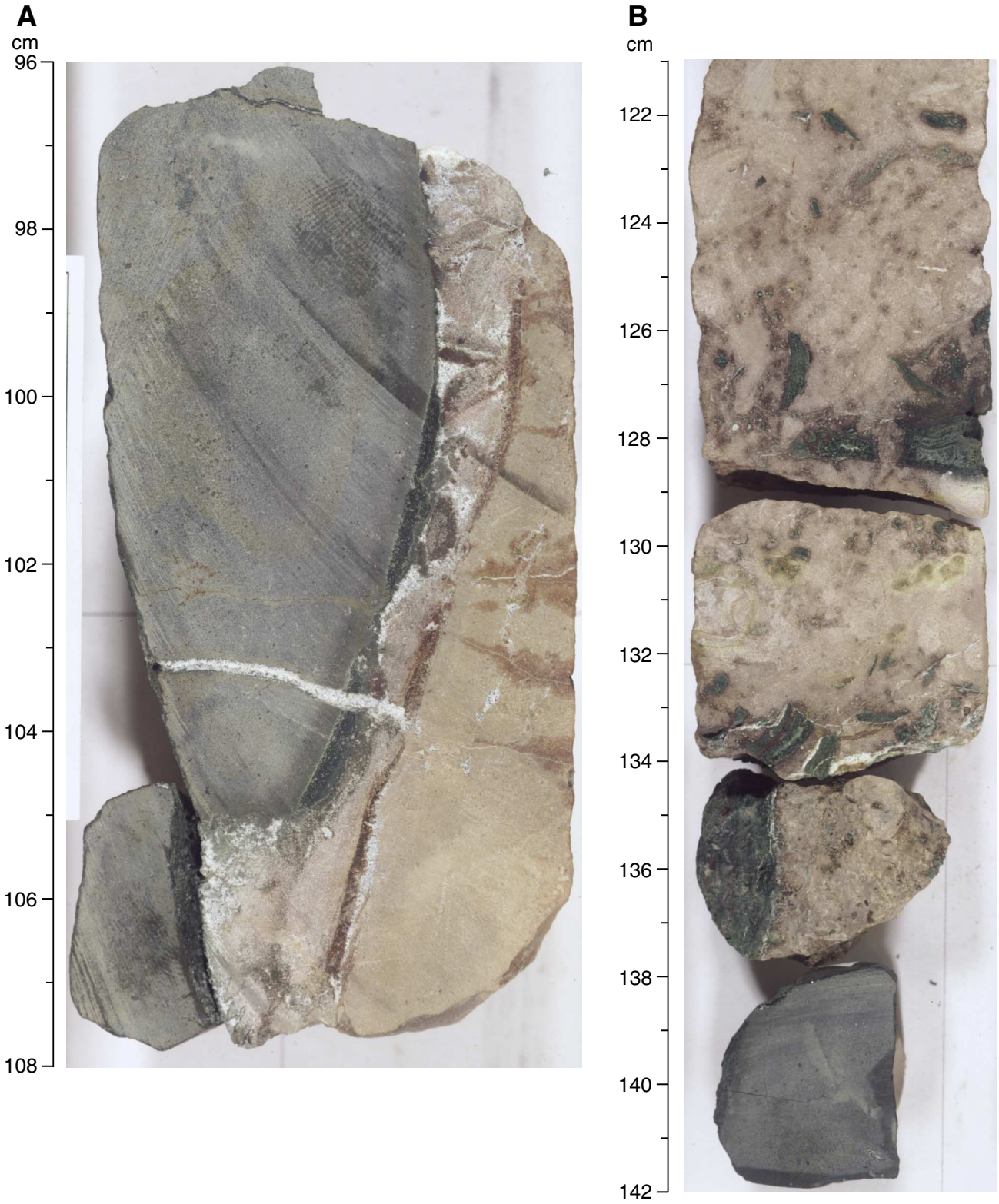

Figure F45. Photomicrograph in plane-polarized light of calcified radiolarian fossils and fragment of basalt in Unit 3 (Sample 191-1179D-12R-1 [Piece 15A,120–122 cm]) (see **"Site 1179 Thin Sections,"** p. 162).

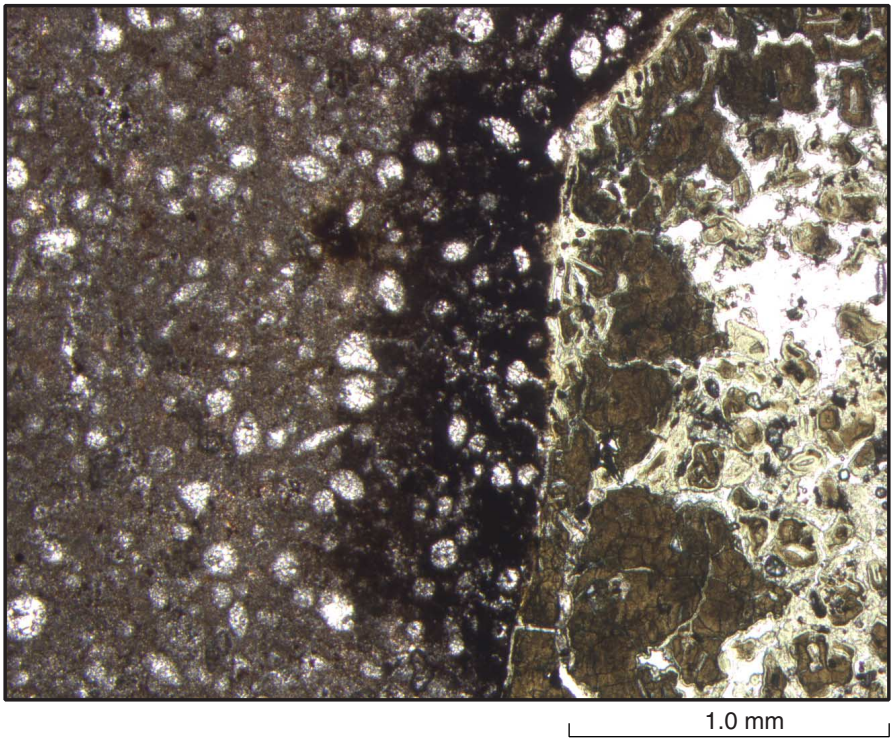

Figure F46. Close-up photographs of basaltic breccia with hyaloclastite. **A.** Hyaloclastite at the base of Unit 5 (interval 191-1179D-12R-3, 41–44 cm). **B.** Pillow breccia in Unit 16 (interval 191-1179D-17R-2, 124–136 cm).

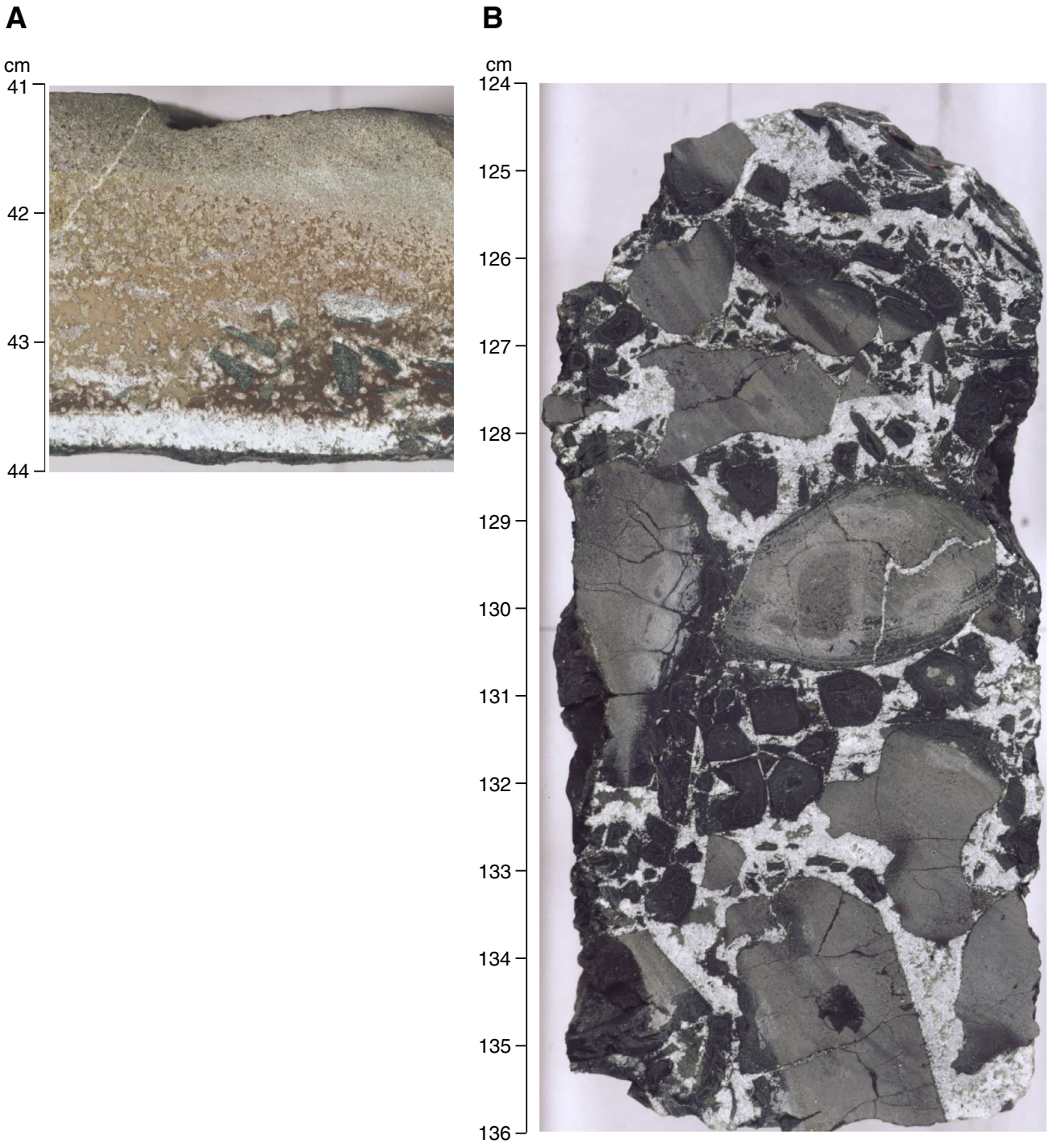

Figure F47. Close-up photograph of vesicle-rich massive flow in Unit 48, the lowermost part of the Hole 1179D. Vesicles are filled mainly with calcite and partly with saponite (interval 191-1179D-22R-5, 115–139 cm).

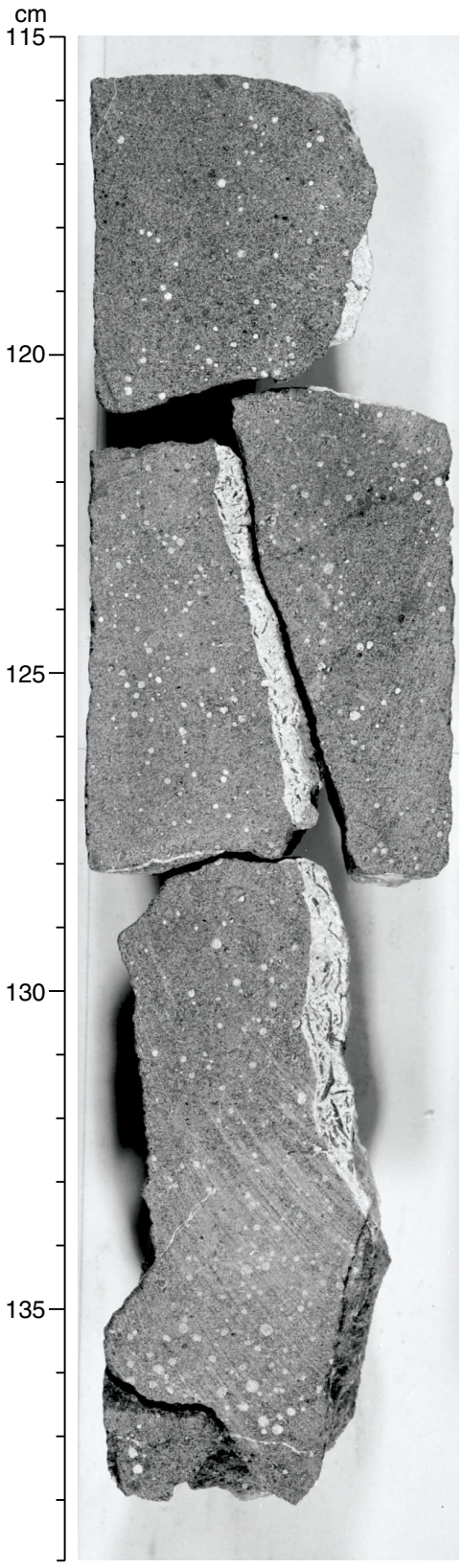

Figure F48. Close-up photograph of pillows with altered glassy shard and interpillow materials in Unit 44. White veinlets are filled with calcite (interval 191-1179D-22R-1, 130–147 cm).

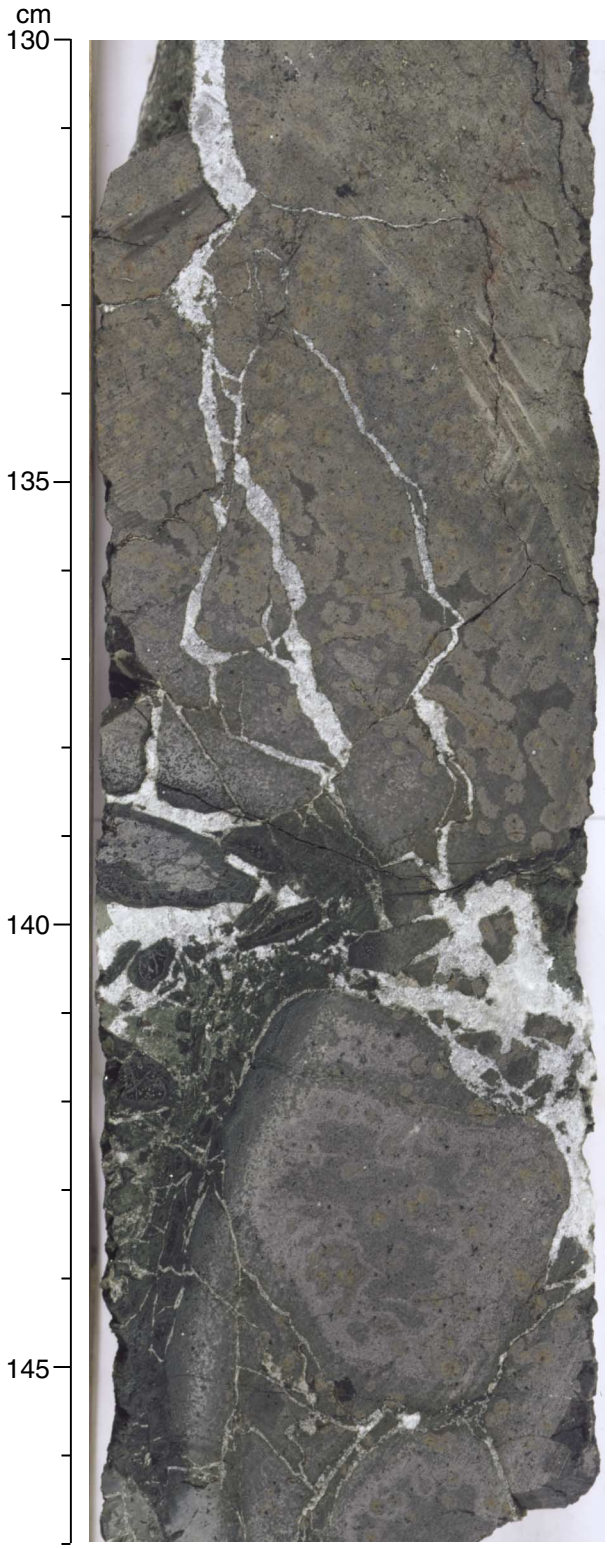

Figure F49. Photomicrographs showing phenocrysts in basalts from Hole 1179D. **A.** Plagioclase in cross-polarized light (Sample 191-1179D-12R-4 [Piece 1A, 0–2 cm]) (see **"Site 1179 Thin Sections,"** p. 123). **B.** Plagioclase in plane-polarized light with groundmass inclusions, slightly altered, forming smectite (Sample 191-1179D-13R-1 [Piece 8, 38–40 cm]) (see **"Site 1179 Thin Sections,"** p. 125). **C.** Euhedral olivine replaced by iddingsite in plane-polarized light (Sample 191-1179D-11R-1 [Piece 4A, 99–101 cm]) (see **"Site 1179 Thin Sections,"** p. 117). **D.** Cr spinel in plane-polarized light (Sample 191-1179D-22R-5 [Piece 7, 135–137 cm]) (see **"Site 1179 Thin Sections,"** p. 160).

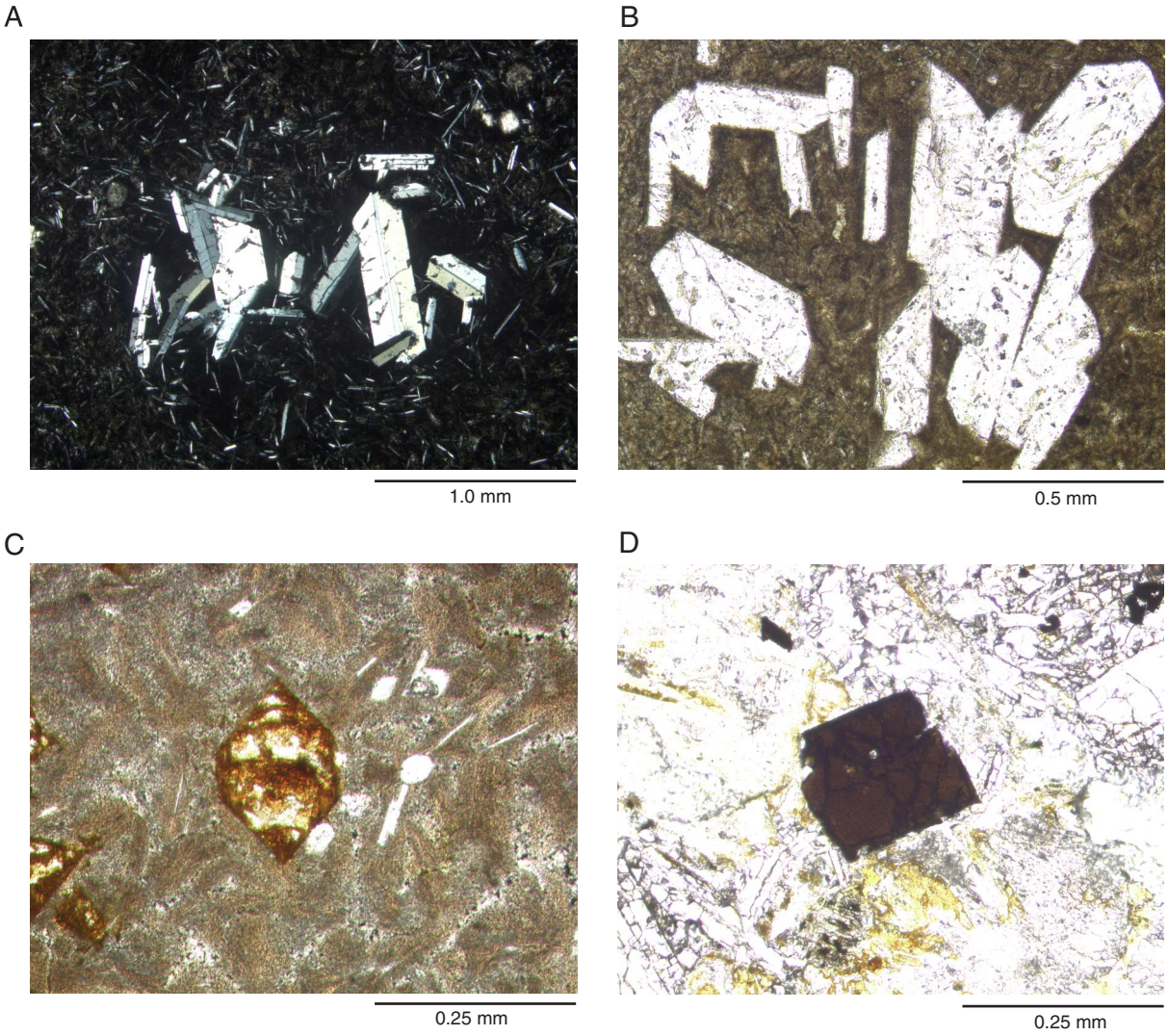

Figure F50. Photomicrographs showing accessory minerals and microcrystalline texture in basalts from Hole 1179D. **A.** Zircon in plane-polarized light with a halo in clinopyroxene (Sample 191-1179D-14R-2 [Piece 15B, 117–119 cm]) (see **"Site 1179 Thin Sections,"** p. 130). **B.** Apatite in cross-polarized light in clinopyroxene (Sample 191-1179D-11R-2 [Piece 9, 81–83 cm]) (see **"Site 1179 Thin Sections,"** p. 119). **C.** Radial clusters of clinopyroxene and magnetite in plane-polarized light in palagonitized glass (Sample 191-1179D-18R-1 [Piece 2B, 47–50 cm]) (see **"Site 1179 Thin Sections,"** p. 135). **D.** Clinopyroxene clusters in cross-polarized light in glass (Sample 191-1179D-22R-1 [Piece 6A, 59–61 cm]) (see **"Site 1179 Thin Sections,"** p. 152).

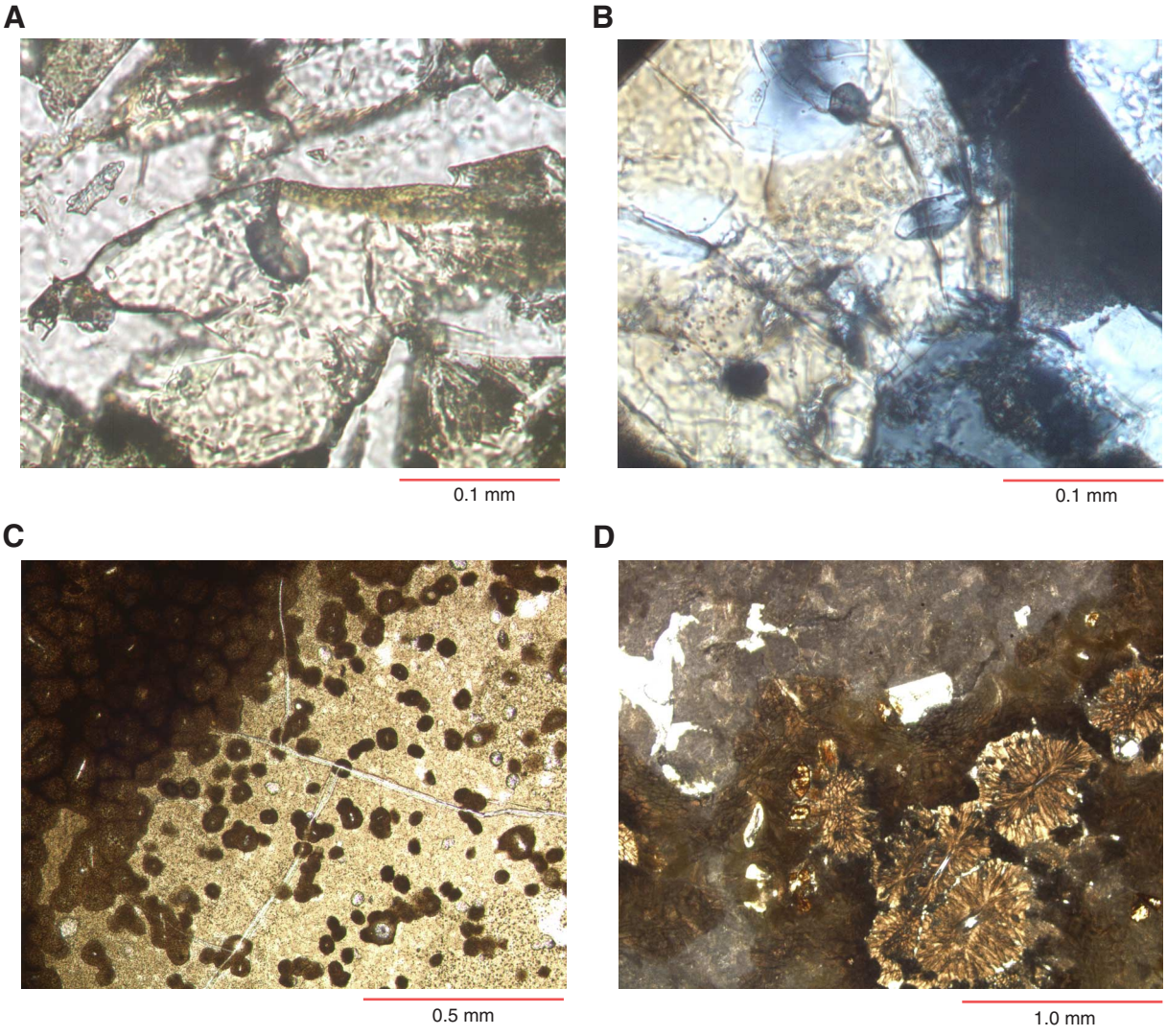

Figure F51. Photomicrographs in plane-polarized light showing groundmass texture of basalt from Hole 1179D. **A.** Clinopyroxene bunches with plagioclase (Sample 191-1179D-10R-1 [Piece 1, 44–46 cm]) (see "Site 1179 Thin Sections," p. 115). **B.** Plagioclase and plumose crystallites (Sample 191-1179D-20R-4 [Piece 1C, 21–23 cm]) (see "Site 1179 Thin Sections," p. 146). **C.** Plagioclase clusters with magnetite and clinopyroxene (Sample 191-1179D-21R-1 [Piece 1C, 28–30 cm]) (see "Site 1179 Thin Sections," p. 148). **D.** Hyalopilitic texture (Sample 191-1179D-10R-1 [Piece 5B, 102–104 cm]) (see "Site 1179 Thin Sections," p. 116).

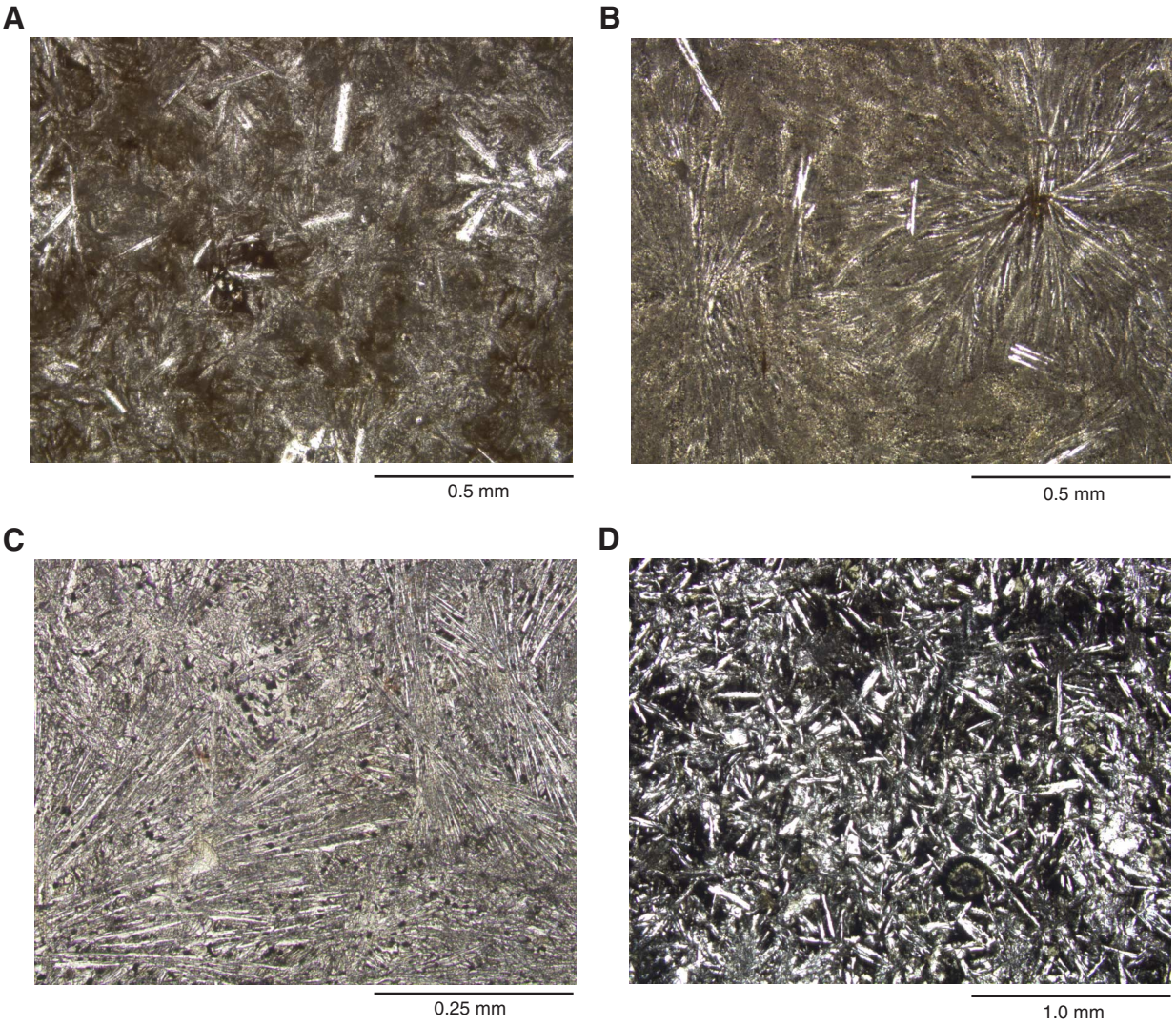

Figure F52. Photomicrographs showing representative textures of basalts from Hole 1179D. **A.** Microcrystalline texture in plane-polarized light (Sample 191-1179D-12R-2 [Piece 1A, 1–3 cm]) (see **"Site 1179 Thin Sections,"** p. 120). **B, C.** Rosettelike bundles of plagioclase crystals in plane-polarized light (Sample 191-1179D-10R-1 [Piece 1, 44–46 cm]) (see **"Site 1179 Thin Sections,"** p. 115). **D.** Subophitic texture in cross-polarized light (Sample 191-1179D-13R-4 [Piece 4, 77–79 cm]) (see **"Site 1179 Thin Sections,"** p. 128).

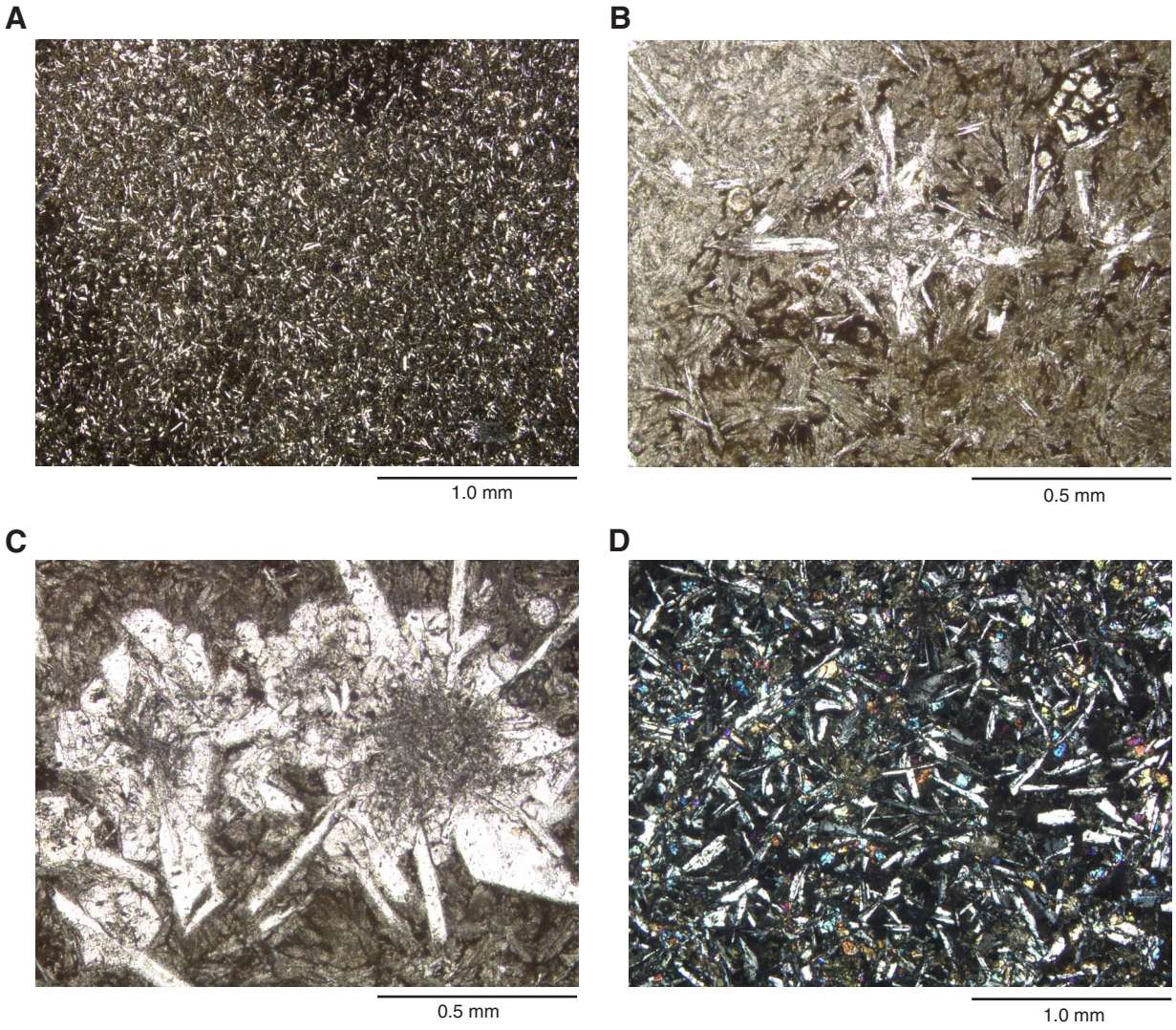

Figure F53. Photomicrographs showing fine-grained groundmass textures of basalts from Hole 1179D. **A.** Subophitic texture in cross-polarized light (Sample 191-1179D-22R-5 [Piece 6B, 114–116 cm]) (see **"Site 1179 Thin Sections,"** p. 158). **B.** Subophitic texture in cross-polarized light (Sample 191-1179D-12R-1 [Piece 15A, 120–122 cm]) (see **"Site 1179 Thin Sections,"** p. 140). **C.** Skeletal plagioclase in plane-polarized light (Sample 191-1179D-22R-4 [Piece 4A, 80–82 cm]) (see **"Site 1179 Thin Sections,"** p. 156). **D.** Lathlike plagioclase in plane-polarized light (Sample 191-1179D-22R-5 [Piece 7, 135–137 cm]) (see **"Site 1179 Thin Sections,"** p. 160).

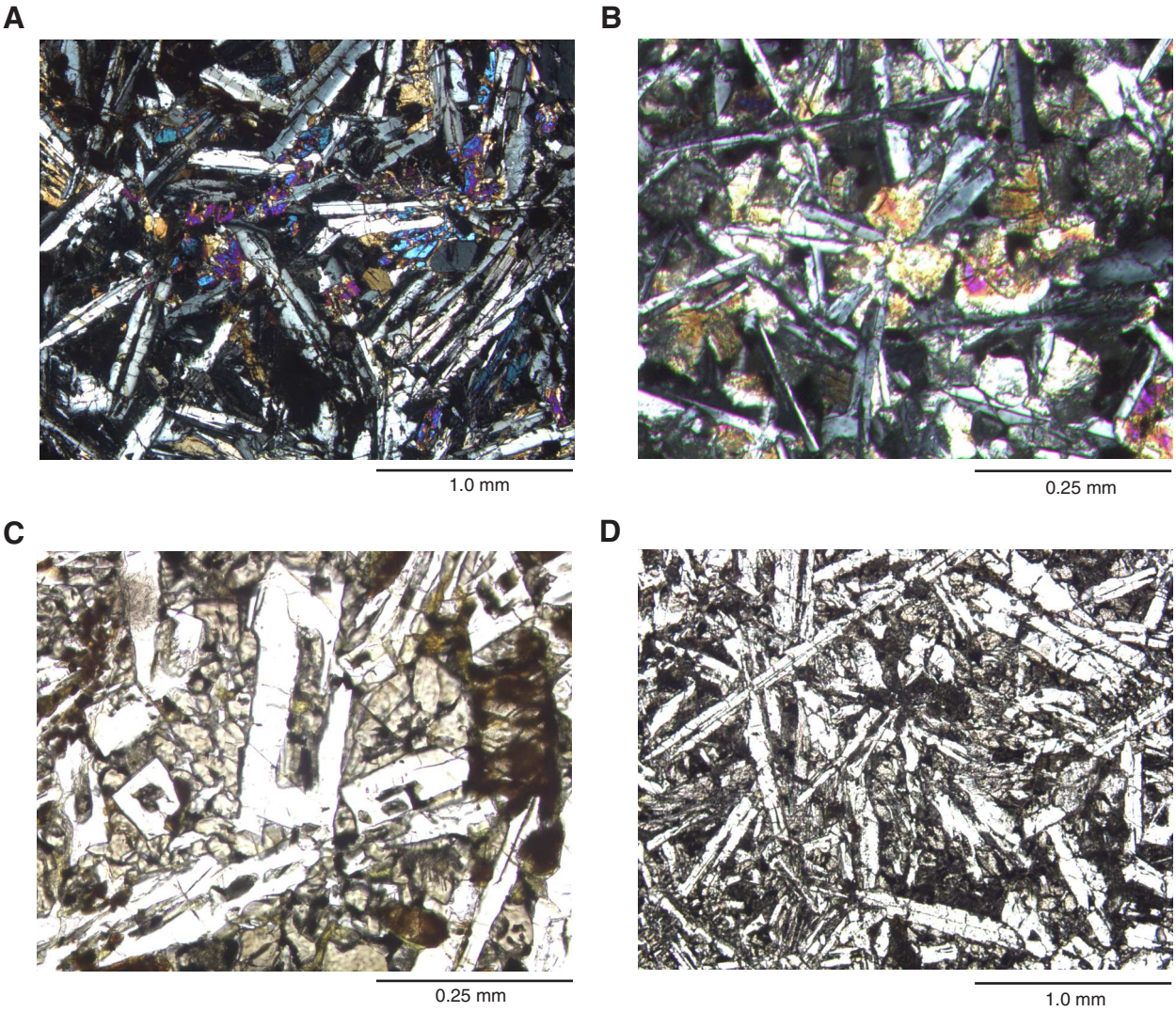

Figure F54. FeO*/MgO vs. TiO_2 plot for basalts from Site 1179D. Reference data sources from Pacific Ocean are Mariana Basin, Floyd and Castillo (1992); Ontong Java Plateau, Mahoney et al. (1993); East Pacific Rise (EPR) 10°–12°N, Thompson et al. (1989); EPR Leg 54 (open diamonds), Humphris et al. (1980); EPR Leg 54 (open squares) and Galapagos Rift, Srivastava et al. (1980); northwestern Pacific DSDP Leg 32, Marshall (1975); northern Pacific DSDP Leg 86, Fountain et al. (1985). All data having H_2O^+ (or loss on ignition) >5 wt% are omitted.

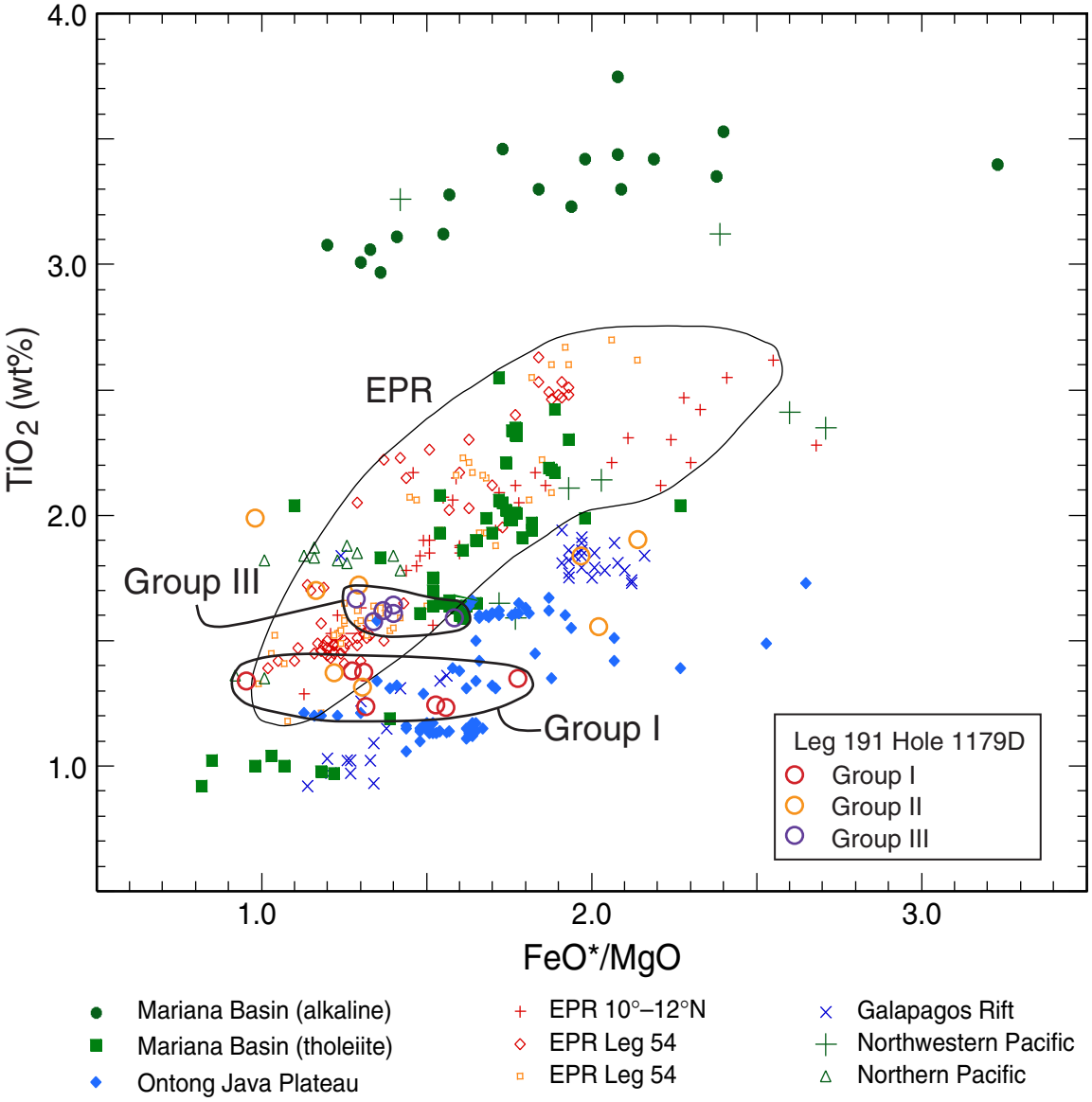

Figure F55. Photomicrographs showing secondary minerals in basalts from Hole 1179D. **A.** Palagonitized glass in hyaloclastite in plane-polarized light (Sample 191-1179D-20R-3 [Piece 3D, 139–142 cm]) (see "Site 1179 Thin Sections," p. 145). **B.** Vein with calcite and celadonite in matrix with smectite in plane-polarized light (Sample 191-1179D-12R-4 [Piece 1D, 83–86 cm]) (see "Site 1179 Thin Sections," p. 124). **C.** Vesicles with calcite and zeolite in cross-polarized light (Sample 191-1179D-22R-5 [Piece 7, 135–137 cm]) (see "Site 1179 Thin Sections," p. 160). **D.** Vesicles with smectite and celadonite in plane-polarized light (Sample 191-1179D-12R-2 [Piece 3, 13–15 cm]) (see "Site 1179 Thin Sections," p. 121).

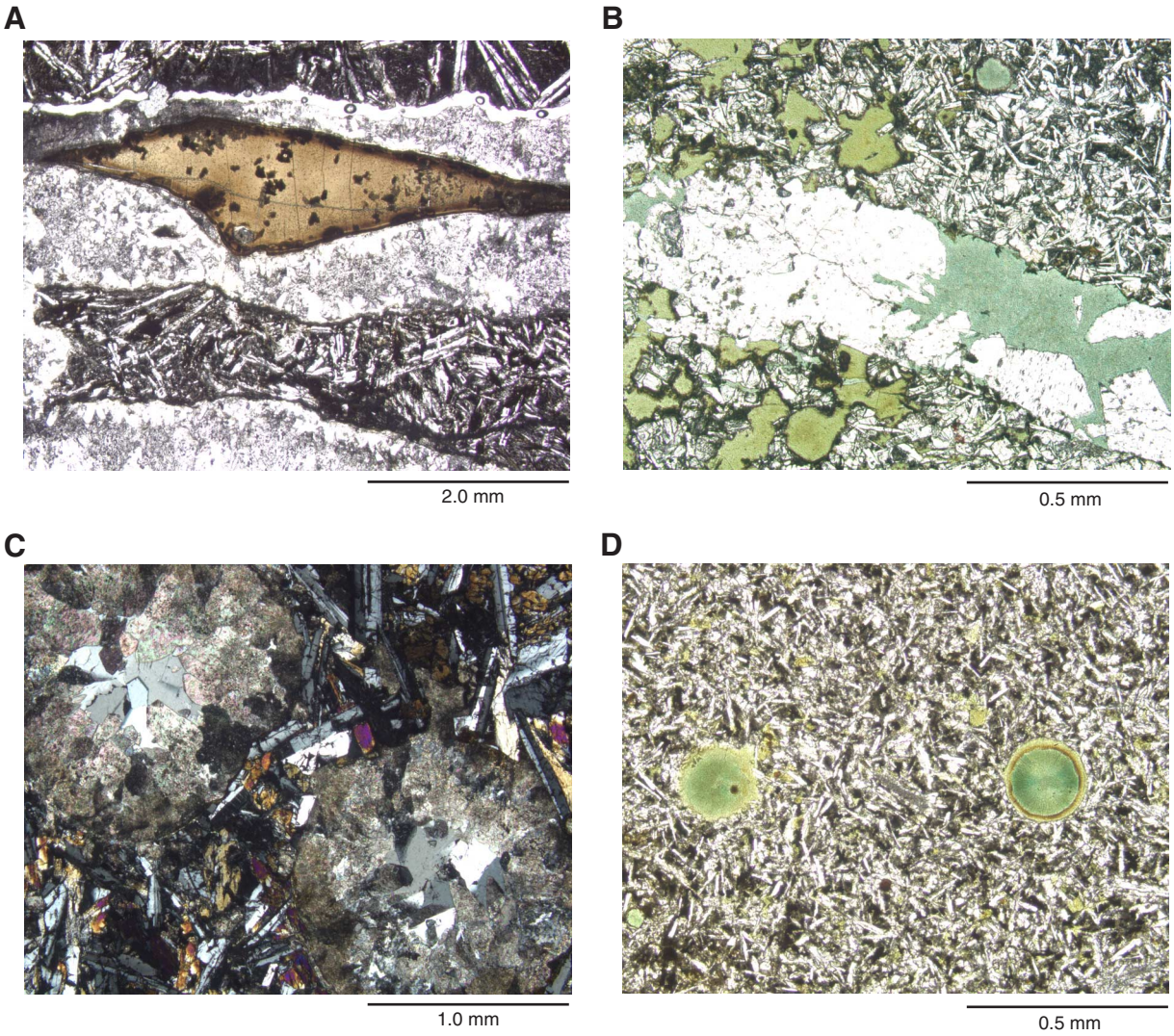

Figure F56. Photomicrographs in plane-polarized light showing secondary minerals in basalts from Hole 1179D. **A.** Vesicles with celadonite and collomorphic FeOOH/hematite (Sample 191-1179D-14R-2 [Piece 15B, 117–119 cm]) (see **"Site 1179 Thin Sections,"** p. 130). **B.** Smectite replacement spots and smectite fissure (Sample 191-1179D-12R-2 [Piece 1A, 1–3 cm]) (see **"Site 1179 Thin Sections,"** p. 120). **C.** Olivine and plagioclase replaced by smectite and/or celadonite + FeOOH (Sample 191-1179D-11R-1 [Piece 4A, 99–101 cm]) (see **"Site 1179 Thin Sections,"** p. 117). **D.** Smectite and celadonite replacing groundmass (Sample 191-1179D-12R-4 [Piece 1D, 83–86 cm]) (see **"Site 1179 Thin Sections,"** p. 124).

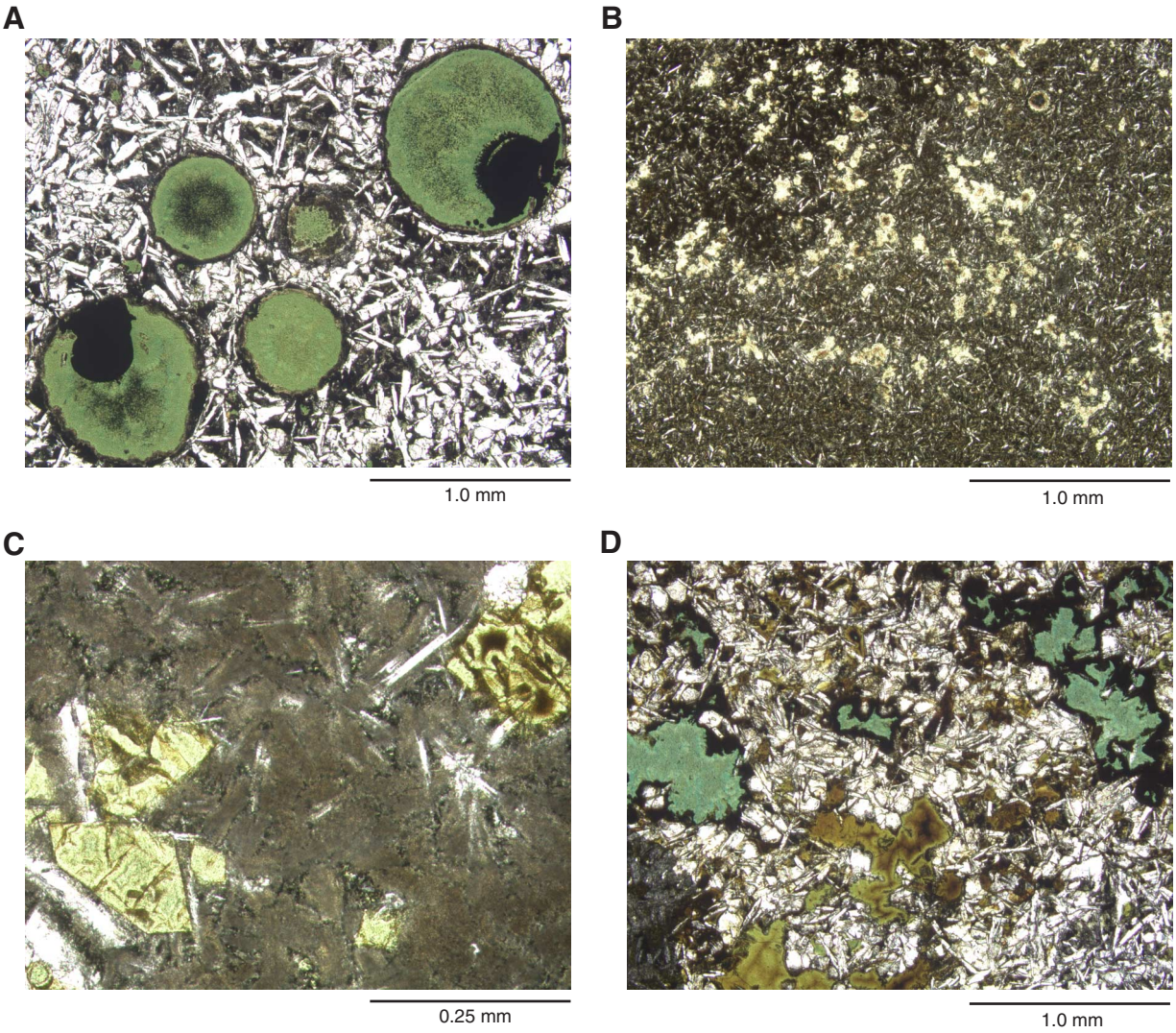

Figure F57. Variations of *P*-wave velocity, bulk density, and porosity with depth. Discrete sample data are shown by open symbols; a 19-point median filter was applied to the MST velocity and GRA density profiles.

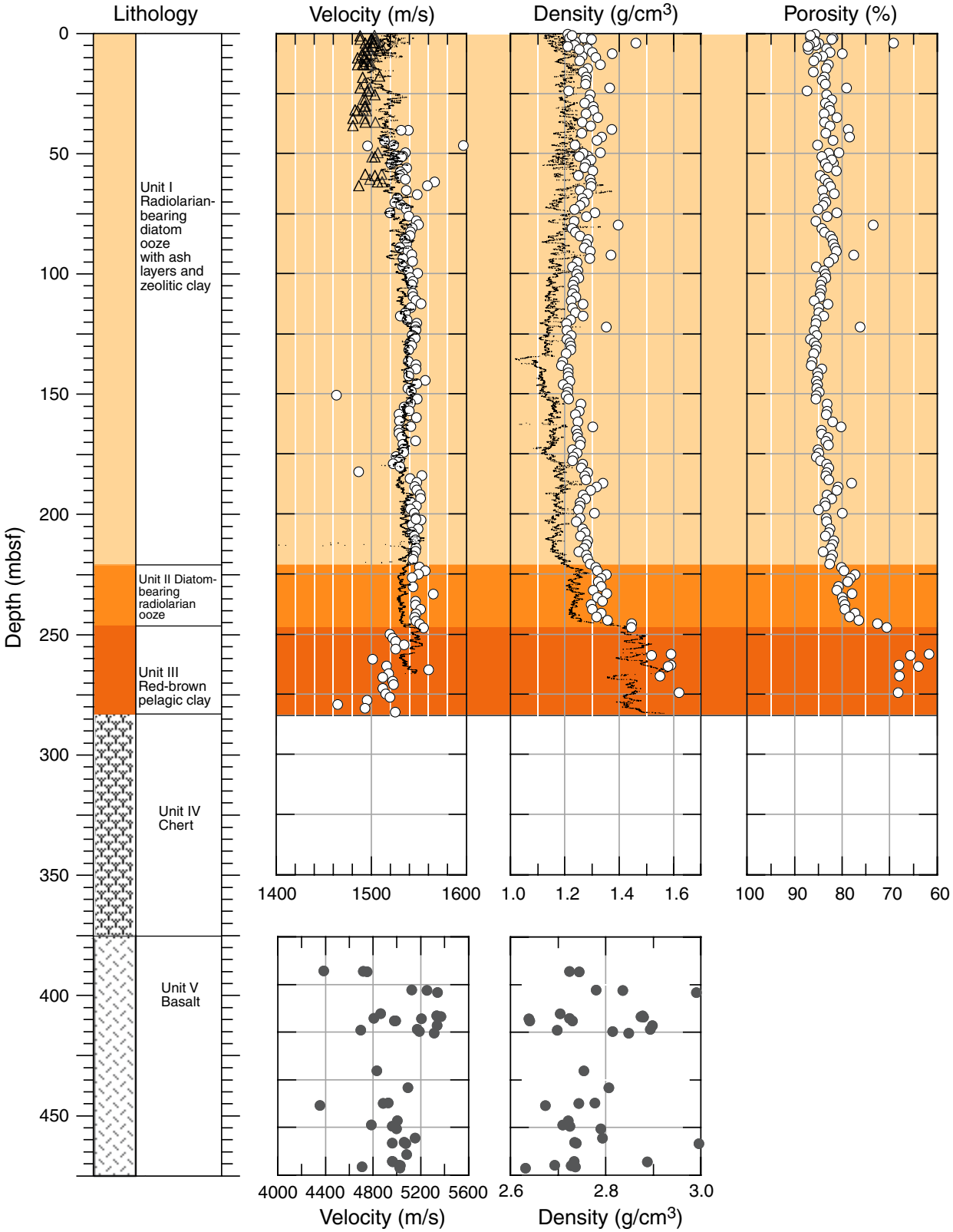

Figure F58. Variations of thermal conductivity, natural gamma radiation (NGR), and magnetic susceptibility (MS) with depth. Discrete sample data are shown by open symbols; a 19-point median filter was applied to the NGR and MS profiles.

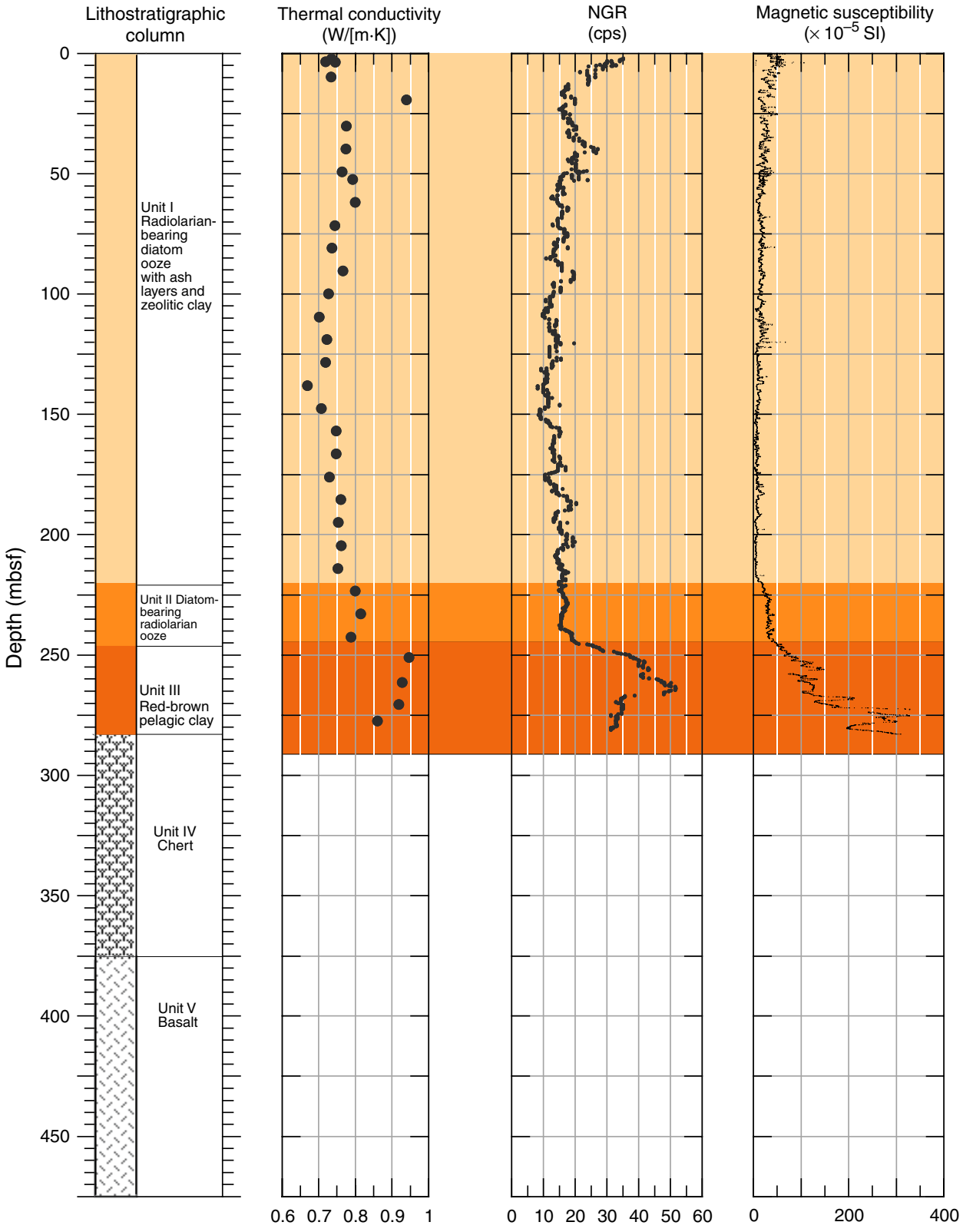

Figure F59. Variation of bulk density with depth in Unit I.

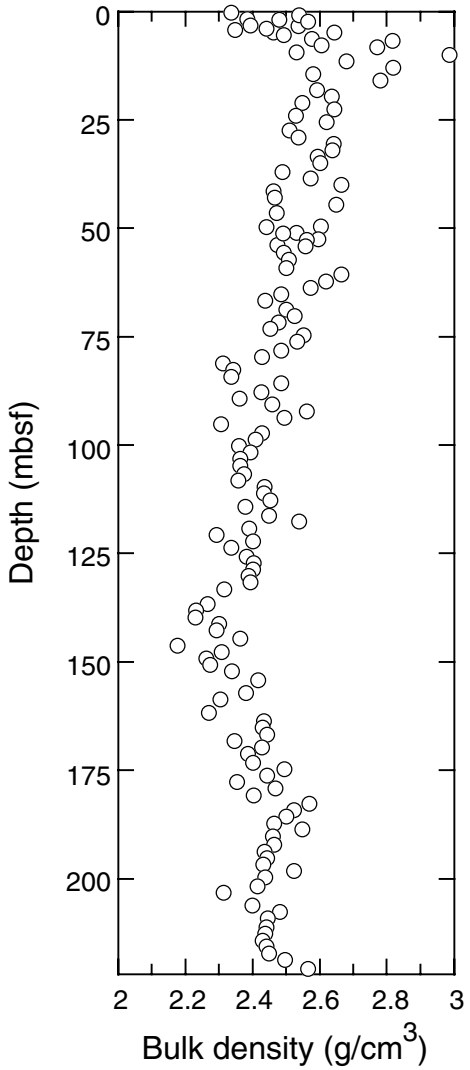

Figure F60. Variation of peak shear strength with depth in Unit I.

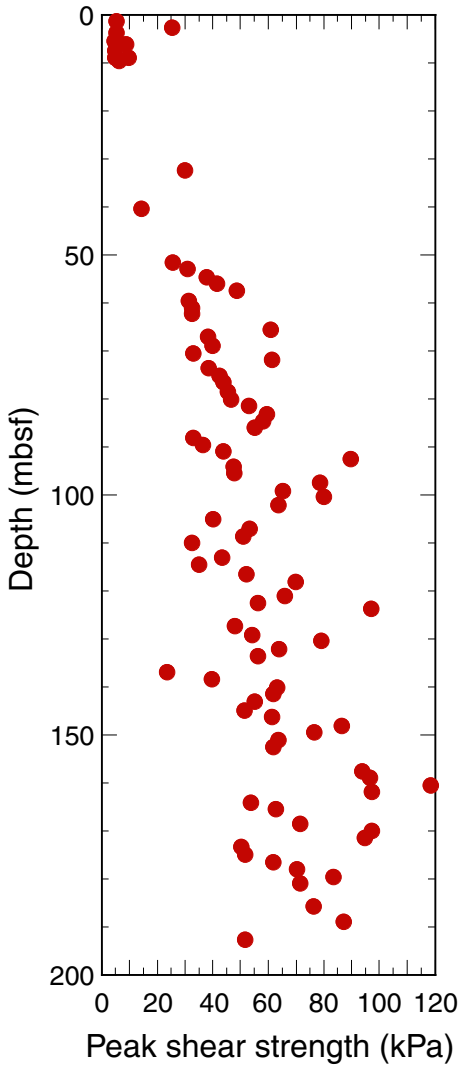

Figure F61. Multichannel seismic profile across Site 1179 (*Hakuho Maru* Cruise KH96-3-1; line 2-1) with one-way traveltime scale used for comparison with calculated reflector depths (see Table **T19,** p. 157).

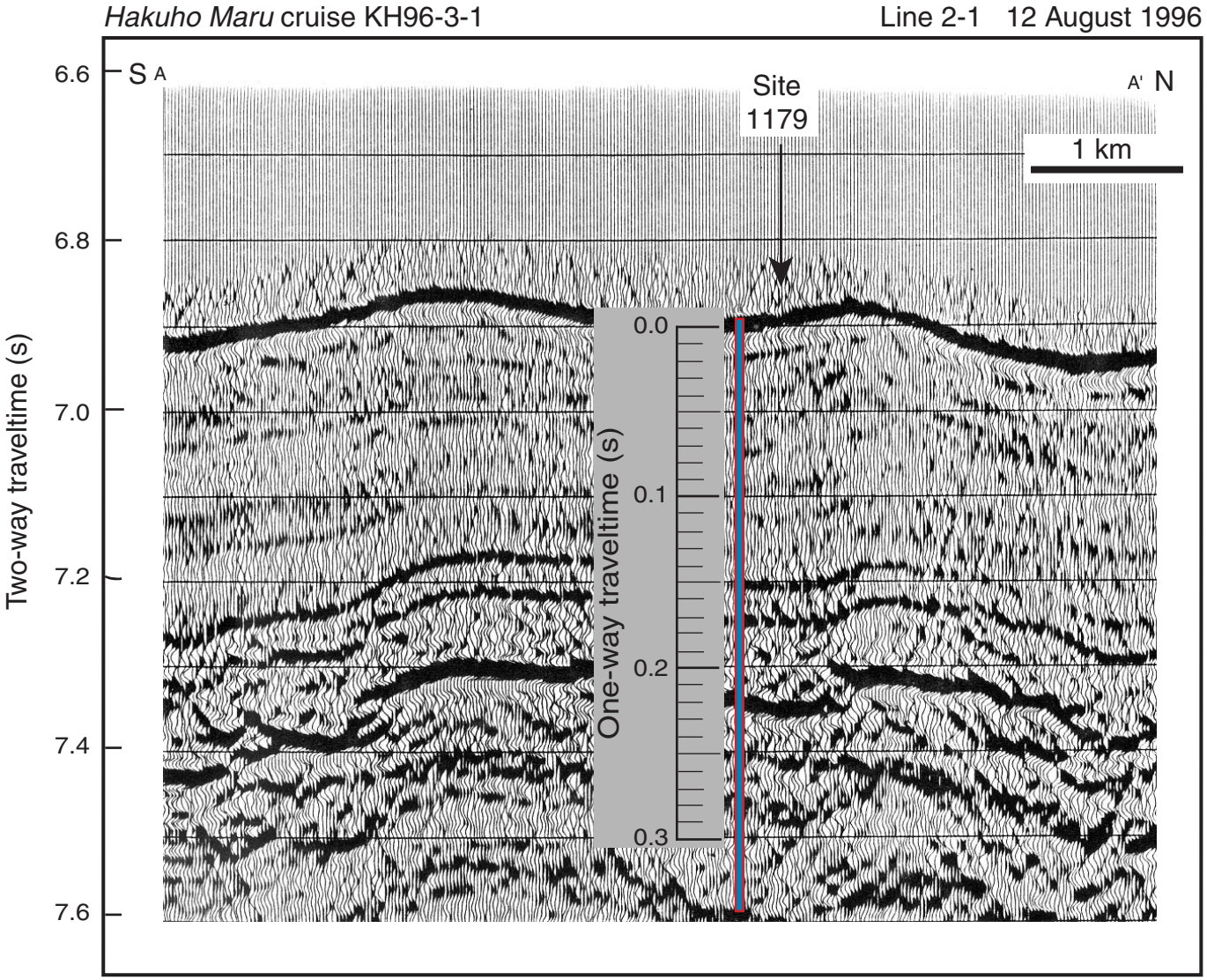

Figure F62. Multichannel seismic profile across Site 1179 (*Hakuho Maru* Cruise KH96-3-1; line 2-4) with one-way traveltime scale used for comparison with calculated reflector depths (see Table **T19,** p. 157).

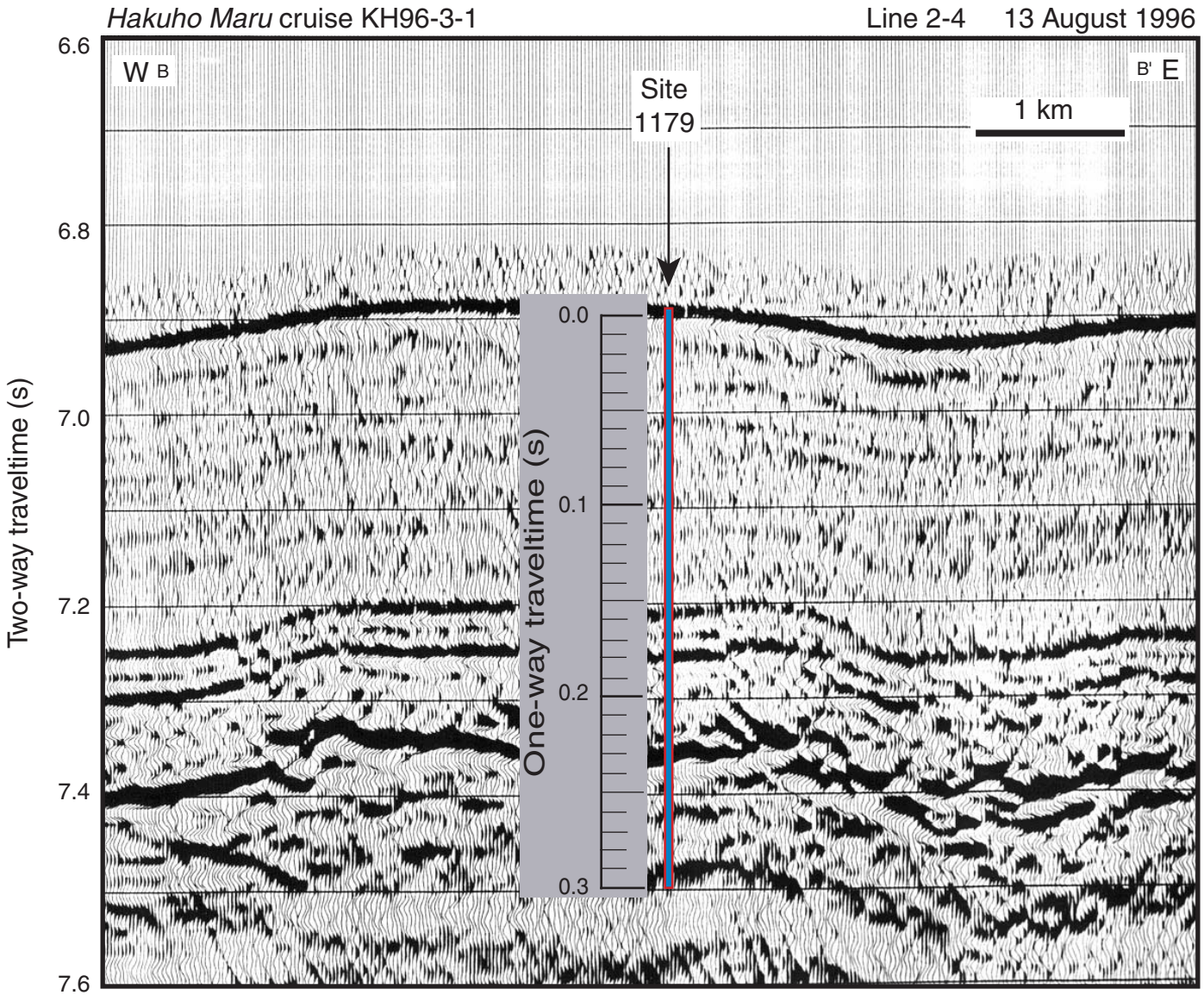

Figure F63. Natural radioactivity measurements in Hole 1179D are shown with caliper data and lithostratigraphic units from Hole 1179C core descriptions. TD = total depth, MGT = multisensor gamma-ray tool, HNGS = hostile environment natural gamma sonde.

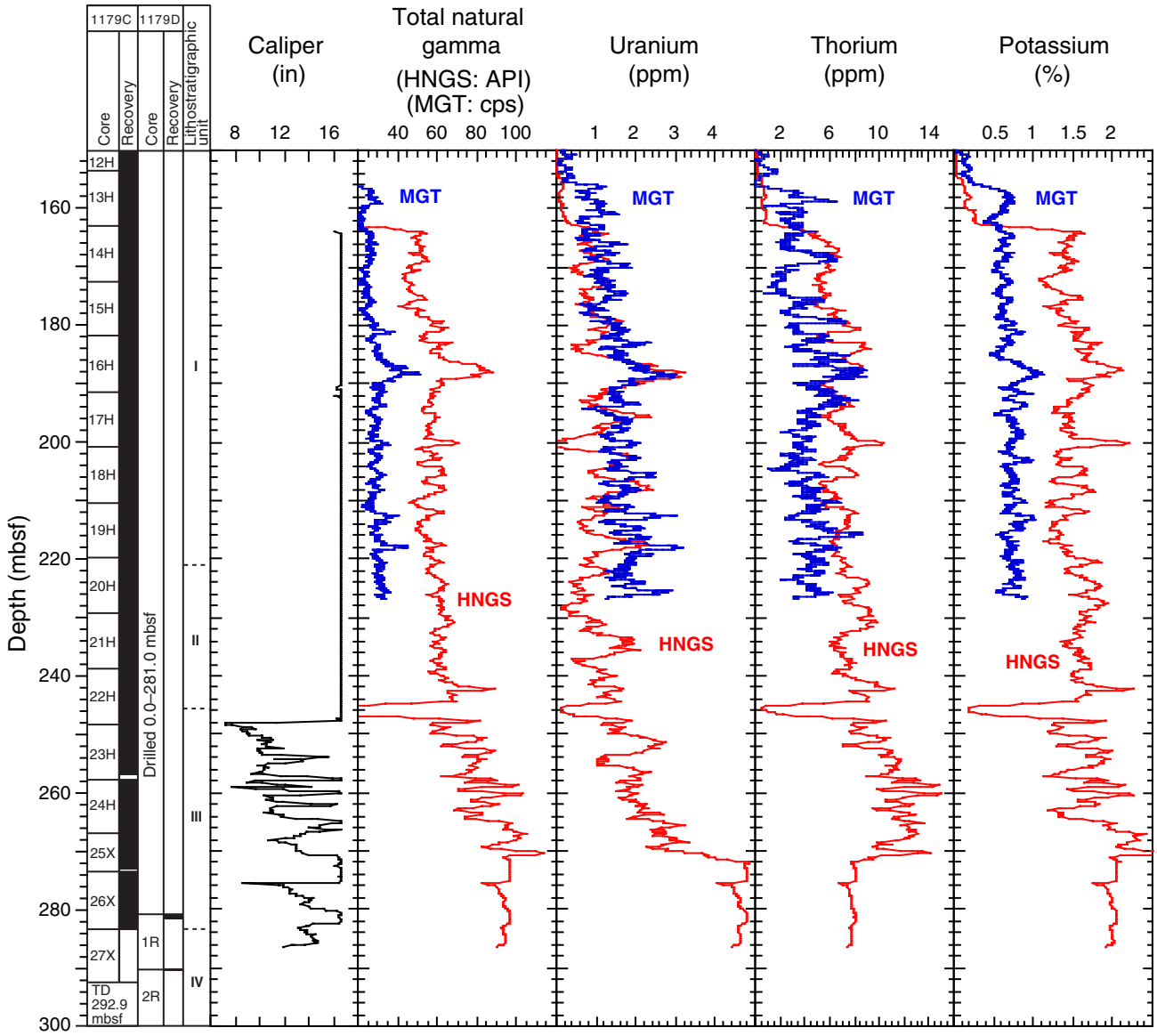

Figure F64. Comparison between the hostile environment natural gamma sonde (HNGS) and the multisensor gamma-ray tool (MGT). For comparison, high-resolution natural gamma radioactivity measurements on cores from Hole 1179C, measured on the MST, are shown at right.

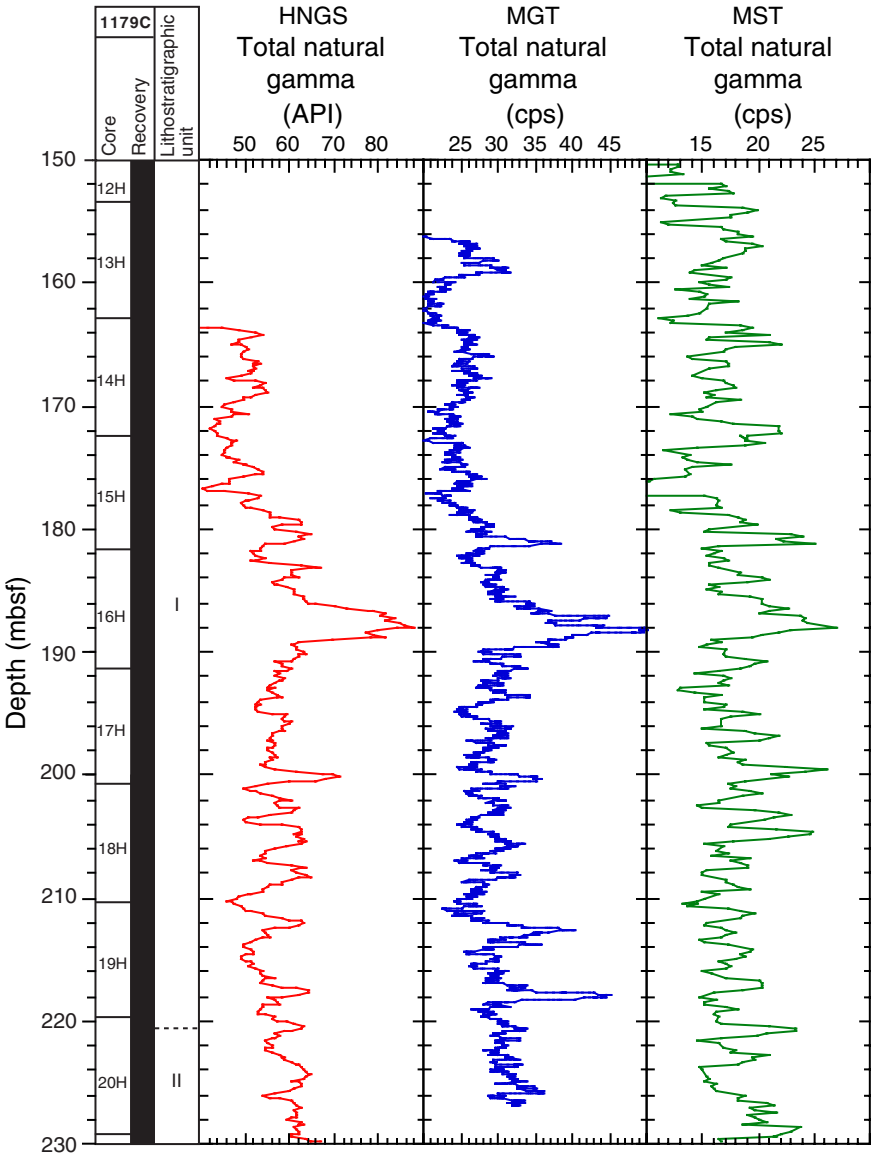

Figure F65. Electrical resistivity measurements in Hole 1179D are shown with caliper data and lithostratigraphic units determined from Hole 1179C core descriptions. The expanded section shows the good correlation between natural radioactivity and resistivity measurements. Both measurements allow the identification of ash layers, which are marked by increases in both resistivity and natural gamma ray. IDPH = deep induction spherically focused resistivity, IMPH = medium induction spherically focused resistivity, SFLU = shallow induction spherically focused resistivity, MST = multisensor track, TD = total depth.

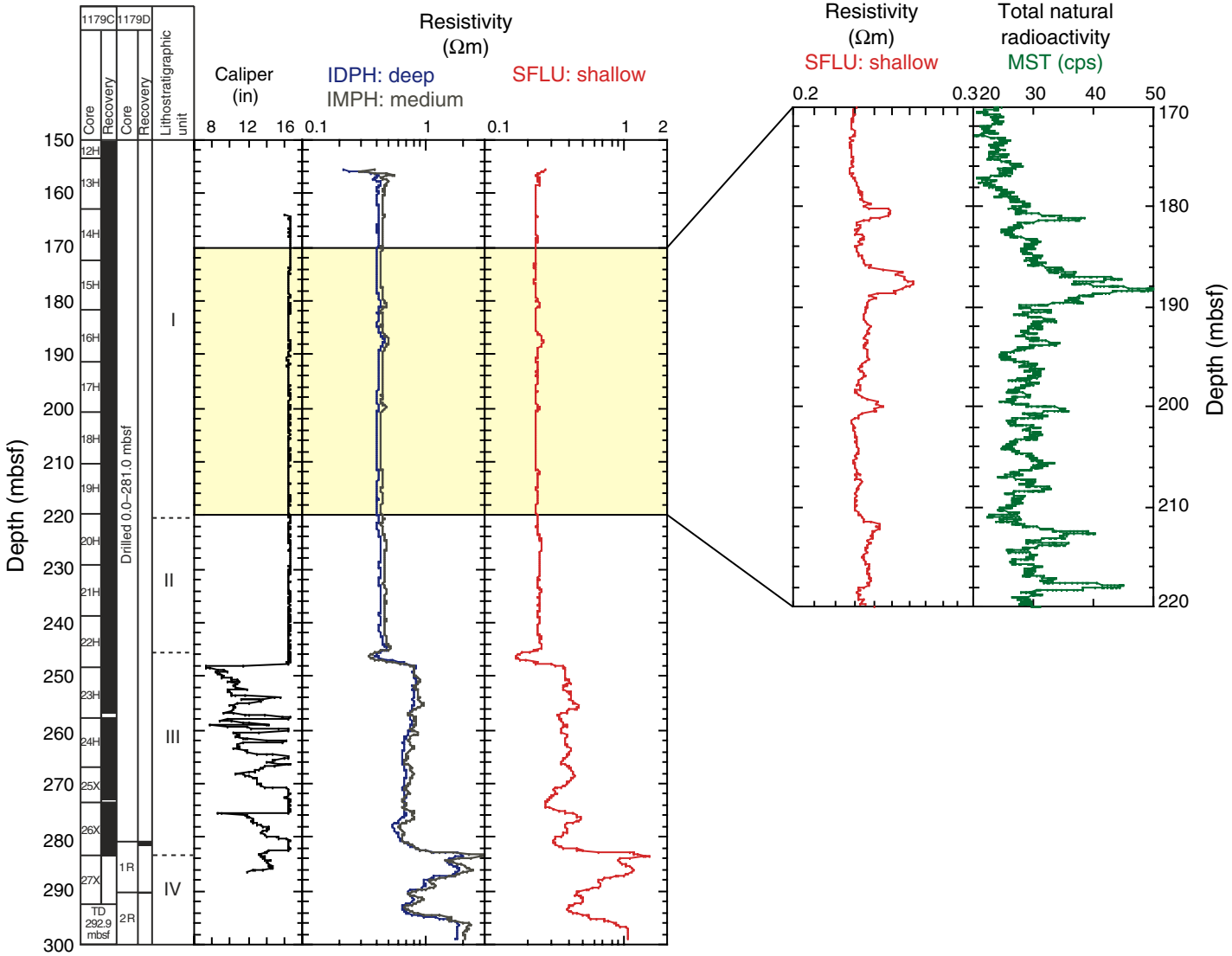

Figure F66. Acceleration along the x- and y-axes, recorded by the drill-string acceleration tool during APC coring in Hole 1179C.

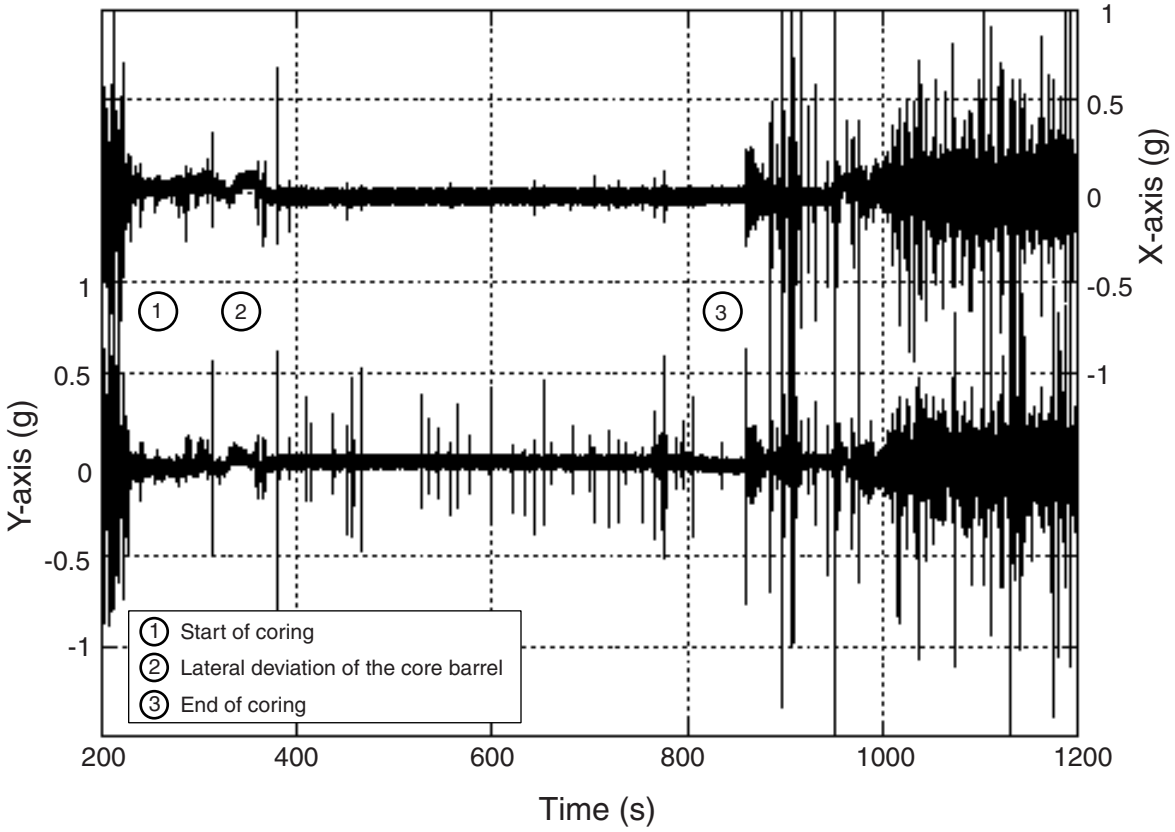

Figure F67. Heave recorded by the drill-string acceleration tool during APC coring in Hole 1179C.

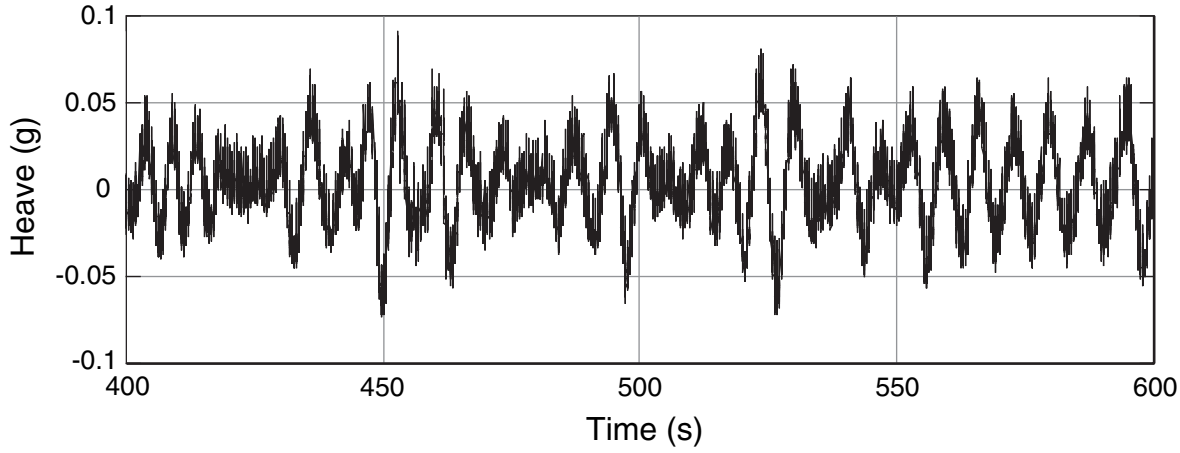

Figure F68. Borehole instrument assembly (BIA) on the rig floor. After preparing and placing the ocean borehole seismometer (OBH) on the BIA frame, the BIA sensor assembly was moved to the rig floor.

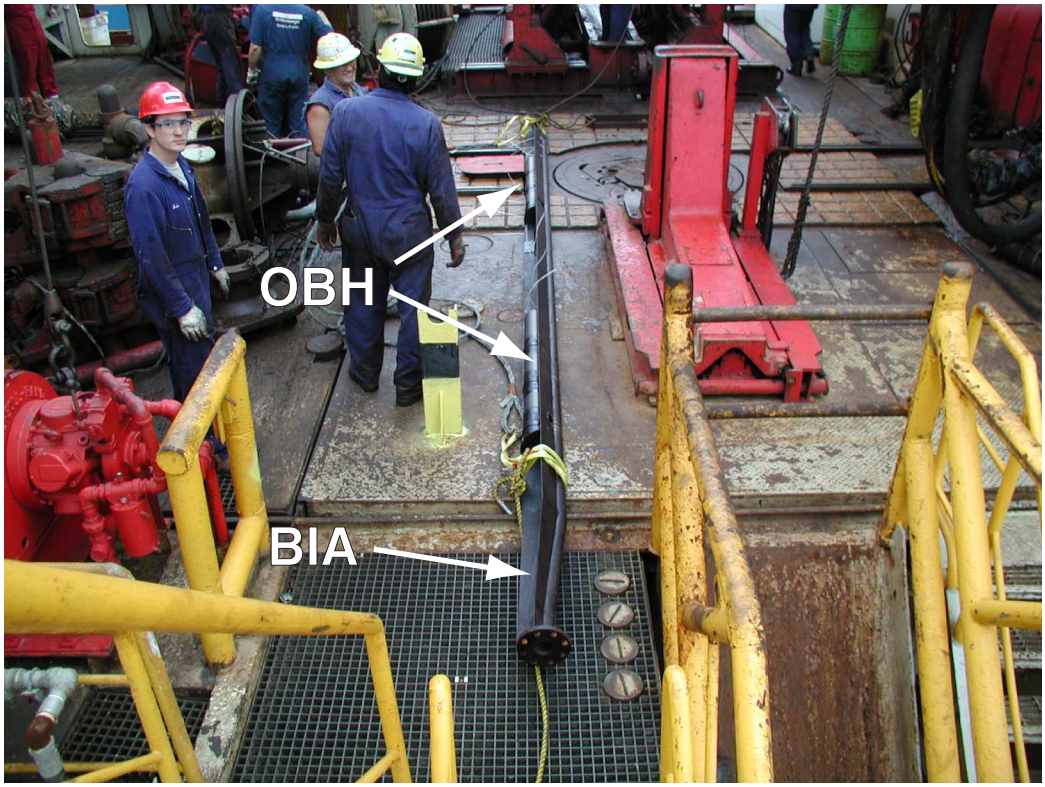

Figure F69. Stinger pipe jointed to the lower end of the borehole instrument assembly (BIA).

Figure F70. Borehole instrument assembly (BIA) in the moonpool area. OBH = ocean borehole seismometer.

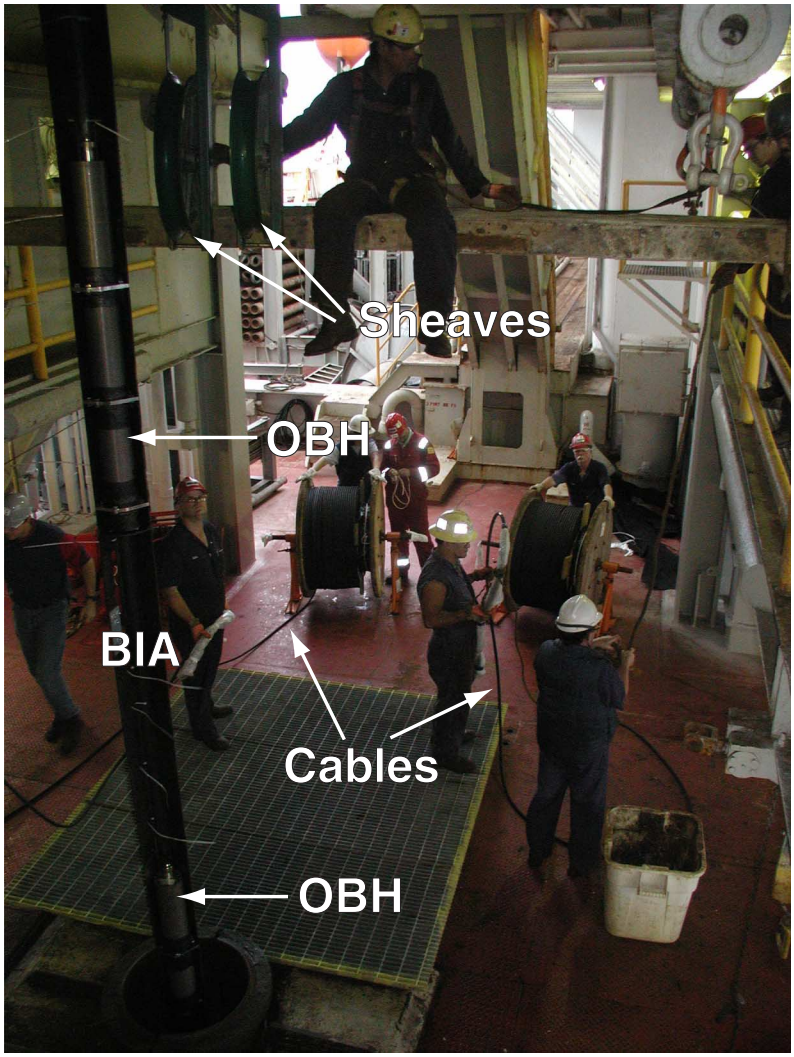

Figure F71. Instrument cable connected to the ocean borehole seismometer (OBH). BIA = borehole instrument assembly.

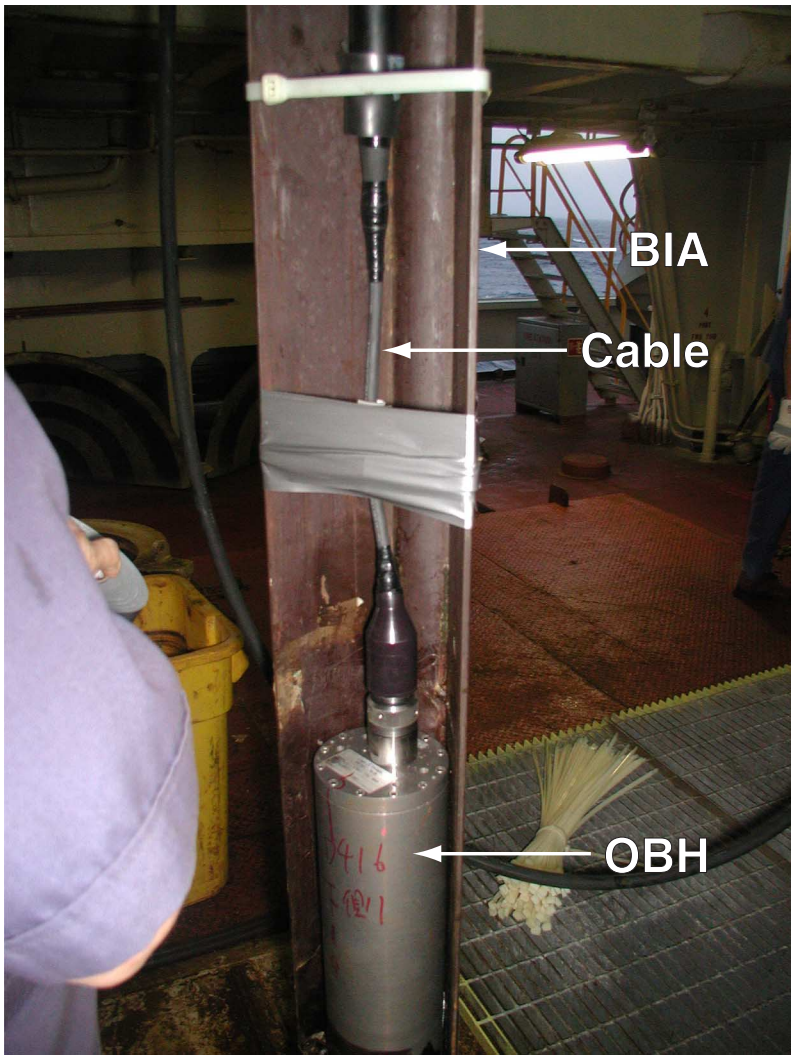

Figure F72. Centralizer attached on the 4.5-in casing pipe. Centralizer spacing is approximately every 1.5 m.

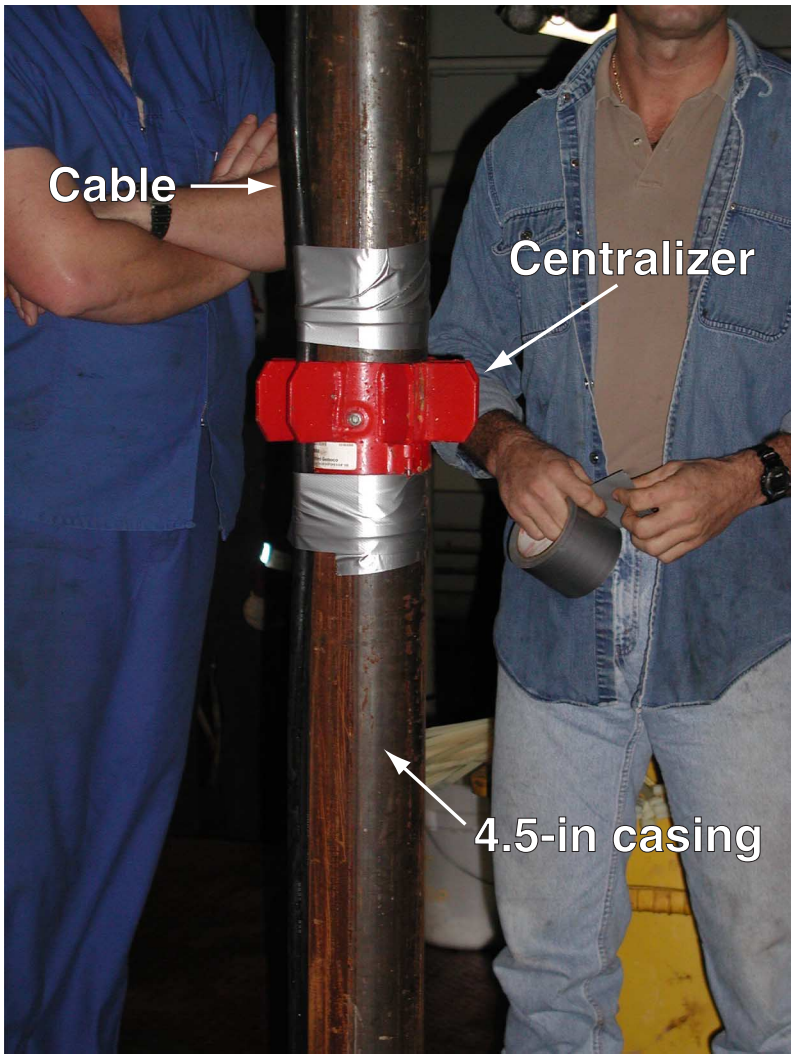

Figure F73. Multiple-access expandable gateway (MEG) frame mounted on the riser/hanger.

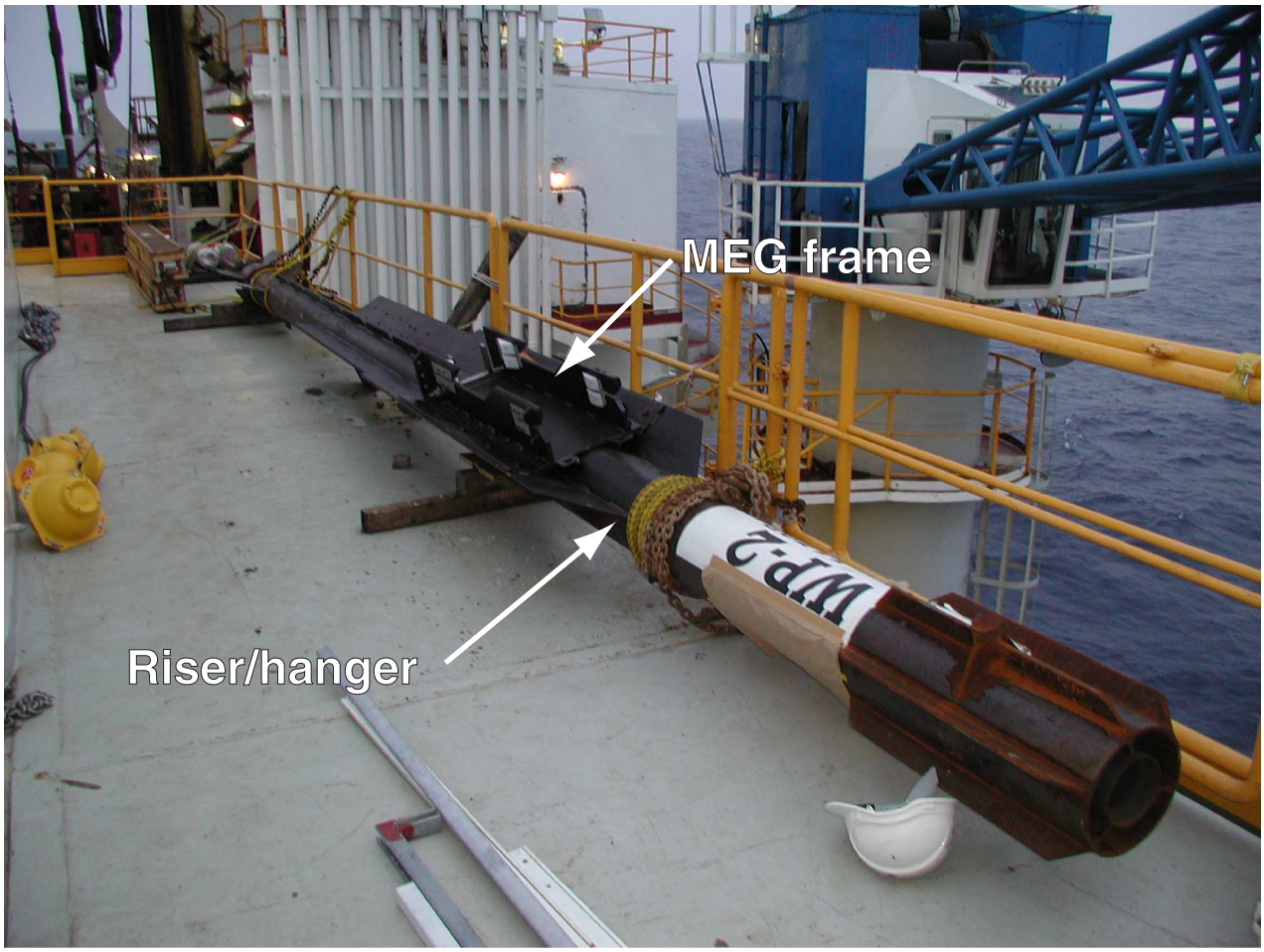

Figure F74. Multiple-access expandable gateway (MEG-191) installed on the MEG frame. Cables were secured to the riser/hanger with tie wraps and stainless steel banding. UMC = underwater mateable connector.

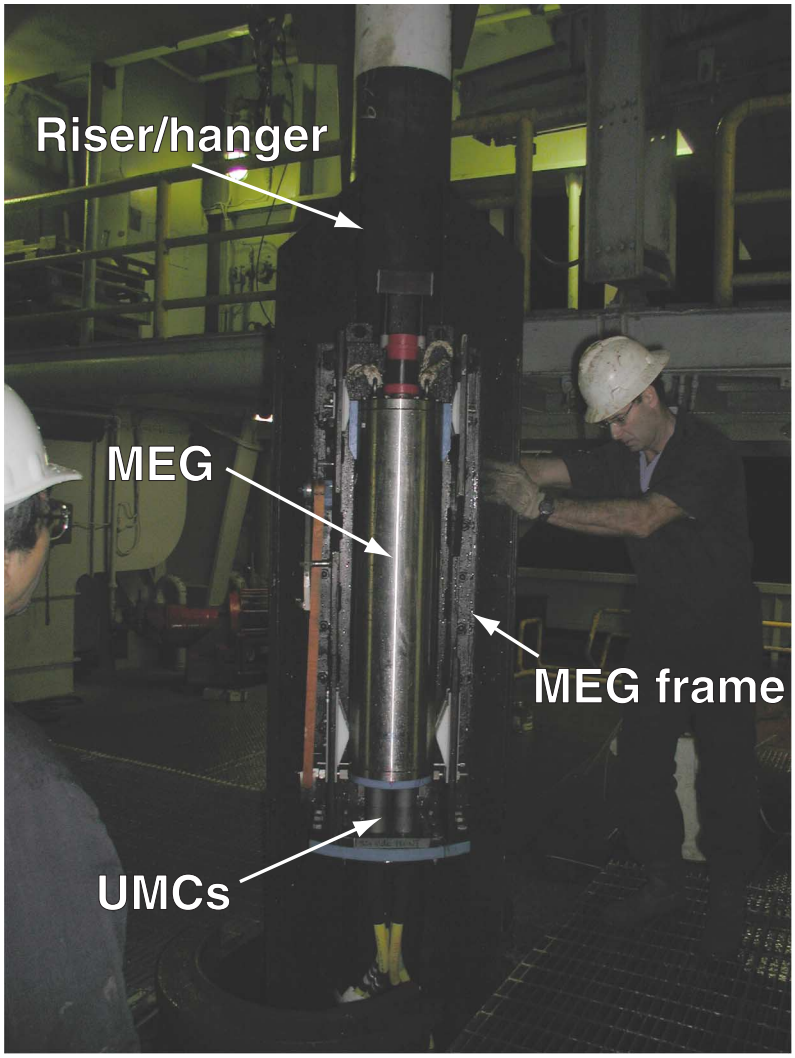

Figure F75. Multiple-access expandable gateway (MEG-191) on the riser/hanger, lowered into the moonpool.

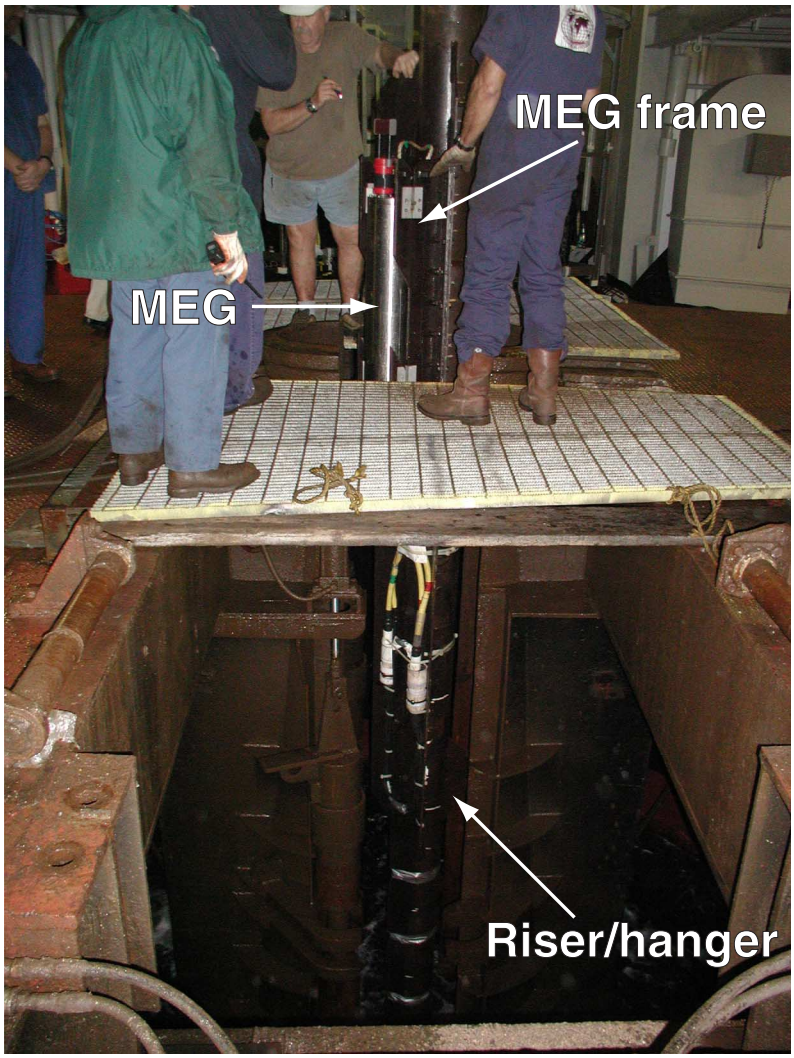

Figure F76. Snapshots from the vibration-isolated television/subsea television camera. BIA = borehole instrument assembly, OBH = ocean borehole seismometer, MEG = multiple-access expandable gateway, PAT = power access terminal. **A.** BIA (OBH sensors), lowered into the borehole. **B.** MEG-191 on the riser/hanger, landed on the reentry cone. **C.** PAT battery frame, landed on the edge of the reentry cone. (**Figure shown on next page.**)

Figure F76 (continued). (Caption shown on previous page.)

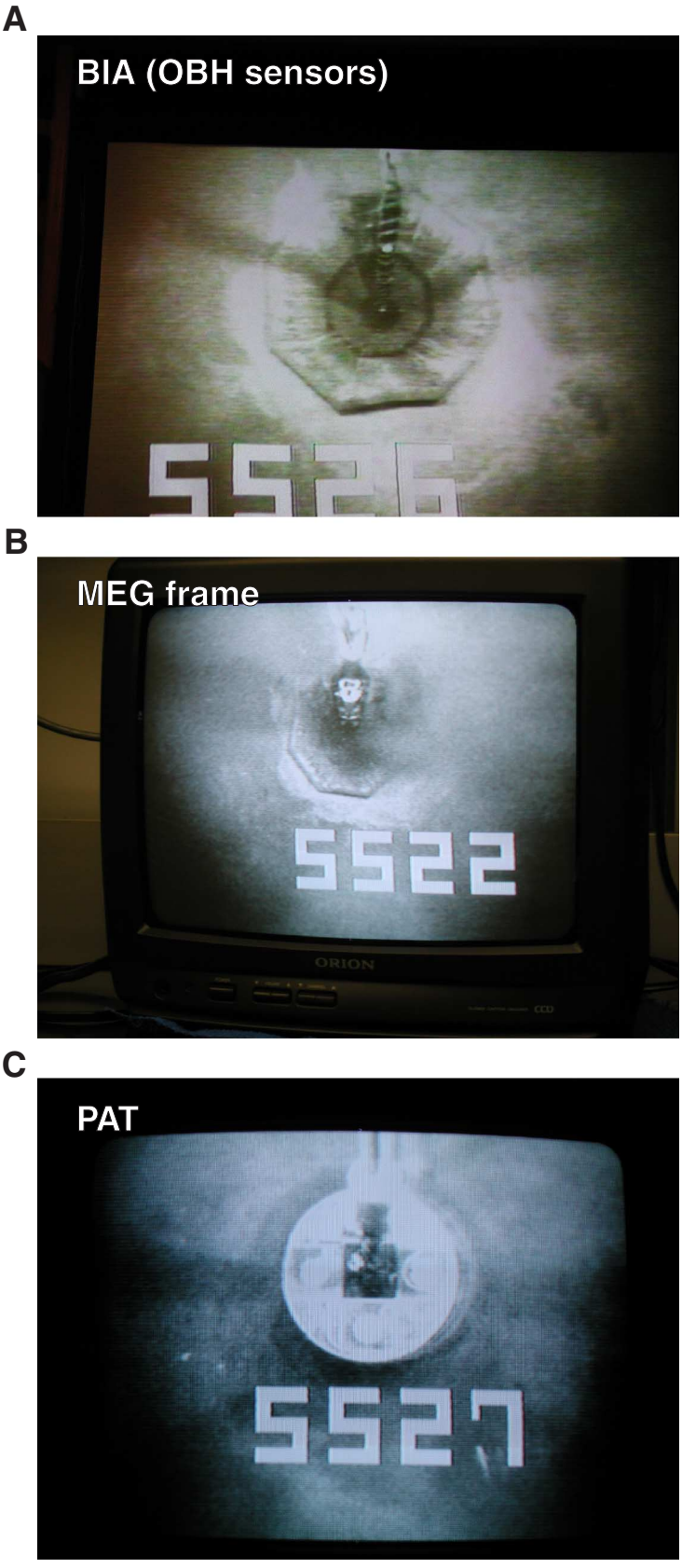

Figure F77. Preparations for the deployment of the power access terminal (PAT) battery frame. The halves of the PAT were positioned around the drill string, bolted, and welded together. Cable connections among all instruments (the seawater battery [SWB] cells, the accumulator, the power control system, the data logger, and the underwater mateable connectors) on the PAT were secured. From Sacks, Suyehiro, Acton, et al., 2000.

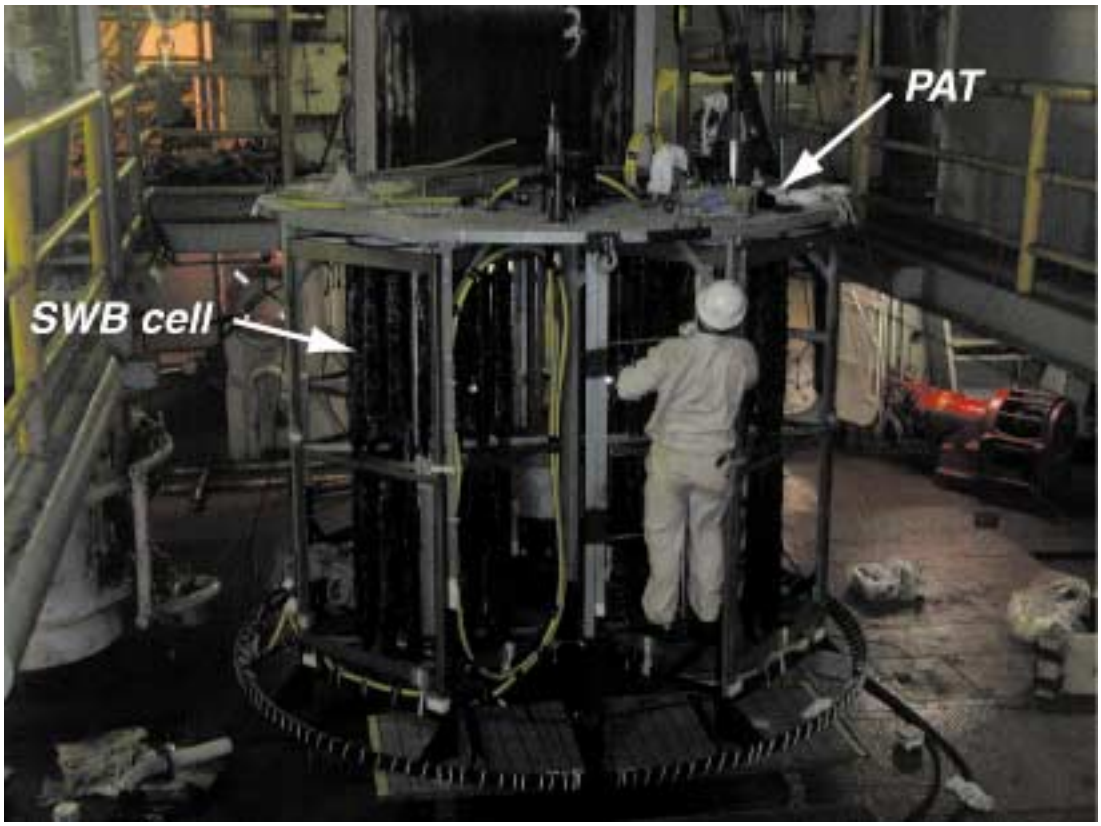

Figure F78. Schematic diagram of the power access terminal bridle assembly.

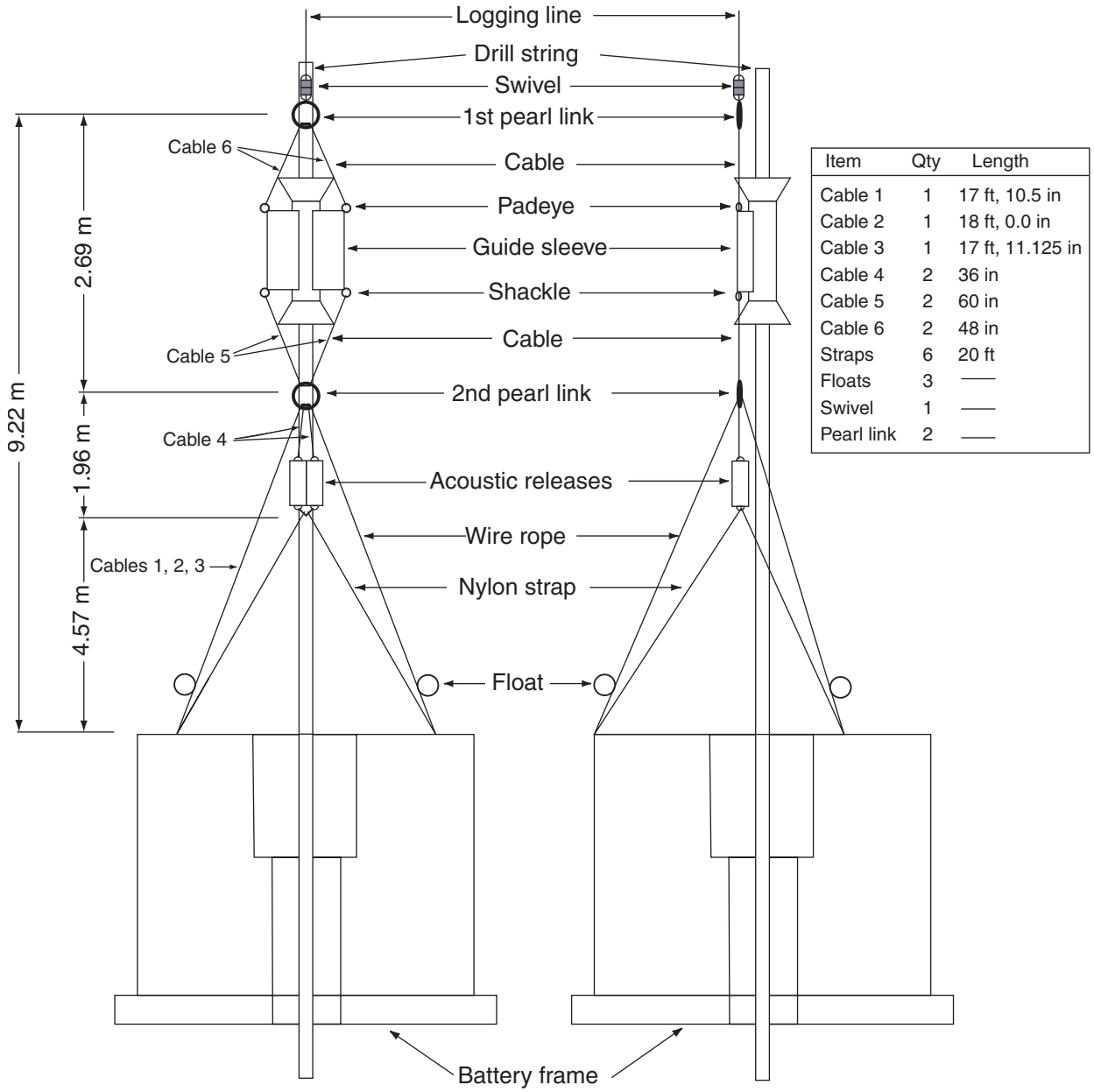

Figure F79. Power access terminal (PAT) battery frame lowered into the sea through the moonpool. The PAT was hung on the logging line with the aid of the PAT bridle assembly that consists of wire cables, nylon straps, three glass balls, and acoustic releasers.

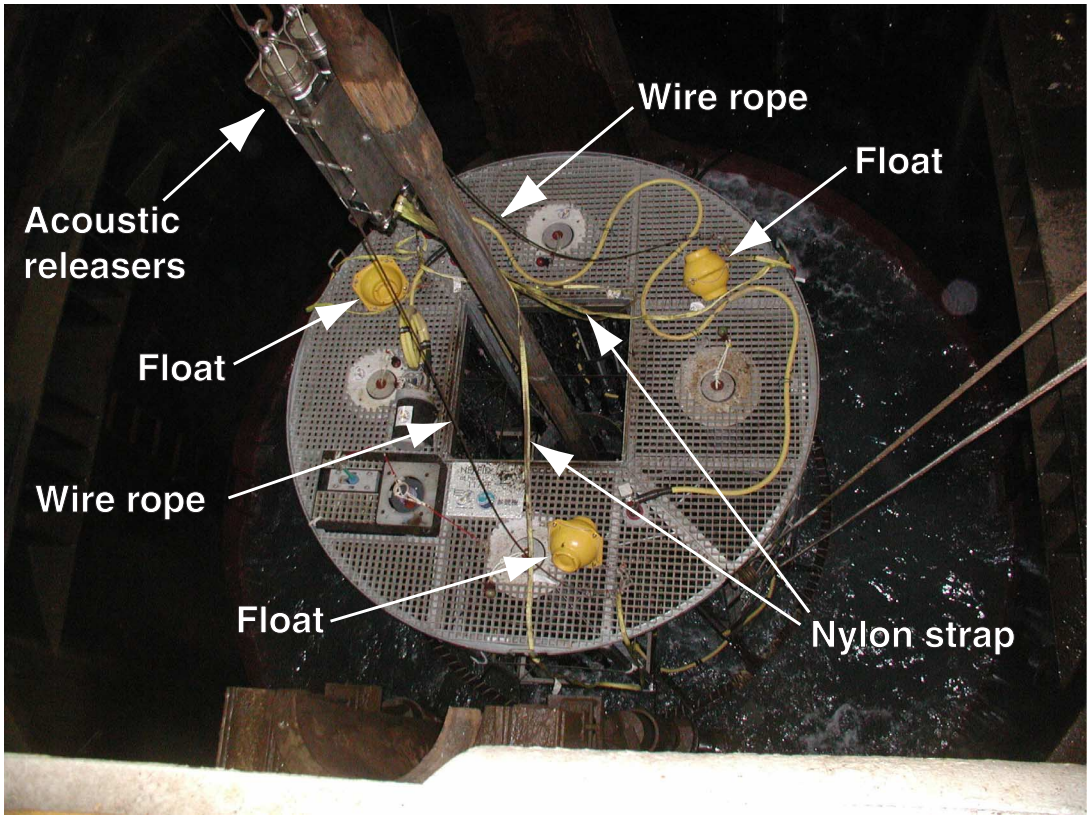

Table T1. Coring summary, Site 1179. (See table note. Continued on next two pages.)

Hole 1179A
Latitude: 41°4.7884′N
Longitude: 159°57.7877′E
Time on site (hr): 730.5 (30 days 10 hr 30 min)
Time on hole (hr): 18 (2215 hr, 25 July–1615 hr, 26 July 2000)
Seafloor (drill-pipe measurement from rig floor, mbrf): 5576.5
Distance between rig floor and sea level (m): 11.0
Water depth (drill-pipe measurement from sea level, m): 5565.5
Total depth (drill-pipe measurement from rig floor, mbrf): 5586.5
Total penetration (meters below seafloor, mbsf): 10.0
Total length of cored section (m): 10.0
Total core recovered (m): 10.02
Core recovery (%): 100.2
Total number of cores: 1

Hole 1179B
Latitude: 41°4.7887′N
Longitude: 159°57.7879′E
Time on hole (hr): 11.75 (1615 hr, 26 July–0400 hr, 27 July 2000)
Seafloor (drill-pipe measurement from rig floor, mbrf): 5574.90
Distance between rig floor and sea level (m): 11.00
Water depth (drill-pipe measurement from sea level, m): 5563.90
Total depth (drill-pipe measurement from rig floor, mbrf): 5630.00
Total penetration (meters below seafloor, mbsf): 55.10
Total length of cored section (m): 55.10
Total length of drilled intervals (m): 0.00
Total core recovered (m): 55.89
Core recovery (%): 101.4
Total number of cores: 6

Hole 1179C
Latitude: 41°4.7871′N
Longitude: 159°57.7856′E
Time on hole (hr): 70.5 (0400 hr, 27 July–0230 hr, 30 July 2000)
Seafloor (drill-pipe measurement from rig floor, mbrf): 5576.7
Distance between rig floor and sea level (m): 12.8
Water depth (drill-pipe measurement from sea level, m): 5563.9
Total depth (drill-pipe measurement from rig floor, mbrf): 5869.6
Total penetration (meters below seafloor, mbsf): 292.9
Total length of cored section (m): 249.9
Total length of drilled intervals (m): 43.0
Total core recovered (m): 246.89
Core recovery (%): 98.8
Total number of cores: 27

Hole 1179D
Latitude: 41°4.8122′N
Longitude: 159°57.7862′E
Time on hole (hr): 177.5 (0230 hr, July 30–1200 hr, 6 August 2000)
Seafloor (drill-pipe measurement from rig floor, mbrf): 5577.0
Distance between rig floor and sea level (m): 11.0
Water depth (drill-pipe measurement from sea level, m): 5566.0
Total depth (drill-pipe measurement from rig floor, mbrf): 6052.0
Total penetration (meters below seafloor, mbsf): 475.0
Total length of cored section (m): 194.0
Total length of drilled intervals (m): 281.0
Total core recovered (m): 50.36
Core recovery (%): 26.0
Total number of cores: 22

Hole 1179E
Latitude: 41°4.7729′N
Longitude: 159°57.7973′E
Time on hole (hr): 362.75 (1200 hr, 6 August–21 August 2000)
Seafloor (drill-pipe measurement from rig floor, mbrf): 5577.0
Distance between rig floor and sea level (m): 11.1
Water depth (drill-pipe measurement from sea level, m): 5565.9
Total depth (drill-pipe measurement from rig floor, mbrf): 5976
Total penetration (meters below seafloor, mbsf): 475.0
Total length of drilled intervals (m): 475.0
Comments: Dedicated hole for seismometer emplacement. No coring.

Table T1 (continued).

Core	Date (2000)	Ship time (local)	Depth (mbsf) Top	Depth (mbsf) Bottom	Length (m) Cored	Length (m) Recovered	Recovery (%)
191-1179A-							
1H	26 July	1615	0.0	10.0	10.0	10.02	100.2
				Total:	10.0	10.02	100.2
191-1179B-							
1H	26 July	1745	0.0	7.6	7.6	7.53	99.1
2H	26 July	1900	7.6	17.1	9.5	9.14	96.2
3H	26 July	2020	17.1	26.6	9.5	10.04	105.7
4H	26 July	2200	26.6	36.1	9.5	9.46	99.6
5H	26 July	2340	36.1	45.6	9.5	10.07	106.0
6H	26 July	0110	45.6	55.1	9.5	9.65	101.6
				Totals:	55.1	55.89	101.4
191-1179C-							
1H	27 July	1435	0.0	5.8	5.8	5.83	100.5
			*****Drilled from 5.8 to 48.8 mbsf*****				
2H	27 July	1615	48.8	58.3	9.5	10.02	105.5
3H	27 July	1845	58.3	67.8	9.5	9.56	100.6
4H	27 July	2025	67.8	77.3	9.5	10.11	106.4
5H	27 July	2145	77.3	86.8	9.5	9.78	103.0
6H	27 July	2320	86.8	96.3	9.5	10.06	105.9
7H	28 July	0100	96.3	105.8	9.5	9.62	101.3
8H	28 July	0245	105.8	115.3	9.5	10.01	105.4
9H	28 July	0445	115.3	124.8	9.5	9.25	97.4
10H	28 July	0610	124.8	134.3	9.5	9.84	103.6
11H	28 July	0900	134.3	143.8	9.5	9.62	101.3
12H	28 July	1105	143.8	153.3	9.5	10.17	107.1
13H	28 July	1310	153.3	162.8	9.5	9.65	101.6
14H	28 July	1430	162.8	172.3	9.5	10.12	106.5
15H	28 July	1545	172.3	181.8	9.5	9.66	101.7
16H	28 July	1705	181.8	191.3	9.5	10.04	105.7
17H	28 July	1850	191.3	200.8	9.5	9.82	103.4
18H	28 July	2015	200.8	210.3	9.5	9.96	104.8
19H	28 July	2145	210.3	219.8	9.5	9.60	101.1
20H	28 July	2310	219.8	229.3	9.5	9.97	105.0
21H	29 July	0050	229.3	238.8	9.5	9.71	102.2
22H	29 July	0225	238.8	248.3	9.5	10.12	106.5
23H	29 July	0410	248.3	257.8	9.5	8.73	91.9
24H	29 July	0535	257.8	266.8	9.0	9.17	101.9
25X	29 July	0755	266.8	273.7	6.9	6.44	93.3
26X	29 July	0930	273.7	283.3	9.6	9.83	102.4
27X	29 July	1135	283.3	292.9	9.6	0.20	2.1
				Coring totals:	249.9	246.89	98.8
				Drilled totals:	43.0		
				Total:	292.9		
191-1179D-							
			*****Drilled from 0 to 281.0 mbsf*****				
1R	31 July	0950	281.0	290.6	9.6	0.98	10.2
2R	32 July	1130	290.6	300.2	9.6	0.19	2.0
3R	33 July	1425	300.2	309.8	9.6	0.26	2.7
4R	34 July	1655	309.8	319.4	9.6	0.99	10.3
5R	35 July	2015	319.4	329.0	9.6	0.57	5.9
6R	36 July	2235	329.0	338.6	9.6	0.82	8.5
7R	1 Aug	0110	338.6	348.2	9.6	1.10	11.5
8R	1 Aug	0325	348.2	357.9	9.7	0.25	2.6
9R	1 Aug	0625	357.9	367.5	9.6	0.65	6.8
10R	1 Aug	0930	367.5	377.1	9.6	1.09	11.4
11R	1 Aug	1410	377.1	386.7	9.6	2.53	26.4
12R	1 Aug	2045	386.7	390.4	3.7	4.58	123.8
13R	2 Aug	0305	390.4	396.4	6.0	5.00	83.3
14R	2 Aug	0955	396.4	406.0	9.6	3.85	40.1
15R	2 Aug	1515	406.0	415.7	9.7	0.19	2.0
16R	2 Aug	2115	415.7	418.8	3.1	0.18	5.8
17R	3 Aug	0425	418.8	425.3	6.5	2.67	41.1
18R	3 Aug	1040	425.3	434.9	9.6	4.69	48.9
19R	3 Aug	1830	434.9	444.6	9.7	3.36	34.6
20R	4 Aug	0420	444.6	454.2	9.6	5.20	54.2
21R	4 Aug	1140	454.2	463.8	9.6	4.79	49.9
22R	4 Aug	2140	463.8	475.0	11.2	6.42	57.3

Table T1 (continued).

Core	Date (2000)	Ship time (local)	Depth (mbsf) Top	Depth (mbsf) Bottom	Length (m) Cored	Length (m) Recovered	Recovery (%)
				Coring totals:	194.0	50.36	26.0
				Drilled totals:	281.0		
				Total:	475.0		

Note: This table is also available in **ASCII format.**

Table T2. Carbon and elemental analyses of Site 1179 sediments. (See table notes. Continued on next page.)

Core, section, interval (cm)	Depth (mbsf)	IC (wt%)	$CaCO_3$ (wt%)	TC (wt%)	OC (wt%)	N (wt%)	S (wt%)	H (mg HC/g)
191-1179B-								
1H-1, 5-10	0.05	0.00	0.05	0.52	0.52	0.08	0.31	1.19
1H-1, 10-16	0.10	0.00	0.06	0.43	0.43	0.07	0.22	1.04
1H-1, 20-25	0.20	0.00	0.08	0.41	0.41	0.06	0.18	1.01
1H-1, 45-50	0.45	0.01	0.09	0.47	0.46	0.05	0.11	0.74
1H-1, 70-75	0.70	0.06	0.52	0.58	0.51	0.07	0.13	0.91
1H-1, 95-100	0.95	0.05	0.42	0.63	0.58	0.07	0.17	0.93
1H-2, 49-50	1.99	0.08	0.69	NA	NA	NA	NA	NA
1H-3, 95-100	3.95	0.10	0.90	0.47	0.36	0.06	0.17	0.82
1H-4, 3-8	4.53	0.06	0.52	0.08	0.01	0.01	0.04	0.46
1H-4, 145-150	5.95	0.08	0.73	0.31	0.23	0.05	0.14	0.94
1H-5, 45-50	6.45	0.09	0.80	0.29	0.19	0.04	0.15	1.04
1H-5, 49-50	6.49	0.00	0.08	NA	NA	NA	NA	NA
2H-2, 49-50	9.59	0.01	0.09	NA	NA	NA	NA	NA
2H-3, 145-150	12.05	0.12	1.06	0.43	0.31	0.05	0.19	1.06
2H-5, 52-53	14.12	0.01	0.09	NA	NA	NA	NA	NA
3H-2, 49-50	19.09	0.11	0.94	NA	NA	NA	NA	NA
3H-3, 145-150	21.55	0.08	0.69	0.22	0.14	0.03	0.20	1.05
3H-5, 49-50	23.59	0.04	0.37	NA	NA	NA	NA	NA
4H-2, 49-50	28.59	0.08	0.67	NA	NA	NA	NA	NA
4H-3, 145-150	31.05	0.07	0.66	0.31	0.23	0.04	0.14	0.92
4H-5, 3-4	32.63	0.19	1.62	NA	NA	NA	NA	NA
5H-2, 49-50	38.09	0.01	0.13	NA	NA	NA	NA	NA
5H-3, 145-150	40.55	0.19	1.62	0.42	0.22	0.03	0.08	0.79
5H-5, 78-79	42.88	0.02	0.19	NA	NA	NA	NA	NA
6H-1, 98-99	46.58	0.01	0.12	NA	NA	NA	NA	NA
6H-3, 145-150	50.05	0.07	0.62	NA	NA	NA	NA	NA
6H-5, 96-97	52.56	0.04	0.35	NA	NA	NA	NA	NA
191-1179C-								
1H-3, 145-150	4.45	0.09	0.75	0.40	0.31	0.05	0.21	0.86
2H-2, 99-100	51.29	0.02	0.20	NA	NA	NA	NA	NA
2H-5, 99-100	55.79	0.02	0.18	NA	NA	NA	NA	NA
3H-2, 99-100	60.79	2.48	20.70	NA	NA	NA	NA	NA
3H-3, 145-150	62.75	0.08	0.74	0.30	0.21	0.03	0.08	0.80
3H-6, 99-100	66.79	0.01	0.16	NA	NA	NA	NA	NA
4H-1, 99-100	68.79	0.24	2.02	NA	NA	NA	NA	NA
4H-3, 145-150	72.25	0.06	0.52	0.14	0.07	0.02	0.09	0.75
4H-5, 99-100	74.79	0.05	0.42	NA	NA	NA	NA	NA
5H-2, 99-100	79.79	0.01	0.09	NA	NA	NA	NA	NA
5H-3, 145-150	81.75	0.11	0.98	0.57	0.45	0.06	0.18	0.91
5H-5, 99-100	84.29	0.02	0.24	NA	NA	NA	NA	NA
6H-2, 99-100	89.29	0.04	0.41	NA	NA	NA	NA	NA
6H-3, 145-150	91.25	0.05	0.49	0.22	0.16	0.01	0.48	0.68
6H-5, 99-100	93.79	0.17	1.46	NA	NA	NA	NA	NA
7H-2, 99-100	98.79	0.02	0.24	NA	NA	NA	NA	NA
7H-3, 145-150	100.75	0.06	0.51	0.18	0.12	0.03	0.16	0.98
7H-5, 99-100	103.29	0.01	0.16	NA	NA	NA	NA	NA
8H-2, 101-102	108.31	0.02	0.20	NA	NA	NA	NA	NA
8H-3, 145-150	110.25	0.06	0.56	0.22	0.15	0.02	0.12	0.91
8H-4, 99-100	111.29	0.02	0.17	NA	NA	NA	NA	NA
9H-2, 99-100	117.79	1.75	14.60	NA	NA	NA	NA	NA
9H-5, 99-100	122.29	0.00	0.05	NA	NA	NA	NA	NA
10H-2, 99-100	127.29	0.01	0.13	NA	NA	NA	NA	NA
10H-5, 99-100	131.79	0.01	0.13	NA	NA	NA	NA	NA
11H-2, 99-100	136.79	0.01	0.15	NA	NA	NA	NA	NA
11H-3, 142-148	138.72	0.07	0.63	0.40	0.33	0.03	0.21	1.13
11H-5, 99-100	141.29	0.09	0.78	NA	NA	NA	NA	NA
12H-2, 99-100	146.29	0.01	0.12	NA	NA	NA	NA	NA
12H-5, 99-100	150.79	0.01	0.15	NA	NA	NA	NA	NA
13H-3, 99-100	157.29	0.01	0.14	NA	NA	NA	NA	NA
13H-6, 99-100	161.79	0.02	0.19	NA	NA	NA	NA	NA
14H-2, 99-100	165.29	0.02	0.18	NA	NA	NA	NA	NA
14H-3, 142-148	167.22	0.07	0.63	0.38	0.30	0.05	0.17	0.98
14H-6, 99-100	171.29	0.01	0.16	NA	NA	NA	NA	NA
15H-2, 99-100	174.79	0.01	0.11	NA	NA	NA	NA	NA
15H-5, 99-100	179.29	0.01	0.09	NA	NA	NA	NA	NA
16H-2, 99-100	184.29	0.01	0.10	NA	NA	NA	NA	NA

Table T2 (continued).

Core, section, interval (cm)	Depth (mbsf)	IC (wt%)	$CaCO_3$ (wt%)	TC (wt%)	OC (wt%)	N (wt%)	S (wt%)	H (mg HC/g)
16H-5, 99-100	188.79	0.16	1.35	NA	NA	NA	NA	NA
17H-2, 99-100	193.79	0.01	0.09	NA	NA	NA	NA	NA
17H-3, 145-150	195.75	0.05	0.49	0.17	0.11	0.04	0.13	1.06
17H-4, 99-100	196.79	0.01	0.14	NA	NA	NA	NA	NA
18H-2, 99-100	203.29	0.06	0.57	NA	NA	NA	NA	NA
18H-5, 99-100	207.79	0.01	0.14	NA	NA	NA	NA	NA
19H-2, 99-100	212.79	0.02	0.18	NA	NA	NA	NA	NA
19H-5, 99-100	217.29	0.01	0.15	NA	NA	NA	NA	NA
20H-2, 99-100	222.29	0.01	0.14	NA	NA	NA	NA	NA
20H-3, 145-150	224.25	0.05	0.45	0.09	0.04	0.03	0.09	0.94
20H-5, 99-100	226.79	0.01	0.13	NA	NA	NA	NA	NA
21H-2, 99-100	231.79	0.01	0.08	NA	NA	NA	NA	NA
21H-5, 99-100	236.29	0.03	0.25	NA	NA	NA	NA	NA
22H-2, 98-99	241.28	0.01	0.11	NA	NA	NA	NA	NA
22H-5, 98-99	245.78	0.00	0.06	NA	NA	NA	NA	NA
23H-2, 97-98	249.91	0.01	0.12	NA	NA	NA	NA	NA
23H-3, 140-150	251.84	0.01	0.15	0.06	0.04	0.04	0.02	NA
23H-5, 98-99	254.42	0.00	0.08	NA	NA	NA	NA	NA
24H-2, 97-98	260.27	0.01	0.11	NA	NA	NA	NA	NA
24H-5, 97-98	264.77	0.01	0.12	NA	NA	NA	NA	NA
25X-2, 98-99	269.28	0.01	0.10	NA	NA	NA	NA	NA
25X-4, 99-100	272.29	0.01	0.14	NA	NA	NA	NA	NA
26X-2, 99-100	276.19	0.02	0.20	NA	NA	NA	NA	NA
26X-3, 142-148	278.12	0.03	0.25	0.02	0.00	0.02	0.03	1.35
26X-5, 99-100	280.69	0.02	0.18	NA	NA	NA	NA	NA

Notes: IC = inorganic carbon, $CaCO_3$ = carbonate, TC = total carbon, OC = organic carbon, mg HC/g = milligrams of hydrocarbon per gram of sediment, NA = not analyzed. This table is also available in **ASCII format.**

Table T3. Distribution and relative abundance of radiolarians, Site 1179.

Core, section, interval (cm)	Depth (mbsf)	Zone	Group abundance	Group preservation	*Amphirhopalum ypsilon*	*Botryostrobus aquilonaris*	*Diartus petterssoni*	*Didymocyrtis antepenultima*	*Didymocyrtis penultima*	*Didymocyrtis tetrathalamus tetrathalamus*	*Eucyrtidium calvertense*	*Eucyrtidium matuyamai*	*Lamprocyrtis heteroporos*	*Lamprocyrtis nigriniae*	*Lamprocyrtis neoheteroporos*	*Saturnalis circularis*	*Sphaeropyle robusta*	*Stichocorys delmontensis*	*Stichocorys peregrina*	*Stylacontarium acquilonium*	*Stylatractus universus*	*Theocorythium vetulum*
191-1179B-																						
1H-CC, 5	7.48	*B. aquilonaris*	C	G		C					C											
2H-CC, 8	16.69	*B. aquilonaris*	C	G		C					C			C		C						
3H-CC, 16	27.09	*S. universus*	C	G		C					C			C		C						
4H-CC, 0	36.02	*S. universus*	F	G		C					C			C		C						
5H-CC, 19	46.12	*E. matuyamai* (N. Pacific)	C	G		F				F	C			C		C					F	C
6H-CC, 0	55.20	*E. matuyamai* (N. Pacific)	C	G		F					C	C		C	C							
191-1179C-																						
2H-CC, 22	58.77	*E. matuyamai* (N. Pacific)	F	G		F						C										
3H-CC, 11	67.81	*L. heteroporos*	C	G							C					C					F	C
4H-CC, 23	77.86	*L. heteroporos*	C	G						F			C									C
5H-CC, 10	87.03	*L. heteroporos*	F	G						F	C		C									C
6H-CC, 40	96.83	*L. heteroporos*	A	G									C							F	F	
7H-CC, 0	105.85	*L. heteroporos*	C	G	F								C							F		C
8H-CC, 12	115.74	*S. langii* (N. Pacific)	C	G	F															F		C
10H-CC, 24	134.57	*S. langii* (N. Pacific)	C	G															C			
11H-CC, 0	143.84	*S. langii* (N. Pacific)	A	G							C					C			C			C
12H-CC, 25	153.87	*S. langii* (N. Pacific)	F	M															C			
13H-CC, 0	162.89	*D. penultima/S. peregrina* (N. Pacific)	C	G					C							C		C	C			
14H-CC, 26	172.87	*D. penultima/S. peregrina* (N. Pacific)	C	M												C	C					
15H-CC, 0	181.94	*D. penultima/S. peregrina* (N. Pacific)	C	M							C							C	C			
16H-CC, 17	191.79	*D. penultima/S. peregrina* (N. Pacific)	C	M							C							C				
17H-CC, 18	201.08	*D. penultima/S. peregrina* (N. Pacific)	C	M							C							C				
18H-CC, 13	210.71	*D. penultima/S. peregrina* (N. Pacific)	C	M							C							C				
20H-CC, 18	229.72	*D. antepenultima*	A	G			C	C			C											

Notes: Abundance: A = abundant, C = common, F = few. Preservation: G = good, M = moderate. This table is also available in **ASCII format.**

Table T4. Core samples collected for microbiological experiments and results of chemical analyses.

				Method ISE	Method T	Method R	Method T	Method I					Method S			Method ICP				
Interval (cm)	Depth (mbsf)	PFT tracer	Incubation experiments*	pH	Alk (mM)	Sal	Cl (mM)	SO_4 (mM)	Na (mM)	Mg (mM)	Ca (mM)	K (mM)	NH_4 (μM)	NO_3 (μM)	PO_4 (μM)	Sr (μM)	Fe (μM)	Mn (μM)	B (μM)	Li (μM)
191-1179B-																				
1H-1, 5-10	0.05	No		7.32	2.56	34.0	549.7	29.0	475	52.0	10.7	11.0	10.3	77.4	2.3	79.5	0.9	2.7	382.1	19.2
1H-1, 10-16	0.10	No		7.27	2.19	34.0	556.6	28.5	472	51.0	11.2	11.1	2.5	66.4	3.3	77.0	3.2	2.4	414.8	21.1
1H-1, 20-25	0.20	No		7.30	2.28	35.5	553.7	28.6	477	50.5	10.2	11.2	7.7	61.7	3.7	76.3	13.7	13.9	470.6	21.0
1H-1, 45-50	0.45	No		7.38	2.46	34.0	550.7	29.4	476	50.8	11.0	11.2	3.8	35.5	6.8	85.8	15.6	60.8	435.0	18.6
1H-1, 70-75	0.70	No		7.38	2.57	34.0	548.7	28.4	473	50.5	10.9	11.1	1.2	18.3	9.3	87.0	3.0	87.0	416.6	17.8
1H-1, 95-100	0.95	No		7.43	2.74	34.0	548.7	29.6	476	50.1	11.3	11.1	0.1	5.8	13.3	89.0		101.2	432.9	20.1
1H-3, 95-100	3.95	No		8.00	3.47	34.0	550.6	28.1	475	49.5	11.2	12.2	73.5	1.4	23.4	89.1	17.5	199.0	442.2	12.4
1H-4, 3-8	4.53	No	Yes	8.27	3.66	34.5	556.5	28.5	479	48.8	11.3	12.0	68.7	2.6	21.8	89.1	5.2	213.7	404.1	12.6
1H-4, 143-148	5.95	No		7.86	3.37	34.5	550.6	28.9	478	49.3	11.3	11.7	75.1	0.5	34.4	88.6	13.3	252.3	415.3	12.0
1H-5, 43-48	6.45	No		7.60	3.31	34.5	551.6	29.4	481	47.8	11.4	11.5	71.9	0.8	34.2	89.8	29.5	255.6	458.9	12.6
2H-3, 143-148	12.05	No		7.84	3.90	34.5	556.5	28.0	486	46.3	11.2	12.8	128.2	0.5	36.3	85.1	9.3	169.2	454.2	14.1
3H-3, 143-148	21.55	No		7.93	4.50	35.0	552.6	28.4	485	46.3	11.5	12.4		1.7	34.8	91.3	10.7	138.2	430.6	14.3
4H-3, 143-148	31.05	No	Yes	8.24	5.10	35.0	557.5	27.1	490	45.0	11.7	14.0	222.9	1.1	36.1	90.9	2.8	97.2	382.7	16.3
5H-3, 143-148	40.55	Yes		7.61	4.76	35.0	557.5	25.9	487	44.0	11.7	12.3	247.0	0.8	32.5	90.5	14.0	127.6	455.5	19.7
6H-3, 143-148	50.05	No		8.16	5.37	35.0	558.5	26.5	488	43.6	12.0	12.8	256.6	0.5	33.1	85.2	2.2	90.9	382.4	23.1
191-1179C-																				
1H-3, 143-148	4.45	No		7.65	3.40	34.5	554.0	28.5	478	47.5	11.3	11.5	53.6	0.5	36.7	88.4	8.5	245.2	437.1	14.1
3H-3, 143-148	62.75	No		7.73	5.00	35.0	558.5	26.0	486	43.6	12.4	11.9	288.8	1.1	28.2	86.3	14.4	109.4	441.3	25.7
4H-3, 143-148	72.25	No		7.94	5.28	35.0	563.5	25.8	486	42.6	12.1	12.3	259.2	0.8	26.7	90.7	11.0	101.9	402.3	29.0
5H-3, 143-148	81.75	No		7.96	5.27	35.0	559.5	25.6	485	42.4	12.1	12.0	292.0	1.4	23.4	89.9	13.3	99.5	382.5	33.7
6H-3, 143-148	91.25	No		7.92	5.27	35.0	554.5	24.8	487	42.2	12.4	12.0	298.4	0.8	21.8	89.4	5.7	104.7	470.8	35.7
7H-3, 143-148	100.75	No	Yes	8.09	5.43	35.0	557.5	25.3	489	41.6	12.5	12.2	298.4	1.1	16.4	80.7	2.6	74.4	341.4	39.0
8H-3, 143-148	110.25	No		7.89	4.97	34.5	556.5	24.6	484	41.4	12.7	14.2	295.2	2.3	15.3	88.2	8.8	85.3	434.9	41.1
11H-3, 142-148	138.72	No		7.55	4.69	34.5	556.5	25.0	485	41.3	13.3	10.2	272.7	0.5	10.1	87.8	23.2	98.5	451.3	48.8
14H-3, 143-148	167.25	No		7.65	4.44	34.5	556.5	24.8	482	40.3	13.4	10.7	235.6	1.4	2.9	85.4	24.9	109.1	478.2	58.4
17H-3, 143-148	195.75	No	Yes	7.72	4.36	34.5	563.5	24.3	480	39.9	14.1	10.8	219.7	0.8	4.3	86.8	1.4	106.2	404.6	63.1
20H-3, 143-148	224.25	No		7.36	3.80	34.5	557.5	23.0	483	39.3	14.3	10.1	206.9	4.6	3.1	89.5	8.1	167.7	439.5	68.1
21H		Yes																		
23H-3, 140-150	251.84	No		7.66	3.22	34.0	543.7	22.0	459	39.5	14.8	9.6	174.7	7.0	0.2	83.9	6.1	190.8	582.7	64.0
26X-3, 142-148	278.12	No		7.19	3.43	34.0	550.6	21.2	470	38.7	15.4	9.3	113.7	1.4	0.0	81.5	5.4	7.4	615.3	62.6

Notes: ISE = ion-specific electrode, T = titration, R = refractometer, I = ion chromatograph, S = spectrophotometer, ICP = inductively coupled plasma emission spectroscopy. Alk = alkalinity, Sal = salinity. * = 10-cm whole-round cores (WRCs) for incubation experiments were collected just above WRCs collected for interstitial water (IW). A 15-cm WRC was collected from Core 191-1179B-1H-4 (working half). SiO_2 was not measured. This table is also available in **ASCII format.**

Table T5. Magnetic susceptibility tie point depths correlating cores from Holes 1179A, 1179B, and 1179C.

Tie point	Depth (mbsf)		
	Hole 1179A	Hole 1179B	Hole 1179C
1		1.44	1.32
2		1.84	1.60
3	0.90	2.92	2.72
4	2.04	4.32	3.88
5	2.22		4.04
6	3.22	5.73	5.04
7	3.94	6.66	
8	4.32	6.94	
9	6.74	8.24	
10	6.92	8.36	
11	8.38	9.70	
12	8.68	10.00	
13		50.90	49.08
14		51.92	50.10
15		52.98	51.20
16		54.18	52.44

Note: This table is also available in **ASCII format.**

Table T6. Magnetic polarity reversal boundary depths.

Core, section	Depth (mbsf)	GPTS age (Ma)	Reversal boundary
191-1179B-			
4H-4	31.12	0.780	C1n to C1r.1r
5H-2	38.57	0.990	C1r.1r to C1r.1n
5H-4	41.82	1.070	C1r.1n to C1r.2r.1r
6H-1	45.60	1.200	C1r.2r.1r to C1r.2r-1n
6H-1	45.92	1.210	C1r.2r-1n to C1r.2r.2r
191-1179C-			
3H-5	65.42	1.770	C1r.2r.2r to C2n
4H-2	69.82	1.950	C2n to C2r.1r
4H-6	76.67	2.140	C2r.1r to C2r.1n
4H-7	77.27	2.150	C2r.1n to C2r.2r
6H-7	96.17	2.581	C2r.2r to C2An.1n
8H-1	106.52	3.040	C2An.1n to C2An.1r
8H-3	109.42	3.110	C2An.1r to C2An.2n
8H-5	112.72	3.220	C2An.2n to C2An.2r
9H-1	115.52	3.330	C2An.2r to C2An.3n
9H-6	123.77	3.580	C2An.3n to C2Ar
12H-1	143.80	4.180	C2Ar to C3n.1n
12H-4	149.87	4.290	C3n.1n to C3n.1r
13H-2	155.92	4.480	C3n.1r to C3n.2n
13H-5	160.02	4.620	C3n.2n to C3n.2r
14H-1	164.12	4.800	C3n.2r to C3n.3n
14H-3	166.92	4.890	C3n.3n to C3n.3r
14H-5	169.85	4.980	C3n.3r to C3n.4n
15H-3	175.72	5.230	C3n.4n to C3r
17H-1	192.67	5.894	C3r to C3An.1n
17H-5	197.85	6.137	C3An.1n to C3An.1r
17H-7	200.67	6.269	C3An.1r to C3An.2n
18H-5	206.97	6.567	C3An.2n to C3Ar
19H-3	214.22	6.935	C3Ar to C3Bn
19H-5	216.52	7.091	C3Bn to C3Br.1r
19H-5	217.27	7.135	C3Br.1r to C3Br.1n
19H-6	217.97	7.170	C3Br.1n to C3Br.2r
20H-1	219.85	7.341	C3Br.2r to C3Br.2n
20H-1	220.02	7.375	C3Br.2n to C3Br.3r
20H-1	220.22	7.432	C3Br.3r to C4n.1n
20H-2	221.52	7.562	C4n.1n to C4n.1r
20H-2	222.12	7.650	C4n.1r to C4n.2n
20H-4	225.37	8.072	C4n.2n to C4r.1r
20H-5	226.42	8.225	C4r.1r to C4r.1n
20H-5	226.57	8.257	C4r.1n to C4r.2r
20H-7	229.35	8.635	C4r.2r to C4r.2r-1
21H-1	229.67	8.651	C4r.2r-1 to C4r.3r
21H-1	230.12	8.699	C4r.3r to C4An
21H-3	233.47	9.025	C4An to C4Ar.1r
21H-4	234.67	9.230	C4Ar.1r to C4Ar.1n
21H-5	235.67	9.308	C4Ar.1n to C4Ar.2r
21H-6	237.38	9.580	C4Ar.2r to C4Ar.2n
21H-6	238.03	9.642	C4Ar.2n to C4Ar.3r
21H-7	238.42	9.740	C4Ar.3r to C5n.1n
22H-1	239.17	9.880	C5n.1n to C5n.1r
22H-1	239.37	9.920	C5n.1r to C5n.2n
22H-6	246.52	10.949	C5n.2n to C5r.1r
22H-6	246.80	11.052	C5r.1r to C5r.1n
22H-6	246.96	11.099	C5r.1n to C5r.2r
22H-6	247.31	11.476	C5r.2r to C5r.2n
22H-6	247.47	11.531	C5r.2n to C5r.3r
22H-7	248.37	11.935	C5r.3r to C5An.1n
23H-1	248.83	12.401	C5An.2n to C5Ar.1r
23H-2	249.09	12.678	C5Ar.1r to C5Ar.1n
23H-2	249.27	12.708	C5Ar.1n to C5Ar.2r
23H-2	249.37	12.775	C5Ar.2r to C5Ar.2n
23H-2	249.51	12.819	C5Ar.2n to C5Ar.3r
23H-2	249.80	12.991	C5Ar.3r to C5AAn
23H-2	250.21	13.139	C5AAn to C5AAr
23H-3	250.44	13.302	C5AAr to C5ABn
23H-3	251.01	13.510	C5ABn to C5ABr
23H-3	251.17	13.703	C5ABr to C5ACn
23H-4	252.81	14.612	C5ADn to C5ADr
23H-4	252.99	14.800	C5ADr to C5Bn.1n
23H-4	253.29	14.888	C5Bn.1n to C5Bn.1r
23H-4	253.40	15.034	C5Bn.1r to C5Bn.2n
23H-5	253.68	15.155	C5Bn.2n to C5Br
23H-5	254.70	16.014	C5Br to C5Cn.1n
23H-6	255.22	16.293	C5Cn.1n to C5Cn.1r
23H-6	255.32	16.327	C5Cn.1r to C5Cn.2n
23H-6	255.40	16.488	C5Cn.2n to C5Cn.2r
23H-6	255.51	16.556	C5Cn.2r to C5Cn.3n
23H-6	255.72	16.726	C5Cn.3n to C5Cr
23H-6	256.10	17.277	C5Cr to C5Dn
23H-7	256.60	17.615	C5Dn to C5Dr

Note: GPTS = geomagnetic polarity time scale.

Table T7. Subdivision of the basalt pile, Hole 1179D.

Basalt group	Unit	Depth (mbsf)	Cored interval (m)	Recovery (m)	Olivine (%)
I	1-8	375-396	21	14.5	0.2
II	9-24	396-446	50	18.4	
III	25-48	446-475	29	19.4	>3

Note: This table is also available in **ASCII format.**

Table T8. Phenocryst distribution in basalts, Hole 1179D.

Basalt group	Plagioclase phenocrysts (%)			Olivine phenocrysts (%)	
	All	Massive (mean)	Pillow (mean)	Range	Mean
I	0.1-1.8	0.9	0.5	0.1-0.35	0.2
II	0.1-1.0	0.5	0.4		
III	0.2-3.0	1.1	0.5	0.2-1.8	0.5

Note: This table is also available in **ASCII format.**

Table T9. Glass/palagonite contents of basalts, Hole 1179D.

	Basalt Group I (% glass)		Basalt Group II (% glass)		Basalt Group III (% glass)	
	Rock	Margin	Rock	Margin	Rock	Margin
Pillow	~17	80	~45	90	~20	85
Massive	~11		~12	70	~5	55

Notes: Rock = normal parts of the interior. Margin = quenched and cryptocrystalline parts of pillows or flows. This table is also available in **ASCII format.**

Table T10. Chemical analyses of basalts, Hole 1179D.

Core-section:	11R-1	11R-2	12R-2	12R-4	12R-4	13R-3	13R-4	14R-1	14R-2	17R-1	17R-1	17R-2	18R-1	18R-4	19R-2	20R-1	20R-3	21R-4	22R-3	22R-4	22R-4
Interval (cm):	86-88	84-86	69-71	2-4	86-88	11-13	83-85	18-20	63-65	40-42	111-113	11-13	25-28	87-90	121-124	72-75	64-67	112-115	88-91	72-75	120-123
Depth (mbsf):	377.96	378.30	388.89	390.73	391.57	393.47	395.6	396.58	398.53	419.2	419.92	420.21	425.55	430.34	437.3	445.32	447.49	459.33	467.56	468.82	469.3
Major oxides (wt%)																					
SiO_2	49.84	49.45	48.16	48.19	48.55	48.49	48.70	49.71	48.49	47.67	48.82	48.27	51.43	50.07	49.20	47.21	47.47	46.74	47.42	48.32	47.71
TiO_2	1.34	1.38	1.23	1.24	1.24	1.34	1.37	1.37	1.32	1.46	1.85	1.90	1.99	1.72	1.70	1.60	1.58	1.56	1.63	1.67	1.62
Al_2O_3	15.11	15.39	14.21	14.58	14.55	14.20	14.45	14.63	14.55	15.83	13.70	14.03	14.71	14.63	14.43	16.38	16.37	15.48	16.21	16.83	15.91
Fe_2O_3*	8.79	10.42	11.62	11.09	10.85	12.94	10.52	9.98	10.10	11.62	13.75	14.20	8.21	10.20	9.76	9.55	10.74	10.81	9.80	9.30	10.41
MnO	0.15	0.15	0.18	0.19	0.19	0.17	0.17	0.16	0.16	0.14	0.23	0.21	0.14	0.18	0.21	0.20	0.21	0.20	0.17	0.28	0.17
MgO	8.31	7.35	6.77	6.52	7.39	6.59	7.23	7.39	6.99	5.17	6.27	5.99	7.55	7.14	7.59	6.16	6.13	7.26	6.31	6.57	6.87
CaO	11.77	11.18	12.82	12.87	12.22	10.96	12.01	11.70	12.45	11.52	10.42	10.03	10.78	11.39	11.24	12.56	12.69	11.74	12.40	12.48	11.34
Na_2O	2.40	2.57	2.08	2.09	2.07	2.41	2.48	2.42	2.43	2.37	2.52	2.61	2.88	2.51	2.48	2.55	2.53	2.44	2.55	2.64	2.53
K_2O	0.17	0.42	0.54	0.48	0.35	0.95	0.62	0.61	0.48	0.77	0.73	0.70	0.47	0.34	0.22	0.20	0.22	0.25	0.25	0.06	0.53
P_2O_5	0.10	0.11	0.11	0.11	0.09	0.11	0.13	0.11	0.12	0.17	0.14	0.17	0.16	0.15	0.13	0.15	0.15	0.14	0.16	0.16	0.17
LOI	0.68	1.79	1.63	2.31	1.89	2.37	1.87	1.48	2.83	1.86	2.45	0.86	2.27	0.79	1.92	3.62	1.51	4.18	3.73	0.90	1.91
Total	98.67	100.20	99.34	99.68	99.40	100.53	99.55	99.55	99.92	98.58	100.87	98.97	100.59	99.12	98.88	100.20	99.59	100.78	100.62	99.22	99.16
FeO†/MgO	0.95	1.28	1.55	1.53	1.32	1.77	1.31	1.22	1.30	2.03	1.97	2.14	0.98	1.29	1.16	1.40	1.58	1.34	1.40	1.28	1.37
Trace elements (ppm)																					
Sc	47	49	45	44	44	47	49	49	46	44	50	50	50	51	48	42	42	39	41	42	42
V	366	358	338	348	336	356	326	325	352	324	433	457	326	377	380	324	315	307	314	323	318
Cr	283	279	310	318	314	212	227	219	236	318	100	105	107	161	169	343	333	354	360	355	342
Ni	93	87	73	86	89	67	76	80	91	57	51	51	72	66	80	152	111	141	157	173	144
Cu	99	116	92	87	104	58	59	52	55	66	83	71	35	54	183	94	123	49	130	84	88
Zn	108	89	87	88	88	102	87	86	83	82	112	122	67	106	107	90	99	83	90	88	99
Ga	17	17	17	15	16	17	18	18	17	18	18	20	19	19	17	17	18	15	18	18	18
Rb	1.5	8.7	12	12	20	24	15	15	18	16	18	15	6.7	6.9	24	6.7	5.1	6.4	6.8	2.5	11
Sr	96	102	86	84	81	95	102	95	97	150	99	103	106	98	93	167	164	166	177	181	165
Y	34	29	32	32	25	32	32	27	33	38	44	46	48	44	31	32	32	29	33	32	34
Zr	67	72	64	62	63	74	76	73	71	90	107	108	113	95	88	106	99	105	110	112	108
Nb	3.3	2.5	2.2	2.4	2.0	2.8	3.3	3.0	3.0	4.5	2.9	1.6	3.8	4.1	3.7	3.4	4.5	3.7	5.4	5.5	4.8
Cs	3.4	3.9	<1.0	3.3	3.4	2.3	<1.0	<1.0	5.1	<1.0	<1.0	1.5	<1.0	2.2	3.6	1.4	3.3	<1.0	<1.0	<1.0	2.5
Ba	17	21	24	17	18	36	36	29	30	37	29	32	38	20	18	35	25	32	37	38	55
La	2.8	2.6	3.3	2.6	1.7	3.6	2.8	2.3	3.1	5.2	3.2	3.6	3.7	4.4	3.5	4.5	3.7	5.2	4.8	4.7	3.2
Ce	6.8	7.3	7.4	7.4	4.6	8.9	8.0	6.6	7.6	12.8	10.1	11.5	10.9	10.7	8.5	10.4	11.4	12.1	13.0	11.7	11.0
Nd	7.9	7.9	7.5	6.5	6.4	8.0	8.0	7.5	7.6	9.6	10.7	11.7	11.9	10.6	9.1	10.1	9.4	10.3	11.4	9.7	11.4
Sm	3.0	2.8	2.1	2.5	2.4	2.3	2.8	3.5	3.1	3.1	4.2	5.3	4.3	4.2	3.7	4.4	4.2	3.8	2.7	5.2	3.7
Gd	4.5	3.4	2.8	4.1	3.9	3.2	4.7	3.2	3.3	3.9	5.1	5.1	5.5	4.1	5.1	4.3	4.3	4.5	3.9	4.6	4.5
Dy	4.8	5.0	6.0	5.6	4.5	5.6	5.5	4.5	5.3	6.7	6.1	7.0	5.9	7.2	6.8	5.9	5.7	3.1	6.3	4.8	5.1
Er	3.2	3.0	2.9	3.2	2.6	3.3	3.4	3.0	3.0	3.1	3.2	4.1	4.4	4.3	4.2	2.9	2.8	2.1	3.0	2.5	3.3
Yb	3.7	3.5	3.6	3.6	4.4	4.8	3.8	3.9	5.0	3.4	5.5	4.5	5.6	4.8	6.3	4.2	3.9	4.5	4.8	3.5	3.5
Hf	1.7	1.6	1.2	1.1	1.6	2.0	1.4	1.7	1.5	1.8	2.1	2.0	2.6	2.2	1.8	2.6	2.3	1.9	2.3	1.7	2.1
Pb	<0.5	<0.5	1.5	<0.5	<0.5	<0.5	<0.5	<0.5	<0.5	1.0	0.9	<0.5	0.5	<0.5	<0.5	<0.5	<0.5	<0.5	<0.5	0.8	<0.5
Th	<1.0	3.4	1.2	<1.0	<1.0	2.7	4.5	2.7	<1.0	3.6	2.7	4.7	3.6	<0.5	<0.5	5.6	<0.5	2.0	5.0	6.2	3.1

Notes: * = total Fe as Fe_2O_3. † = total Fe as FeO. LOI = loss on ignition (at 1025°C). This table is also available in **ASCII format.**

Table T11. CIPW norm composition of basalts, Hole 1179D.

Core, section, interval (cm)	Unit	Structure	q	or	ab	an	ne	di			hy		ol		mt	il	ap	sum
								wo	en	fs	en	fs	fo	fa				
191-1179D-																		
11R-1, 86-88	2	Pillow	0.12	0.99	20.32	29.94	0.00	11.60	7.67	3.10	13.02	5.26	0.00	0.00	2.55	2.55	0.25	97.36
11R-2, 84-86	2	Pillow	0.00	2.50	21.73	29.21	0.00	10.67	6.48	3.61	9.88	5.51	1.35	0.83	3.02	2.62	0.25	97.66
12R-2, 69-71	4	Flow	0.00	3.17	17.58	27.86	0.00	14.61	8.21	5.80	6.30	4.45	1.64	1.28	3.37	2.33	0.27	96.87
12R-4, 2-4	6	Flow	0.00	2.85	17.70	28.96	0.00	14.27	8.07	5.61	6.95	4.83	0.85	0.65	3.22	2.36	0.26	96.57
12R-4, 86-88	6	Flow	0.00	2.08	17.48	29.39	0.00	12.78	7.59	4.54	10.48	6.27	0.23	0.15	3.15	2.35	0.22	96.72
13R-3, 11-13	8	Flow	0.00	5.59	20.42	25.11	0.00	11.92	6.38	5.15	5.86	4.73	2.92	2.60	3.75	2.55	0.26	97.23
13R-4, 83-85	8	Flow	0.00	3.63	20.99	26.48	0.00	13.45	8.08	4.66	5.36	3.09	3.20	2.03	3.05	2.59	0.32	96.92
14R-1, 18-20	10	Flow	0.00	3.62	20.48	27.25	0.00	12.55	7.74	4.08	9.69	5.11	0.68	0.40	2.89	2.59	0.26	97.35
14R-2, 63-65	10	Flow	0.00	2.84	20.52	27.40	0.00	14.02	8.45	4.82	5.53	3.16	2.40	1.51	2.93	2.51	0.28	96.37
17R-1, 40-42	14	Pillow	0.00	4.57	20.05	30.27	0.00	10.75	5.54	4.93	6.10	5.44	0.85	0.84	3.37	2.77	0.41	95.89
17R-1, 111-113	15	Flow	0.00	4.28	21.29	23.94	0.00	11.20	5.85	5.03	9.39	8.09	0.27	0.25	3.99	3.52	0.34	97.43
17R-2, 11-13	15	Flow	0.00	4.14	22.10	24.48	0.00	10.08	5.10	4.75	8.60	8.01	0.84	0.87	4.12	3.60	0.41	97.09
18R-1, 25-28	18	Flow	1.77	2.75	24.36	25.85	0.00	11.09	7.57	2.65	11.23	3.93	0.00	0.00	2.38	3.78	0.39	97.73
18R-4, 87-90	21	Flow	1.31	2.00	21.19	27.69	0.00	11.63	7.16	3.80	10.62	5.64	0.00	0.00	2.96	3.27	0.35	97.60
19R-2, 121-124	23	Pillow	0.74	1.27	20.93	27.64	0.00	11.39	7.22	3.44	11.68	5.57	0.00	0.00	2.83	3.22	0.31	96.26
20R-1, 72-75	25	Pillow	0.00	1.18	21.56	32.68	0.00	11.97	7.17	4.17	3.73	2.17	3.11	1.99	2.77	3.04	0.36	95.89
20R-3, 64-67	29	Flow	0.00	1.32	21.41	32.64	0.00	12.24	6.98	4.73	3.07	2.08	3.66	2.73	3.12	3.00	0.36	97.31
21R-4, 112-115	43	Flow	0.00	1.45	20.62	30.57	0.00	11.16	6.69	3.87	4.61	2.67	4.74	3.02	3.14	2.96	0.34	95.83
22R-3, 88-91	45	Flow	0.00	1.46	21.55	32.07	0.00	11.87	7.12	4.12	4.26	2.47	3.04	1.94	2.84	3.09	0.38	96.19
22R-4, 72-75	45	Flow	0.00	0.36	22.30	33.90	0.00	11.26	6.94	3.67	6.01	3.18	2.38	1.39	2.70	3.18	0.38	97.66
22R-4, 120-123	46	Pillow	0.00	3.13	21.39	30.51	0.00	10.29	6.19	3.55	5.76	3.30	3.61	2.28	3.02	3.08	0.39	96.51

Notes: CIPW norms are calculated assuming $Fe^{2+}/(Fe^{2+} + Fe^{3+}) = 0.80$. q = norm quartz, or = norm orthoclase, ab = norm albite, an = norm anorthite, ne = norm nepheline, di = norm diopside (wo = wollastonite component, en = enstatite component, fs = ferrosilite component), hy = norm hyperthene (en = enstatite component, fs = ferrosilite component), ol = norm olivine (fo = forsterite component, fa = fayalite component), mt = norm magnetite, il = norm ilmenite, ap = norm apatite. This table is also available in **ASCII format.**

Table T12. PWS3 split-core *P*-wave velocities. (See table notes. Continued on next page.)

Core, section, interval (cm)	Depth (mbsf)	Velocity* (m/s)	Lithostratigraphic unit
191-1179B-			
5H-3, 81	39.9	1539	I
5H-3, 136	40.5	1532	I
5H-6, 109	44.7	1514	I
6H-1, 131	46.9	1496	I
6H-2, 118	48.3	1597	I
6H-3, 89	49.5	1524	I
6H-4, 108	51.2	1525	I
6H-5, 106	52.7	1528	I
6H-6, 120	54.3	1521	I
191-1179C-			
2H-1, 94	49.7	1536	I
2H-2, 88	51.2	1533	I
2H-2, 108	51.4	1532	I
2H-4, 118	54.5	1776	I
2H-5, 123	56.0	1537	I
2H-6, 126	57.6	1530	I
3H-1, 44	58.7	1533	I
3H-1, 91	59.2	1530	I
3H-2, 110	60.9	1536	I
3H-3, 61	61.9	1567	I
3H-4, 70	63.5	1559	I
3H-5, 116	65.5	1537	I
3H-6, 52	66.3	1549	I
4H-1, 76	68.6	1528	I
4H-2, 115	70.5	1525	I
4H-3, 66	71.5	1531	I
4H-4, 92	73.2	1537	I
4H-5, 92	74.7	1520	I
4H-6, 84	76.1	1539	I
5H-1, 74	78.0	1548	I
5H-2, 90	79.7	1550	I
5H-3, 78	81.1	1543	I
5H-4, 90	82.7	1541	I
5H-5, 93	84.2	1541	I
5H-6, 90	85.7	1536	I
6H-1, 88	87.7	1537	I
6H-2, 84	89.1	1530	I
6H-3, 74	90.5	1539	I
6H-4, 85	92.1	1543	I
6H-5, 89	93.7	1533	I
6H-6, 76	95.1	1543	I
7H-1, 77	97.1	1533	I
7H-2, 93	98.7	1539	I
7H-3, 66	100.0	1549	I
7H-4, 91	101.7	1541	I
7H-5, 86	103.2	1544	I
7H-6, 87	104.7	1542	I
8H-2, 91	108.2	1543	I
8H-3, 81	109.6	1544	I
8H-4, 88	111.2	1547	I
8H-5, 86	112.7	1552	I
8H-6, 84	114.1	1542	I
9H-1, 85	116.2	1536	I
9H-2, 89	117.7	1531	I
9H-3, 93	119.2	1538	I
9H-4, 85	120.7	1548	I
9H-5, 74	122.0	1546	I
9H-6, 58	123.4	1547	I
10H-1, 83	125.6	1543	I
10H-2, 62	126.9	1546	I
10H-3, 93	128.7	1541	I
10H-4, 63	129.9	1543	I
10H-5, 93	131.7	1540	I
11H-2, 74	136.5	1539	I
11H-3, 69	138.0	1547	I
11H-4, 89	139.7	1547	I
11H-5, 78	141.1	1539	I
11H-6, 88	142.7	1540	I
12H-1, 71	144.5	1557	I
12H-2, 54	145.8	1548	I
12H-3, 90	147.7	1538	I
12H-4, 76	149.1	1542	I
12H-5, 85	150.7	1463	I
12H-6, 87	152.2	1548	I
13H-1, 78	154.1	1541	I
13H-2, 82	155.6	1535	I
13H-3, 88	157.2	1540	I
13H-4, 71	158.5	1529	I
13H-5, 76	160.1	1548	I
13H-6, 60	161.4	1530	I
14H-1, 88	163.7	1542	I
14H-2, 75	165.1	1530	I
14H-3, 74	166.5	1529	I
14H-4, 76	168.1	1532	I
14H-5, 78	169.6	1546	I
14H-6, 75	171.0	1533	I
15H-1, 68	173.0	1534	I
15H-2, 68	174.5	1534	I
15H-3, 86	176.2	1526	I
15H-4, 81	177.6	1530	I
15H-5, 87	179.2	1523	I
15H-6, 69	180.5	1530	I
16H-1, 73	182.5	1487	I
16H-2, 76	184.1	1553	I
16H-3, 54	185.3	1541	I
16H-4, 58	186.9	1548	I
16H-5, 79	188.6	1546	I
16H-6, 69	190.0	1548	I
17H-1, 66	192.0	1552	I
17H-2, 85	193.7	1552	I
17H-3, 69	195.0	1541	I
17H-4, 85	196.7	1547	I
17H-5, 77	198.1	1541	I
17H-6, 89	199.7	1545	I
18H-1, 79	201.6	1547	I
18H-2, 29	202.6	1552	I
18H-3, 79	204.6	1543	I
18H-4, 90	206.2	1549	I
18H-5, 94	207.7	1543	I
18H-6, 91	209.2	1545	I
19H-1, 56	210.9	1546	I
19H-2, 88	212.7	1558	I
19H-3, 90	214.2	1547	I
19H-4, 78	215.6	1547	I
19H-5, 121	217.5	1545	I
19H-6, 113	218.9	1544	I
20H-2, 79	222.1	1551	II
20H-3, 86	223.7	1557	II
20H-4, 73	225.0	1550	II
20H-5, 79	226.6	1543	II
21H-1, 113	230.4	1544	II
21H-3, 108	233.4	1565	II
21H-5, 111	236.4	1547	II
21H-6, 125	238.1	1547	II
22H-1, 92	239.7	1552	II
22H-2, 137	241.7	1547	II
22H-3, 121	243.0	1546	II
22H-4, 128	244.6	1547	II
22H-5, 119	246.0	1551	II
22H-6, 122	247.5	1555	III
23H-2, 110	250.0	1520	III
23H-3, 117	251.6	1523	III
23H-4, 112	253.1	1525	III
23H-5, 111	254.6	1534	III
23H-6, 129	256.2	1525	III
24H-1, 103	258.8	1507	III
24H-2, 108	260.4	1501	III

Table T12 (continued).

Core, section, interval (cm)	Depth (mbsf)	Velocity* (m/s)	Lithostratigraphic unit
24H-4, 106	263.4	1516	III
24H-5, 105	264.9	1560	III
24H-6, 108	266.4	1519	III
25X-1, 129	268.1	1512	III
25X-2, 136	269.7	1523	III
25X-3, 124	271.0	1524	III
25X-4, 127	272.6	1512	III
26X-1, 123	274.9	1515	III
26X-2, 114	276.3	1519	III
26X-3, 86	277.6	1496	III
26X-4, 116	279.4	1465	III
26X-5, 117	280.9	1493	III
26X-6, 130	282.5	1525	III

Notes: * = velocities recalculated using new calibration. This table is also available in **ASCII format.**

Table T13. Index properties of discrete samples, Holes 1179A, 1179B, and 1179C. (See table note. Continued on next two pages.)

Core, section, interval (cm)	Depth (mbsf)	Density (g/cm³)		Porosity (%)	Void ratio	Lithostratigraphic unit
		Bulk	Grain			
191-1179A-						
1H-1, 39-41	0.39	1.21	2.34	85.7	6.01	I
1H-2, 39-41	1.89	1.27	2.39	81.9	4.51	I
1H-3, 29-31	3.29	1.22	2.39	85.7	6.01	I
1H-4, 36-38	4.36	1.23	2.35	84.9	5.60	I
1H-5, 39-41	4.99	1.23	2.46	85.6	5.93	I
1H-6, 29-31	6.39	1.29	2.58	83.2	4.96	I
1H-7, 29-31	7.89	1.30	2.61	82.5	4.72	I
1H-8, 39-41	9.49	1.26	2.53	84.1	5.29	I
191-1179B-						
1H-2, 49-51	1.99	1.22	2.48	86.7	6.54	I
1H-3, 49-51	3.49	1.24	2.54	85.8	6.03	I
1H-4, 49-51	4.99	1.24	2.64	86.9	6.62	I
1H-5, 79-81	6.79	1.25	2.82	87.1	6.78	I
2H-1, 79-81	8.39	1.38	2.77	79.9	3.98	I
2H-2, 99-101	10.09	1.31	2.99	85.3	5.80	I
2H-3, 99-101	11.59	1.26	2.68	86.0	6.17	I
2H-4, 99-101	13.09	1.33	2.82	82.9	4.85	I
2H-5, 99-101	14.59	1.28	2.58	83.3	4.99	I
2H-6, 99-101	16.09	1.27	2.78	86.1	6.21	I
3H-1, 109-111	18.19	1.28	2.59	83.7	5.13	I
3H-2, 109-111	19.69	1.28	2.64	84.2	5.35	I
3H-3, 109-111	21.19	1.28	2.55	83.5	5.07	I
3H-4, 109-111	22.69	1.37	2.65	79.0	3.76	I
3H-5, 99-101	24.09	1.21	2.53	87.4	6.93	I
3H-6, 99-101	25.59	1.29	2.62	83.2	4.94	I
4H-1, 99-101	27.59	1.29	2.51	82.2	4.63	I
4H-2, 99-101	29.09	1.27	2.54	83.5	5.05	I
4H-3, 99-101	30.59	1.31	2.64	82.7	4.77	I
4H-4, 99-101	32.09	1.31	2.64	82.5	4.71	I
4H-5, 99-101	33.59	1.28	2.60	83.8	5.18	I
4H-6, 99-101	35.09	1.32	2.60	81.1	4.29	I
5H-1, 99-101	37.09	1.26	2.49	83.7	5.13	I
5H-2, 99-101	38.59	1.30	2.57	82.5	4.72	I
5H-3, 99-101	40.09	1.37	2.67	78.7	3.69	I
5H-4, 99-101	41.59	1.26	2.46	83.4	5.02	I
5H-5, 99-101	43.09	1.34	2.47	78.4	3.62	I
5H-6, 99-101	44.59	1.32	2.65	81.9	4.52	I
6H-1, 99-101	46.59	1.24	2.47	85.2	5.77	I
6H-3, 99-101	49.59	1.33	2.61	80.6	4.16	I
6H-4, 99-101	51.09	1.28	2.53	82.8	4.81	I
6H-5, 99-101	52.59	1.28	2.60	83.9	5.22	I
6H-6, 89-91	53.99	1.29	2.48	81.8	4.49	I
191-1179C-						
1H-1, 99-101	0.99	1.23	2.54	86.7	6.50	I
1H-2, 99-101	2.49	1.30	2.57	82.2	4.62	I
1H-3, 99-101	3.99	1.46	2.44	69.2	2.24	I
1H-4, 101-103	5.51	1.21	2.49	87.2	6.83	I
2H-1, 103-105	49.83	1.27	2.44	82.8	4.81	I
2H-2, 99-101	51.29	1.25	2.49	84.3	5.37	I
2H-3, 99-101	52.79	1.30	2.56	82.2	4.63	I
2H-4, 99-101	54.29	1.28	2.56	83.5	5.07	I
2H-5, 99-101	55.79	1.27	2.49	83.0	4.89	I
2H-6, 99-101	57.29	1.30	2.51	81.2	4.33	I
3H-1, 99-101	59.29	1.25	2.50	84.7	5.55	I
3H-2, 99-101	60.79	1.29	2.67	83.6	5.09	I
3H-3, 99-101	62.29	1.30	2.62	82.9	4.84	I
3H-4, 99-101	63.79	1.30	2.58	82.4	4.67	I
3H-5, 109-111	65.39	1.26	2.49	84.1	5.30	I
3H-6, 99-101	66.79	1.29	2.44	81.6	4.43	I
4H-1, 99-101	68.79	1.26	2.50	83.8	5.17	I
4H-2, 99-101	70.29	1.27	2.53	83.4	5.03	I
4H-3, 99-101	71.79	1.26	2.48	84.0	5.26	I
4H-4, 99-101	73.29	1.24	2.45	85.1	5.73	I
4H-5, 99-101	74.79	1.31	2.55	81.1	4.30	I

Table T13 (continued).

Core, section, interval (cm)	Depth (mbsf)	Density (g/cm³)		Porosity (%)	Void ratio	Lithostratigraphic unit
		Bulk	Grain			
4H-6, 99-101	76.29	1.28	2.53	83.1	4.92	I
5H-1, 99-101	78.29	1.24	2.49	85.6	5.92	I
5H-2, 99-101	79.79	1.40	2.43	73.4	2.77	I
5H-3, 99-101	81.29	1.23	2.31	84.3	5.36	I
5H-4, 99-101	82.79	1.24	2.34	83.7	5.14	I
5H-5, 99-101	84.29	1.26	2.34	82.4	4.67	I
5H-6, 99-101	85.79	1.29	2.49	82.0	4.57	I
6H-1, 103-105	87.83	1.28	2.43	81.8	4.49	I
6H-2, 99-101	89.29	1.27	2.36	81.4	4.39	I
6H-3, 99-101	90.79	1.29	2.46	81.2	4.32	I
6H-4, 99-101	92.29	1.37	2.56	77.5	3.45	I
6H-5, 99-101	93.79	1.29	2.50	81.8	4.50	I
6H-6, 99-101	95.29	1.25	2.31	82.8	4.80	I
7H-1, 99-101	97.29	1.23	2.43	85.4	5.86	I
7H-2, 99-101	98.79	1.25	2.41	83.8	5.16	I
7H-3, 99-101	100.29	1.24	2.36	83.5	5.07	I
7H-4, 99-101	101.79	1.25	2.40	83.4	5.03	I
7H-5, 99-101	103.29	1.24	2.37	84.3	5.37	I
7H-6, 99-101	104.79	1.23	2.36	84.6	5.49	I
8H-1, 99-101	106.79	1.24	2.38	84.4	5.40	I
8H-2, 99-101	108.29	1.23	2.36	84.7	5.52	I
8H-3, 99-101	109.79	1.24	2.44	84.7	5.55	I
8H-4, 99-101	111.29	1.22	2.44	85.9	6.07	I
8H-5, 99-101	112.79	1.27	2.45	83.0	4.89	I
8H-6, 99-101	114.29	1.23	2.38	84.9	5.61	I
9H-1, 99-101	116.29	1.24	2.45	84.9	5.63	I
9H-2, 99-101	117.79	1.27	2.54	83.9	5.20	I
9H-3, 99-101	119.29	1.22	2.39	85.5	5.92	I
9H-4, 99-101	120.79	1.21	2.29	85.6	5.93	I
9H-5, 99-101	122.29	1.35	2.40	76.2	3.21	I
9H-6, 99-101	123.79	1.21	2.34	85.9	6.10	I
10H-1, 99-101	125.79	1.22	2.38	85.3	5.80	I
10H-2, 99-101	127.29	1.21	2.41	86.7	6.50	I
10H-3, 99-101	128.79	1.22	2.40	85.9	6.08	I
10H-4, 99-101	130.29	1.22	2.39	85.5	5.90	I
10H-5, 99-101	131.79	1.22	2.40	85.6	5.94	I
10H-6, 99-101	133.29	1.21	2.32	86.0	6.15	I
11H-2, 99-101	136.79	1.19	2.27	86.4	6.33	I
11H-3, 99-101	138.29	1.19	2.23	86.5	6.38	I
11H-4, 99-101	139.79	1.21	2.23	84.3	5.39	I
11H-5, 99-101	141.29	1.21	2.30	85.2	5.76	I
11H-6, 99-101	142.79	1.21	2.29	85.1	5.73	I
12H-1, 99-101	144.79	1.22	2.37	85.5	5.88	I
12H-2, 99-101	146.29	1.19	2.18	85.2	5.77	I
12H-3, 99-101	147.79	1.21	2.31	85.3	5.82	I
12H-4, 99-101	149.29	1.21	2.26	84.8	5.58	I
12H-5, 99-101	150.79	1.21	2.28	85.5	5.91	I
12H-6, 99-101	152.29	1.21	2.34	85.6	5.94	I
13H-1, 103-105	154.33	1.26	2.42	83.1	4.90	I
13H-3, 99-101	157.29	1.25	2.38	83.1	4.92	I
13H-4, 99-101	158.79	1.24	2.31	83.3	4.97	I
13H-6, 99-101	161.79	1.25	2.27	82.0	4.55	I
14H-1, 99-101	163.79	1.30	2.44	80.2	4.05	I
14H-2, 99-101	165.29	1.24	2.43	84.4	5.42	I
14H-3, 99-101	166.79	1.25	2.44	84.3	5.36	I
14H-4, 99-101	168.29	1.25	2.35	83.0	4.90	I
14H-5, 99-101	169.79	1.26	2.43	83.4	5.01	I
14H-6, 99-101	171.29	1.26	2.39	82.9	4.84	I
15H-1, 99-101	173.29	1.23	2.40	85.1	5.72	I
15H-2, 99-101	174.79	1.25	2.50	84.9	5.62	I
15H-3, 99-101	176.29	1.23	2.44	85.4	5.85	I
15H-4, 99-101	177.79	1.23	2.36	84.6	5.51	I
15H-5, 99-101	179.29	1.27	2.47	83.2	4.97	I
15H-6, 109-111	180.89	1.26	2.41	82.8	4.80	I
16H-1, 99-101	182.79	1.28	2.57	83.2	4.95	I
16H-2, 99-101	184.29	1.27	2.53	83.4	5.01	I

Table T13 (continued).

Core, section, interval (cm)	Depth (mbsf)	Density (g/cm³)		Porosity (%)	Void ratio	Lithostratigraphic unit
		Bulk	Grain			
16H-3, 99-101	185.79	1.28	2.50	82.8	4.82	I
16H-4, 99-101	187.29	1.34	2.47	78.0	3.55	I
16H-5, 99-101	188.79	1.32	2.55	80.8	4.21	I
16H-6, 99-101	190.29	1.30	2.46	81.1	4.29	I
17H-1, 89-91	192.19	1.27	2.47	83.1	4.90	I
17H-2, 99-101	193.79	1.28	2.44	82.2	4.61	I
17H-3, 99-101	195.29	1.26	2.44	83.6	5.10	I
17H-4, 99-101	196.79	1.26	2.43	83.5	5.05	I
17H-5, 99-101	198.29	1.25	2.52	85.0	5.65	I
17H-6, 99-101	199.79	1.31	2.44	79.9	3.97	I
18H-1, 101-103	201.81	1.26	2.42	83.3	4.98	I
18H-2, 99-101	203.29	1.24	2.32	83.2	4.94	I
18H-4, 99-101	206.29	1.27	2.40	82.5	4.70	I
18H-5, 99-101	207.79	1.28	2.48	82.8	4.82	I
18H-6, 99-101	209.29	1.26	2.45	83.5	5.05	I
19H-1, 99-101	211.29	1.28	2.44	81.7	4.46	I
19H-2, 99-101	212.79	1.28	2.44	82.0	4.56	I
19H-3, 99-101	214.29	1.27	2.43	82.4	4.69	I
19H-4, 99-101	215.79	1.25	2.44	84.0	5.25	I
19H-5, 99-101	217.29	1.28	2.45	82.0	4.56	I
19H-6, 99-101	218.79	1.29	2.50	82.3	4.65	I
20H-1, 99-101	220.79	1.29	2.57	82.6	4.73	I
20H-2, 99-101	222.29	1.31	2.47	80.1	4.02	II
20H-3, 99-101	223.79	1.32	2.48	79.6	3.91	II
20H-4, 99-101	225.29	1.35	2.46	77.2	3.39	II
20H-5, 99-101	226.79	1.34	2.45	78.3	3.60	II
20H-6, 109-111	228.39	1.32	2.44	78.8	3.72	II
21H-1, 99-101	230.29	1.33	2.63	80.7	4.18	II
21H-2, 99-101	231.79	1.31	2.51	81.1	4.28	II
21H-3, 99-101	233.29	1.35	2.52	77.9	3.53	II
21H-4, 99-101	234.79	1.32	2.50	79.9	3.97	II
21H-5, 99-101	236.29	1.34	2.57	79.7	3.92	II
21H-6, 99-101	237.79	1.30	2.35	79.4	3.86	II
22H-1, 99-101	239.79	1.30	2.37	79.4	3.85	II
22H-2, 99-101	241.29	1.33	2.39	77.3	3.40	II
22H-3, 99-101	242.79	1.32	2.38	78.4	3.62	II
22H-4, 99-101	244.29	1.36	2.45	76.5	3.25	II
22H-5, 99-101	245.79	1.45	2.57	72.5	2.64	III
22H-6, 99-101	247.29	1.44	2.45	70.6	2.40	III
24H-1, 59-61	258.40	1.59		61.7		III
24H-1, 114-116	258.96	1.52		65.6		III
24H-4, 59-61	262.90	1.59		68.0		III
24H-4, 114-116	263.45	1.58		63.9		III
25X-1, 79-81	267.60	1.55		67.9		III
26X-1, 79-81	274.50	1.62		68.2		III

Note: This table is also available in **ASCII format.**

Table T14. Thermal conductivity values, Holes 1179A, 1179B, and 1179C.

Core, section, interval (cm)	Depth (mbsf)	Thermal conductivity (W/[m·K])	Lithostratigraphic unit
191-1179A-			
1H-3, 65	3.65	0.72	I
191-1179B-			
1H-2, 75	2.25	0.74	I
2H-2, 75	9.85	0.73	I
3H-2, 75	19.35	0.94	I
4H-3, 75	30.35	0.78	I
5H-3, 75	39.85	0.78	I
6H-3, 75	49.35	0.76	I
191-1179C-			
1H-3, 75	3.75	0.75	I
2H-3, 75	52.55	0.79	I
3H-3, 75	62.05	0.80	I
4H-3, 75	71.55	0.74	I
5H-3, 75	81.05	0.74	I
6H-3, 75	90.55	0.77	I
7H-3, 75	100.05	0.73	I
8H-3, 75	109.55	0.70	I
9H-3, 75	119.05	0.72	I
10H-3, 75	128.55	0.72	I
11H-3, 75	138.05	0.67	I
12H-3, 75	147.55	0.71	I
13H-3, 75	157.05	0.75	I
12H-3, 75	166.55	0.75	I
15H-3, 75	176.05	0.73	I
16H-3, 75	185.55	0.76	I
17H-3, 75	195.05	0.75	I
18H-3, 75	204.55	0.76	I
19H-3, 75	214.05	0.75	I
20H-3, 75	223.55	0.80	II
21H-3, 75	233.05	0.82	II
22H-3, 75	242.55	0.79	II
23H-3, 75	251.19	0.95	III
24H-3, 75	261.55	0.93	III
25X-3, 75	270.55	0.92	III
26X-3, 75	277.45	0.86	III

Note: This table is also available in **ASCII format.**

Table T15. *P*-wave velocities and densities in basalts.

Core, section, interval (cm)	Depth (mbsf)	Velocity (m/s)	Density (g/cm^3)
191-1179D-			
10R-1, 52	368.02	4389	2.56
10R-1, 63	368.13	4718	2.72
10R-1, 101	368.51	4751	2.75
11R-1, 85	377.95	5124	2.78
11R-1, 108	378.18	5253	2.84
11R-2, 84	379.44	5342	2.99
12R-4, 44	391.64	5335	2.88
12R-4, 78	391.98	5370	2.87
12R-4, 108	392.28	5346	2.88
12R-5, 13	392.83	4808	2.72
13R-1, 11	390.51	4862	2.71
13R-2, 110	393.00	5210	2.64
13R-3, 67	394.07	4982	2.73
13R-3, 86	394.26	4991	2.64
14R-1, 23	396.63	5338	2.90
14R-2, 77	398.67	5174	2.89
14R-2, 124	399.14	4698	2.70
14R-3, 44	399.84	5190	2.82
14R-3, 138	400.78	5315	2.85
17R-2, 19	420.49	4833	2.75
18R-3, 113	429.43	5093	2.81
19R-2, 97	437.37	4928	2.78
19R-2, 116	437.56	4886	2.74
19R-3, 65	438.55	4355	2.67
20R-2, 67	446.77	5004	2.72
20R-3, 132	448.92	4787	2.71
20R-4, 39	449.49	4964	2.73
20R-5, 20	450.80	5001	2.79
21R-2, 10	455.80	5155	2.79
21R-3, 74	457.94	5064	2.74
21R-3, 115	458.35	4964	2.74
21R-4, 2	458.72	5077	3.00
22R-1, 68	464.48	5085	1.81
22R-3, 123	468.03	4964	2.73
22R-4, 7	468.37	4966	2.89
22R-5, 26	470.06	5018	2.69
22R-5, 41	470.21	5032	2.73
22R-5, 103	470.83	4708	2.74
22R-6, 21	471.51	5026	2.63

Note: This table is also available in **ASCII format.**

Table T16. Average physical properties by lithostratigraphic unit.

Lithostratigraphic unit	Density (g/cm³)		Porosity (%)	Void ratio	*P*-wave velocity (m/s)	Thermal conductivity (W/[m·K])
	Bulk	Grain				
I	1.265 ± 0.003	2.470 ± 0.010	83.3 ± 0.2	5.11 ± 0.06	1541.0 ± 2.4	0.75 ± 0.01
II	1.329 ± 0.005	2.463 ± 0.023	78.8 ± 0.4	3.74 ± 0.09	1549.6 ± 1.8	0.80 ± 0.01
III	1.54 ± 0.02	2.5	67.3 ± 1.2	2.52	1517.6 ± 4.4	0.91 ± 0.02
IV						
V	2.745 ± 0.029				5002 ± 39	

Note: This table is also available in **ASCII format.**

Table T17. Vane shear data, Holes 1179A, 1179B, and 1179C.

Core, section, interval (cm)	Depth (mbsf)	Peak strength (kPa)
191-1179A-		
1H-1, 140	1.40	5.3
1H-5, 144	6.04	5.5
1H-6, 142	7.51	4.9
1H-7, 141	9.01	9.8
1H-8, 64	9.73	6.4
191-1179B-		
1H-2, 121	2.71	25.5
1H-3, 78	3.78	5.3
1H-4, 107	5.57	4.8
1H-5, 19	6.19	8.8
2H-1, 139	8.99	5.0
4H-4, 140	32.50	30.1
5H-3, 133	40.43	14.3
191-1179C-		
2H-2, 138	51.68	25.7
2H-3, 125	53.05	31.0
2H-4, 138	54.68	37.9
2H-5, 131	56.11	41.6
2H-6, 132	57.62	48.7
3H-1, 140	59.70	31.4
3H-2, 138	61.18	32.6
3H-3, 111	62.41	32.5
3H-5, 135	65.65	61.0
3H-6, 133	67.13	38.4
4H-1, 120	69.00	40.0
4H-2, 131	70.61	32.9
4H-3, 115	71.95	61.3
4H-4, 142	73.72	38.6
4H-5, 141	75.21	42.5
4H-6, 134	76.64	43.9
5H-1, 124	78.54	45.6
5H-2, 140	80.19	46.7
5H-3, 128	81.57	53.0
5H-4, 140	83.20	59.7
5H-5, 142	84.72	58.2
5H-6, 131	86.11	55.1
6H-1, 137	88.17	32.9
6H-2, 134	89.64	36.5
6H-3, 123	91.03	43.8
6H-4, 134	92.64	89.7
6H-5, 139	94.19	47.6
6H-6, 126	95.56	47.7
7H-1, 127	97.57	78.6
7H-2, 143	99.23	65.4
7H-3, 116	100.46	80.2
7H-4, 140	102.20	63.6
7H-6, 136	105.16	40.3
8H-1, 135	107.15	53.3
8H-2, 141	108.71	51.1
8H-3, 131	110.11	32.5
8H-5, 136	113.16	43.4
8H-6, 134	114.64	35.2
9H-1, 135	116.65	52.2
9H-2, 138	118.18	69.9
9H-4, 135	121.15	66.1
9H-5, 124	122.54	56.3
9H-6, 108	123.88	97.1
10H-2, 112	127.42	48.1
10H-3, 143	129.23	54.2
10H-4, 113	130.43	79.1
10H-5, 143	132.23	63.9
10H-6, 143	133.73	56.4
11H-2, 124	137.04	23.5
11H-3, 119	138.49	39.8
11H-4, 139	140.19	63.2
11H-5, 128	141.58	61.8
11H-6, 137	143.17	55.1
12H-1, 121	145.01	51.5
12H-2, 104	146.34	61.3
12H-3, 140	148.20	86.6
12H-4, 126	149.56	76.6
12H-5, 135	151.15	63.8
12H-6, 136	152.66	61.9
13H-3, 138	157.68	93.9
13H-4, 121	159.01	96.6
13H-5, 126	160.56	118.6
13H-6, 110	161.90	97.4
14H-1, 137	164.17	53.9
14H-2, 125	165.54	62.9
14H-4, 126	168.56	71.4
14H-5, 128	170.08	97.5
14H-6, 124	171.54	94.7
15H-1, 117	173.47	50.3
15H-2, 118	174.98	51.8
15H-3, 135	176.65	61.8
15H-4, 131	178.11	70.3
15H-5, 137	179.67	83.5
15H-6, 119	180.99	71.6
16H-3, 104	185.84	76.4
16H-5, 124	189.04	87.2
17H-1, 140	192.70	51.8
17H-6, 139	200.19	78.8
18H-3, 129	205.09	65.3

Note: This table is also available in **ASCII format.**

Table T18. Correlation of reflection traveltime with the lithostratigraphic column using measured *P*-wave velocities, Site 1179.

Traveltime (s)		Depth	Velocity (m/s)		Reflection	
Observed	Estimated	(mbsf)	Corrected*	Interval	strength	Correlation
0		0	1470		Strong	Seafloor
0.018				1579	Weak	?
0.038	0.040	60	1486		Weak	Small perturbation in PWL velocity at 60 mbsf
				1622		
0.075	0.080	120	1502		Weak	Very slight increase in velocity at 120 mbsf
				1400		
0.100	0.105	155	1512		Weak	Slight increase in density at 155 mbsf
				2000		
0.115	0.125	185	1520		Weak	Increases in velocity and density at 185 mbsf
0.132				1027	Weak	?
			1530			
0.152	0.149	223			Weak	Unit I/Unit II: increase in density at 215–225 mbsf
			1540			
				2400		
			1546			
0.162	0.165	247			Weak	Unit II/Unit III: abrupt change in velocity and density at 245 mbsf
			1556			
0.172					Strong	?
			1566			
?	0.188	283			Strong	Unit III/Unit IV: top of chert
0.220					Strong	?
0.250		275			Moderate	Unit IV/Unit V: top of basement

Notes: * = Measured velocities have been corrected for in situ temperature at top and bottom of each lithostratigraphic unit: d*V*/d*T* = 3.2 m/s/°C. PWL = *P*-wave logger. Data from seismic profile line 2-1, *Hakuho Maru,* August 1996. ? = no correlation. This table is also available in **ASCII format.**

Table T19. Correlation of reflection traveltime with the lithostratigraphic column, Site 1179.

Seismic line 2-1				Seismic line 2-4					
One-way traveltime (s)	Depth* (mbsf)	Velocity (m/s) Calculated†	Velocity (m/s) Interval	One-way traveltime (s)	Depth* (mbsf)	Velocity (m/s) Calculated†	Velocity (m/s) Interval	Reflection strength	Correlation
0	0	1590		0	0	1590			
			1556				1556		
0.018	28	1605		0.018	28	1605		Weak	?
			1600						
0.038	60	1622					1607	Weak	Small perturbation in PWL velocity at 60 mbsf
			1649	0.057	91	1639		Weak	Very slight change in GRA density
0.075	121	1655					1615	Weak	Very slight increase in velocity at 120 mbsf
			1651						
0.100	162	1677		0.100	162	1677		Weak	Slight increase in density at 155 mbsf
			1669				1669		
0.115	187	1691		0.115	187	1691		Weak	Increases in velocity and density at 185 mbsf
			1684				1687		
0.132	215	1707		0.138	226	1713		Weak	Unit I/Unit II at ~221–222 (221.5) m: increase in density at 215–225 mbsf
			1701				1706		
0.152	249	1726		0.155	255	1729		Strong	Unit II/Unit III at ~247 m: abrupt changes in velocity and density at 245 mbsf
			1716				1721		
0.162	267	1736		0.170	280	1744		Weak	Changes in PWL velocity, GRA density, and NGR at 260–270 mbsf
			1725				1733		
0.172	284	1746		0.180	298	1754		Strong	Unit III/Unit IV: top of chert at ~283 mbsf
			1755				1764		
0.220	368	1795		0.230	386	1806		Strong	Unit IV/Unit V: top of basement at ~375 mbsf
			1795						
0.250	422	1828						Moderate	?

Notes: * = Depths estimated using $z = -3030 \times \ln(1 - 0.52t)$ (Carlson et al., 1986). † = Velocity estimated from $v(z) = 1590\exp(0.00033z)$ (Carlson et al., 1986). PWL = *P*-wave logger, GRA = gamma-ray attenuation, NGR = natural gamma ray. ? = no correlation. This table is also available in **ASCII format.**

Table T20. Instrument package deployment, Site 1179.

Step	Start time/date	Cumulative time (hh:mm:ss)	Description
0	1445 21 Aug		Make up seismometer string; weld lifting eyes to battery frame; move battery frame to moonpool; install cable reel stands and rig sheaves in moonpool
1	1557 21 Aug	0	Move seismometer string to rig floor
2	1608 21 Aug	0:11:00	Make up 4.5-in casing joint to seismometer, horizontal on deck
3	1627 21 Aug	0:30:00	Pick up seismometer and make up seismometer to stinger
4	1635 21 Aug	0:38:00	Slowly lower stinger/seismometer into moonpool
5	1643 21 Aug	0:46:00	Make up instrument cable connections in moonpool
6	1757 21 Aug	2:00:00	Test seismometer through instrument cable
7	1813 21 Aug	2:16:00	Begin strapping and wrapping two cables as instrument package is lowered; install centralizers
8	1830 21 Aug	2:33:00	Run 39 joints (~454 m) of 4.5-in casing
9	0215 22 Aug	10:18:00	Move hanger/riser on rig floor
10	0302 22 Aug	11:05:00	Make up hanger/riser to 4.5-in casing
11	0330 22 Aug	11:33:00	Pick up hanger/riser and lower to moonpool level
12	0435 22 Aug	12:38:00	Cut two cables to length
13	0444 22 Aug	12:47:00	Raise hanger/riser, feeding free end of cables into subsea shop
14	0500 22 Aug	13:03:00	Make up cable terminations
15	2210 22 Aug	30:13:00	Make up cables to the multiple-access expandable gateway
16	0016 23 Aug	32:19:00	Test seismometer/multiple-access expandable gateway
17	0102 23 Aug	33:05:00	Test vibration-isolated television over riser/hanger
18	0130 23 Aug	33:33:00	Lower landing assembly of seismometer
19	0945 23 Aug	41:48:00	Reenter (~11 hr, 15 min); lower vibration-isolated television and inspect installation
20	1500 23 Aug	47:03:00	Land hanger/riser in reentry cone Maintain compression on hanger/riser to prevent it from lifting off the landing seat
21	1515 23 Aug	47:18:00	Pump 50 bbl of 15.8 lb/gal (~1900 kg/m^3) cement slurry/drop dart; recover vibration-isolated television
22	2000 23 Aug	52:03:00	Prepare battery frame in moonpool; test power control system/storage acquisition module (~0130 hr)
23	0023 24 Aug	56:26:00	Attach bridle assembly to battery frame; wait on daylight
24	0415 24 Aug	60:18:00	Slowly lower battery frame on logging line to reentry cone
25	0905 24 Aug	65:08:00	Land battery frame in cone; activate acoustic release; recover logging line/bridal assembly/acoustic releaser
26	1229 24 Aug	68:32:00	Lower vibration-isolated television to inspect
27	1445 24 Aug	70:48:00	Release running tool

Note: This table is also available in **ASCII format.**

Table T21. Remotely operated vehicle tasks to start the NEREID-191 system, Site 1179.

Step	Task
1	Activate the NEREID observatory
1.1	Dive with the SAM-191 and the SAM-ROV interface
1.2	Locate Hole 1179E
1.3	Check the status of the Hole 1179E reentry cone area
1.4	Check the status of the instruments and cables on the PAT
1.5	Replace the SAM-191 dummy for the SAM-191
1.5.1	Land the ROV on the top of the PAT
1.5.2	Put the SAM-191 on the top of the PAT temporarily
1.5.3	Cut the ropes fixing the SAM dummy to the SAM seating frame
1.5.4	Remove the SAM dummy from the SAM seating frame
1.5.5	Grip the SAM-191 and place it on the SAM seating frame
1.6	Make the connection between the MEG-191 and the PAT
1.6.1	Remove the trigger pins fixing the ROV jumper cable to the top of the PAT
1.6.2	Move and land the ROV at the ROV-UMC parking position
1.6.3	Remove the ROV-UMC from its parking position
1.6.4	Move the ROV to the front side of the MEG-191 by gripping the ROV-UMC
1.6.5	Insert the ROV-UMC to the UMC on the top of the MEG-191
1.7	Check the status of the NEREID observatory
1.7.1	Land the ROV by the SAM-191 on the top of the PAT
1.7.2	Remove the dummy plug from the UMC on the SAM-191
1.7.3	Connect the SAM-ROV interface with the SAM-191
1.7.4	Make an RS232C connection between the SAM-191 and computer on the surface
1.7.5	Check the status of the system
1.7.6	Disable the connection between the SAM-191 and the computer
1.7.7	Remove the SAM-ROV interface from the SAM-191
1.7.8	Put the dummy plug on the UMC of the SAM-191
1.7.9a	If there is no problem with the system:
1.7.9a.1	Go back to the surface and wait 1–2 days for the SAM-191 to record data
1.7.9a.2	Go to step 2 (data recovery)
1.7.9b	If there is a problem with the system:
1.7.9b.1	Cut the string fixing the releasing lever for the SAM-191 to the PAT
1.7.9b.2	Remove the SAM-191 from its seating frame using the releasing lever
1.7.9b.3	Place the SAM-191 on the PAT temporarily
1.7.9b.4	Insert the dummy SAM to the SAM seating frame
1.7.9b.5	Bring the SAM-191 to the surface
1.7.9b.6	Check the system of the SAM-191
1.7.9b.7	If something is wrong with the SAM-191, replace it with another one
1.7.9b.8	Dive with the SAM-191 and the SAM-ROV interface
1.7.9b.9	Go to step 1.5.1
2	Data recovery
2.1	Prepare the SAM-191
2.2	Dive with the SAM (new) and the SAM-ROV interface
2.3	Locate Hole 1179E
2.4	Replace the SAM-191
2.4.1	Land the ROV by the SAM-191 on the top of the PAT
2.4.2	Place the SAM (new) on the PAT temporarily
2.4.3	Remove the SAM-191 from its seating frame using the releasing lever
2.4.4	Place the SAM-191 (previous one) on the PAT temporarily
2.4.5	Grip the SAM-191 (new) and insert it to its seating frame
2.4.6	Go to steps 1.7.2–1.7.8
2.4.7a	If there is no problem with the system:
2.4.7a.1	Grip the SAM-191 (previous one) and return to the surface
2.4.7b	If there is a problem with the system:
2.4.7b.1	Leave the SAM-191 (new) in its seating frame
2.4.7b.2	Grip the SAM-191 (previous one) and return to the surface
2.4.7b.3	Analyze the data from the SAM-191 (previous one) and work out countermeasures
3	Recovery of the DL
3.1	Dive after confirmation that the NEREID observatory works well
3.2	Locate Hole 1179E
3.3	Land the ROV by the DL on the top of the PAT
3.4	Remove the trigger pins fixing the DL to the PAT
3.5	Grip the rope of the DL and return to the surface

Note: SAM = storage acquisition module, ROV = remotely operated vehicle, PAT = power access terminal, MEG = multiple-access expandable gateway, UMC = underwater mateable connector, DL = data logger.